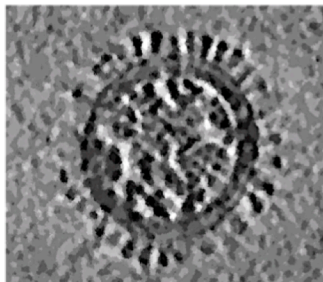


Influenza A virus: Investigation of novel therapeutic treatments and underlying mechanisms

Oliver James Debski-Antoniak

Submitted in accordance with the requirements for the degree of
Doctor of Philosophy



The University of Leeds
Faculty of Biological Sciences
School of Molecular and Cellular Biology

September 2021

Intellectual Property and Publication Statements

The candidate confirms that the work submitted is his own and that appropriate credit has been given where reference has been made to the work of others.

This copy has been supplied on the understanding that it is copyright material and that no quotation from the thesis may be published without proper acknowledgement.

The right of Oliver James Debski-Antoniak to be identified as Author of this work has been asserted by him in accordance with the Copyright, Designs and Patents Act 1988.

© 2021 The University of Leeds and Oliver James Debski-Antoniak

Acknowledgements

Chapter 3: Dr. Christian Tiede (BSTG, University of Leeds) carried out IAV HA-specific Affimer screening.

Chapter 4: Dr. Ian Wilson (Scripps research institute) for providing trimeric HA for any single particle cryo-Electron microscopy (EM) undertaken. David Klebl (University of Leeds) for help making rapid spray-cryo-EM HA/HA-Affimer grids, resolving the native HA structure and guidance in processing structural data of HA-Affimer complexes. Alex Flynn (University of Leeds) for compound selection based from Affimer molecules loops.

First things first, I would like to give Juan a huge thank you for the opportunity to develop my scientific skills, the platform to enhance my career and the continual support and guidance (and the occasional comment to bring me back down to earth). Thank you to Chris Randall and Eric Hewitt for the continual guidance and encouragement throughout my development in Leeds. To the EM facility staff and its members, Becky, Emma, Dan and Martin, your hard work, often behind the scenes, is appreciated by many besides me. I appreciate you hosting me for 4 years without a single complaint. Cheers to everyone in the office over the years who have offered help when needed and made my time completing this PhD truly enjoyable. To the Fontana group, in particular Sammy, Alex and Ellie, who have provided great scientific conversation, advice and okay friendship (I guess). Sammy you've been exceptional since you joined the team and a huge asset to us all, thanks for not murdering me.

Josh, thanks for being a friend at work and at home, for your tips and support whilst I carried out processing jobs, and for all the enjoyable times as a housemate. Last but by no means least, Molly, congratulations for your unrivalled patience combing through my whole thesis and helping to correct my terrible grammar throughout (no doubt this very acknowledgment section is riddled with terrible grammar). I'm sure you already know how much I appreciate everything you do for me, but thanks for continually being my rock

Abbreviations

-ssRNAs	Single-stranded, negative sense RNAs
Abs	Antibodies
ADCC	Antibody-dependent cell-mediated cytotoxicity
AS	Antigenic sites
BaCl₂	Barium Chloride
BKCa	Ca ²⁺ activated K ⁺ channel
BSTG	BioScreening Technology Group
BUNV	Bunyamwera virus
Ca²⁺	Calcium
CAP	Community acquired pneumonia
CCD	Charge coupled device
CCHFV	Crimean-Congo haemorrhagic fever virus
CDR	Complementary-determining regions
Cl⁻	Chloride
CLIC	Cl ⁻ intracellular channels
COBRA	Computationally optimised broadly reactive antigen
CPMV	Cowpea Mosaic virus
cRNA	Complimentary RNA
cryo-EM	Cryo-electron microscopy
cryo-ET	Cryo-electron tomography
CTD	C-terminal domain
dAbs	Domain antibodies
DARPs	Designed ankyrin repeat proteins
DC-SIGN	Dendritic cell-specific intercellular adhesion molecule-3-grabbing nonintegrin
ED	Ectodomain
EE	Early endosome
EGFR	Epidermal growth factor receptor
ELISA	Enzyme-linked immunosorbent assay
Fab	Antigen-binding fragment
FcyRs	Fcy receptors
FRET	Förster resonance energy transfer
GIRK	G protein coupled
GPCR	G-protein-coupled receptor
H	Heavy chains
HA	Hemagglutinin
HAI	Hemagglutination inhibition assay
HAZV	Hazara virus
HCV	Hepatitis C virus
HIV	Human immunodeficiency virus
IAV	Influenza A virus

IBV	Influenza B virus
ICVs	Irregularly coated vesicles
IFN-γ	Interferon- γ
Ig	Immunoglobulins
IMPα	Importin α
IMPβ	Importin β
IVs	Influenza viruses
K⁺	Potassium ions
K⁺ channel	Potassium channel
K2P	Two-pore-domain K ⁺ channel
KATP	ATP sensitive K ⁺ channel
KCa	Intermediate conductance Ca ²⁺ activated K ⁺ channel
KCl	Potassium Chloride
Kir	Inward rectifier K ⁺ channels
KV	Voltage-gated K ⁺ channels
L	Light chains
LC-MS	Liquid chromatography–mass spectrometry
LEs	Late endosomes
M	Matrix
M1	Matrix 1
M2	Matrix 2
mAbs	Monoclonal antibodies
MCPyV	Merkel cell polyomavirus
MDCK	Madin-Darby Canine Kidney
MGL1	Macrophage galactose-type lectin 1
MHC-II	MHC class II
MHRA	Medicines and Healthcare products Regulatory Agency
MMR	Macrophage mannose receptor
MOI	Multiplicity of infection
MTOC	Microtubule organising centre
MVA	Modified Vaccinia Ankara
NA	Neuraminidase
Na⁺	Sodium
NADPH	Nicotinamide adenine dinucleotide phosphate
NAIs	Neuraminidase inhibitors
NaV	Voltage-gated Na ⁺ channels
NEP	Nuclear export protein
NESs	Nuclear export signals
Neu5Ac	N-acetylneuraminic
Neu5Gc	N-glycolylneuraminic
Ni	Nickel
NK	Natural killer

NKP44	Natural killer P44-related protein
NKP46	Natural killer cell p46-related protein
NMDAR	N-methyl-d-aspartate receptor
NMR	Nuclear magnetic resonance
NP	Nucleoprotein
NPC	Nuclear pore complex
NS1	Non-structural protein 1
PBS	Phosphate buffered saline
PBS-T	Phosphate buffered saline with Tween
PCR	Polymerase chain reaction
Qd	Quinidine
RBC	Human red blood cell
RBS	Receptor binding site
RCA	Ricinus communis Agglutinin I
RdRp	RNA dependant RNA polymerase
RT	Room temperature
RT-PCR	Reverse polymerase chain reaction
SA	Sialic acid
scFv	Single chain fragment variables
SDM	Site-directed mutagenesis
SHAPE-MAP	Selective 2'-hydroxyl acylation analysed by primer extension and mutational profiling
SPLASH	Sequencing of psoralen-cross- linked, ligated and selected hybrids
SPR	Surface plasmon resonance
ssNCRs	Segment specific noncoding regions
TB	Terrific broth
TEA	Tetraethylammonium
TMD	Transmembrane domain
UTRs	Untranslated regions
VHH	Variable heavy homodimers
VLP	Virus-like particle
VNAR	Variable new antigen receptor
VOPBA	Virus overlay protein binding assay
vRNA	Virus ribonucleic acid
vRNPs	Virus ribonucleoproteins
WB	Western blot
WHO	World health organisation
ZIKV	Zika virus

Abstract

Influenza viruses (IVs) are one of the most widespread, medically important family of viruses. One of the key characteristics of IVs, is the large and diverse host species pool, owed to the characteristic rapid evolution this family of viruses undergo, enabling the successful global spread. This rapid evolution is especially important in influenza A virus (IAV) infections. All current antiviral drugs, which target the viral proteins directly, lead to resistance. Seasonal infection by IVs are the cause of up to 650,000 deaths worldwide annually, whilst the potential for a pandemic variant emerging, which would likely lead to an even greater magnitude of mortalities, is high. Therefore, the requirement for novel treatments is essential.

Here Affimer molecules, often termed 'antibody mimics', due to characteristic high affinity and specificity were investigated. Affimer molecules were isolated, specific to the IAV glycoprotein hemagglutinin (HA), which is crucial for facilitating entry to host cells. Potent neutralisers of multiple IAV strains have been isolated and characterised both biochemically and structurally. In which Affimer molecules were found to prevent entry, through the disruption of IAVs interaction with the host-cell receptor. Further still, structural information reveals the interaction between one Affimer molecule and HA induces a rare conformational change to HA. These findings, give promise to a novel method of treating IAV infection, with the potency of antibody treatment, whilst removing many of the drawbacks of these molecules.

The investigation of IAV therapeutics, through indirect methods are also investigated here, in which the role of potassium ions (K^+) during IAV infection was explored. Ion channel modulators are a large family of FDA approved drugs used for the treatment of channelopathies. Here, broad-spectrum potassium channel (K^+ channel) inhibitors were exploited, revealing inhibition of multiple strains of IAV, suggesting inhibition of a conserved mechanism required for infection. This mechanism was further characterised by biochemical and visual investigation, which agree with recent findings in the literature, that K^+ plays a role in the early stages of IAV infection, specifically as it passes through the endocytic pathway. Structural work shows this ionic prompt, increases the efficiency of the disassembly of the matrix layer, crucial for the release of viral ribonucleoproteins (vRNPs).

Ultimately, this work highlights the potential for alternative treatments of IAV infection, alongside providing further insight into IAVs mechanism of infection.

Table of Contents

Abstract.....	2
Chapter 1 Introduction.....	11
1.1.1 Influenza virus origins and discovery.....	12
1.1.2 Classification.....	12
1.1.3 Epidemiology and zoonosis	13
1.1.4 Seasonal influenza	16
1.1.5 Pandemic influenza	17
1.2 IAV genome and structure.....	18
1.2.1 Genome organisation	20
1.2.3 Viral proteins	20
1.3 IAV life cycle.....	26
1.3.1 Entry, Fusion and vRNP release	27
1.3.3 Nuclear import, transcription, and replication.....	30
1.3.4 Egress, assembly and release	31
1.4 Influenza vaccine strategies.....	32
1.4.1 Current vaccine strategies.....	33
1.4.2 Next generation vaccine strategies	35
1.4.3 Alternative targets	36
1.5 Current and perspective antiviral treatments	38
1.5.1 Influenza licensed treatments	38
1.5.2 Antibody treatments	39
1.5.3 Antibody Fragments	40
1.5.4 Non-antibody proteins/ antibody mimics	42
1.6 Affimer molecules	44
1.6.1 Structure and isolation of specific Affimer molecules.....	44
1.6.2 Applications of Affimer molecules	46
1.7 Host cell ion channels.....	47
1.7.1 Potassium channels.....	50
1.8 Project aims	53
Chapter 2 Materials and Methods	55
2.1 Materials.....	56
2.1.1 Chemicals & reagents.....	56
2.1.2 Bacterial strains	56
2.1.3 Plasmids.....	57
2.1.4 Mammalian cell lines, cell culture and storage	57
2.1.5 Virus strains	58
2.1.6 Recombinant HA proteins	58
2.1.7 Compounds	60
2.1.8 Antibodies and conjugates	61
Anti-H3N2 NP	61
2.1.9 Growth media.....	62
2.1.10 Buffer recipes	62
2.1.11 Microscopes	63
2.2 Mammalian cell culture and virus work.....	63
2.2.1 Passaging mammalian cells	63

2.2.2 IAV propagation.....	63
2.2.3 IAV storage	64
2.2.4 IAV titre determination via plaque assay	64
2.2.5.....	64
2.2.6 Cell viability via MTT assay	65
2.3 Manipulation of DNA	65
2.3.1 Polymerase chain reaction	65
2.3.2 DNA restriction digest	66
2.3.3 Agarose gel electrophoresis	67
2.3.4 Ligations	67
2.3.5 DNA measurement	67
2.3.6 DNA sequencing	67
2.4.1 Transformation of <i>E.coli</i> by heat shock	68
2.4.2 Generation of glycerol stocks	68
2.4.3 Purification of DNA via miniprep	68
2.5 Protein analysis.....	68
2.5.1 Protein concentration measurement	68
2.5.2 Dialysis of purified protein	68
2.5.3 SDS-polyacrylamide gel electrophoresis (SDS-PAGE)	69
2.5.4 Western blotting	69
2.6 Production and purification of IAV to electron microscopy standards.....	69
2.6.1 IAV propagation for purification.....	69
2.6.2 IAV high-grade purification	70
2.7 Isolation of Hemagglutinin from whole virus	70
2.7.1 Hemagglutinin crude extraction.....	70
2.7.2 Affinity chromatography	70
2.7.3 Anion exchange chromatography	71
2.8 Phage display techniques	71
2.8.1 Biotinylation of target proteins with EZ-Link® NH-SS-Biotin	71
2.8.2 ELISA to confirm biotinylation	71
2.8.3 Phage display against biotinylated targets.....	72
2.6.4 Phage ELISA	77
2.9 Affimer production and purification	78
2.9.1 Affimer expression and purification	78
2.9.2 Sub-cloning Affimer from phagemid vector to pET-11a plasmid	79
2.9.3 Affimer Maleimide labelling	80
2.9.4 Mass spectrometry to assess biotinylation of Affimers	81
2.10 Characterisation of Affimer-HA interactions	81
2.10.1 Affinity assessment via HA-ELISA	81
2.10.2 Microneutralisation assay	81
2.10.3 Surface plasmon resonance affinity determination of Affimers	82
2.10.4 Hemagglutination assay	82
2.10.5 Fusion assay.....	82
2.10.6 Egress Assay	83
2.10.5 <i>In-silico</i> predictive protein-protein interactions.....	83
2.10.6 Affimer loop compound selection.....	83
2.11 Electron microscopy	84
2.11.1 Negative stain EM grid preparation	84
2.11.2 Transmission electron microscopy (TEM)	84
2.11.3 HA and HA-Affimer Cryo-EM rapid grid preparation.....	84
2.11.4 HA and HA-Affimer Cryo-EM detergent grid preparation	85
2.11.5 IAV - K+	85

2.11.6 Cryo-EM grid screening	86
2.11.7 Cryo-EM single particle collection	86
2.11.8 Image processing HA/HK68 homotrimer.....	88
2.11.9 Image processing of A31-HA/HK68 homotrimer complex	89
2.12 K⁺ channel and its influence on IAV infection	90
2.12.1 Plaque reduction assay.....	90
2.12.2 Pre-Infection K ⁺ channel broad spectrum inhibitor treatments	90
2.12.3 Ammonium chloride time course.....	91
2.12.4 K ⁺ channel broad spectrum inhibitor time course	91
2.12.5 IAV priming with broad spectrum K ⁺ channel inhibitor	91
2.12.6 Priming buffers	92
2.2.7 IAV priming with pH and K ⁺ ions	92
2.2.8 IAV priming with broad spectrum K ⁺ channel inhibitor and with pH and K ⁺ ions.....	92
2.12.9 Cryo-electron tomography collection	92
2.12.10 Reconstructing 3D tomograms.....	93
2.13 Data presentation and analysis	93
2.13.1 Data presentation and analysis	93
<i>Chapter 3 Isolation and production of IAV HA-specific Affimer molecules</i>	<i>94</i>
3.1 Chapter introduction.....	95
3.2 Isolation of cross-reactive Affimer molecules	98
3.3 Expression and purification of Affimer molecules.....	103
3.4 Broad spectrum Affimer molecules show no inhibition <i>in vitro</i>.....	104
3.5 Isolation of Aichi-specific Affimer molecules	106
3.6 Expression and purification of HA-specific Affimer molecules.....	109
3.7 Initial assessment of Affimer molecules <i>in vitro</i>.....	109
3.8 Selection of Affimer molecules to be further characterised	111
3.9 Expression and purification of HA-specific Affimers with free cysteine	111
3.10 Biotinylation of HA-specific Affimer molecules	112
3.11 Alexa Fluor-488 labelling of Affimer molecules.....	116
3.12 Discussion	117
<i>Chapter 4 HA-Specific Affimer molecules can trap intermediate conformations of HA....</i>	<i>121</i>
4.1 Chapter introduction.....	122
4.1.1 Head domain binding antibodies	123
4.1.2 Stalk domain binding antibodies	124
4.1.3 Design and discovery of novel anti-HA drugs.....	125
4.2 Affimer molecules show high affinity interactions to HA	126
4.3 Affimer molecules show potent inhibition against target strain.....	128
4.4 Affimer molecules show potency against other H3N2 subtypes.....	129
4.4 Affimer molecules show potency to pandemic H1N1.....	131
4.5 Affimer molecules block sialic acid binding.....	134
4.6 Cryo-electron microscopy confirms A31 binds to HA globular head	138
4.6.1 Cryo-grid preparation.....	138
4.6.2 Data collection and image processing.....	139

4.6.3 Flexible fitting of crystal structure.....	143
4.7 Affimer variable loops can be used to identify novel anti-IAV small molecules	145
4.7.1 Variable loop compound selection.....	145
4.7.2 Initial characterisation shows promise for therapeutic variable loop mimic compounds	147
4.8 Discussion	150
<i>Chapter 5 Targeting K⁺ ion channels as therapeutic targets for IAV infections.....</i>	155
5.1 Introduction	156
5.2 Initial probing with K ⁺ channel inhibitors confirms K ⁺ plays a significant role in IAV infection	158
5.3 Selection of channel modulators based on previously published RNAi knockout studies ...	159
5.4 K ⁺ channel modulators reduce IAV (H3N2 A/Aichi/1968) infectivity in A549 cells	161
5.5 K ⁺ channel modulators inhibit infection of multiple IAV strains in A549 cells	164
5.6 Treatment of A549 cells with dalfampridine affects IAV entry via the endocytic pathway .	165
5.7 Priming of IAV virions confirms K ⁺ plays a role in early stages of infection	168
5.8 Priming of influenza virions with K ⁺ enhances the uncoating of the M1 layer.....	171
5.9 Structural information provides visual insight into virion entry and fusion mechanisms....	175
5.10 Discussion	178
<i>Chapter 6 Concluding remarks</i>	185
Objective 1: Isolation, expression and production of monomeric HA-specific Affimer molecules.	186
Objective 2: Characterisation and validation of HA-specific Affimer molecules using a range of virology, biophysical and biochemical techniques.	186
Objective 3: Screening and characterisation of a panel of broad-inhibiting K ⁺ channel inhibitors as therapeutics of IAV	188
<i>Chapter 7 References.....</i>	190

List of Figures:

Figure 1.1: Zoonotic transmission of IAV (HA subtypes)	16
Figure 1.2: Schematic of an influenza A virion	19
Figure 1.3: Phylogenetic tree of HA subtypes and functionally labelled HA structure.....	22
Figure 1.4: IAV life cycle.....	27
Figure 1.5: Vaccine effectiveness determined by the CDC and regional vaccine roll-out ...	35
Figure 1.6: Antibodies and engineered antibody-like constructs.....	42
Figure 1.7: Crystal structure of an Affimer molecule.....	45
Figure 1.8: 'Phage display for Affimer screening	47
Figure 1.9: Structural comparison of a K ⁺ channel and IAV M2 viroporin.....	49
Figure 1.10: Figure 1.8 K ⁺ channel classification	52
Figure 3.1: Alignment of antigenic sites of IAV (H3N2) surrounding the RBS by year	96
Figure 3.2: Alignment of antigenic sites of A/(H1N1) virus RBS by year	97
Figure 3.3: Pipeline carried out to isolate broadly binding Affimer molecules against a variety of different HA proteins (H3/1968 Aichi, H3/2002 Fijian, H3/2004 California).....	99
Figure 3.4: Phage ELISA results for Affimer molecules selected against individual H3 proteins H3/1968 Aichi, H3/2002 Fijian, H3/2004 California).....	100
Figure 3.5: Phage ELISA to assess intra-HA subtype (H3/1968 Aichi, H3/2002 Fijian, H3/2004 California) and inter-HA subtype (Albany/1951, New York/1918 and USSR/1977) binding of Affimer molecules	102
Figure 3.6: Consensus residues of isolated Affimer molecules and purification	103
Figure 3.7: Broad-spectrum Affimer cytotoxicity and inhibition properties against A/Aichi/1968 (H3N2)	105
Figure 3.8: Pipeline carried out to isolate Affimer molecules against A/Aichi/1968 (H3N2) HA.....	106
Figure 3.9: Phage ELISA to assess binding of Affimer candidates to H3/Aichi/68	107
Figure 3.10: Consensus residues of isolated Affimer molecules and phylogenetic tree of sequence similarity between unique Affimer molecules	108
Figure 3.11: Expression and purification of pDhis -Affimer Vectors in Jm83 cells	109
Figure 3.12: Affimer cytotoxicity and microneutralisation assay against A/Aichi/1968(H3N2)	110
Figure 3.13: Expression and purification of pET-11a-Affimer Vectors in DE3 cells	112
Figure 3.14: Biotinylation of Affimer molecules	113
Figure 3.15: LC-MS confirmation of biotinylation.....	115
Figure 3.16: Alexa Fluor-488 linking of Affimer molecules.....	116
Figure 3.17: Schematic showing the difference in phage display selection and assessment when compared to neutralising IAV	118
Figure 4.1: Schematic illustrating mechanisms of inhibition monoclonal antibodies undertake when targeting HA.....	122
Figure 4.2: SPR analysis of binding kinetics between Affimer molecules and HA	127
Figure 4.3: A5 and A31 show high affinity to HA via ELISA.....	128
Figure 4.4: Microneutralisation of Affimer isolated IAV	129
Figure 4.5: Microneutralisation of a range of H3N2 viruses.....	131
Figure 4.6: Microneutralisation of members of H1N1 subtype.....	133

Figure 4.7: TCID50 values of microneutralisation assays and RBS sequence alignments of virus strains used	133
Figure 4.8: Unravelling HA mechanism of action and region of function	135
Figure 4.9: Affimer molecules mechanism of action	137
Figure 4.10: Micrographs of HA and HA in complex with Affimers A5 or A31	139
Figure 4.11: 2D classes selected for downstream processing	140
Figure 4.12: 3D classes showing extra density in both C1 and C3 imposed symmetry	141
Figure 4.13: : Final reconstruction of HA-A31 at 4.8 Å resolution	143
Figure 4.14: Fit comparison of the HA-A31 map to the structural conformations of HA ..	144
Figure 4.15: HA-A31 reconstruction with flexibly fitted HA model.....	145
Figure 4.16: Affimer-mimic compound Cytotoxicity.....	148
Figure 4.17: Microneutralisation of Affimer loop compounds.....	149
Figure 4.18: Schematic showing the potential mechanism in which A31 alters HA structure	153
Figure 5.1: Initial assessment shows quinidine inhibits IAV plaque formation	159
Figure 5.2: A panel of K⁺ channel inhibitors can be utilised in A549s at non-cytotoxic doses	162
Figure 5.3: K⁺ channel modulators inhibit IAV (A/Aichi/1968/H3N2) infection when challenged in A549 cells	163
Figure 5.4: K⁺ channel modulators reduce infection across multiple IAV strains	165
Figure 5.5: Time of addition assay to define the mode of IAV inhibition by dalfampridine	166
Figure 5.6: Priming IAV virions reduces ion channel modulator inhibition	169
Figure 5.7: Effect of IAV priming with ion channel modulators	170

List of Tables:

Table 1.1: Antibody mimics properties and isolation strategy	44
Table 2.1: Bacterial E. coli strains used during this project	56
Table 2.2: Plasmids used during this project. amp: ampicillin, carb: carbenicillin	57
Table 2.3: Mammalian cell lines used during this project	57
Table 2.4: Viral strains used during this project.....	58
Table 2.5: Recombinant proteins used during this project	60
Table 2.6: Compounds used during this project	61
Table 2.7: Antibodies and conjugates used during this project.....	62
Table 2.8: : Reaction components for PCRs carried out using Phusion HF DNA polymerase	66
Table 2.9: Reaction conditions for PCRs carried out using Phusion HF DNA polymerase ...	66
Table 2.10: Kingfisher Flex 'Phage_display_pH_elution' protocol.....	76
Table 2.11: Extraction buffer composition	79
Table 2.12: PCR primer sequences, cystine is highlighted in bold	80
Table 2.13: Cryo-EM priming buffer contents.....	86
Table 2.14: David Klebls overnight data collection for HA/HK68	87
Table 2.15: 72 hr data collection for HA/HK68 complexed with A31.....	88
Table 4.1: Table showing compounds selected using variable loop regions of A5.....	147
Table 5.1: Top K ⁺ channels implicated in IAV infection, along with known ion channel modulators.....	161
Table 5.2: Summary of drugs used and inhibition of IAV	179

Chapter 1

Introduction

1.1 Influenza virus

1.1.1 Influenza virus origins and discovery

Influenza viruses have been well documented through the course of history, with recordings of epidemic outbreaks featuring across the timeline of recorded human civilisation. Scholars claim the first historical reference of influenza stems back to over 2400 years ago, in 412 BC. Hippocrates, considered the father of modern medicine, recorded an outbreak relating to an infectious disease dubbed “Fever of Perinthus” which he documented as an epidemic of the upper respiratory tract (1). There are many references to “Influenza” outbreaks throughout the human records, though many are scarce in detail. In fact, influenza was not officially recognised as a viral infection in humans until 1933, and was previously thought to be a bacterial infection. English scientists Sir Christopher Andrews and Sir Patrick Laidlaw first isolated the IAV from a patient’s nasal secretions (2). At this point, understanding and ways to combat infection rapidly developed. The 1930s saw the discovery of allotropic membrane propagation of Influenza virus within chicken eggs and the isolation of the first neutralising antibodies (Abs) against Influenza (3). Since its first identification, influenza has continued to be a threat to human health and economic stability, with the WHO listing an Influenza pandemic as one of the ten greatest threats to global health, since the 20th century began, there has been 5 influenza pandemics (1918, 1957, 1968, 1977 and 2009), causing huge impacts to society (4). In this report, the WHO have stressed a new global influenza pandemic is a matter of “when” and not “if” a pandemic will occur.

1.1.2 Classification

The Influenza viruses belong to the *Orthomyxoviridae* family. Orthomyxoviridae family members contain an RNA genome that is negative sense in polarity, with the viral genome segmented between six and eight segments dependant on genera. Currently, this family is separated into seven different genera, based on serological characteristics and nucleotide sequence homology. Members of the family are: *Alphainfluenzavirus* (Influenza A virus), *Betainfluenzavirus* (Influenza B virus), *Gammainfluenzavirus* (Influenza C virus), *Deltainfluenzavirus* (Influenza D virus), *Isavirus* (Isavirus),

Thogotovirus (Araguari, Aransas Bay, Dhori, Jos, Thogoto and Upolu), and more recently *Quaranjavirus* (Quaranfil, Cygnet River, Johnston Atoll, Tyulek Wellfleet Bay and Lake Chad viruses).

The influenza viruses share a common genetic ancestry, and are classified by sequence homology of internal nucleoprotein (NP) and matrix (M) proteins. These viruses have genetically diverged such that the individual genera cannot undergo reassortment of vRNPs between each other (5). Influenza A and influenza B viruses are by far the most researched in the family of *Orthomyxoviridae*. Both viruses cause seasonal global epidemics which can cause severe infection in the human upper respiratory tract, leading to possible hospitalisation or death, and are considered a major concern to public health. In this body of work, IAV will be the main focus.

All influenza viruses are classified into strains, according to a standardised naming convention employed by the world health organisation (WHO) (6). The nomenclature organises viruses into: antigenic type (A/B/C), species of the host it was isolated from (if human this is omitted), followed by geographic origin, strain number and finally the year of isolation. If IAV is being named, this is also followed by the subtype. An example of this, and the main strain utilised in this body of work is: A/Aichi/2/1968 (H3N2). IAV itself consists of a wide range of distinct virions, which are further categorised into subtypes. Typically, these subtypes are identified by the glycoproteins which decorate the surface of virions, HA and neuraminidase (NA), utilising reverse-transcriptase polymerase chain reaction (RT-PCR) to define these. To date, there are 11 NA (N1-N11) and 18 HA (H1-H18) subtypes identified for IAV, the combination of these providing the subtype. Potentially there are 144 different subtype combinations, though only 131 subtypes have been detected so far in nature (7).

1.1.3 Epidemiology and zoonosis

Influenza virus the causative agent of flu, is an acute respiratory disease in humans. The global burden of this disease to population and economy is significant (8,9). Estimates by the WHO state there are 1 billion cases of flu, 3-5 million cases of severe illness and between 300,000 and 650,000 deaths annually worldwide (10). Influenza virus is transmitted through aerosols and infection is particularly severe in neonates, the elderly and the immunocompromised. Community acquired pneumonia (CAP), hypoxemia and leukopenia are often linked with more severe infection. Whilst bacteria are the most common cause of pneumonia, viruses also cause pneumonia, whether as the primary infection or co-pathogen alongside bacteria. Currently, influenza induced pneumonias, are extremely difficult

to distinguish from other viral (including SARS-CoV-2), bacterial and atypical pneumonias, making accurate diagnosis and treatment a limiting factor during hospital treatment. This results in a significant complication for treatment of severe influenza-like illnesses. A systematic review prior to the COVID-19 outbreak of 28 studies identified respiratory viruses in 22 % of CAP patients (n= 8,777). With a further 10% of CAP patients isolated for mixed respiratory virus and bacterial co-infections. Of these respiratory virus associated infections, influenza accounted for 9 %, rhinoviruses 5 % and coronaviruses 4 % (11).

IAV is a paradigm for emerging viruses, with the largest and antigenically diverse host range of the orthomyxoviruses (**Figure 1.1**). The virus infects more than 100 species of water fowl which are its typical reservoir. Additionally, mammalian hosts include humans, swine, seals, whales, mink, horses, guinea pigs, bats and dogs; and domestic or wild bird hosts including chicken and ostriches (12,13). The virus is capable of jumping across the species barrier, with interspecies transmission commonly occurring, particularly between humans and pigs, and poultry and pigs. Transmission between other species is more sporadic. The ability to transmit between species is determined by the virions capacity to adapt specificity to the target species, which can partly be determined by the promiscuity and/or mutation propensity of HA decorating the virion, which binds to sialic acid (SA) on cellular receptors of the host cell. This tropism is affected by the type of SA linkage in the host. For example, the site of primary infection in avian species is the gut, where the epithelial cells are predominantly decorated with α (2,3) sialic linkages (14). Virions decorated with HA that has a high affinity to this linkage therefore can infect this host. Human primary infections occur in the upper respiratory epithelial cells, predominantly decorated with α (2,6) linkages (15); infections are therefore carried out by subtypes with affinity to this linkage. On the other hand, α (2,3) linkages are found in the lower respiratory tract of humans (16), allowing avian strains such as H5N1 viruses to infect (17), though human to human infection requires upper respiratory tract infection, leaving avian infections predominantly self-limiting . Of major concern for interspecies transmission are swine, the respiratory tract of swine contains SA with both α (2,3) and α (2,6) linkages. As a result, swine are often referred to as 'mixing vessels' (18): swine allow a range of subtypes to co-infect respiratory epithelial cells, enabling the interchange of different genomic segments, giving rise to pandemic strains (19).

IAV is notorious for its ability to promote antigenic diversity, which is achieved through two particular mechanisms, antigenic drift and antigenic shift (20). The IAV RNA polymerase is key to antigenic drift due to its error prone nature. It has no proof-reading mechanism thus mutations arise at a rate of $7.26 \times 10^{-5} \text{ bp}^{-1}$ (21). Functional mutations are localised largely to HA and NA, resulting in antigenic variants

which have the potential to re-infect a host and avoid pre-existing immunity, creating epidemics (22). Typically infection rates of 10-30 % in adults and 20-50 % in children, spanning at least 6-12 weeks occur due to these epidemics (23). Antigenic shift on the other hand, is the process of much larger genetic alterations, in which different subtypes of IAV co-infect 'mixing vessels' such as swine, allowing the reassortment of genetic segments. A novel segment is often not sufficient on its own to introduce a pandemic strain, requiring additional mutations to enable sustained human infection. For example, the HA sequence of the pandemic A/California/04/2009 (H1N1) was sequenced and an α (2,6) glycan binding adaption was introduced through the E225D mutation, alongside a lysine at residue 145, accommodating for both α (2,3) and α (2,6) binding (24).

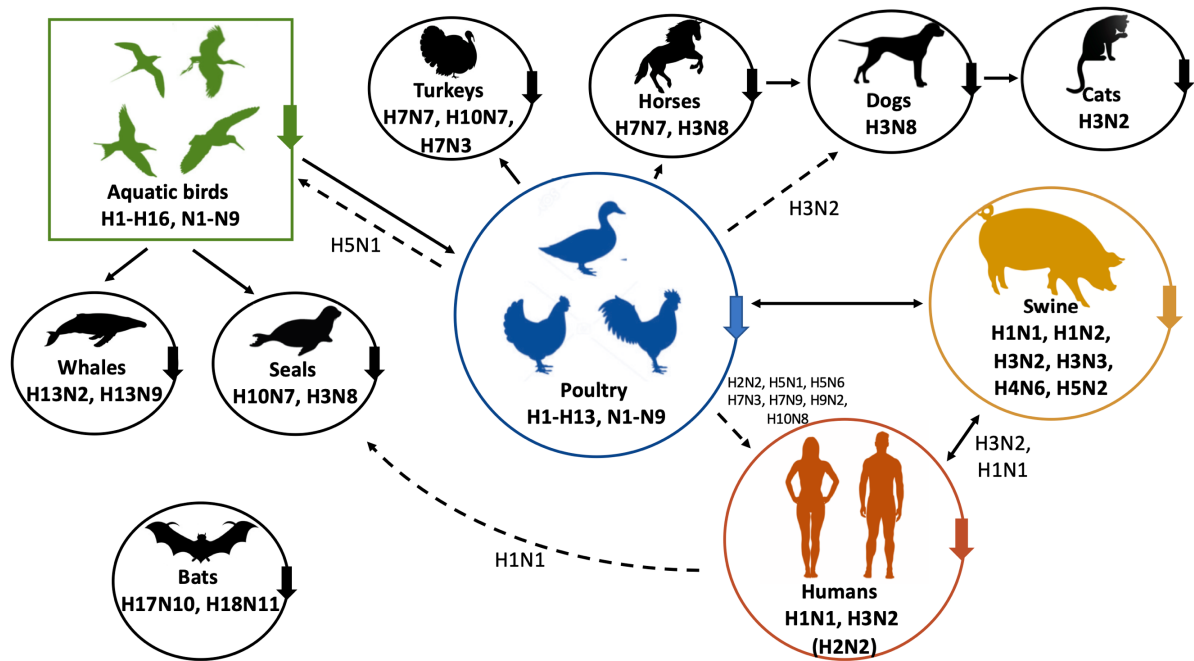


Figure 1.1: Zoonotic transmission of IAV (HA subtypes)

IAVs (H1-H16) natural reservoir is aquatic birds, subtypes are transmissible to many different species directly or, sometimes through intermediate hosts (12,13). Human-adapted influenza viruses H1, H2 and H3 subtypes have circulated since the 20th century (species-adapted influenzas located within the species circle/square). H1N1 and H3N2 are the current circulatory strains found amongst human populations whilst H2N2 was previously a circulatory strain; the same three subtypes are found to circulate amongst swine. Avian influenza viruses subtypes H2, H5, H7, H9 and H10 have infected humans following exposure to poultry, but do not exhibit human-human transmissibility (self-limiting transmission represented by dotted lines) (17). H17 and H18 only circulate amongst bat species. Made in Microsoft PowerPoint adapted from (25).

1.1.4 Seasonal influenza

The major burden of influenza disease to human health is caused by seasonal epidemics of IAV and IBV. IBV has separated into two distinct lineages, B/Victoria/2/1987-like and B/Yamagata/16/1988-like, these have been in circulation globally since 1983 (26,27). Seasonal IAV on the other hand is currently dominated by the circulation of H1N1 and H3N2 strains in humans, each year new variants

of these strains are introduced and cause epidemics. Following the 1918 pandemic, H1N1 were the only circulatory strains of IAV, while between 1957 and 1968 H2N2 viruses became the only human strains circulating. Introduction of IAV from avian or swine populations has given rise to four pandemics since 1918, these viruses subsequently became the seasonal epidemic strains for the years following.

1.1.5 Pandemic influenza

Pandemic influenza virus strains have arisen semi-frequently, with 4 pandemics occurring from the 20th century alone. The 1918 pandemic is estimated to have claimed more than 50 million lives and caused more than 500 million infections worldwide (28), highlighting how devastating pandemic infections have the potential to be. There has been three pandemics in which novel IAV strains have emerged and re-emerged since 1918. During these pandemics, IAV typically spread rapidly from the point of origin to the rest of the world during several waves of infection. The 1918 H1N1 virus was a result of an avian influenza virus acquiring functional mutations to enable human transmission (25). Epidemiological data suggest the driving factor of the pandemic was a novel HA which large portions of the populations did not have immunity to (28). All influenza pandemics since appear to have been due to antigenic shift: the 1957 Asian flu (H2N2) arose from a reassortment of 1918 H1N1 with HA/NA/PB1 segments of an avian IAV; whilst the 1968 Hong Kong flu (H3N2), was also a result of the reassortment in swine, H2N2 and HA/PB1 segments from another avian IAV, likely H3N1 replaced the circulating H2N2 strain (28). Notably, both the Asian and Hong Kong originating pandemics ended with a mortality of up to 2 million people each. Finally, the first pandemic of the 21st century, the 2009 ((H1N1 (pdm09))) is considered to have a unique genome, in which segments originating from swine, human and avian strains of IAV, co-infected swine, leading to a reassortment event across three viral subtypes (29).

The possibility of another influenza pandemic is extremely high, with the WHO stating it is an inevitable (4). This could be catastrophic both to global health and the economy. The World Bank estimates that the potential economic losses for an influenza pandemic outbreak could lead to 71 million human deaths and would cost the global economy US \$3 trillion (30). With vast numbers of households being pushed below the poverty line as a long-term effect of an outbreak. As an example,

COVID-19 has caused high global mortalities alongside crippling global and local economies of up to US \$3.8 trillion in costs (at the time of writing) (31). Currently there are large concerns surrounding avian strains H5N1 and H7N9, which have sporadically been isolated in the human population. H5N1 is a highly pathogenic avian influenza (HPAI), and in 2003 H5N1 gained a mutation in its HA, creating the emergence of a novel strain 'Z', which was able to readily infect humans (32). H5N1 has a mortality rate as high as 60 % amongst young children (33), as of 2006 was circulating Europe and Asia, outbreaks in 13 new countries have been recorded (32). H7N9 is also of worry, although this strain is considered a low pathogenic avian influenza (LPAI) as it cannot sustain human-human transmission (34). The mutational switch in HA SA linkage preference is likely required for avian epidemics to persist to pandemics, samples from H7N9 infected humans and avian species have been isolated with some key mutations required for this transition (35). This virus has caused five human epidemics in China since 2013 causing severe respiratory disease and high mortalities (~39 %) (36).

1.2 IAV genome and structure

IAV is a pleomorphic virion and appears as either spherical virions, with a diameter typically between 80 nm and 120 nm, or as filaments, which can extend in length as far as 20 μ m (37). When passaging IAV through the allotonic fluid of eggs or MDCK cells, the population of virions is largely spherical (38), though, clinical isolates are typically populated with elongated filamentous virions (39), though the reason for this difference is currently unclear. Both forms of virion are composed of a host-derived membrane, referred to as an envelope (**Figure 1.2**). The envelope is decorated with the glycoproteins HA and NA and to a lesser extent the viral ion channel matrix 2 (M2), which also spans the envelope (40,41). Supporting the envelope, a matrix layer consisting of matrix 1 (M1) proteins forms a viral core within the envelope. This M1 layer interacts with the viral segments containing the viral ribonucleic acid (vRNA) required to produce progeny virions (42). These segments contain a single RNA dependant RNA polymerase (RdRp) coated by the NP, consisting of three subunits of viral polymerase (PA, PB1, PB2). IAV also produces 2 non-structural proteins: non-structural protein 1 (NS1) and the nuclear export protein (NEP). The 8 vRNPs encode for 10 essential proteins for progeny survival, though several strain-dependant proteins may also be expressed (43). More recently 8 further proteins were identified, produced through splicing frame shift and truncation of the coding region of the structural proteins : PB1-F2, PB1-N40, PA-X, NS3, PA-N155, PA-N182, M42 and most recently PB2-S1 (44). These NSPs have been found to play crucial, though not essential roles in host defence suppression, virulence and pathogenicity, though non-essential unlike NS1 and NS2.

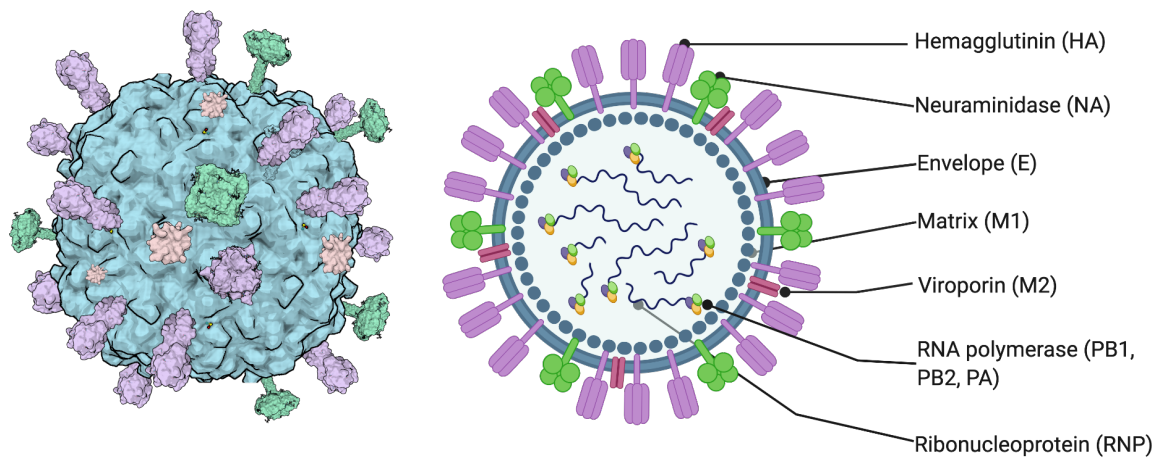


Figure 1.2: Schematic of an influenza A virion

IAV is a pleomorphic virus typically with a diameter of 80-120 nm. The 8 single-stranded, negative-sense RNAs (-ssRNA) segments are associated with the RdRp forming vRNPs. The vRNPs are packaged within a M1 matrix layer and a lipid-envelope which is decorated in trimeric HA and tetrameric NA glycoproteins. M2 viroporin channels enable the passage of ions into the viral core during endosomal trafficking. Structures used for schematic (PDB: 6CRD, 2RLF and 5hmg) Created with BioRender.com

1.2.1 Genome organisation

The genome of IAV is segmented into 8 -ssRNAs. These RNA segments are concealed by multiple copies of nucleoprotein, to form viral vRNPs (45,46). Each vRNP segment is bound to a single copy of the heterotrimeric viral polymerase (PB1, PB2 and PA), at a helical hairpin, which is a result of conserved semi-complementary base pairing between the 5' and 3' ends (47–49). Recent work was carried out utilising high-throughput selective 2'-hydroxyl acylation analysed by primer extension and mutational profiling (SHAPE-MaP) (50), which enables analysis of the IAV RNA structure at single-nucleotide resolution by probing the conformational flexibility (base pairing) of each nucleotide. This technique suggests the parts of the -ssRNA of the vRNPs is exposed and accessible in order to form intermolecular RNA–RNA interactions between segments (51). This was further validated *in virio* using sequencing of psoralen-cross-linked, ligated and selected hybrids (SPLASH)(51,52). Transmission electron microscopy has revealed the vRNPs are organised within virions in a 7 + 1 arrangement, with a central segment surrounded by seven other vRNPs (53). These separate findings suggest the coating of vRNA segments is organised enabling these crucial interactions between vRNPs facilitating the packaging of segments during budding of progeny virions.

1.2.2 Untranslated regions

IAV RNA segments consist of an open reading frame flanked by untranslated regions (UTRs), typically between 19 and 58 nucleotides in length (54). The UTRs of IAV genes consist of a highly conserved motif sequence, which can be found at the 3' and 5' termini of each of the eight segments amongst all viral strains. The UTRs also consist of segment specific noncoding regions (ssNCRs), the sequence and length of the ssNCRs are specific to each vRNA segment, whilst also differing between species and are were also believed to be responsible for the organisation and packaging of the viral genome, though more recent studies utilising SHAPE-MaP and SPLASH suggest organisation of the vRNPs relies on specific regions of both translating and untranslating regions (55,56).

1.2.3 Viral proteins

1.2.3.1 HA

HA, a glycoprotein and class 1 fusion protein, decorates the viral envelope, it is the most prominent glycoprotein (300-400 spikes/virion) and is responsible for viral entry to the host cell. Structurally, HA is a glycosylated homotrimer with each monomer composed of two subunits: globular head (HA1) and a stem region (HA2), which are the result of the HA0 precursor being proteolytically cleaved by host proteases (57). The HAs of different subtypes, though structurally similar, have distinct amino acid sequences (58). The 18 known HA subtypes can be divided into 2 groups, based on sequence similarity: Group 1 and Group 2 (Figure 1.3a). A central dogma in IAV research has been that a difference in species subtypes is determined by the receptor binding site (RBS) preference for differing SA linkages (avian receptors have largely α (2,3) linkages as opposed to humans α (2,6) linkages) (15). This SA specificity can change, due to a number of well characterised amino acid substitutions. Mutations in avian HA RBS that have caused human pandemics are well illustrated such as: E190D and G225D in H1 subtypes and Q226L and G228S in H2 and H3 (59). The disparity between amino acid sequences, alongside the rapid mutation HA undergoes (particularly in the globular head) is the main challenge in the treatment of IAV infection, as there are very limited conserved regions for a universally potent neutralising antibody or antiviral treatment. The globular head of HA bears a N-acetylneuraminic acid (Neu5Ac) (SA) binding pocket, and the surrounding regions to this pocket are the focal points of these antigenic drift mutations (60,61) (Figure 1.3b). The SA binding pocket is essential for the recognition and attachment to host cell receptors and one of the main targets for neutralising Abs. The stem domain anchors HA to the viral membrane and facilitates the fusion of viral and cellular membranes in order to release IAV vRNPs to the cellular cytosol. Though the stalk region is far more conserved, the different glycosylated regions of different subtypes, creates a further challenge in the pursuit of universal treatment (62,63).

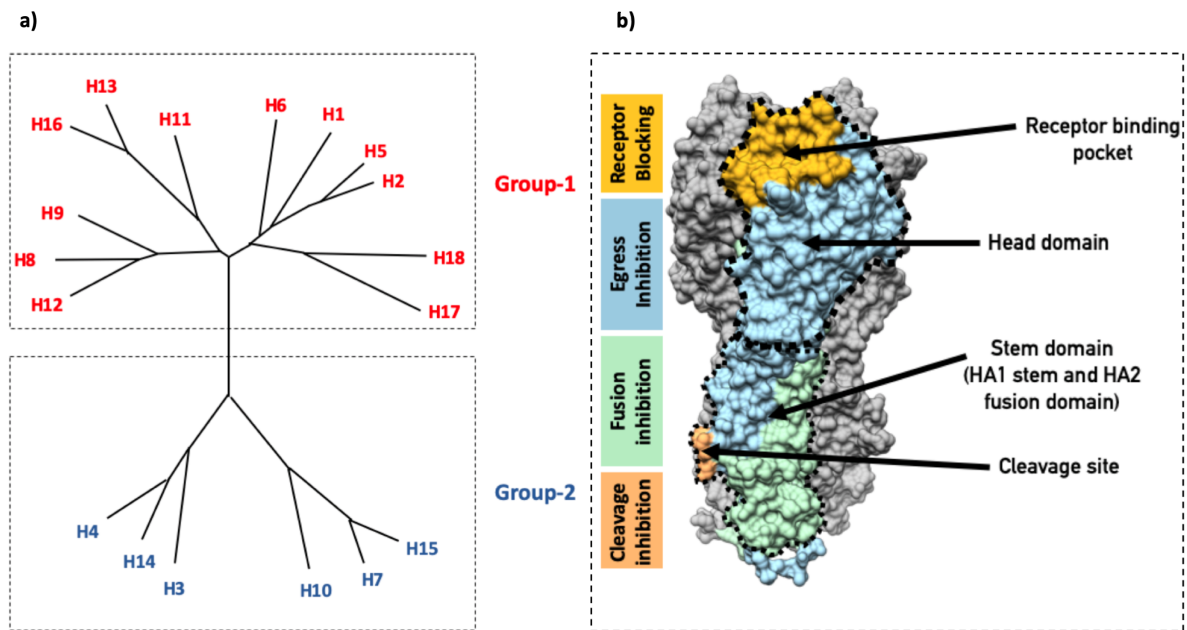


Figure 1.3: Phylogenetic tree of HA subtypes and functionally labelled HA structure

a) Phylogenetic tree of the 18 IAV subtypes, classified into two groups. A representative HA protein sequence was selected for each subtype from the following subtypes of viruses: H1N1, H2N2, H3N2, H4N6, H5N1, H6N2, H7N3, H8N4, H9N2, H10N7, H11N6, H12N5, H13N6, H14N5, H15N9, H16N3, H17N10, and H18N11. The phylogenetic tree was made utilising Clustal Omega. **b)** Space-fill HA structure (A/Aichi/1968/H3N2 PDB: 6WXB). One monomer, along with HA1 and HA2 domains are highlighted by dotted lines, the remaining 2 monomers are coloured grey. Regions of functional importance and antibody targets are highlighted in different colours: Yellow-Orange (RBS), Blue (Egress), Green (Fusion of viral and cellular membranes) and Orange (HA0 cleavage site) (64).

1.2.3.2 NA

NA is the other glycoprotein decorating IAV, though it is far less abundant (40-50 spikes/virion). Structurally NA forms a glycosylated tetramer of 4 identical monomers, which fold into four distinct domains: the catalytic head, stalk, transmembrane region and cytoplasmic tail (65). In total there are 11 subtypes of NA based on phylogenetic mapping. These are divided into 3 groups, including the 2 bat NAs (N10 and N11). Group 1 consists of: N1, N4, N5, and N8, and group 2: N2, N3, N6, N7, and N9 serotypes (66). NA, like HA, is involved in sialic acid binding. Though, its major function is at the end of the viral life cycle, when it cleaves sialic acid from cellular receptors interacting with HA and NA of nascent virions (viral glycoproteins sialylated by the host cell as part of the glycosylation process) (67,68). More recently NA has also been shown to interact with sialidase 'decoy' receptors, such as

mucins, which are found in high concentrations in mucus, though little is understood about this interaction (69). The catalytic domain referred to as the '150 loop', forms part of the cavity for substrate binding (69). NA inhibitors are based off the crystal structures of group 2 cavities: these sialic acid derivatives selectively lock the 150-loop cavity in an open confirmation (70,71). Whilst still in use, similarly to HA-targeting therapeutics, resistance acquired through antigenic drift has largely made these inhibitors obsolete (20).

1.2.3.3 M2

The M2 ion channel is a class 1 viroporin and type 3 integral membrane protein (72). Structurally, the M2 channel is a homotetramer connected by 2 disulphide bonds per monomer. Each monomer can be divided further into an N-terminal ectodomain (ED), middle transmembrane domain (TMD) and C-terminal domain (CTD) (73). The M2 homotetramer is a pH-regulated ion channel that is selective for protons. The channel is activated by a low exterior pH, which in turn opens the channel and allows an influx of these protons. M2 has a preference for protons, though the channel has some permeability for Na⁺ and K⁺ (10⁶-10⁷ fold less permeability) (74,75). The regulation of protons and cations is necessary in order to destabilise the core of virion, an essential mechanism for efficient unpackaging of the vRNPs (76). The M2 viroporin also influences viral morphology and genome packaging through its cytoplasmic interaction with the M1 layer, alongside its role in the destabilisation of the M1 layer and vRNP bundle (73,77). Finally, M2 plays a role in budding and release of progeny virions, in which abscission of host/progeny virion is localized to the site of M2 proteins on the membrane (73,77). Anti-viral therapeutics such as adamantane have been identified which block the influenza virus viroporin, causing complete inhibition of infection (78,79). These inhibitors are however quickly being rendered ineffective through production of progeny virions with mutations in the viroporin, with 100% and 50% of circulating H3N2 and H1N1 IAVs (respectively) conferring resistance to adamantane (Reviewed in (72)).

1.2.3.4 M1

The most abundant and highly conserved protein of IAV is the M1 protein (95% amino acid sequence identity for the M1 protein amongst globally sampled IAV strains in humans and other species (80)). It is highly conserved (5-10 fold slower evolution than HA amongst seasonal IAV (80)), likely due to its multifunctionality, playing a role in many essential roles throughout the viral life cycle (81). M1 is a small, two-domain protein consisting of a NTD and CTD. Though the structure of the NTD has been resolved for some time by crystallography (82), the whole structure of M1 was only recently described

by cryo-ET and sub-tomogram averaging, in which monomers consisting of 12 alpha helices show a disordered CTD in solution, which becomes organised upon interaction with other M1 monomers (83). The monomers form a tightly packed layer mediated by intricate interactions between one another. The oligomerised layer is closely associated with the viral membrane and thought to aid in the structural integrity of influenza virions (84). The M1 layer is associated with many of the virally expressed proteins, likely due to its role in genome packaging, viral assembly and budding. The vRNPs are also tethered to the inside of the M1 layer, the release of this interaction is required in order to achieve successful infection (85,86). NEP interactions with the M1 layer are thought to enable the successful export of vRNPs from the nucleus in a 'daisy-chain complex' and facilitates assembly into progeny virions (87). Alongside the interaction with M2, the M1 layer interacts with the CTD of both glycoproteins (HA and NA) due to its role in viral assembly (88). Thus far there are no approved M1 targeting therapeutics, largely due to the previous lack of structural information. An M1 assembly blocker has recently been identified through *in situ* drug discovery, giving promise for this viral protein as an antiviral target, particularly as M1 is highly conserved, likely making it hard for escape mutants (89).

1.2.3.5 NP

NP is also highly expressed and conserved, many regions of the NP sequence are highly conserved across IAV, IBV and ICV (90), highlighting its functional importance. Influenza viruses' RNA is coated in NP, which is a small basic protein consisting of an N-terminal region (91), the RNA-binding region, and 2 domains responsible for NP-NP interactions for polymerisation (92). These interacting regions are crucial for the organisation of the vRNPs. NP is a multifunctional protein which plays roles in many key life cycle events. In the early stages of the viral life cycle, NP facilitates vRNP import to the nucleus via the nuclear localisation signals (NLSs) (93). It is required for RNA synthesis within the nucleus, aiding in the synthesis of longer RNAs, whilst also interacting with PB1 and PB2 of the RdRp, suggesting a role in the regulation of the polymerase (94,95). The interaction between NEP, NP, M1 and newly synthesised vRNA is believed to be required for nuclear export and budding (87). Furthermore, NP also functions as an adaptor molecule, mediating interactions between viral and cellular processes. Through the yeast 2-hybrid assay NP has been shown to interact with NPI-1 and NPI-3, cellular proteins which help facilitate the transport of vRNPs to the nucleus (93,96). Due to its multifunctionality and consequently highly conserved regions, antivirals targeting NP would make an ideal broadly acting treatment. This has led to the high-throughput breakthrough of potential drugs which act directly on the NP, such as Nucleozin, an inhibitor of the pockets Y52 and the Y289/N309 pocket, found directly opposite the RNA binding domain (97,98).

1.2.3.6 PA, PB1, PB2

The RdRp consists of three proteins PA, PB1 and PB2, forming a heterotrimer and making it one of the largest viral polymerases identified (99). It plays a key role in the replication and transcription of the vRNAs, discussed further in 1.3.3. RdRp is bound to both 5' and 3' ends of the vRNAs and further wrapped by NP, to resemble a corkscrew structure (100). The subunits of the RdRp work in cooperation with one another during transcription, in which PB2 is responsible for the 5' cap snatching of host cell mRNA (101), followed by cleavage of the cap by the endonuclease activity of PA (102,103), and finally the elongation of the capped RNA along the vRNA genome and polyubiquitination addition by PB1 (104). During replication both PB1 and PB2 form a large cavity in order for replication to be carried out (105,106). Currently there are three different classes of drugs being developed targeting the RdRp: RNA synthesis inhibitors, cap snatching inhibitors and those which target the protein-protein interactions between the RdRp subunits (107).

1.2.3.7 NS1

NS1 is a small multifunctional, non-structural protein encoded by influenza. The multifunctionality of NS1 includes the inhibition of the host innate immune defences, control of viral RNA synthesis and splicing, restriction of cellular mRNA polyadenylation alongside the interaction with various cellular signalling pathways (108–110). Due to its multifunctional role, chiefly in the suppression of the host cell immune system, such as the IFN cascade response, makes it a promising antiviral candidate (111). The three domains of NS1 consist of: a N-terminal RNA binding domain, an effector domain and a C-terminal tail. NS1 is well characterised in the literature and is known to interact with a large array of host cellular factors, many of which subdue the immune response to viral presence. NS1 binds to the RBD of RIG-I, this RBD identifies viral dsRNA inducing an immune response upon recognition. NS1 actively inhibits this recognition site, preventing viral dsRNA binding. Structural information of potential therapeutic targets aids the drug discovery process and as such NS1 has ~45 structures available on the protein databank (PDB), most of which are in complex with cellular proteins (112,113).

1.2.3.8 NS2/NEP

The NEP protein, also known as NS2 for its role in the export of vRNPs from the nucleus, is a small non-structural protein encoded on the same RNA segment as NS1 (114,115). NEP consists of an NTD and

CTD; the NTD contains 2 nuclear export signals (NESs) and interacts with the chromosome region maintenance 1 (CRM1), a host cellular export protein (116–118). The CTD of NEP binds to the M1 protein, creating a nuclear export complex enabling progeny vRNPs to be exported from the nucleus to the cytoplasm. Though there are currently no therapeutic drugs available for the treatment of IAV via the NEP, a compound 'DP2392-E', has been shown to bind CRM-1 and inhibit its interaction with the nuclear export complex, inhibiting infection. This may be a better target when treating influenza infections as it is likely broadly acting and less prone to mutational escape (119).

1.3 IAV life cycle

An unusual feature of the Influenza viruses when compared to other ssRNA viruses, is that the replication site for the virus takes place in the nucleus of the host cell. Due to the small viral genome, RNA viruses depend on subverting host-cell proteins, and cellular structures and functions to facilitate the viral life cycle (**Figure 1.4**).

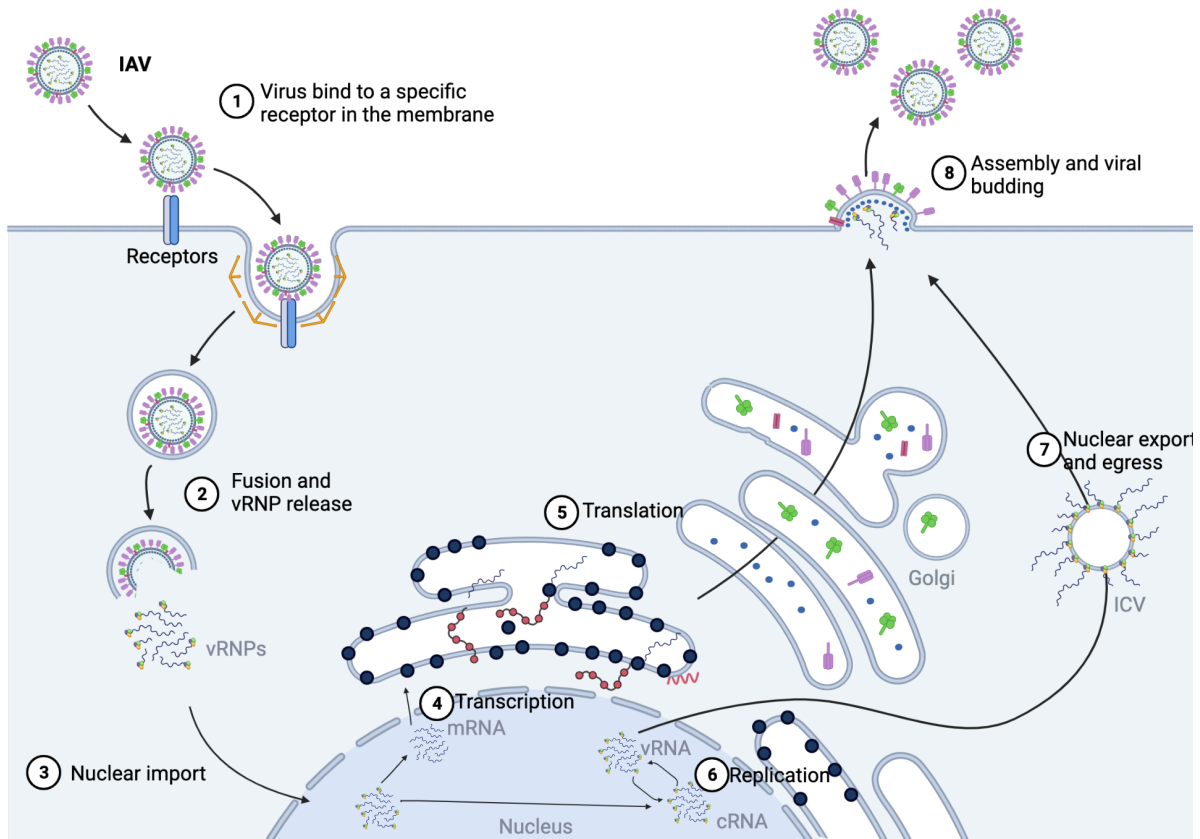


Figure 1.4: IAV life cycle

Schematic representation of the different stages of the IAV life cycle. (1) Attachment and entry, (2) fusion and vRNP release, (3) Nuclear import, (4) transcription, (5) viral protein production, (6) viral replication, (7) nuclear export of progeny vRNPs and egress (8) assembly and viral budding. Created with [BioRender.com](https://www.biorender.com)

1.3.1 Entry, Fusion and vRNP release

It has been known for decades the importance of IAV specificity for host cell receptors via sialylated glycoproteins and/or glycolipids (with the exemption of bat IAVs), with its linkage to galactose playing a crucial role in strain preference (120,121). Recently, through *in vivo* and structural studies it has been recognised that both the composition (containing either a *N*-acetyl or *N*-glycolyl group, yielding Neu5Ac or *N*-glycolylneuraminic (Neu5Gc) acid) and topology (human IAVs preferably

recognise long 'umbrella-shaped' glycans, whilst avian IAVs preferentially recognise short 'cone-shaped' glycans) contribute to the receptor specificity of IAV (Reviewed in (122)).

Not all binding events lead to internalisation, which is dependent on the glycoprotein or glycolipid which is engaged by IAV. Several specific cellular glycoproteins have now been implicated in viral attachment and successful internalisation. Sialic acid dependant receptor binding includes: nucleolin (H7N9, H3N2, PR8 and H5N1) (123), Natural killer (NK) cell p44-related protein (NKP44) and NK cell p46-related protein (NKP46) (H3N2) (124,125), epidermal growth factor receptor (EGFR) (H7N9 and PR8) (126) and more recently, the voltage-dependant calcium channel $Ca_v1.2$ (H1N1, H3N2 and PR8) (127). Utilising a virus overlay protein binding assay (VOPBA) and HA pulldowns, nucleolin was shown to play a role in internalisation, rather than attachment, making it unclear whether nucleolin involvement is sialic acid dependant (123). Though, NK cell receptors NKP44 and NKP46 have been shown to interact with HA in a sialic acid-dependent manner, in which binding to these receptors activated NK cells. The direct role these receptors play in attachment and internalisation has not yet been described, but these cells can be infected by IAV, suggesting NKP44 and NKP46 contribute to entry in this cell type (124,125). EGFR is believed to play a central role in IAV entry. Sialidase treatment hampers IAV endocytosis but not EGF-dependant endocytosis, whilst IAV and EGFR have been shown to co-localise on lipid rafts, with disruption of these lipid rafts causing impaired uptake of both IAV and EGFR (126). Further evidence of specific glycoproteins for IAV entry has arose in work carried out by Fujioka *et al*, who identified voltage-dependent calcium channel $Ca_v1.2$ as a sialic-dependant cellular entry factor. Through the use of Förster resonance energy transfer (FRET)-based imaging of Ca^{2+} sensor Yellow Cameleon (YC3.60), oscillations in Ca^{2+} were found to be caused by a specific channel, $Ca_v1.2$. Further work showed $Ca_v1.2$ knockdown by siRNA inhibits these oscillations, including IAV-induced Ca^{2+} oscillations and inhibition of virus internalisation, continued work validated this further by blocking Ca^{2+} channels with diltiazem, causing the inhibition of IAV infection *in vivo* and *ex vivo* (127).

Surprisingly, there has been recent studies which suggest a sialic-independent interaction of HA with host cells. The *N*-glycome of human lungs was isolated in order to assess binding capability IAV of different strains from different hosts via glycan array (128). Following sialidase treatment, it was found that virus binding was inhibited for sialyated glycans but enhanced for phospho-glycans, whilst phosphatase treatment inhibited phospho-glycan binding and enhanced sialyated glycan binding. Furthermore, pre-incubation with sialic acid did not affect binding to phospho-glycans, suggesting the binding site for non-sialyated receptors is different to the canonical RBS of HA (128). Distinct cell

surface proteins lacking sialic acid have been described which bind IAV and facilitate virus infection. These sialic acid-independent IAV receptors belong to the family of calcium-dependent (C-type) lectins and are largely identified on immune cells. dendritic cell-specific intercellular adhesion molecule-3-grabbing nonintegrin (DC-SIGN) has probably been the most extensively studied sialic acid-independent IAV receptor and has been implicated in promoting other viral infections: Dengue virus, human immunodeficiency virus (HIV) and hepatitis C virus (HCV) (129–131). Wang *et al*, propose the N-linked glycans located on HA may facilitate the interaction with DC-SIGN, particularly as the amount of HA glycosylation has been correlated with virus infectivity of cells over-expressing DC-SIGN (132). The endocytic receptors expressed on macrophage and DCs such as the macrophage mannose receptor (MMR) and the macrophage galactose-type lectin 1 (MGL1) have also been shown to interact directly with IAV in a sialic-independent manner, suggesting alternate mechanism for IAV entry (132,133).

Bat IAVs differ in that the unique HAs have the inability to bind sialic acid or other glycans of traditional IAVs. Work carried out utilising nuclear magnetic resonance (NMR) spectroscopy has shown bat IAVs bind MHC class II (MHC-II) receptors of the immune cells as an essential entry determinant(134,135), the interaction sites on either MHC-II or bat IAV HA currently remain unknown, whilst the mechanism of internalisation is also not well described.

Following this initial viral attachment, the interaction with the receptor results in IAV uptake through either receptor-mediated endocytosis (clathrin dependant or independent) or micropinocytosis (136–138), into the endocytic pathway. The endocytic pathway consists of a network of membranous compartments which facilitate cargo transport (139). Following uptake into the cell, IAV is internalised into an early endosome (EE), a compartment with pH of 6.0-7.0. Typically, a pathogen filled EE is targeted towards lysosomes, through the maturation of the EE, enabling the degradation of foreign bodies. IAV utilises the endosomal maturation of EEs to late endosomes (LEs), which contain a pH 5.0-6.0 (140). This acidic cue activates the viroporin M2, causing an influx of protons to the viral core. This has long been known to both activate and trigger conformational changes in the HA of IAV (though the pH in which this occurs is different dependant on subtype) (141), this enables the fusion of viral and host membranes, allowing for the release of the vRNPs. The pre- and post-fusion conformations of HA have long been described (142,143), yet the intermediate conformational changes of HA have only recently been illustrated through the power of modern cryo-EM, in which a series of intermediate structures were visualised by incubating recombinant HA at pH 5.0 for a range of timepoints (144). The low pH cue of maturing endosomes not only triggers HA-mediated fusion, but

is important in the disorganisation and disassembly of both the vRNP bundle and the M1 layer. The efficient disruption of these is crucial for the successful release of the vRNPs to the cytosol. More recently, it has been shown that the maturation of endosomes is far more complex and dynamic, involving the regulation of a range of ions as the endosomes matures (145). This has led to further understanding of early IAV infections, alongside many other viral infections, in which cations have been shown to also play important roles in the efficient infection of the host cell (Reviewed in (146)). Specifically for IAV, it has been shown biochemically through tools such as FRET that Ca^{2+} influx is important for regulation of clathrin-mediated and independent endocytosis, which is required for successful intake of IAV, further validated by the inhibition of the $\text{Ca}_v1.2$ receptor (127), whilst K^+ has been shown to play an important role in the disruption of vRNP and M1 layer organisation (76).

1.3.3 Nuclear import, transcription, and replication

Following the fusion of viral and host endosomal membrane, disassembly and disorganisation of the vRNP bundle and M1 layer, the vRNPs are released into the cytoplasm and transported into the nucleus for replication. However, IAV replication occurs in the nucleus. Proteins larger than 40 kDa require transporting across the nuclear pore complex (NPC) by cargo proteins, which recognise proteins through NLSs (147). IAV PB1, PB2, PA, NP, M1 and NS1 all contain NLSs and so are transported across the NPC via the importin α (IMP α) and importin β (IMP β) complexes, whilst NEP does not require aid by importins due to its small size (~14kDa) allowing passive diffusion.

Following nuclear import, vRNAs are transcribed to produce viral mRNAs, which in turn enable the production of viral proteins and replication to take place using the host cell machinery. Primary transcription is primer dependant: capped pre-mRNAs are arrested and cap-snatching of the 5' cap is carried out by the viral polymerase complex proteins PB2 and PA (101–103). Viral mRNA is then produced using the vRNPs as a template. The polymerase complex of the vRNP completes transcription by producing a poly-A tail, which is achieved by reiterative stuttering and copying of the poly-U sequence located at the 5' end of the vRNPs (104). The viral mRNAs are then spliced by cellular proteins and exported to enable viral protein production by the host ribosomes. Relevant viral proteins are then imported to the nucleus (via their NLS) to aid production of progeny vRNPs and to export them from the nucleus (148).

The replication of complementary RNA (cRNA) from vRNPs and vRNA from cRNPs requires the newly translated NP and polymerase complex components to be imported into the nucleus in order to protect genomic RNA from degradation (148). EM analyses of the vRNP replication complex suggests a trans genome replication model, as multiple branched RNP-like structures have been observed from parental RNPs (149). Further structural models of the complex suggest RNA packaging in NP protein is initiated by the polymerase complex which binds the 5' terminus of progeny RNAs, initiating the sequential addition of NP oligomers in the 5' to 3' direction (46).

1.3.4 Egress, assembly and release

Following successful replication, the progeny vRNPs are exported from the nucleus to the cytoplasm where egress from/of the plasma membrane occurs, allowing viral assembly and budding. Translated viral proteins re-enter the nucleus as previously described (**1.3.3**). In order for export to occur, the nuclear export complex is assembled, comprising of the newly produced vRNPs, M1 and NEP. This complex then associates with exportin1/CRM1 (108,110,135). A typical characteristic for IAV infection is increased activation of caspase 3, which through fluorescent and transmission electron microscopy techniques, it has been shown Nup153 displacement occurs due to IAV-induced caspase activity, leading to the enlargement of nuclear pores, ultimately allowing for shuttling of the export complex (151). The mechanism of newly synthesised vRNPs egress is not well established. Recently it has been found that IAV infection induces a major remodelling of the ER around the microtubule organising centre (MTOC) (152,153), alongside the formation of new organelles, referred to as irregularly coated vesicles (ICVs). Though it is unclear what the function of these ICVs is, currently, it is widely believed the IAV infection reorganises the ER for immediate uptake of newly synthesised vRNPs following nuclear export, utilising the MTOC to carry this out. The ER is then involved in Rab11-dependant biogenesis of the ICVs which display both Rab11 and vRNPs (154), these ICVs are thought to transport vRNPs from the ER to the plasma membrane.

The exact mechanism of assembly and budding is not clear, likely due to it being a complex process with a multitude of viral protein and host cell protein interactions required to assemble infectious virions. What is clear from quantitative shotgun mass spectrometry is that budding occurs on the apical side of infected cells, localised to regions of the envelope which are enriched with cholesterol and sphingolipids, referred to as lipid rafts (155). Mutagenesis studies suggest the fatty acid

modifications of the C-terminus of both HA and NA by the Golgi allows the glycoproteins to localise to these lipid rafts, in which certain mutated regions reduced this association (156–158). Through microscopy techniques, the M2 viroporin appears to localise to the periphery of the budding regions. M1 appears to orchestrate the key assembly steps of IAV, in which it localises to the CTDs of both HA and NA and in turn, the vRNPs are translocated via the ICVs to the budding site and bind to M1. Detergent and sucrose-flotation studies show Membrane-bound M1 colocalised with HA and NA to be detergent resistant and show improved floating (154).

In order to release progeny virions, budding needs to be induced, which requires significant curvature of the membrane to enable scission of the two membranes. It is likely that the molecular 'crowding' of the glycoproteins heavily influences membrane bending, especially as NA has been visualised through microscopy techniques clustered on the viral membrane (159,160). M1 likely plays a significant role in membrane bending as it is thought to localise to glycoproteins where it undergoes oligomerisation, suggesting it heavily influences the budding of the virions. M2 is found structurally at the budding site boundary, due to this it has been implicated in the bending and scission of membranes. Studies in which M2 is not present shows attenuated infection in both cell culture and mice models (73,77). Following scission, NA plays an important role in cleaving SA from cellular receptors along with cleavage from HA and NA of nascent virions which are sialylated as they are processed by the host cell (67,68).

1.4 Influenza vaccine strategies

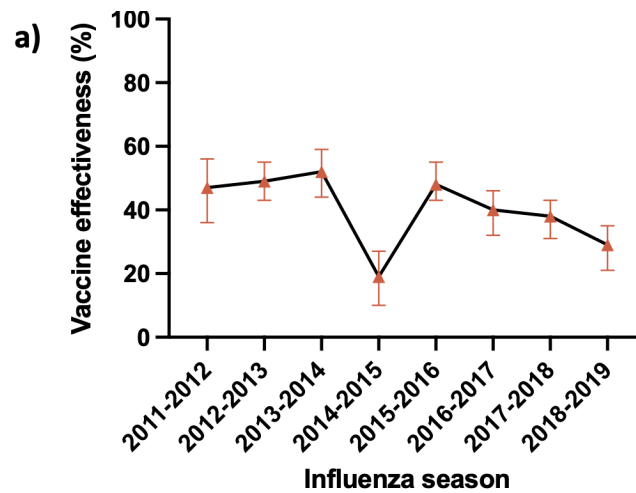
In the 1930's, the same decade that influenza was identified as a virus, studies were carried out to determine whether it was possible to vaccinate against it (2). The first vaccine, an inactivated IAV was then developed in the 1940s using fertilised chicken eggs and since then, a seasonal vaccine has been utilised to save countless lives and limit the effects of pandemic strains (161). Though we have extensive knowledge of influenza and vaccinated against it for over 70 years, an annual vaccine is still required to maintain protection against ever-evolving strains, requiring constant viral surveillance. Typically, this is by monitoring Northern or Southern Hemispheres winter seasons for drift in circulatory strains and producing relevant protection in time for these seasons in the opposite hemisphere. Vaccination efforts aim to evoke a humoral immune response in those vaccinated, raising neutralising Abs which target antigenic sites of the virus. The glycoproteins of influenza are exposed

to the immune system and are therefore immunodominant during immune responses. HA exhibits further immunodominance over NA during natural infection and after vaccination (162,163), perhaps due to its greater abundance on the viral surface. The hemagglutination inhibition assay (HAI), an assay which takes advantage of IAVs hemagglutinating properties when added to red blood cells is therefore the recognised tool to assess protection from influenza infection (164). As a result of this, HA is a target for both current seasonal vaccination efforts and for many candidates being developed for universal influenza treatment. Due to advances in immunology and virology, alongside information provided by modern structural biology and bioinformatics, there has been hope for the production of a single 'universal' vaccine, capable of evoking a broadly neutralising antibody response, preventing a breadth of different IAV strains (165,166). This broadly neutralising antibody response has been identified in naturally infected individuals and also elicited in those who have been immunised, though very rare (167–170).

1.4.1 Current vaccine strategies

Currently, seasonal vaccines contain either live attenuated or inactivated influenza viruses. Live attenuated vaccines consist of cold-adapted viruses, which are incapable of replicating efficiently at body temperature and intranasally administered. These vaccines induce strong localised mucosal immunity, but are not recommended for those who are pregnant or outside the age range of 2-49 years of age (171). Inactivated virus vaccines are either split viruses or subunit influenza antigens. The split virus vaccines are made by disrupting the viral structure with chemicals or detergents; due to the ease of this method, this approach is commonly utilised. The subunit influenza antigens are made of HA or NA partially purified from virions which are disrupted as for the split virus vaccine (172). Vaccination is either provided as a trivalent or quadrivalent vaccine, where the trivalent has viral components of 2 IAV strains and 1 influenza B virus (IBV) strain, and the quadrivalent vaccine has an additional IBV strain included. A range of these vaccines are available across the world (Figure 1.5b), however only a few hundred million doses are produced annually for the ~7 billion inhabitants of the globe, with the majority given to those in more economically developed countries. Furthermore, the vaccines efficacy is at best 60 %, and only in years when the vaccines viruses are well matched to those circulating (**Figure 1.5a**) (173,174). Whilst the pursuit for a true universal vaccine is ongoing, it is important to improve the efficacy of current vaccination strategies.

Typically, the viruses which are added to vaccines are propagated through eggs. This method of propagation introduces mutations in progeny virions, resulting in the reduction in efficiency of these vaccines. It has been found that H3N2 strains are particularly susceptible to these egg-derived mutations and as such there is a lower efficacy to H3N2 strains as opposed to H1N1 and IBV strains (2004-2015: 33 % for H3N2, vs. 61 % and 54 % efficacy for H1N1 and IBV strains, respectively) (175). Cell culture propagation is now available for many strains reducing progeny mutations, though manufacturing costs are high. HA subunit vaccines have recently been produced through recombinant expression of HA in insect cells, potentially paving the way for more efficient vaccine production (176). It has also been found that giving a high-dosed quadrivalent inactivated vaccine is far more effective than a standard dose (0.5 ml) at reducing clinical outcomes associated with influenza infection, making this practice recommended in the elderly (177,178). Increased protection in the elderly has also been found when a recombinant protein-based vaccine (FluBlok) is implemented, alongside vaccines with adjuvants included (176,179), which is likely due to enhanced subtype coverage, protecting beyond the matched vaccine strains. Utilising computer algorithms, computationally optimised broadly reactive antigen (COBRA) has been implemented to design 'consensus sequences' of antigens for vaccines. These antigens induce a more broad antibody response within subtypes such as H1, H3, and H5 strains (180–182). This new approach to vaccine design shows much more robust coverage of strains, improving efficacy and giving potential to expand coverage to different subtypes, including potential pandemic strains such as H2N2, H5N1 and H7N9 (183).



b)

Region	Manufacturer	Vaccine	Vaccine type	MOA	Adjuvant	
United States	Afluria (Seqirus)	Inactivated virus	Split virus	HAI	None	
	Fluarix (GSK)					
	FluLevel (GSK)					
	Fluzone (Sanofi Pasteur)					
	Fluad (Seqirus)		Subunit			
	Fluvirin (CLS Limited)					
	Flucelvax (Novartis)		Live-attenuated			Cold-adapted
	FluMist (AstraZeneca)		Recombinant protein			Non-purified HA
Europe	Influvac, Imuvac (Abbot)	Inactivated virus	Split virus	HAI	None	
	Fluarix, Alpharix, Influsplit (GSK)				Alum	
	3Fluart (Omninvest)				None	
	Afluria, Enzira (Pfizer/CSL)				Subunit	
	Vaxigrip, Vaxigrip Tetra (Sanofi Pasteur)					
	Agrippal (Seqirus)		Live-attenuated		Cold-adapted	MF59
	Fluad (Seqirus)					None
	Fluenz Tetra (AstraZeneca)					

Figure 1.5: Vaccine effectiveness determined by the CDC and regional vaccine roll-out
 a) Vaccine effectiveness taken from CDC estimates for influenza seasons 2011-2019. b) Vaccine availability for the United States and Europe including vaccine type, method of action and inclusion of an adjuvant.

1.4.2 Next generation vaccine strategies

The ultimate goal in influenza vaccine strategies is the production of a true universal vaccine, which provides protection against all strains. A few recent strategies have had some success in producing such a vaccine. It has been found that though far rarer than head-binding monoclonal Abs (mAbs), stem-binding mAbs are capable of inducing heterosubtypic protection. Subsequently stem-binding antibodies isolated from humans have been extensively characterised and shown to cross-react with

many strains within either group 1 or group 2 of the HA family (167,184). This is likely due to the stem domain having a greater proportion of conserved regions across each subtype, allowing for broad protection. Some of these antibodies, such as the antibody CR9114, have been shown to protect mice against both groups within IAV and against IBV (185,186). Due to the promise in stem-binding antibodies, new methods of vaccinating to induce stem-binding mAbs have been employed. Two groups recently developed 'headless' HA independently. Both of these headless immunogens were found to elicit broad protection in animals, including a heterologous lethal H5N1 infection. A chimeric HA used to prime or boost immunity has also been deployed which has shown great success in providing protection against a broad range of group 1 HAs (H1, H2, H9 and even H18) (187,188). These chimeric HAs consist of different HA1 domains but maintain the same stem domain, and are currently being evaluated at phase 1 of clinical trials. Though stem-binding mAbs present promising heterosubtypic coverage of influenza and are present in humans, they appear to be far less prevalent in human sera and less potent at neutralising compared to the mAbs directed to the HA head domain (189).

Some broadly neutralising antibodies that target the head domain of HA have also been described, such as C139/1, which neutralises many IAV subtypes (H1, H2, H3, H5, H9 and H13) (190). As an alternative approach to stem-binding antibodies, there has recently been characterisation of precise epitopes on the head domain of HA which elicit broad protection when targeted, especially those directed at the RBS or surrounding regions. However, the main challenge for this form of vaccine design will be to present as many of the conserved residues in the RBS whilst presenting minimal residues of the surrounding variable regions in order to identify truly universal mAbs.

1.4.3 Alternative targets

Whilst HA-targeting mAbs are the most predominant elicited by the immune system, other viral proteins are also targeted to some degree. Though HA is multifunctional and critical for viral entry, it is also the most variable viral protein due to selection pressures, so targeting alternative proteins in combination with HA is likely an effective method of protection. The NA glycoprotein induces some mAbs, which have been partially characterised, though little is known about the effect of these antibodies on preventing viral infection, in part due to the reliance on standardised HAI tests to measure vaccine efficiency (191). Recently broadly protective mAbs have been characterised which target the active site of NA, which is the target of previously successful antivirals (192), suggesting it is possible to induce protection through vaccines. Based on this, the development of 'consensus' NA immunogens has been carried out and testing in animal models is underway (193), giving promise for NA as a component of a universal vaccine.

Another viral protein which is targeted by antivirals is the M2 viroporin, and the ectodomain of this protein has been proposed as a potential universal vaccine component (194). Due to its multifunctionality, being critical for IAV budding and disassembly, many regions are highly conserved. Though, M2 shows good potential as a universal target, its surface exposed ectodomain shows poor immunogenicity (195). A mAb has been identified which targets the ectodomain and decreases human IAV infection (196), showing M2 as a target is still viable. Furthermore, the immunogenicity of this protein can be improved by conjugating it to various carriers or through the delivery of M2 as a Virus-like particle (VLP) (197,198). Ultimately, it is unlikely that M2-alone would be deployed as a universal vaccine, as similarly to HA and NA, escape mutants have been identified to the mAbs, increasing emphasis on the need for combination treatments.

Unconventionally, NP could be a good component in a universal vaccine in order to elicit a rounded immune response. Though NP is an internal viral protein, which prevents targeting via antibodies, it is conserved across all IAV strains. Furthermore, it has been identified that NP is a target of T cell immunity, capable of inducing CD4 and CD8 T cell responses, alongside detection by interferon- γ (IFN- γ). In an early phase clinical trial, an attenuated poxvirus vaccine - Modified Vaccinia Ankara (MVA) - M1 + NP vectored vaccine was found to elicit T cell immunity in the young and in older participants (199). It also enhanced T cell and strain specific antibody responses when used in conjunction with seasonal vaccines (200).

It is clear great advances towards a universal vaccine have been made in the last decade, largely in part due to advances in immunology and virology alongside technological improvements in computational and structural methods. Despite progress, a universal vaccine will likely take many additional years to be approved as it would require extensive testing through clinical trials before bodies such as the FDA approve its safety and efficacy.

1.5 Current and perspective antiviral treatments

1.5.1 Influenza licensed treatments

There are currently three classes of antivirals available globally for treatment of influenza infection. These are: M2 viroporin blockers (the adamantanes), neuraminidase inhibitors (NAIs) and polymerase inhibitors. The adamantanes (adamantine and rimantadine) are approved by the FDA and CDC for use against IAV infection, however they are no longer recommended due to many circulating IAV strains, alongside the 2009 H1N1 pandemic strain, developing resistance to them (201). However, these recommendations may change depending on the re-emergence of strains which show susceptibility.

NAIs were developed in the 1990s and have shown effectiveness in reducing symptoms of infection (202). NAIs include Oseltamivir (Tamiflu®) and Zanamivir (Relenza®), which are used worldwide; Laninamivir (INAVIR®), which is available in Japan; and Peramivir (Rapivab®) which is approved in China, Japan, South Korea and the United States. NAIs work by acting as SA analogues, which competitively bind to the active site of NA, preventing the release of progeny virions from the host cell surface. Oseltamivir is the most commonly used NAI due to its activity against human and avian strains of IAV alongside IBV strains. However, between 2007 and 2009, seasonal strain resistance to Oseltamivir surged from 1 % to greater than 90 %, creating concerns for the future of these antivirals (203). Several resistance mutations in NA have been reported, though the most common mutation is the amino acid substitution H274Y, preventing binding pocket rearrangements, crucial for Oseltamivir to bind and ultimately inhibit (203). Fortunately, the 2009 H1N1 pandemic, and subsequent circulatory strains show little resistance. Clusters of localised resistant IAV strains have been recorded (204), and therefore this group of antiviral is still at threat of becoming redundant.

The third type of influenza antivirals act upon the polymerase. Baloxavir marboxil (Xofluza®) was recently approved in 2018 in both Japan and the United States (205), and works by inhibiting the cap snatching and endonuclease activity of PB2 and PA of the viral polymerase complex, ultimately preventing viral mRNA copies from being made. Perhaps unsurprisingly, IAVs capacity for antigenic drift has introduced strains of IAV with resistance; in this instance resistant variants were identified during the follow up treatments of those who partook in the clinical trials, with strong resistance found to Baloxavir marboxil by PA from a single mutation I38T (205). These mutants do show impaired viral fitness compared to the non-resistant strains, yet *in vitro* and *in vivo* studies have shown mutants with

only minor consequences to viral fitness (206). Additionally, several new antivirals targeting the RdRp are under clinical development. PB2 inhibitor Pimodivir® (VX-787, JNJ-63623872) which prevents binding to host mRNA caps (207), and Favipiravir® a nucleoside analogue interrupts primer extension by mimicking adenosine and guanosine. Of note, Japan have licensed Favipiravir® since 2014 for stockpiling against pandemic strains (208).

Though there are a range of antivirals currently approved and licensed against influenza infection, it is clear many of these are redundant or have potential to rapidly become so. The error-prone RdRp creates significant challenges when combating influenza infections, making it clear there is a large gap in our current capability to effectively combat severe infections. In order to confidently manage influenza infections, in particular IAV infections, there is a need for novel treatments targeting a range of proteins or mechanisms.

1.5.2 Antibody treatments

Antibodies are immunoglobulins (Ig) produced by the B cells in the adaptive immune response of most high-order animals. Structurally they are a heterodimeric glycosylated protein consisting of 2 heavy chains (H) and 2 light chains (L) (209). A small number of species (sharks and camels) express antibodies with only 1 heavy chain, making them significantly smaller in size. Both the heavy and light chains contain a variable region in the N-terminal domain which act as the antigen binding sites, and one or multiple constant regions in the CTD (210). Igs can be separated into 5 classes due to differences in the constant regions. These isotypes are: IgG, IgM, IgD, IgA and IgE. The isotype IgG is the predominant isotype found in sera and accounts for ~75 % of the Ig, and can be further divided into IgG 1-4 based on structural and functional differences in the constant region (211). IgG1 and IgG3 are important and induced when a protein antigen is introduced, making them a pivotal response when the body is invaded by a virus. Besides direct or indirect neutralisation of targets, IgG1 can elicit pro-inflammatory cytokine production, antibody-dependent cell-mediated cytotoxicity, antibody-dependent cellular phagocytosis, and complement-dependent cytotoxicity through the activation or inhibition of Fcγ receptors (FcγRs) (212). Antibody therapies have recently emerged as a way to treat a variety of diseases, including viral infections. All current marketed mAbs are IgGs, largely due to the natural abundance of IgG1s and their ability to elicit a large immune response.

The first mAb authorised for therapeutic use was OKT3 (muromonab®), for organ transplant rejections in 1986 (213). Since then, a large number of therapeutic mAbs have been approved for many cancer

treatments, and a handful of viral treatments. Of note, human immunodeficiency virus (HIV) is treated with Ibalizumab (Trogarzo®), which is a mAb that binds CD4, preventing HIV from recognising its primary receptor (214). REGN10933 and REGN10987 (Casirivimab® and imdevimab®) are mAbs which have recently been approved by the FDA to be used as a combined therapy for emergency treatment of the ongoing pandemic COVID-19. They non-competitively bind the viral spike proteins via the receptor binding domain and provide a 70 % reduction in severe symptoms (215). Given the importance of mAbs in the natural and vaccination modulated-immune response to seasonal and pandemic strains of IAV, mAbs are being heavily investigated as prospective therapeutic treatments. As such, MHAA45449A and MEDI8852 are stem binding mAbs with high-affinity binding to 16 IAV HA subtypes, and are currently undergoing clinical trials (216,217). Both have been shown to be effective in pre-clinical animal models by preventing pulmonary viral loads in infected hosts, and are showing similar results in humans in phase 2a clinical trials, in which they are performing comparably to Oseltamivir (218,219).

Though mAbs are a useful therapeutic tool there are many set-backs for their wide use. Full-size mAbs are initially raised by producing an immune response in animals with a selected antigen, before mass producing the specific mAbs in hybridomas. This practice raises ethical questions, and the presence of several disulphide bonds makes mAbs unstable and challenging to express, purify and distribute, complicating mass-production (220). The large size of mAbs (~150 kDa) is also self-limiting, as the bulky size may render small targetable pockets on antigens partially or completely inaccessible. mAbs leave a large footprint, which can potentially cover regions which are prone to mutation, these mutations leave mAbs vulnerable to loss of affinity, making resistance to mAbs likely (221). Another setback of their large size is the inability to penetrate into certain tissues. Ultimately mAbs are expensive to produce due to the complications associated with production, making them inaccessible to many patients who become 'cashed-out' (222), with this in mind, mAbs are unlikely to be a favourable solution for potential future pandemics.

1.5.3 Antibody Fragments

Over the last decade, rapid advances have been made in the isolation and production of novel high affinity molecules, either as antibody fragments or antibody mimics, that are structurally unique but maintain high affinity antigen binding (**Figure 1.6**).

Camelids and sharks both produce heavy chain only antibodies, devoid of light chains. The heavy chain homodimers contain antigen-binding fragment (Fab) regions called variable heavy homodimers (VHH)

in camelids and variable new antigen receptor (VNAR) in sharks. These molecules have gained interest as therapeutics as they maintain high affinity binding, whilst being the smallest naturally occurring antigen binders (80 kDa). Furthermore, they have been used to develop recombinant VHH derived 'nanobodies' and 'bivalent nanobodies' which are smaller yet in size (15 kDa and 30 kDa respectively) and extremely stable. Additionally, it is possible to produce nanobodies in vast quantities cheaply through simple microbial systems. Research into these has shown success against a range of targets, there are a number of nanobodies currently in clinical trials, the large majority of these targeting oncological targets and 1 treating thrombotic thrombocytopenic purpura and thrombosis approved by the FDA (223). Of note, anti-NP or anti-HA VHH molecules have been identified which inhibit infection against pandemic PR8 strains and epidemic H7N9 strains respectively (224,225).

Aberrant glycosylation of proteins can cause unfavourable molecular properties and also be immunogenic. Unlike naturally occurring mAbs, Fabs are generally not glycosylated, meaning that they avoid issues occasionally encountered with traditional mAbs, and they may also be produced in microbial systems, alleviating the time-consuming and expensive production process. Additionally, they are much smaller than mAbs (55 kDa – 110 kDa), but not so small that they are rapidly renally extracted like smaller antibody-like proteins (226). The majority of these antibody fragments are currently being developed for oncology as alongside the benefits of conventional mAbs, they present excellent tissue and tumour penetration due to their small size, and the lack of Fc domain reduces the non-specific activation of innate immune cells (Reviewed in (226)).

Genetically engineered approaches have been also employed to overcome many of the typical issues that have been associated with conventional mAbs, whilst maintaining or even improving upon the high specificity and affinity. As such, many Ab like and non-Ab like structures have been developed in recent years. For example, single chain fragment variables (scFv) were first described in 1988 and consist of the variable region of the light chain (VL) and heavy chain (VH) of an antibody linked by a flexible peptide (227). The flexible linker enables multivalent molecules to be produced, improving affinity to the intended target (226). They have a small size (~27 kDa) making them ideal for large-scale microbial production alongside greater tissue penetration and access to small/cryptic epitopes. Moreover, the lack of an Fc region reduces unwanted innate immune responses. Since scFv discovery, diabodies, minibodies and domain antibodies (dAbs) are the smallest known antigen-binding fragments of antibodies and have been developed with similar properties.

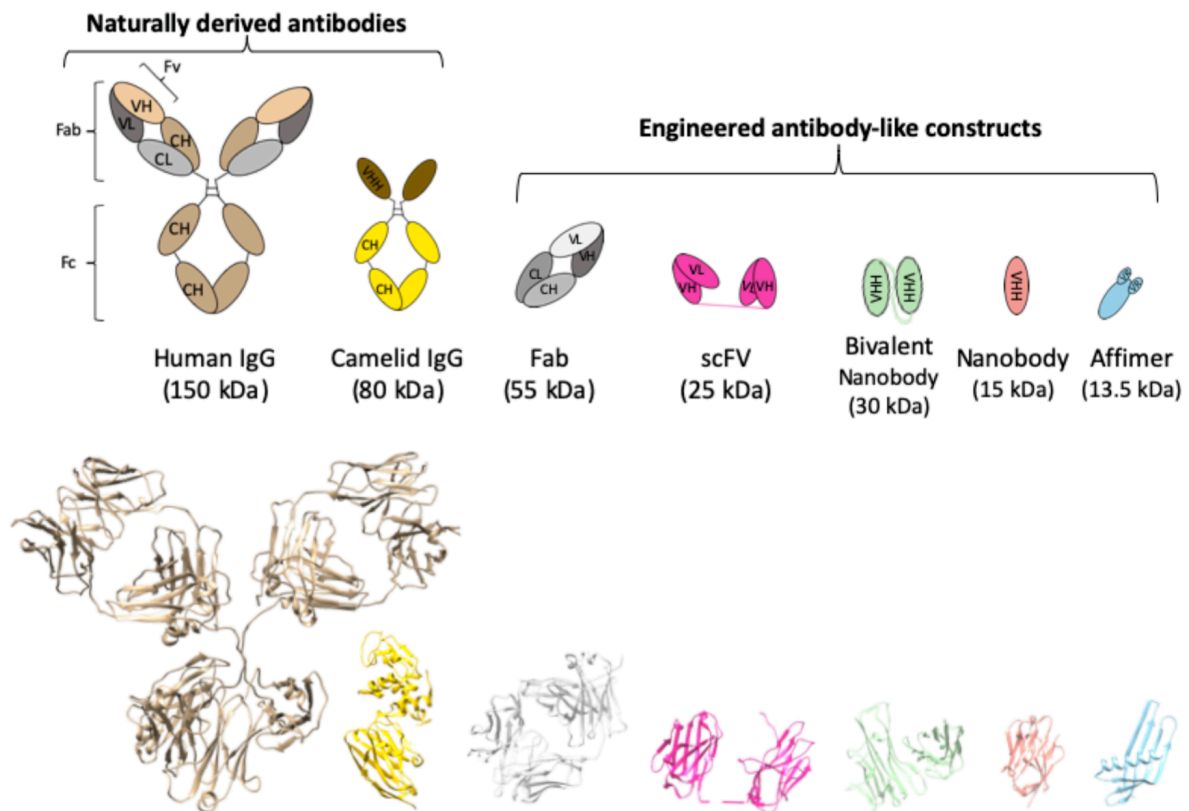


Figure 1.6: Antibodies and engineered antibody-like constructs

Schematic representation of antibodies and engineered antibody-like constructs, alongside the molecular weights. The different subunits of the molecules are indicated: Fab, Fc, Fv, Variable (VL) and constant (CL) regions of light chains and variable (VH) and constant (CH) regions of heavy chains and variable heavy homodimers (VHH). Structures of each of the antibody or antibody-like engineered constructs: Antibody (Brown, PDB:1IGY), Camelid (Yellow, PDB:4I0C), Fab (Silver, PDB:5UR8), scFV (Pink, PDB:4OUO), Bivalent nanobody (Green, PDB:5m2j), nanobody (Orange, PDB:5IVO), Affimer (Blue, PDB:5OHM)

1.5.4 Non-antibody proteins/ antibody mimics

Thanks to advancing biochemical and molecular engineering techniques, antibody mimics are being rapidly developed (**Table 1.1**). These molecules are based off naturally occurring proteins or protein domains, and are typically small molecules (6 kDa – 20 kDa) that are pH and thermally stable. These molecules are referred to as antibody mimics, as they have high affinity to antigens on par with mAbs and in some cases exceeding them. The scaffold is typically a simple structure consisting of a small number of α -helices, β -sheets, or random coils, and the molecules are generated from synthetic libraries, enabling the isolation of multiple specific binders to any given antigen without the

requirement for animals. Antibody mimics are not glycosylated, enabling high-yield, quick and cheap production through simple expression systems. Due to the small size of these molecules, they are highly soluble, protease resistant and have reduced potential to elicit an unwanted innate immune response (228).

Antibody mimic libraries are developed utilising *in silico* methods to design and molecular biological techniques to produce the large libraries. This is typically done by performing site-directed and randomised mutagenesis to produce a library of mutants differing in their variable regions (229). Specific isotypes are then isolated through display systems such as: phage display, ribosome display, mRNA display, yeast display, and bacterial cell-surface display (230). These display systems reveal isotypes which specifically bind to the antigen presented (e.g. a subunit of interest of an antigenic protein or a small region of interest). The *in vitro* selection process negates the ethically complicated need for sera from patients or animals alongside the need for the whole antigen. Additionally, the antibody mimic selection process takes up to a few weeks, whereas antibody development can take up to several months (212).

Due to the speed and cost of isolation and production, alongside the high affinity of these molecules, antibody mimics have a huge range of applications: 1) They have been exploited for biotechnological applications: affinity chromatography, flow cytometry and western blotting (231). 2) The high affinity molecular recognition enables these antibody mimics to distinguish between high homology proteins for diagnostic tests, such as lateral flow tests. For example, Affimer molecules, one type of antibody mimic molecule, have recently been shown to be able to distinguish between Crimean-Congo haemorrhagic fever virus (CCHFV) NP, and its homologue and non-pathogenic human Hazara virus (HAZV) NP (232). An Affimer based lateral flow test with high accuracy identification (96.7 %) for COVID-19 virus, including all known variants (at the point of writing), has been developed and recently been approved by the Medicines and Healthcare products Regulatory Agency (MHRA) for use in the UK, enabling the pandemic strain to be distinguished from other respiratory diseases (233). 3) Antibody mimics have also been shown in many instances to be effective as functional inhibitors or antagonists. Recently designed ankyrin repeat proteins (DARPs), genetically engineered antibody mimetic proteins, have shown great promise at inhibiting COVID-19, with molecules preventing infection in the pM range (234).

A large portion of the work carried out during this PhD project has been focused around the use of Affimer molecules against the HA protein of IAV, to determine whether Affimer molecules show potential as therapeutic candidates against influenza virus infection. As such, section: **1.6** will discuss the Affimer molecules in further detail.

Scaffold	Parental Protein	Expression	Size (kDa)	Stability (T _m)	Binder identification	Company
Adnectins	Fibronectin type III domain	<i>E.coli</i>	10	37°C - 73°C	Phage display, ribosome display, mRNA display, yeast display	Adnexus
Affibodies	Z domain of protein A (<i>staphylococcal</i>)	<i>E.coli</i>	6	42°C - 71°C	Phage display, ribosome display	Affibody AB
Affilins	γ-B-crystallin or ubiquitin	<i>E.coli</i>	8.5 or 20	56°C - 72 °C or 54°C - 66°C	Phage display, ribosome display	SCIL Proteins
Affimer	Type 1: human protease inhibitor Stefin A Type 2: Consensus plant phytocystatin A	<i>E.coli</i>	~13.5	~101°C	Phage display	Avacta
Alphabody	Computer-based rational design	<i>E.coli</i>	10		Phage display	Complix
Anticalins	Human lipocalin	<i>E.coli</i>	20	53°C - 73°C	Phage display	AstraZeneca
Atrimers	C-type lectin (human tetranectin)	<i>E.coli</i>	60-70	70°C - 80°C	Phage display	Pieris AG
Avimers	A domains of human membrane receptors	<i>E.coli</i>	Sep-18	>50 °C	Phage display	Anaphore
Bicyclic Peptides	Synthetic peptide	HEK-293	1.5-2	N/A	Phage display	Amgen
Centryns	Fibronectin type III domain	<i>E.coli</i>	10	46°C - 87°C	DNA display	Aro
Cys-knots	Diverse structural motifs	<i>E.coli</i>	Vairable	>100°C	Phage display	Painceptor
DARPinS	Ankyrin repeats (human)	<i>E.coli</i>	14-18	66°C - 89°C	Ribosome display	Molecular partners
Fynomers	SH3 domain fyn kinase (human)	<i>E.coli</i>	7	~70°C	Phage display, DNA display	Covagen
Kunitz domains	Serine protease inhibitor (human)	<i>Pichia pastoris</i>	6	~95°C	Phage display	DYAX
Obodies	OB-fold (<i>Archea Probaculum aerophilum</i>)	<i>E.coli</i>	11	~83°C	Phage display	Obodies

Table 1.1: Antibody mimics properties and isolation strategy

Summary of the major antibody mimics and properties currently available. (Reviewed further in:(229))

1.6 Affimer molecules

1.6.1 Structure and isolation of specific Affimer molecules

Affimer molecules, previously named Aptamers, are antibody mimics which consist of a scaffold protein containing an α -helix and 4 β -sheets, alongside 2 variable loop regions located between pairs of the β -sheets. These loops act as the antigen recognition sites (**Figure 1.7**). Affimer molecules are divided into 2 classes on the basis of the scaffold protein origin. Type I Affimer molecules have a scaffold based off human Stefin A protein, whilst Type II, have a scaffold based on the sequence consensus of plant phytocystatin (235–237).

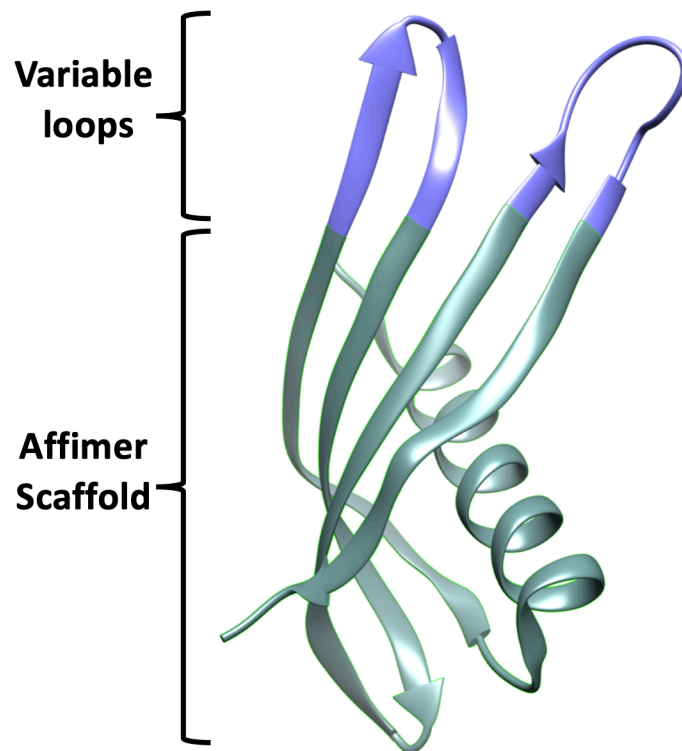


Figure 1.7: Crystal structure of an Affimer molecule

Crystal structure of a representative Affimer molecule (PDB: 5A00), showing 2 variable loop regions (Purple) and the Affimer scaffold (Green). Affimer scaffolds consist of an α -helix and 4 anti-parallel β -sheets

Affimer molecules are isolated against specific targets through the use of a phage display system (**Figure 1.9**). The Affimer phage libraries required for this system are first generated by codon-selected semi-trinucleotide cassette synthesis, in which random amino acids (excluding cysteine) are introduced to the variable loops 1 and 2 allowing for 9 random amino acids per loop. These variable loops are then introduced to the Affimer scaffold through overlap extension gene splicing, Affimer phage libraries are estimated to consist of 1.3×10^{13} unique clones. The filamentous M13 bacteriophage is utilised in this instance for phage display.

Following the curation of the library via gene splicing, sub cloning the constructed Affimer molecules into phagemid vectors was carried out. The vectors consist of the g3p M13 attachment protein, essential for *E. coli* infection, which is fused with the variable region of the Affimer molecule. In order for specific binders to be isolated, *E. coli* are transfected with the phagemid vector via heat shock alongside a helper phage, which carries all genes necessary for infection, replication, assembly, and budding, therefore providing the phagemid, which primarily carries the gene encoding the g3p-

Affimer fusion protein, with the proteins needed for amplification, enabling the production of phages with the g3p-Affimer attachment protein and the use of these phage for the phage display screening. The employment of phage display for identifying specific antigen binders is high-throughput, allowing for the identification of a plethora of unique antigen binders with relative speed and ease (Figure 1.9). Firstly, the antigen is presented via an adsorption or capture system, in the instance of phage-Affimer isolation, a streptavidin-biotin capture system is employed, in which the antigen is biotinylated and captured on streptavidin coated wells or magnetic beads. The phage display library is then added to the captured antigen, where the highest affinity binders bind to the relevant epitopes. Wash steps are carried out in order to remove any non-specific binders and the high-affinity phages are then eluted using a weak acid. Bound phages are then amplified in *E. coli* using helper phage, after which panning is repeated 2-3 times to isolate desirable high-affinity binders. Following phage display, a phage enzyme-linked immunosorbent assay (ELISA) is typically employed to confirm the affinity of binders to the target antigen. Clones which are then selected as the highest affinity binders are sequenced and the coding region for the Affimers is sub cloned into bacterial expression vectors in order to express and purify large quantities of the selected Affimers for further testing.

1.6.2 Applications of Affimer molecules

Affimers have proven to be versatile antibody-like molecules, there have been >350 Affimer molecules isolated against various targets by the BSTG at Leeds (238). Most of these Affimers target cellular proteins, particularly those described as the hallmarks of cancers. More recently, Affimer molecules have been used to target viral antigens. An Affimer against the NP of CCHFV was shown to interfere with the interaction between CCHFV-NP and its RNA and to present highly specific low nM affinity to the CCHFV-NP globular head (232). Additionally the Affimer presented has been shown to specifically bind the icosahedral capsid L subunit of Cowpea Mosaic virus (CPMV) (239). Both of these show the potential for the use of Affimer molecules in the diagnostic and therapeutic capabilities against viral protein targets. What is most exciting about the new era of antibody mimics is that the whole antigen is no longer required to isolate high affinity binders. This facilitates production as whole, live virus is not required. For instance, the Affimer against CCHFV-NP was isolated employing recombinant CCHFV-NP protein, whereas the use of whole virus would require a containment level 4, making work arduous and costly, and limiting the number facilities where work could be carried out. The CPMV Affimer on the other hand, was isolated utilising CPMV empty virus like particles, emphasising the ease in which

these binders can be isolated. In the work presented here, the recombinantly expressed monomeric HA of IAV was used as an antigenic target for Affimer molecule isolation, acting as a flagship for work using these antibody mimics against IAV infection.

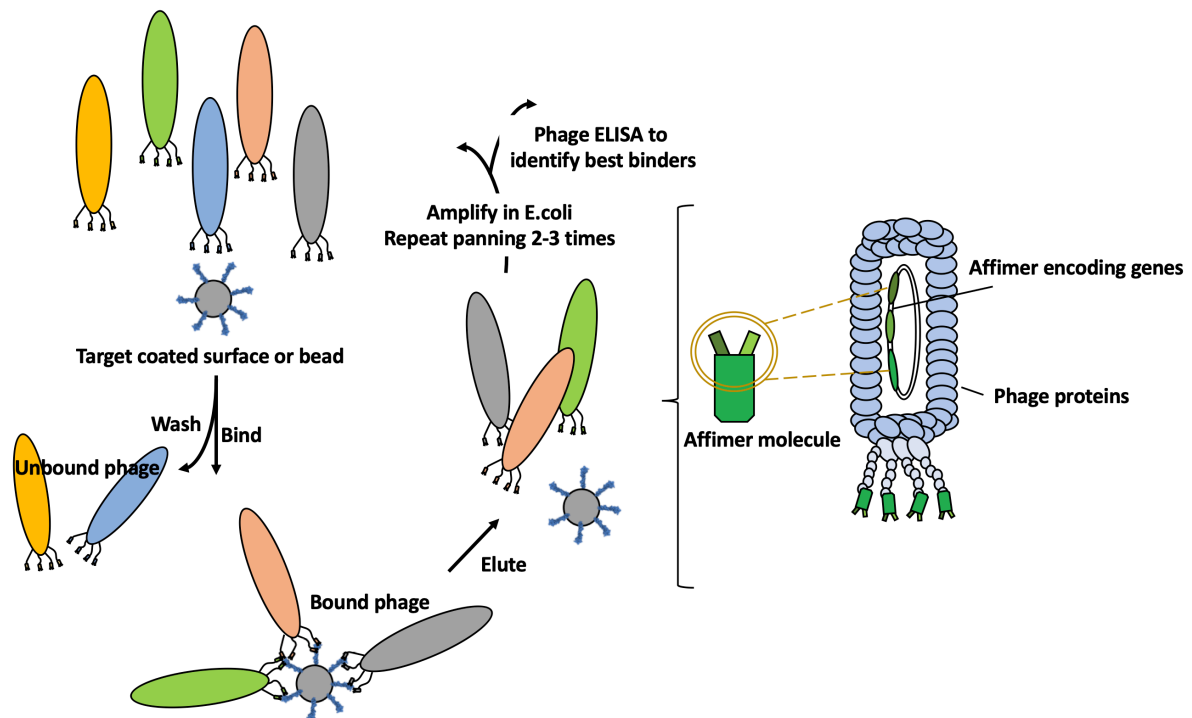


Figure 1.8: 'Phage display for Affimer screening

Schematic representation of the Affimers screening process. Target molecule (in this studies case monomeric HA) is immobilised in micro-wells or magnetic beads and incubated with the Affimer 'phage library. Non-bound phage are washed off and bound phage eluted with a slightly acidic buffer before being amplified in bacterial cells for a consecutive panning round. After two-three rounds of selection, individual phage displaying the selected binders are tested by 'phage ELISA to confirm the selectivity for the target antigen.

1.7 Host cell ion channels

Ion channels are transmembrane proteins which form hydrophilic pores across lipid membranes, enabling the passage of specific ions across cellular membranes. They have a plethora of diverse roles in the regulation of cells, including trans-epithelial transport and the control of electrical excitability of cells, alongside intracellular roles such as the acidification of endosomes and the regulation of

endocytosis (240). There are 60 genes that code for K⁺ channels alone (240), and over 300 ion channel subunits are expressed per cell on cellular membranes(241). Ion channels are crucial in homeostasis, thus many diseases are associated with the dysfunction of them (coined 'channelopathies') (241).

Many ion channels are protein complexes of identical or homologous subunits that contribute to the formation of the pore. Ion channels contain a selectivity filter, which selectively permits ion transport and defines the type of channel (**Figure 1.9**) (240). These may be: Potassium (K⁺), Calcium (Ca²⁺), Sodium (Na⁺) or Chloride (Cl⁻) channels. K⁺ channels' signature sequencing selectivity filter 'TXGXG' is key to their specificity, which makes them 10,000 times more selective to K⁺ ions than Na⁺ ions (240). Not all channels show this magnitude of selectivity; for example, Cl⁻ channels are much less specific, allowing the passage of a range of anions. Activating ion channels through pore opening is regulated by many cellular factors. Voltage, membrane-stretch, ion sensing and ligand binding have all been associated as gating mechanisms, where voltage is key in the gating mechanisms for K⁺, Ca²⁺, Na⁺, and Cl⁻ channels. Whilst Ion transporters or pumps are capable of transporting one or two ions at a time requiring the input of cellular energy to facilitate this. Ion channels allow ions to cross the membrane through passive diffusion, a rapid process transferring around ~1-100 million ions/second (240).

There have been large contributions to the literature over the last decade illustrating the dependence for the ionic balance within host cells during viral infection, emphasising further the importance of these ion channels. Above (**section 1.3.1**), the requirement for Ca_v1.2 was discussed as a receptor which enables IAVs binding and internalisation into host cells (127). Ion channels are increasingly being identified as key host proteins required for successful viral infection (146). Alongside viral entry, ion channels have been shown to play a role in viral replication. Müller et al. demonstrated through a sub-genomic replicon system of Chikungunya virus (CHIKV) in both mammalian and invertebrate cells that Cl⁻ intracellular channels (CLIC) 1 and 4 are required for successful replication, through SiRNA silencing of the channels (242). Viral infections appear to be directly associated with acquired channelopathies. Neuronal pathologies have recently been linked to Zika virus (ZIKV) infection, causing hyperstimulation of the N-methyl-d-aspartate receptor (NMDAR) causing a Ca²⁺ overload and postsynaptic neuronal death (243). This can be circumvented through the use of Memantine, which directly acts on the NMDAR, surprisingly this has no effect on ZIKV infection (243).

The identification of ion channels role in viral infection is an attractive target for a new antiviral strategy. Targeting the cellular channels rather than viral targets, might circumvent the risks of resistance which are associated with directly acting antivirals. Moreover, mechanisms of hereditary and acquired channelopathies have been shown to overlap and occasional be caused under certain

viral infections, making manipulation of homeostasis an attractive target. This project investigates the role of K^+ ions and K^+ channels in the early stages of IAV infection. As such section: **1.7.1** highlights the different members of the K^+ superfamily.

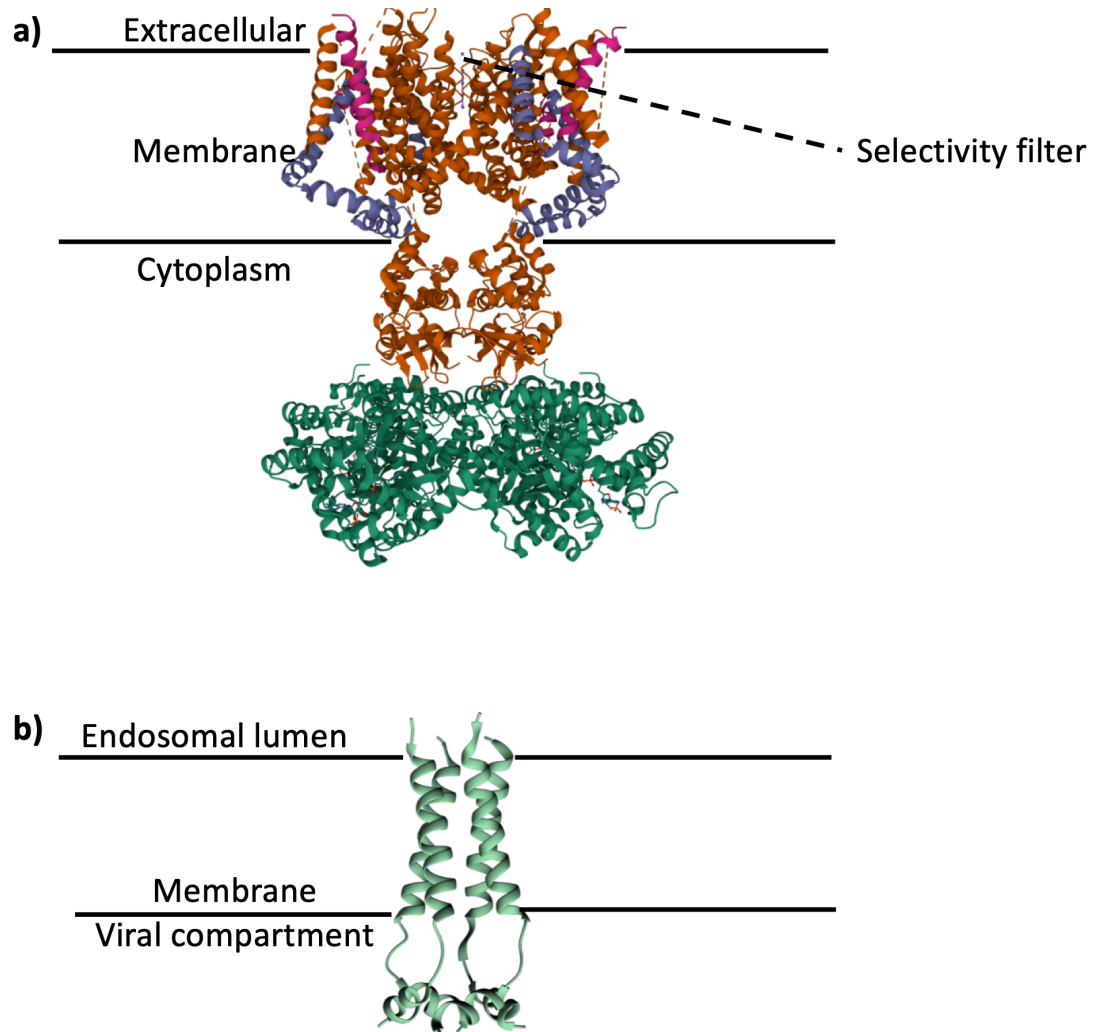


Figure 1.9: Structural comparison of a K^+ channel and IAV M2 viroporin

a) Crystal structure of the voltage-gated channel Kv1.2 (PDB :2A79). Kv1.2 is a homotetramer with four voltage sensors and one central pore domain. In each subunit, four transmembrane helices make up a sensitivity domain, and two transmembrane helices contribute to the central pore domain. b) Crystal structure of the IAV M2 viroporin (PDB: 2RIF). M2 is a simplistic homotetramer consisting of only four transmembrane helices.

1.7.1 Potassium channels

Potassium channels (K^+ channels) localise to specific membrane compartments or organelles and regulate many physiological processes. As our understanding of these ion channels increases, an ever-growing list of examples can be found in the literature. For example, it has recently been discovered 2 K^+ channels are localised and play a role in the regulation of lysosomal ion potential. Novel TMEM175 channel and Ca^{2+} activated K^+ channel (BK_{Ca}) have both been shown to regulate lysosomal membrane potential and pH (244).

Though K^+ channels share a highly conserved selectivity filter, enabling the high specificity diffusion of K^+ ions, the K^+ channel superfamily exhibits high divergence amongst the sensing domains. This divergence enables the superfamily to respond to a variety of signals, owing to the range of roles these channels play (245). Structurally, the K^+ channels can be separated into distinct groups (**Figure 1.10**). The inward rectifier K^+ channels (K_{IR}), the ATP sensitive K^+ channel (K_{ATP}), and the G-protein-coupled K^+ channels are tetramers, consisting of 2 TMD and 1P subunit. The P domain which contains the K^+ conductance domain is localised between the 2 TMDs. The Two-pore-domain K^+ channel (K_{2P}) sub-family consist of channels with 4TMDs; these channels are formed by tetramers, the K_{2P} channels are unique in that the channels have 4 TMDs with 2 pore domains; therefore, the subunits dimerise to form a functional channel, the 2 P domains form between the 1st and 2nd TMD and 3rd and 4th TMD (Figure 1.11b). The voltage-gated K^+ channels (K_V) and small and intermediate conductance Ca^{2+} activated K^+ channel (K_{Ca}) are homotetramers, with each monomer containing 6 TMDs with only 1 P region located between the 5th and 6th TMD (**Figure 1.11c**). Finally, the large K_{Ca} channels (not shown in Figure 1.10) are homotetramers consisting of 7 TMDs with 1 P region these are unique in that the N-terminus is extracellular (246).

1.7.1.1 K_{IR} channels

K_{IR} channels are largely voltage-gated, though, can be regulated by a host of intracellular ligands, including G-proteins, ATP, protein kinases or other ions. K_{IR} channels not only orchestrate the regulation of membrane potentials, but are also involved in G-protein-coupled receptor (GPCR) signalling due to ligand binding, as well as regulating the metabolic state of cells (247). K_{IR} channels are unique in that they have an asymmetric open channel pore, which shows a greater flow of K^+ ions

into rather than out of cells (248). This is biochemically possible due to the smaller intracellular end of the pore, being 'blocked' by larger divalent cations such as Mg^{2+} and other molecules (247).

1.7.1.2 K_{ATP} channels

K_{ATP} channels are inhibited by ATP and activated by Mg-ADP, and so couple cellular metabolic state (ADP/ATP ratio) with the depolarisation of the cellular membrane. In the pancreas for example, K_{ATP} channels are key regulators in Beta cells of insulin and glucose secretion (249). The depolarisation of these channels caused by depletion of cytosolic ATP, leads to a large influx of Ca^{2+} ions in cells, key to hormone secretion. K_{ATP} channels are part of the same subfamily as K_{IR} channels which have 2 TMDs. They are found on almost all human cell types and expressed on the plasma membrane and membranes of subcellular organelles (250).

1.7.1.3 K_{2P} channels

There are 15 known K_{2P} channels in mammals, which are separated into 6 subfamilies based on structural and functional properties (251) (Figure 1.11 b). In addition to forming homodimers, there is evidence suggesting K_{2P} channels form heterodimers both within families (TASK-1/TASK2; THIK-1/THIK-2) (252), and more rarely between families (TREK-1/TWIK-1) (253,254). This heterodimerisation makes it increasingly difficult to study the cellular roles of K_{2P} channels, especially as the specific pharmacological inhibitors are sparse. Alongside ionic potential regulation, these channels have been identified to play a role in cytoskeletal organisation, cell proliferation and hormone secretion through knock down experiments. Though the specific roles of each of the subfamily channel members is not well characterised (255).

1.7.1.4 K_V channels

Similarly, to K_{IR} , K_V channels are activated by the depolarisation of membranes. Voltage sensors initialise the opening of the K_V pore, allowing the efflux of K^+ ions from the cells, re-polarising the membrane (240). This regulation is important both in excitable and non-excitable cells regulating cell volume, hormone secretion and apoptosis in non-excitable cells. In excitable cells, K_V channels work in combination with voltage-gated Na^+ channels (Na_V) channels, to regulate action potentials (256).

1.7.1.5 K_{Ca} channels

The K_{Ca} channels were first discovered in cells of haemopoietic lineage, including red blood cells and lymphocytes (257), and consist of 3 different types of channel based on the biophysical and pharmacological properties (rate of K⁺ conduction and channelopathies). The K_{Ca} channels possess ligand binding domains on each subunit, binding of Ca²⁺-calmodulin to these domains activates pore opening enabling the passage of K⁺ ions. These K⁺ channels regulate Ca²⁺ homeostasis, controlling membrane potential. Further cellular roles have been suggested such as the regulation of secretion, cell proliferation and cell volume regulation (258).

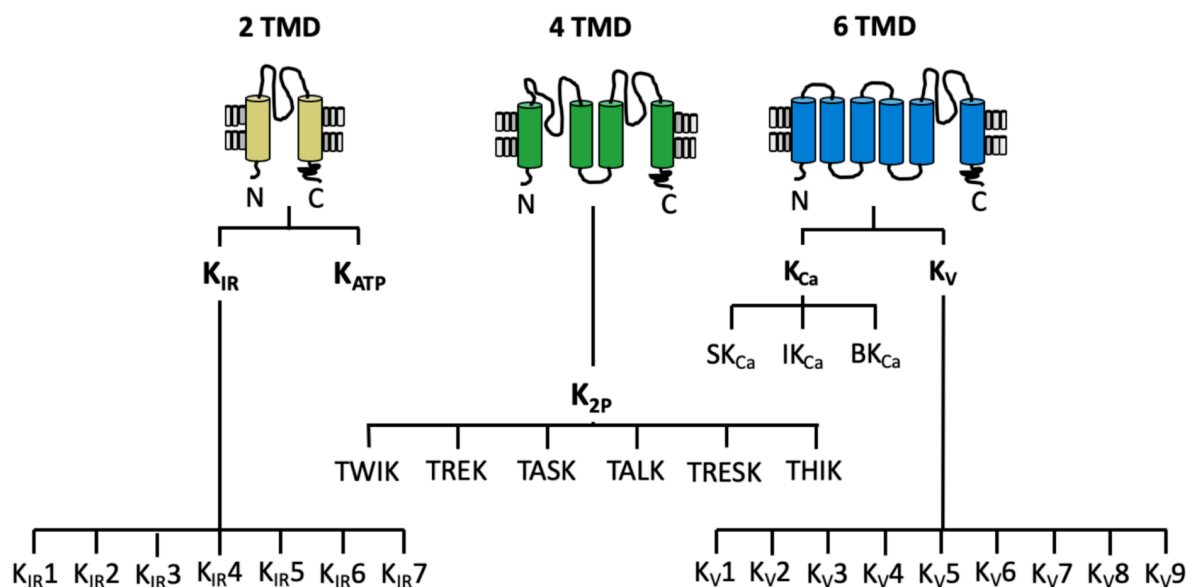


Figure 1.10: Figure 1.8 K⁺ channel classification

K⁺ channels are made up of subunits containing 2, 4, 6 or 7 TMDs (7 TMD channels not shown here) and are classified into different channel families; K_V (K_V1-9), K_{Ca} (SK_{Ca}, IK_{Ca}, BK_{Ca}), K_{IR} (K_{IR}1-7), K_{ATP} and K_{2P} (Tandem-pore domain in Weak Inwardly rectifying K⁺ channel (TWIK), TREK (TWIK-Related), TASK (TWIK-related Acid Sensitive), TALK (TWIK-related Alkaline-activated), TRESK (TWIK-Related Spinal cord) and THIK (TWIK-related Halothane-Inhibited). Adapted from *Zhong et al* (2013) (259).

1.8 Project aims

The work presented in this thesis investigates alternative methods for the potential treatment of IAV, exploring the potential of novel direct-acting antivirals and host cell targeting therapies. Additionally, this work aims to further improve understanding of IAV and the mechanisms which facilitate its success as an infectious pathogen.

Affimer molecules were selected as a potential therapeutic tool for both seasonal and pandemic outbreaks. Affimer molecules are advantageous as they can be isolated against recombinant proteins, in this case the monomeric form of the IAV glycoprotein, HA. Furthermore, Affimer molecules are small (13.5 kDa) (235–237), potentially allowing novel antigenic sites to be targeted, or limiting interactions with residues at the focal point of mutations. Expression through bacterial systems means production is not only rapid, but cheap.

On the other hand, it has been widely found that to effectively infect a host, many viruses are reliant on the ionic profile across the cell, in some cases viruses manipulate this ionic balance to enhance infection (127,242,243). The previously described role of K^+ during the early stages of IAV infection was investigated using a panel of broad-spectrum K^+ channel inhibitors (76), many of which are already clinically approved for channelopathies. Use of such channel inhibitors may be prove to be an excellent alternative to directly-acting antiviral treatments, circumventing the risk of resistance.

In this context, three main objectives were set out for this project:

1. Isolation, expression and production of HA-specific Affimer molecules. Two approaches were carried out for this purpose: Isolation of Affimer molecules against a range of monomeric HA proteins, with the aim of isolating broadly neutralising Affimer molecules; and isolation of Affimer molecules against a single monomeric HA protein, with the aim of isolating high potency anti-HA Affimer molecules.
2. Characterisation and validation of HA-specific Affimer molecules. For this I used a range of virology, biophysical and biochemical techniques, including neutralisation assays, mode of inhibition assays, surface plasmon resonance (SPR) and cryo-electron microscopy (cryo-EM).
3. Screening and characterisation of a panel of broad-inhibiting K^+ channel inhibitors as therapeutics of IAV. This includes illustrating the biochemical and structural significance of K^+ concentration on the virion structure.

Chapter 2

Materials and Methods

2.1 Materials

2.1.1 Chemicals & reagents

All standard chemicals and solvents were obtained from Fisher Scientific, Invitrogen, New England Biolabs, Oxoid or Sigma-Aldrich.

2.1.2 Bacterial strains

Bacterial strains were used for plasmid maintenance, protein expression, cloning and site-directed mutagenesis (SDM). All bacterial *E. coli* strains are listed in **(Table 2.1)**.

Strain	Function	Genotype
ER2738	Phage propagation	<i>F' proA⁺B⁺ lacI^q Δ(lacZ)M15 zzzf::Tn10(Tet^R)/ fhuA2 glnV Δ(lac-proAB) thi-1 Δ(hsdS-mcrB)5</i>
JM83	Protein expression	<i>F⁻ ara Δ(lac-proAB) rpsL (Str^R)[φ80 dlacΔ(lacZ)M15] thi</i>
BL21 Star™ (DE3)	Protein expression	<i>FompT hsdS_B (r_B,m_B)galdcmrne13 1</i>
DH5α	Cloning, site directed mutagenesis and plasmid maintenance	<i>F- endA1 glnV44 thi-1 recA1 relA1 gyrA96 deoR nupG Φ80dlacZΔM15 Δ(lacZYA-argF)U169, hsdR17(rK- mK+), λ-</i>

Table 2.1: Bacterial *E. coli* strains used during this project

2.1.3 Plasmids

Bacterial expression plasmids are detailed (**Table 2.2**).

Plasmid	Promoter	Bacterial strain	Antibiotic (working conc.)	Gene expressed
pET-11a-Affimer	T7	DH5 α	Amp (100 μ g/mL)	Affimer-cys-8xhis
Jm83-Affimer	T7	JM83	Carb (100 μ g/mL)	Affimer-cys-8xhis

Table 2.2: Plasmids used during this project. amp: ampicillin, carb: carbenicillin

2.1.4 Mammalian cell lines, cell culture and storage

Mammalian cell lines, origins and growth/storage media are detailed (**Table 2.3**). Cells were stored by flash freezing before storing at -80 °C or in LN₂ storage dewars.

Cell line	Growth/storage media	Origin	Supplier
A549	Minimum Essential Media (MEM, Sigma) supplemented with 10% FBS and 1x Antibiotic-Antimycotic/supplemented with 10% DMSO	adenocarcinoma human alveolar basal epithelia	Dr. Lee Sherry (University of Leeds)
MDCK	Dulbecco's Modified Eagle Medium (DMEM, Sigma) supplemented with 10% fetal bovine serum (FBS) and 1x Antibiotic-Antimycotic (Gibco) /supplemented with 10% DMSO	Madin-Darby Canine Kidney	Dr. Lee Sherry (University of Leeds)

Table 2.3: Mammalian cell lines used during this project

2.1.5 Virus strains

Virus strains used during this project are listed (**Table 2.4**).

Virus	Viral subtype	Origin
Influenza A virus, A/Aichi/2/1968	H3N2	ATCC® VR-1680™
Influenza A virus, A/Aichi/2/1968	H3N2	Charles River 10100375
Influenza A virus, A/Udorn/307/1972	H3N2	Dr. Lee Sherry (University of Leeds)
Influenza A virus, A/Brisbane/10/2007	H3N2	BEI resources, NIAID, NIH: NR-12283
Influenza A virus, A/Victoria/361/2011	H3N2	BEI resources, NIAID, NIH: NR-44022
Influenza A virus, A/WSN/1933	H1N1	Dr. Samantha Hover (University of Leeds)
Influenza A Virus, A/Puerto Rico/8/1934	H1N1	BEI resources, NIAID, NIH: NR-29028
Influenza A virus, A/England/195/09	H1N1	Dr. Steven Griffin (University of Leeds)

Table 2.4: Viral strains used during this project

2.1.6 Recombinant HA proteins

Recombinant HA proteins used during this project are listed (**Table 2.5**).

HA protein	Expression vector	Information	Supplier
Influenza A H3N2 (A/Aichi/2/1968) Hemagglutinin protein	HEK293 Cells	His tag, monomeric	SinoBiological Cat: 11707-V08H
Influenza A H3N2 (A/Aichi/2/1968) Hemagglutinin Protein (HA1 Subunit)	HEK293 Cells	His tag, monomeric	SinoBiological Cat: 11707-V08H1
Influenza A H3N2 (A/HongKong/1968) Hemagglutinin protein	Baculovirus expression	Trimeric	Dr. Ian Wilson (Scripps research institute)
Influenza A H3N2 (A/Fujian/411/2002) Hemagglutinin protein	HEK293 Cells	His tag, monomeric	SinoBiological Cat: 40488-V08H1
Influenza A H1N1 (A/California/07/2009) Hemagglutinin protein	HEK293 Cells	His tag, monomeric	SinoBiological Cat: 11085-V08H
Influenza A H1N1 (A/USSR/90/1977) Hemagglutinin protein	HEK293 Cells	His tag, monomeric	SinoBiological Cat: 40711-V08H
Influenza A H1N1 (A/Albany/12/1951) Hemagglutinin protein	HEK293 Cells	His tag, monomeric	SinoBiological Cat: 40464-V08H1
Influenza A H1N1 (A/New York/1/1918) Hemagglutinin Protein	HEK293 Cells	His tag, monomeric	SinoBiological Cat: 40090-V08H1

Table 2.5: Recombinant proteins used during this project**2.1.7 Compounds**

All compounds used throughout this project are described (**Table 2.6**)

Compound	Stock concentration	Type	Supplier
Quinidine (Qd)	100 mM	Broad-spec K ⁺ channel inhibitor	Dr Jamel Mankouri
Quinine	100 mM	Broad-spec K ⁺ channel inhibitor	Dr Jamel Mankouri
Tetraethylammonium (TEA)	1 M	Broad-spec K ⁺ channel inhibitor	Dr Jamel Mankouri
Amiloride	1 M	Broad-spec K ⁺ channel inhibitor	Dr Jamel Mankouri
Barium Chloride (BaCl ₂)	1 M	Broad-spec K ⁺ channel inhibitor	Dr Jamel Mankouri
Potassium Chloride (KCl)	1 M	Broad-spec K ⁺ channel inhibitor	-
Maurotoxin	1 μM	Broad-spec K ⁺ channel inhibitor	Dr Jamel Mankouri
Ibutilide	1 mM	Broad-spec K ⁺ channel inhibitor	AdooQ Bioscience
Dalfampridine	500 mM	Broad-spec K ⁺ channel inhibitor	FluoroChem
Miconazole	250 mM	Broad-spec K ⁺ channel inhibitor	FluoroChem
OA1	10 mM	A5 variable loop mimic	eMolecules
OA2	10 mM	A5 variable loop mimic	eMolecules

OA3	10 mM	A5 variable loop mimic	eMolecules
OA4	10 mM	A5 variable loop mimic	eMolecules
OA5	10 mM	A5 variable loop mimic	eMolecules
OA6	10 mM	A5 variable loop mimic	eMolecules
OA7	10 mM	A5 variable loop mimic	eMolecules
OA8	10 mM	A5 variable loop mimic	eMolecules

Table 2.6: Compounds used during this project

2.1.8 Antibodies and conjugates

Primary and secondary antibodies used for western blot (WB) and ELISA are detailed in **(Table 2.7)**.

Antibody	Species	Label type	Dilution	Type	Supplier
Anti-H3N2 NP	Rabbit	-	WB (1 in 2,500)	Polyclonal IgG	SinoBiological
Anti-H1N1 NP	Mouse	-	WB (1 in 2,500)	Polyclonal IgG	Generon
Anti-GAPDH	Mouse	-	WB (1 in 5,000)	Polyclonal IgG	SantaCruz Biotechnology, Inc.
Streptavidin-HRP	-	HRP	WB (1 in 5,000)	Conjugate	Fischer Scientific
Anti-mouse	Goat	HRP	WB (1 in 5,000)	Polyclonal IgG	Generon

Anti-Rabbit	Goat	HRP	WB (1 in 5,000)	Polyclonal IgG	Generon
-------------	------	-----	-----------------	----------------	---------

Table 2.7: Antibodies and conjugates used during this project

2.1.9 Growth media

2TY broth

Tryptone (16 g/L), yeast extract (10 g/L) and NaCl (5 g/L) were mixed and dissolved in de-ionised water before being autoclaved at 121 °C, 15 psi for 20 min.

LB broth

LB broth powder (20 g/L) was mixed and dissolved in deionised water before being autoclaved at 121 °C, 15 psi for 20 min.

LB agar plates

LB agar powder (32 g/L) was mixed and dissolved in de-ionised water before being autoclaved at 121 °C, 15 psi for 20 min. Following autoclaving, agar was cooled, prior to the addition of the appropriate concentration of antibiotic. 25 mL was then added per petri dish and left to set under aseptic conditions.

TYH media

Tryptone (20 g/L), yeast extract (10 g/L), HEPES (11 g/L), NaCl (5 g/L) and MgSO₄ (1 g/L) were mixed and dissolved in 1 L of de-ionised water, the pH was adjusted to 7.3 using KOH and autoclaved at 121 °C, 15 psi for 20 min.

2.1.10 Buffer recipes

Phosphate buffered saline with Tween (PBS-T)

1 % (v/v) solution of Tween-20 in PBS

1x blocking buffer

10 x blocking buffer diluted 1:10 in PBS-T

2 X blocking buffer

10 x blocking buffer diluted 1:5 in PBS-T

4x loading buffer

Bio-Rad solution supplemented with 20 % (v/ v) β -mercaptoethanol

10x Orange G loading dye

30 % glycerol, 0.2 % Orange G

Lysis buffer

50 mM NaH₂PO₄; 500 mM NaCl; 30 mM Imidazole; 20% Glycerol; pH 7.4

Wash buffer

50 mM NaH₂PO₄, 500 nM NaCl, 20 mM imidazole, pH 7.4

Elution buffer

50 mM NaH₂PO₄, 500 nM NaCl, 300 mM imidazole, 10 % glycerol, pH 7.4 Lysis buffer 50 mM NaH₂PO₄, 300 mM NaCl, 30 mM Imidazole, 10 % glycerol, pH 7.4 PBS 137 mM NaCl, 4.3 mM Na₂HPO₄, 1.47 mM KH₂PO₄, 2.7 mM KCl, pH 7.4

PEG-NaCl

20% (w/v) PEG 8000, 2.5 M NaCl

2.1.11 Microscopes

When carrying out transmission electron microscopy, a FEI Tecnai T12 was used, operating with a voltage of 120 keV LaB₆ electron source, and a Gatan US4000/SP detector with a charge coupled device (CCD) photon detector camera. Cryo-EM was carried out utilising: FEI Titan Krios G3i 300 KeV, X-FEG and autoloader with either: FEI Falcon E3C direct electron detector or energy filtered Gatan K2 XP summit direct electron detector. For tomography collections a VoltaPhase plate was used.

2.2 Mammalian cell culture and virus work

2.2.1 Passaging mammalian cells

A549 and MDCK cells were maintained in a humidified incubator at 37 °C, with 5 % CO₂. Cells were cultured in media specified in **(TABLE 2.3)**. All cell lines were split every 2-3 days with trypsin. A549 cells were used for all assays on ion channels unless otherwise stated, whilst MDCK cells were used for all experiments in Affimer assays unless otherwise stated.

2.2.2 IAV propagation

IAV A/Aichi/2/1968 (ATCC), was used to infect 1-2 x T175 cm² flasks of 70-90 % confluent MDCK cells, at a multiplicity of infection of 0.001 (MOI = 0.001) in 5 mL infection media per flask: serum-free media, with 1 µg/mL L-1-Tosylamide-2-phenylethyl chloromethyl ketone-trypsin (TPCK-trypsin, Sigma) for 1 hr. Following incubation, a further 10 mL of infection media was added per flask. IAV supernatants were harvested after 48 hrs and clarified by centrifugation at 3,200 x g for 20 mins and filtering via a 0.45 µm filter. Following clarification, IAV titres were determined by plaque assay (2.2.4).

2.2.3 IAV storage

Following clarification, IAV clarified supernatants were aliquoted into 25-50 µL aliquots and flash-frozen in LN₂. Aliquots were then placed in either LN₂ storage dewars or -80 °C freezers.

2.2.4 IAV titre determination via plaque assay

MDCK cells were seeded at 5 x 10⁵ cells per well in a 12 well plate until the following day. IAV infections were performed in duplicate in which, 6 µL of clarified supernatant was added to 54 µL of infection media to produce a 10⁻¹ dilution. This was then serially diluted from 10⁻² to 10⁻⁸ further in infection media. When cells reached 80-90 % confluency, growth media was removed, cells were washed twice with PBS and 250 µL of each dilution was added in duplicate to the cells, alongside an infection media only control. Plates were then incubated for 1 hr at 37 °C, 5 % CO₂ with regular rocking intervals to prevent cell drying. Following incubation, media was removed and replaced with a 1.5 mL solution of 2.4 % low-viscosity Avicel[®] (FMC Corporation) overlay and infection media, mixed in a 1:1 ratio. Infected cells were incubated for a further 48 hrs at which point overlay was removed and cells were fixed with 4 % paraformaldehyde (PFA) for 1 hr at 4 °C. Cells were washed 2 x with dH₂O and stained using a 0.1 % crystal violet solution (Sigma) for 15 mins at room temperature (RT). Cells underwent a final dH₂O wash and plaques were then counted and a viral titre estimate was calculated using the below equation:

$$\frac{\text{Number of plaques}}{\text{(Dilution factor x Volume)}} = \text{Viral titre in PFU/mL}$$

2.2.5 Cell viability via ATPlite assay

ATPlite[™] viability assay was carried out as described by the ATPlite[™] Perkin Elmer 1 step protocol with minor modifications (260). Briefly, MDCK or A549 cells were seeded in 96 well clear-bottom tissue

culture plates at 3×10^4 cells/well and 1.25×10^4 cells/well, respectively and incubated at 37 °C, 5 % CO₂ for 24 hrs. When at 80-90 % confluent, growth media was removed, cells washed 2 x with PBS and 100 µL of relevant drugs conditions were added in triplicate. All drug conditions were made in infection media. Cells with control and drug conditions were incubated at 37 °C, 5 % CO₂ for 48 hrs. 50 µL of mammalian cell lysis solution was added for 5 mins and left on a plate shaker, followed by 50 µL of substrate solution for a further 5 mins. The plate was then dark adapted and luminescence was read at 510 nm by an ELISA plate reader.

2.2.6 Cell viability via MTT assay

MTT cell viability & proliferation Assay protocol was executed as described by the ScienCell™ with minor modifications (260). Briefly, MDCK or A549 cells were seeded in 96 well clear-bottom tissue culture plates at 3×10^4 cells/well and 1.25×10^4 cells/well, respectively and incubated at 37 °C, 5 % CO₂ for 24 hrs. When at 80-90 % confluent, growth media was removed, cells washed twice with PBS and 100 µL of relevant drugs conditions were added in triplicate. Relevant drugs and concentrations were made in infection media. Cells with control and drug conditions were incubated at 37 °C, 5 % CO₂ for 48 hrs. MTT was reconstituted in PBS and briefly vortexed, before immediately adding 10 µL to each well and incubating for 2 hrs. Following incubation, 100 µL of MTT solubilisation was added and test absorbance of 570 nm wavelength and reference wavelength of 690 nm on an ELISA plate reader. Reference wavelength was subtracted from test wavelength to remove background absorbance.

2.3 Manipulation of DNA

2.3.1 Polymerase chain reaction

All Polymerase chain reaction (PCR) reactions were carried out using a G-Storm GS2 thermal cycler in 0.2 mL PCR reaction tubes (**Table 2.8**). Products were isolated and purified by agarose gel electrophoresis (**2.3.3**).

Component	25 μ L reaction	Final concentration
Template DNA	1 μ L	-
Phusion DNA Polymerase	0.25 μ L	0.02 units/ μ L
Forward Primer, 10 μ M	2 μ L	0.8 μ M
Reverse Primer, 10 μ M	2 μ L	0.8 μ M
DMSO	0.75 μ L	3%
dNTP mix (25 mM)	0.2 μ L	200 μ M each
5 x Phusion HF buffer	5 μ L	1 x
dH ₂ O	13.8 μ L	-

Table 2.8: : Reaction components for PCRs carried out using Phusion HF DNA polymerase

Cycle step	Temperature (°C)	Time (s)	Cycles
Initial denaturation	98	30	1
Denaturation	98	20	30
Annealing	54	20	
Extension	72	15 per kb	
Final extension	72	600	1
Hold			

Table 2.9: Reaction conditions for PCRs carried out using Phusion HF DNA polymerase

2.3.2 DNA restriction digest

In order to sub clone DNA plasmids, restriction enzyme digests were carried out. Reactions contained 1 μ g of DNA, 1 x compatible NEBuffer (NEB) and 10 units of each enzyme in a 50 μ L total volume.

Reaction mixtures were incubated at 37°C for 1 hr. Digestion products were isolated and purified by agarose gel electrophoresis (2.3.3).

2.3.3 Agarose gel electrophoresis

To assess DNA, PCR products and restriction digest products size and quality, DNA samples were mixed with 1 x DNA loading buffer ((30 % (v/v) glycerol, 0.25 % (w/v) Orange G)) prior to being loaded onto a 1 % (w/v) agarose gel made up in 1 x TAE buffer (1 mM EDTA, 20 mM glacial acetic acid, 40 mM Tris base). MassRuler DNA Ladder Mix (ThermoFisher) was also loaded to determine DNA size. Gels were run in a Bio-Rad electrophoresis gel tank at 50 V for 40 min and bands were visualised under UV using an Amersham Imager 600 (GE Healthcare).

2.3.4 Ligations

Ligations were carried out in a 4:1 molar ratio of insert: vector DNA, with the addition of 1 x ligase reaction buffer (Life technologies) and 1 unit of T4 DNA ligase (NEB). Ligation reactions were incubated at RT overnight prior to transformation in DH5 α *E. coli* cells.

2.3.5 DNA measurement

Concentration of DNA was measured using a NanoPhotometer NP80 (Implen). The spectrophotometer was blanked buffer made for DNA samples. 2 μ L of the DNA sample was then applied to the Nanodrop and the concentration determined from the A260 reading according to the rearranged Beer-Lambert equation: $A = \epsilon cl$. Where: A=absorbance, ϵ =extinction coefficient ($M^{-1}cm^{-1}$), c= concentration (M), l=optical path length (cm).

2.3.6 DNA sequencing

Purified DNA samples were submitted to GENEWIZ for sequencing via the Sanger sequencing method.

2.4 Bacterial manipulation

2.4.1 Transformation of *E.coli* by heat shock

A 50 μL (BL21 StarTM DE3) aliquot of competent cells was left to thaw on ice prior to addition of ~ 50 ng/mL of plasmid DNA. The mixture was gently agitated before incubating on ice for 30 mins, before being added to a 42 °C water bath for 45 seconds. The mixture was then immediately transferred to ice for 3 mins prior to the addition of 190 μL of SOC media. The culture was then incubated in a shaking incubator at 37 °C, 230 rpm for 1 hr. Following incubation, 100 μL was plated onto a LB agar plate with relevant antibiotic. Once dried, the plate was inverted and incubated at 37 °C overnight.

2.4.2 Generation of glycerol stocks

Overnight cultures were centrifuged for 15 mins at $2,000 \times g$, 4 °C. Media was eluted and pellets resuspended in 60% (v/v) glycerol in LB media. Stocks were then stored at -80 °C until required.

2.4.3 Purification of DNA via miniprep

Following overnight incubation on LB agar plates with relevant antibiotics, single colonies of interest were selected and used to inoculate the appropriate volume of 2TY broth containing relevant selective antibiotics, prior to overnight incubation in a shaking incubator, 37 °C, 23 rpm. Plasmid purification was then carried out using QIAprep spin miniprep kit (Qiagen) according to manufacturers instructions. DNA was eluted in the appropriate volume of dH₂O and stored at -20 °C.

2.5 Protein analysis

2.5.1 Protein concentration measurement

Protein concentration was estimated by utilising a NanoPhotometer NP80 (Implen), using the buffer the sample was in as a blank. Protein was measured at A_{280} and the theoretical coefficient used to calculate protein concentration in mg/mL (Equation previously described in **2.3.5**).

2.5.2 Dialysis of purified protein

Proteins were buffer exchanged into relevant buffers by Slide-A-Lyzer dialysis cassettes (ThermoScientific) with a MWCO of 7000 KDa and a volume capacity of either 0.5 or 3 mL. Cassettes were pre-hydrated in the dialysis buffer by immersion for 5 mins. Protein was then loaded into cassette via syringe injection into one of the syringe ports. Air was removed from the cassette and the cassette attached to a float before being placed in 5 L of the dialysis buffer for 4 hrs at RT or overnight at 4 °C. Dialysed protein was then removed via a different syringe port and stored appropriately.

2.5.3 SDS-polyacrylamide gel electrophoresis (SDS-PAGE)

Protein samples were mixed 3:1 in 4 x Laemmli Sample Buffer (BioRad) with beta-mercaptoethanol before samples were denatured through heating at 95 °C for 5 mins and loaded next to 3 µL of colour pre-stained protein standard, broad range (NEB) on a 4-15% Mini-PROTEAN® TGX™ Precast Protein Gel (BioRad). Electrophoresis was carried out in running buffer (25 mM Tris, 192 mM glycine, pH 8.3) at 180 V for 45 mins-1 hr. Once electrophoresis was complete, InstantBlue® Coomassie Protein Stain (abcam) was added and gel left on a rocker overnight or until protein bands were clearly visible.

2.5.4 Western blotting

Following electrophoresis on an SDS-PAGE gel, samples were transferred onto polyvinylidene fluoride (PVDF) membranes (Millipore) using a trans-blot semi-dry cell (Bio-Rad) in Towbin buffer ((25 mM Tris, 192 mM glycine, 20 % (v/v) methanol)) for 30 mins at 20 V. Membranes were blocked for 1 hr at RT or overnight at 4 °C in blocking buffer ((5 % w/v) reconstituted semi-skimmed milk powder in 1 x TBS buffer). Blocking buffer was replaced with primary antibodies diluted in blocking buffer and membranes incubated for 1 hr at RT or overnight at 4 °C. Membranes were then washed 3 times in 1 x TBST before being added to secondary antibodies diluted in blocking buffer. After a final 3 x washes, 500 µL of EZ-ECL (Biological Industries) was added to membranes and WB imaged using a G: BOX (Syngene).

2.6 Production and purification of IAV to electron microscopy standards

2.6.1 IAV propagation for purification

Similar to previously (2.2.2), IAV A/Aichi/2/1968 (ATCC), was used to infect 10 x T175 cm² flasks of 70-90% confluent MDCK cells, at a MOI of 0.001.

2.6.2 IAV high-grade purification

Following propagation and clarification (2.6.1), clarified supernatant was gently laid on either a 20% or 30% (w/v) sucrose cushion made in 1 x NTC buffer (1 M NaCl, 0.2 M Tris-HCl pH 7.4, 50 mM CaCl₂) in thick wall tubes (Beckman) and ultra-centrifuged at 90,000 x *g* at 4 °C for 90 mins. Following centrifugation, the viral pellet was re-suspended in 1 x NTC buffer by shaking at 4 °C overnight. Ultra-centrifugation was repeated, along with resuspension to improve sucrose removal, viral stocks were then stored at either 4 °C or at -80 °C for further analysis. Aliquots were taken at each stage of purification for analysis by SDS-PAGE (2.4.3) and negative stain electron-microscopy (2.11.1).

2.7 Isolation of Hemagglutinin from whole virus

2.7.1 Hemagglutinin crude extraction

Following IAV purification (2.6.1 & 2.6.2), however post-ultra-centrifugation, rather than resuspending in 1 x NTC buffer, pelleted virions were resuspended in lysis buffer ((1 x NTC buffer supplemented with 2 % (w/v) Octyl-beta-Glucoside (VWR)) overnight at 4 °C on a rocker. Aliquots were collected, mixed and added to a TLA 110 E centrifuge tube which was centrifuged for 1 hr at 100,000 x *g* and 4 °C. Of which supernatant was collected containing viral membrane proteins in detergent micelles.

2.7.2 Affinity chromatography

Following HA crude extraction (2.7.1), 2 mL of agarose: *Ricinus communis Agglutinin I* (RCA) was resuspended in 10 mL binding buffer (20 mM Tris-HCl, 0.5 M NaCl, 1 mM MnCl₂, 1 mM CaCl₂, dH₂O), added to a 50 mL falcon and centrifuged at 2,000 x *g*, 4 °C for 5 mins, buffer was removed, being careful not to elute RCA. Washing was repeated 5 x before RCA was resuspended in 3 mL binding

buffer and packed by gradually adding to a 5 mL polystyrene gravity flow column (ThermoScientific). Membrane protein supernatant was then added at 4 °C for 4 hrs on a rocker before being washed 5 x with 0.5 mL binding buffer to further remove contaminants before finally eluting by washing 8 times with 0.5 mL elution buffer (150 mM NaCl, 30 mM Octyl-Glucoside, 0.2 M D+ galactose, PBS, pH 7.4). Wash steps and Elution steps were retained and ran on SDS-PAGE gels to assess HA purity **(2.5.3)**.

2.7.3 Anion exchange chromatography

Following purification **(2.6.2)**, HA-containing elution samples were injected to a pre-equilibrated (20 mM Tris, pH 7.5, 100 mM NaCl), 1 mL HiTrap Q HP anion exchange chromatography column attached to an ÄKTA system (Cytiva). Elution of HA was carried out by applying a linear gradient of 100-1500 mM NaCl. Each elution protein peak was then dialysed into final protein buffer: 25 mM Tris pH 8.0, 150 mM NaCl (2.5.2) and assessed for presence of HA by WB and negative stain EM **(2.5.4 and 2.11.1)**

2.8 Phage display techniques

2.8.1 Biotinylation of target proteins with EZ-Link® NH-SS-Biotin

In order to biotinylate target proteins for phage display, EZ-Link® NH-SS-Biotin (ThermoScientific) was equilibrated at/to RT and diluted to 5 mg/mL in DMSO immediately prior to use. NH-SS-Biotin was mixed with 1 mg/mL of target protein in a 20-fold molar excess, in a total volume of 100 µL PBS and incubated for 1 hr at RT. Following incubation, excess biotin was removed by using Zeba™ Spin Desalting Columns, 7 KDa MWCO (ThermoScientific) according to the manufacturer's instructions. Samples were then mixed with an equal volume of 80 % (v/v) glycerol and stored at -20 °C.

2.8.2 ELISA to confirm biotinylation

To confirm biotinylation, target proteins were added at a range of dilutions (1, 0.1, 0.01 µL) to 50 µL PBS in Nunc-Immuno™Maxisorp™ strips (ThermoScientific). The strips were incubated overnight at 4 °C prior to washing 3 times with PBST using a HydroFlex plate washer (Tecan), 150 µL of 2 x blocking

buffer (10 x blocking buffer, Sigma, diluted in PBST) was added to each well and incubated at 37 °C for 3 hrs and then washed 3 times again with 300 µL of PBST by plate washer. High Sensitivity Streptavidin-HRP (Thermo Scientific) was diluted 1:1,000 in 2 x blocking buffer and 50 µL was added to each well before incubating for 1 hr at RT on a vibrating platform shaker (Heidolph VIBRAMAX 100; speed setting 3). Wells were washed an additional 6 times with 300 µL of PBST in plate washer before 50 µL of TMB SeramunBlau® fast TMB/substrate solution, Seramun) was added and left to develop for 10 mins before measuring absorbance in a plate reader at 620 nm.

2.8.3 Phage display against biotinylated targets

All phage display screening was carried out kindly by Dr. Christian Teide using protein LoBind tubes (Eppendorf) and EZ-link NH-SS-Biotin biotinylated proteins as targets (as described in **2.8.1** and **2.8.2**).

2.8.3.1 First panning round

A colony of ER2738 *E. coli* cells was added into 5 mL of 2TY media with 12 µg/mL tetracycline and incubated overnight in an orbital incubator at 37 °C, 230 rpm. 300 µL of 2 x blocking buffer was added per well to a Streptavidin Coated (HBC) 8-well strips (Thermo Scientific) and incubated at 37 °C overnight. 4 wells were set up in total for panning against each HA (3 wells for pre-panning the phage and 1 well for binding HA and panning with phage).

On the following day, wells were washed 3 times with 300 µL of PBST on a plate washer before 100 µL of 2 x blocking buffer was added to all wells. 5 µL of phage library was added to the first pre-pan well and mixed and incubated on a vibrating platform shaker for 40 mins. 20 µL of biotinylated HA was added to panning wells and incubated for 1 hr at RT on a vibrating platform shaker. Buffer was removed from the second pre-pan well and buffer containing phage was transferred to the second pre-pan well and incubated for 40 mins. This was repeated for the third pre-pan well. Wells containing HA were washed 6 x with 200 µL of PBST and phage was transferred into these wells for 2 hrs at RT on a vibrating platform shaker, whilst incubating a fresh culture of ER2738 cells (8 mL) was prepared by diluting overnight culture 1/15 and incubating for ~1 hr at 37 °C, 230 rpm until an A_{600} of ~0.6 was achieved. Phage was eluted by adding 0.2 M glycine, pH 2.2 for 10 mins at RT and neutralising with 15 µL of 1M Tris-HCl, pH 9.1 and mixing immediately with the ER2738 cells in a 50 mL falcon tube. 14 µL of Triethylamine (Sigma-Aldrich) was diluted with 986 µL of PBS and 100 µL was added for 6 mins at RT to final well to elute any remaining phage, this was neutralised by adding 50 µL of 1 M Tris-HCl, pH

7 and adding immediately to the ER2738 cells. Cells were incubated at 37 °C for 1 hr before plating 1 µL of phage-infected ER2738 cells onto LB carb plates (LB agar plates containing 100 µg/mL carbenicillin) overnight at 37 °C.

The next day, colonies were counted and multiplied by 8,000 to determine total number of cells per 8 mL and then scraped from plates by adding 5 mL of 2TY carb to the plate and scraping using a disposable plastic spreader, this was transferred to a 50 mL falcon containing 2 mL of 2TY carb. Cells were diluted in 2TY in 50 mL falcon tubes to achieve a A_{600} of 0.2 in 8 mL, these were then incubated for 1 hr at 37 °C, 230 rpm before 0.32 µL of M13K07 helper phage (titre ca. 10^{14} / mL) and incubated at 37°C, 90 rpm, for 30 mins. Finally, 16 µL of kanamycin (25 mg/mL) was added and incubated overnight in an orbital incubator at 25 °C, 170 rpm.

On the final day, phage-Infected cultures were centrifuged at 3,500 x *g* for 10 mins and transferred to fresh tubes. 2 mL of PEG-NaCl precipitation solution (20% (w/v) PEG 8000, 2.5 M NaCl) was added to the remaining supernatant (not required for the second panning round) and incubated at 4 °C overnight. Phage was pelleted by centrifuging for 30 mins at 4,816 x *g*, supernatant eluted and resuspended in 320 µL TE. This was then microcentrifuged at 16,000 x *g* for 10 mins, phage containing supernatant was then stored at 4 °C.

2.8.3.2 Second panning round

On the first day, a colony of ER2738 *E. coli* cells was added into 5 mL of 2TY media with 12 µg/mL tetracycline and incubated overnight in an orbital incubator at 37 °C, 230 rpm. 20 µL of Streptavidin beads (Dynabeads® MyOne™ Streptavidin T1, 10 mg/mL, Invitrogen) were pre-blocked in 2 x Blocking Buffer and incubated overnight at RT on a Stuart SB2 fixed speed rotator (20 rpm).

Both deep well 96 plate (Thermo Scientific) and KingFisher 96 plates (Thermo Scientific) were pre-blocked with 1 mL and 200 µL respectively of 2 x blocking buffer for 2 hrs at 37 °C for the Kingfisher Flex (Thermo Scientific). The following day, pre-blocked streptavidin beads were centrifuged at 800 x *g* for 1 min and immobilised on a magnet to remove blocking buffer. 100 µL of fresh 2 x blocking buffer was added per 20 µL of bead before mixing 25 µL with 250 µL of phage from the first panning round diluted 1:50 with 2 x blocking buffer in Eppendorf Protein LoBind Tubes (Eppendorf) and incubated for 1 hr at RT on a rotator. The solution was centrifuged at 800 x *g* for 1 min and placed on a magnet. Supernatant containing phage was removed and added to a fresh tube with 25 µL of Streptavidin beads to be incubated for 1 hr at RT. 15 µL of biotinylated HA was mixed with 200 µL of

2 x blocking buffer and 50 μ L of the pre-blocked streptavidin beads and incubated at RT for 1 hr on a rotator. Buffer was removed from pre-blocked deep well 96 plate and the pre-blocked elution plate and 100 μ L of 0.2M Glycine, pH 2.2 was added per well. 14 μ L of Triethylamine was diluted with 986 μ L of PBS and 100 μ L added per well into the plate. Tubes containing biotinylated HA were centrifuged at 800 x *g* for 1 min and placed on a magnet, washed 3 x with 500 μ L 2 x blocking buffer before repeating centrifugation. Supernatant containing pre-panned phage were then added to beads containing biotinylated HA, mixed and transferred to the pre-blocked deep well 96 plate. Kingfisher Flex was set up to run protocol "Phage_Display_Standard" (**Table 2.10**). 1 hr prior to this, an 8 mL fresh culture of ER2738 cells was set up by diluting the overnight culture approx. 1/15 and incubating for approx. 1 hour at 37 °C, 230 rpm. As soon as the Kingfisher Flex protocol was finished, elution buffer was neutralised with 50 μ L of 1 M Tris-HCl, pH 7 and mixed with ER2738 cells and incubated for 1 hr at 37 °C. Cells were then centrifuged for 5 mins at 3,000 x *g* and plated onto LB carb plates which were incubated overnight at 37 °C.

On the third day, phage was prepared as described in the first panning round (**2.8.4**).

Protocol Step	Plate	Volume (μ L)	Settings
Tipcomb	96 DW tip comb	-	-
Pick-Up: Tipcomb	KingFisher 96 KF plate	-	-
Collect Beads	Plate: Binding Microtiter DW 96 plate	-	Collect count: 1 Collect time (s): 1
Binding	Plate: Binding Microtiter DW 96 plate	300	Beginning of Step Release beads [hh:mm:ss]: 00:00:00 Mixing/Heating Parameters Mix time [hh:mm:ss]: 00:00:10 Speed: fast Mix time [hh:mm:ss]: 01:00:00 Speed: slow End of step

			Collect beads, count: 5 Collect time (s): 30
Wash 1	Plate: Wash 1 Microtiter DW 96 plate	950	Beginning of Step Release beads [hh:mm:ss]: 00:00:00 Mixing/Heating Parameters Mix time [hh:mm:ss]: 00:01:00 Speed: slow End of step Collect beads, count: 5 Collect time (s): 30
Wash 2	Plate: Wash 2 Microtiter DW 96 plate	950	Beginning of Step Release beads [hh:mm:ss]: 00:00:00 Mixing/Heating Parameters Mix time [hh:mm:ss]: 00:01:00 Speed: slow End of step Collect beads, count: 5 Collect time (s): 30
Wash 3	Plate: Wash 3 Microtiter DW 96 plate	950	Beginning of Step Release beads [hh:mm:ss]: 00:00:00 Mixing/Heating Parameters Mix time [hh:mm:ss]: 00:01:00 Speed: slow End of step Collect beads, count: 5 Collect time (s): 30
Wash 4	Plate: Wash 4 Microtiter DW 96 plate	950	Beginning of Step Release beads [hh:mm:ss]: 00:00:00 Mixing/Heating Parameters Mix time [hh:mm:ss]: 00:01:00 Speed: slow End of step Collect beads, count: 5 Collect time (s): 30

pH Elution	Plate: pH elution KingFisher 96 KF plate	100	Beginning of Step Release beads [hh:mm:ss]: 00:00:00 Mixing/Heating Parameters Mix time [hh:mm:ss]: 00:07:30 Speed: slow Postmix[hh:mm:ss]: 00:00:05 Speed: Bottom mix End of step Collect beads, count: 5 Collect time (s): 30
Triethylamine Elution	Plate: Triethylamine KingFisher 96 KF plate	100	Beginning of Step Release beads [hh:mm:ss]: 00:00:00 Mixing/Heating Parameters Mix time [hh:mm:ss]: 00:03:30 Speed: slow Postmix[hh:mm:ss]: 00:00:05 Speed: Bottom mix End of step Collect beads, count: 5 Collect time (s): 30
Leave: Tipcomb	96 DW tip comb		

Table 2.10: Kingfisher Flex ‘Phage_display_pH_elution’ protocol

2.8.3.3 Third (final) panning round

On the first day, a colony of ER2738 E. coli cells was added into 5 mL of 2TY media with 12 µg/mL tetracycline and incubated overnight in an orbital incubator at 37 °C, 230 rpm. 200 µL of 2 x blocking buffer was added per well to 6 wells of a NeutrAvidin Coated (HBC) 8-well strip (Thermo Scientific) and incubated overnight at 37 °C.

The next day, HBC wells were washed 3 times with 300 µL of PBST on a plate washer, followed by the addition of 200 µL of 2 x blocking buffer to the panning well and 3 of 4 pre-panning wells. 20 µL of 10 x blocking buffer was added to the other pre-panning well along with 200 µL of phage containing

supernatant from the second panning round. These were then incubated for 1 hr at RT on a vibrating platform shaker. At this point, buffer from the second pre-panning well was removed and contents from the first (phage containing) well was transferred and incubated again for 1 hr. This was repeated for the third and fourth pre-panning wells. At this stage, buffer was removed from the panning well, 100 μ L of 2 x blocking buffer and 10 μ L of biotinylated HA was added to the well and was incubated for 1 hr at RT on a vibrating platform shaker. Following incubation, panning well and negative control wells were washed 3 x with PBST and 100 μ L of phage was transferred from the pre-pan wells to HA containing panning well and negative wells. This was incubated for 45 mins at RT on a vibrating platform shaker.

Finally, a fresh 10 mL culture of ER2738 was setup by diluting the overnight culture 1/15 and was incubated for 1 hr at 37 °C, 230 rpm. The panning well was washed 27 x with 300 μ L PBST on a plate washer and phage eluted by adding 100 μ L of 0.2 M Glycine, pH 2.2, and incubating for 10 mins at RT. This was neutralised by adding 15 μ L of 1 M Tris-HCl, pH 9.1. and mixed immediately to 5 mL culture of ER2738 cells in a 50 mL falcon tube. Cells were incubated for 1 hr at 37 °C and plated out in a range of volumes (0.1, 1, 10 and 100 μ L) onto LB carb plates, one volume was selected for the negative control. Plates were incubated overnight at 37 °C.

2.6.4 Phage ELISA

Following work carried out by Dr. Christian Teide, phage was prepared, 200 μ L of 2TY carb was added per well to a 96 well V-bottom deep well plate. Individual colonies were picked from appropriate plates from the final panning round of phage display. These were incubated overnight at 37 °C, 1050 rpm in an incubating microplate shaker (Heidolph Incubator 1000). 200 μ L of fresh 2TY carb was added to 5 new 96-well V-bottom deep well plates and 25 μ L per well of overnight cultures added into this new plate and incubated for 1 hr at 37 °C, 1050 rpm in the incubating microplate shaker. M13K07 helper phage (titre ca. 10¹⁴/mL) was diluted 1/1000 in 2TY carb and added 10 μ L per well to the freshly grown cultures, incubated at RT, 450 rpm for 30 mins in an incubating microplate shaker. Kanamycin (1.25 mg/mL) was added 10 μ L per well to the infected cultures and incubated overnight at RT, 750 rpm in the incubating microplate shaker.

To prepare streptavidin coated 96 well plates, 5 mg of lyophilised streptavidin was reconstituted in dH₂O, diluted to 2.5 µg/mL in PBS and 50 µL added per well to 10 x F96 Maxisorp Nunc-Immuno Plate (Thermo Scientific). These were incubated at 4 °C overnight.

To carry out the phage ELISA, 200 µL of 2 x blocking buffer was added per well to the streptavidin-coated 96-well plates and incubate overnight (without agitation) at 37 °C. Plates were washed once with 300 µL of PBST with plate washer and 50 µL of biotinylated HA (Diluted 1/100 in 2 x blocking buffer) was added to the first 6 columns of the streptavidin-coated plates, whilst 50 µL of 2 x blocking buffer was added to the last 6 columns to act as a negative control. Plates were incubated for 1 hr at RT on a vibrating platform shaker before being washed 1 x with 300 µL of PBST on a plate washer. The phage-infected culture plate was centrifuged at 3,500 x g for 10 mins before 10 µL of 10 x blocking buffer was added to each well of the streptavidin-coated plates and 40 µL of each phage supernatant was added to 1 test well and 1 negative control well (e.g binder A1 is added to wells A1 and A7). Plates were then incubated for 1 hr at RT on a vibrating platform shaker before washing once with 300 µL of PBST per well on a plate washer and adding 50 µL per well of diluted Anti-Fd-Bacteriophage-HRP (1/1000 in 2 x blocking buffer) for 1 hr RT on a vibrating platform shaker. Finally, plates were washed a further 10 times with 300 µL of PBST on a plate washer and 50 µL of TMB (SeramunBlau® fast TMB/substrate solution, Seramun) was added per well. TMB was allowed to develop for 5 mins before being measured at 620 nm on a plate reader.

2.9 Affimer production and purification

2.9.1 Affimer expression and purification

Following transformation (**2.4.1**), day cultures were set up by picking a single colony and inoculating 200 µL of 2YT carb in a 2 mL round bottom tube and incubated for 6 hrs at 37 °C, 230 rpm. 100 µL of the day culture was added to 50 mL of terrific broth (TB) auto-induction media containing carb and incubated at 25 °C, 230 rpm for ~66 hrs before harvesting cells. At ~48 hrs Isopropyl β-d-1-thiogalactopyranoside IPTG was added at a final concentration of 0.1 mM to encourage protein production.

Cell pellets were resuspended with extraction buffer (**Table 2.11**) and transferred to a 15 mL centrifuge tube to incubate at RT for 1 hr on a rotator. To heat denature non-specific proteins, samples were incubated at 50 °C for 20 mins in a water bath before centrifuging to pellet cell debris and insoluble proteins at 4,800 x *g* for 20 mins. Magnetic Nickel (Ni) beads were prepared by thoroughly resuspending and collecting 150 µL of bead slurry per sample into a new tube. A magnetic stand was used to remove storage buffer and 1 mL of wash buffer was added (50 mM NaH₂PO₄; 500 mM NaCl; 20 mM Imidazole; pH 7.4). This was repeated twice before finally resuspending in 50 µL of wash buffer per sample. 950 µL of lysate was added to each of the 3 deep 96 well Kingfisher plates and 50 µL of washed bead slurry added to the top of each lysate in the first binding plate. 3 wash plates were prepared by adding 1 mL of wash buffer to 3 deep well kingfisher plates and finally an elution plate was prepared, in which 150 µL of elution buffer (50 mM NaH₂PO₄, 500 mM NaCl; 300 mM Imidazole; 10 % Glycerol; pH 7.4) was added per well to a Kingfisher shallow 96 well plate. Once all plates were prepared, they were loaded into the kingfisher along with a tip comb and protocol 'chris_protein_purification' was initiated.

	50 mL cell pellet
Lysozyme (10 mg/mL)	30 µL (0.1 mg/mL)
Triton X-100	30 µL (1 %)
Benzonase® Nuclease, Purity > 99% (25 U/µL)	1.2 µL (10 U/mL)
Halt Protease Inhibitor Cocktail (100X)	30 µl (1X)
LYSIS BUFFER	to a total volume of 3 mL

Table 2.11: Extraction buffer composition

2.9.2 Sub-cloning Affimer from phagemid vector to pET-11a plasmid

Affimer DNA sequence was amplified from the pBSTG phagemid vector by PCR (as previously described **2.2.1**) using primers listed below (**TABLE 2.12**) to incorporate a free cysteine for

biotinylation or fluorophore labelling downstream (see both **2.5.1** and **2.6.3**). Following amplification, the reaction mixture was incubated with *DpnI* enzyme (NEB) at 37 °C for 1 hr and purified using a NucleoSpin Gel and PCR Clean-up kit (Machery-Nagel). Linearised Affimer sequence was then digested using *NheI* and *NotI* restriction enzymes and purified again before being ligated with similarly digested pET-11a vectors using T4 DNA ligase (NEB), along with a negative control. Supercompetent XL1-Blue *E. coli* cells were then transformed with the pET-11a/Affimer plasmids (**2.3.1**) and plated onto LB plates containing 100 µg/mL carbenicillin and incubated at 37 °C overnight. Plasmid DNA was extracted from overnight cultures, minipreped as previously described (**2.3.3**) and DNA sequenced to confirm the correct insert (**2.2.6**).

Primer	Sequence
pBSTG-Aff forward	5' - ATGGCTAGCAACTCCCTGGAAATCGAAG
pBSTG-Aff reverse (+ cystine)	5' - TTACTAATGCGGCC GCACA AGCGTCACCAACCGGTTTG

Table 2.12: PCR primer sequences, cystine is highlighted in bold

2.9.3 Affimer Maleimide labelling

Affimer molecules were first prepared by being diluted in 1 x PBS to achieve ~150 µL at a concentration of 0.5 mg/mL. Immobilised TCEP Disulphide-reducing gel (ThermoScientific) was prepared by removing 150 µL from resuspended gel stock before washing with 300 µL of PBS containing 1 mM EDTA and centrifuging for 1 min at 1,000 x *g*. The supernatant was aspirated and resuspension and centrifugation was repeated 3 times. 4 µL of PBS containing 50 mM EDTA was added to 150 µL of diluted Affimer and incubating on a rotator for 1 hr at RT. Following incubation, the solution was centrifuged for 1 min at 1,000 x *g* and 130 µL of supernatant containing Affimer with reduced cysteines was carefully removed. Affimers were immediately added to a tube containing 6 µL of a 2 mM Biotin-Maleimide stock (Sigma-Aldrich) or 488-Maleimide stock (kindly provided by Dr. Glenn Carrington) and incubated at RT for 2 hrs. Finally, Affimer were desalted using Zeba Spin Desalting Columns, 7 KDa

MWCO (Thermo Fisher Scientific) according to manufacturer's instructions and final concentration was measured by BCA assay.

2.9.4 Mass spectrometry to assess biotinylation of Affimers

Biotinylated Affimer molecules were diluted to 20 μM in 1 x PBS before being further diluted to 5 μM in 0.1% TFA and subjected to liquid chromatography–mass spectrometry (LC-MS) mass spectrometry by the Mass Spectrometry facility at the University of Leeds.

2.10 Characterisation of Affimer-HA interactions

2.10.1 Affinity assessment via HA-ELISA

Either monomeric HA Aichi or HA1 head domain Aichi (5 $\mu\text{g}/\text{mL}$) (**Table 2.4**) were bound to Maxisorb plates (Nunc) overnight at 4 °C and then blocked with 1 x casein blocking buffer (Sigma) for 4 hrs at RT. The plates were washed once and incubated with a concentration range (7.41 μM -125.5 pM) of biotinylated anti-HA Affimer for 1 hr at RT. Subsequently, the plate was washed once with PBST and bound anti-HA Affimer molecules were detected by a 1:1000 dilution of HRP-conjugated streptavidin (Pierce) for 1 hr at RT. Following washing 10 times with PBST, Affimer molecules binding was visualised with TMB (Seramun) and measured at 405 nm.

2.10.2 Microneutralisation assay

Virus neutralisation capacity of selected Affimer molecules was determined against a 100 x TCID₅₀ of each virus strain (**Table 2.4**) by crystal violet staining of protected cells. Affimer molecules were serially diluted from top concentration 100 μg ((7.41 μM -125.5 pM (in duplicates)) in 50 μL cell culture medium (MEM) in 96 well plates, or Affimer loop compounds were diluted in a 1:2 dilution series starting from the compound's highest tolerable concentration. The diluted Affimer molecules or loop compounds were exposed to 100 x TCID₅₀ IAV in 50 μL MEM. Affimer/virus mixtures (100 μL) were transferred onto 90 % confluent MDCK cells. Controls consisted of cells exposed to virus suspension only to determine maximal cytopathic effect, cells incubated with medium only to determine baseline

state of cells, and cells exposed to virus/non-HA-specific Affimer to ensure HA isolated Affimer molecules were specific effect. The plates were incubated for 3 days at 37 °C and the cytopathic effect determined by staining with 50 µL/well crystal violet solution (Sigma-Aldrich, V5265) for 15 mins and washing plates with PBS. Wells were visually evaluated for complete protection indicated by intact blue/violet cell layer or partial protection in case of >50 % intact cell layer.

2.10.3 Surface plasmon resonance affinity determination of Affimers

Affimer molecules were biotinylated (**2.9.3**) before being immobilized on a Sensor Chip SA (GE Healthcare) via streptavidin-biotin interaction using a Biacore 3000 (GE Healthcare). Affimer molecules were diluted to 100 nM in PBS supplemented with Tween20 (0.05 %) and injected into their respective flow cells at 5 µL/min until surface density reached 120 response units. Flow cell 1 was not coated as reference surface. Recombinant HA proteins were then diluted in PBST at a concentration range of 800 nM to 3.75 nM and injected at 20 µL/min for 120 seconds. BIAevaluation software was used for double-referencing analysis. Affinity and kinetic constants were calculated using a Langmuir 1:1 binding model and steady-state affinity models.

2.10.4 Hemagglutination assay

Affimer molecules were serially diluted from top concentration 100 µg (7.41 µM-125.5 pM (in duplicates)) in 25 µL PBS in 96-well U-bottom plates (Thermo Scientific™, 163320). The diluted Affimer molecules were exposed to 4 pre-determined HA units of H3N2 (A/Aichi/2/1968) diluted in PBS. Affimer/virus mixtures (50 µL) were then incubated for 45 mins at 37 °C before adding 50 µL of 1 % human red blood cells (RBC) (Cambridge Bioscience, RBC1DC4CIT03-XSXX) and incubating for 1 hr, RT. Hemagglutination effect was recorded by visual inspection.

2.10.5 Fusion assay

The RBC fusion assay was adapted from previously described methods (261). 100 µL of 1 % human RBC and 100 µL of H3N2 (A/Aichi/2/1968) were incubated on ice for 30 mins. Affimer molecules (100, 20, 2 µg/mL), including control Affimer, were then added to the mixtures and incubated on ice for 30 mins. Samples were spun down at 4,000 x *g* for 3 mins, supernatant aspirated and 200 µL of buffered

solution (15 mM citric acid (pH 5.0), 150 mM NaCl₂) before incubating at 37 °C for 30 mins. Samples were spun at 4,000 x g and supernatant harvested. Lysis of RBCs was measured by the presence of nicotinamide adenine dinucleotide phosphate (NADPH) (optical density of 340 nm).

2.10.6 Egress Assay

MDCK cells were first infected with a MOI of 5, H3N2 (A/Aichi/2/1968) diluted in infection media. At 4 hrs post infection, HA-specific Affimer molecules and control Affimer K3 were added to the culture. At 8 hrs post infection, supernatants from cultures were harvested and centrifuged to remove cellular debris. Nascent virus was assessed by using a hemagglutination assay as previously described **(2.10.4)**.

2.10.5 *In-silico* predictive protein-protein interactions

Affimer homology models were made using SWISS-MODEL by inputting Affimer sequences and crystal structure of previously resolved Affimer (PDB: 6HJL), crystal structure of Influenza A virus (A/Aichi/2/1968(H3N2)) HA (PDB: 5HMG) was also utilised. Affimer molecule-HA interactions were predicted using online ClusPro servers with the top-ranking prediction being selected (262–265).

2.10.6 Affimer loop compound selection

All Affimer loop compound selection was kindly carried out by Alex Flynn. The homology model of Affimer molecule A5 was used to select compounds **(2.10.5)**. The two loops of the Affimer molecule were isolated using PyMol, and used as query molecules in the shape comparison software ROCS (OpenEye). The Affimer loops were screened against the full eMolecules library of 1.2 million compounds, which had been prepared with 10 maximum confirmations using Omega (OpenEye). The top 1,000 hits from ROCs were then screened using EON (OpenEye), which compares the electrostatic properties of the ROCS hits against each of the individual Affimer loops. Following comparison, the top 150 compounds were visually inspected manually by Alex Flynn using VIDA (OpenEye) looking for similarities in side chain and structure of hits and Affimer loops, and selecting compounds with maximal coverage of Affimer loops. Following compound screening 8 of the 15 compounds were

selected based on availability. These 8 compounds were then assessed in cellular assays described (2.2.5 and 2.10.2).

2.11 Electron microscopy

2.11.1 Negative stain EM grid preparation

All samples were screened via negative stain TEM prior to cryo-EM work. In-house made (Astbury Biostructure Laboratory) carbon-coated grids were glow discharged (PELCO easyGlow) for 45 secs immediately prior to sample application. 3 μL of sample was applied to a glow discharged grid for 1 min before applying to a 50 μL droplet of dH_2O and instantly blotting with filter paper (Whatman), this was repeated 3 times leaving the grid on the final droplet for 30 secs prior to a final blot. Finally, the grid was placed on a 3 μL droplet of (2% (w/v) uranyl acetate) for 30 secs before a final blot. The stained-sample grid was then left to air dry before loading in to a TEM.

2.11.2 Transmission electron microscopy (TEM)

Stained-sample-grids were loaded into a single tilt holder and inserted into the inserted into a FEI Tecnai T12 electron microscope. Microscope alignments were carried out prior to image acquisition. For imaging, a defocus of (-)1 μm -(-)5 μm was applied.

2.11.3 HA and HA-Affimer Cryo-EM rapid grid preparation

For HA and HA-Affimer screening and collection, grids were made by diluting trimeric HA/HK68 (2.1.6) to a concentration of 2.9 mg/mL in 1 x TBS buffer. David Klebl kindly made cryo-grids by rapid cryo-EM grid preparation, which was carried out using a custom-built setup previously described by Kontziampasis et al (266). QUANTIFOIL[®] 300 mesh Cu R1.2/1.3 grids were glow discharged in a Cressington 208 Carbon coater with glow-discharge unit for 99 seconds at 15 mA and 0.1 mbar. The spray was generated using a gas dynamic virtual nozzle, design and operation of which have been described previously (266). In this work, the nozzle was operated in spraying mode with a gas pressure of 2 bar and a liquid flowrate of 5.2 $\mu\text{L}/\text{s}$. The sample was sprayed onto an EM grid, moving at 1.9 m/s. The nozzle-grid distance at the point of sample application was 1 cm, resulting in a rapid time-of-flight for the droplets of less than 1 ms. With a vertical distance of 2.3 cm between spray nozzle and liquid ethane surface, the time-delay between spraying and vitrification was calculated to be 12 ms (266).

2.11.4 HA and HA-Affimer Cryo-EM detergent grid preparation

For HA and HA-Affimer screening and collection, grids were made by diluting trimeric HA/HK68 (2.1.6) to a concentration of 2.0 mg/mL in 1 x TBS buffer supplemented with 2 % (w/v) Octyl-beta-Glucoside (VWR) final detergent concentration. QUANTIFOIL[®] R1.2/1.3 holey carbon 400 mesh grids (Agar Scientific) were glow discharged using a Tergeo Plasma Cleaner (PIE Scientific), sample was added and then immediately loaded to a FEI Vitrobot Mk IV. Grids were taken into the loading chamber, pre-set at 4 °C, 100 % humidity held for 4 s, then blotted for a further 4 s before finally being plunged into liquid ethane. Frozen grids were clipped for use on the Krios microscopes and stored in LN₂.

2.11.5 IAV - K⁺ virion priming and Cryo-EM grid preparation

EM-grade purified IAV was primed as in (2.12.7), using buffers pH 7.4 +/- 140 mM KCl and pH 5.8 +/- 140 mM KCl. Buffers were produced as in (2.12.6), though concentrations of sample were increased for a 1:1 dilution of IAV:buffer in order to provide sufficient sample for collection. 3 µL of purified IAV was mixed with 3 µL of buffer and incubated for 2 hrs at 37 °C, before being immediately taken for grid preparation. Buffer was pre-warmed to 37 °C overnight to perform pH adjustments immediately prior to IAV addition.

3 µL of gold fiducial markers (Conventional ImmunoGold Reagent, Orion) was added to each priming mixture to produce a final dilution of 1:1:1. QUANTIFOIL[®] lacey-carbon, 400 mesh EM grids (Agar Scientific) were glow discharged using a Tergeo Plasma Cleaner (PIE Scientific), sample was added and then immediately loaded to a FEI Vitrobot Mk IV. Grids were taken into the loading chamber, pre-set at 4 °C, 100 % humidity held for 4 s, then blotted for a further 4 secs before finally being plunged into liquid ethane. Frozen grids were clipped for use on the Krios microscopes and stored in LN₂.

Condition	pH	Buffer	KCl (mM)	NaCl (mM)
7.4 K ⁺	7.4	HEPES (20 mM)	280	10
7.4	7.4	HEPES (20 mM)	0	10
5.8 K ⁺	5.8	MES	280	20
5.8	5.8	MES	0	20

Table 2.13: Cryo-EM priming buffer contents

2.11.6 Cryo-EM grid screening

All grids were loaded by the EM facility staff at the Astbury Biostructure Laboratory to one of the two titan Krios microscopes (2.1.11). All screening images were acquired at a defocus of -3 μm .

2.11.7 Cryo-EM single particle collection

Hardware	Conditions
Microscope	Krios2
Detector (mode)	Counting
Accelerating voltage (keV)	300
Pixel size (\AA)	1.07
Data acquisition parameters	
Nominal magnification	130k
Spot size	6
Illuminated area (μm)	1.3
Dose	
Square pixel (\AA^2)	1.14
Dose per physical pixel per second	8.203
Dose per $\text{\AA}^2/\text{sec}$	7.20
Exposure time (seconds)	7
Total dose ($\text{e}/\text{\AA}^2$)	57.421
Number of fractions	32

Dose per fraction (e/Å ²)	1.79
EPU parameters	
Defocus range (-μm)	-0.75, -1, -1.25, -1.5, -1.75, -2, -2.25, -2.5, -2.75
Autofocus	After distance every 10 μm
Drift measurement	Once per grid square 0.05 nm/s
Delay after stage shift	5
Delay after image shift	5
Exposures per hole	2
Apertures (size in μm)	
C1	2000
C2	70
C3	2000
Objective	100

Table 2.14: David Klebls overnight data collection for HA/HK68

Hardware	Conditions
Microscope	Krios2
Detector (mode)	Counting
Accelerating voltage (keV)	300
Pixel size (Å)	1.07
Data acquisition parameters	
Nominal magnification	130k EFTEM
Spot size	6
Illuminated area (μM)	1.3
Dose	

Square pixel (\AA^2)	1.14
Dose per physical pixel per second	8.203
Dose per $\text{\AA}^2/\text{sec}$	7.20
Exposure time (seconds)	9
Total dose ($e/\text{\AA}^2$)	64.8
Number of fractions	40
Dose per fraction ($e/\text{\AA}^2$)	1.62
EPU parameters	
Defocus range (μm)	-0.75, -1, -1.25, -1.5, -1.75, -2, -2.25, -2.5, -2.75
Autofocus	After distance every 10 μm
Drift measurement	Once per grid square 0.05 nm/s
Delay after stage shift	5
Delay after image shift	5
Exposures per hole	2
Apertures (size in μm)	
C1	2000
C2	70
C3	2000
Objective	100

Table 2.15: 72 hr data collection for HA/HK68 complexed with A31

2.11.8 Image processing HA/HK68 homotrimer

Processing of the rapid-grid prepared HA data was kindly carried out by David Klebl. Single particle processing was performed in RELION version 3.1 (267). Micrograph defocus and astigmatism was determined using Gctf (268). Approximately 982 micrographs were collected from an overnight collection, in which 230,312 particles were selected by crYOLO (269) and classified using reference

free 2D classification performed to provide 50 classes for 25 iterations with a regularised parameter T value of 2 and mask diameter of 160 Å. 151,911 particles from desirable classes were selected and extracted.

3D classification was performed over 25 iterations with a regularised parameter T value of 4. Classification was performed into 3 classes, with C1 symmetry imposed. CTF correction was performed and an angular sampling interval of 7.5 degrees was imposed. An offset angling of 5 pixels and offset search step of 1 pixel was used, with no angular searches performed. Of the 3 classes, one class was selected containing 76,534 particles.

3D refinement was carried out on the selected class imposing C1 symmetry and an initial low-pass filter of 60 Å. CTF correction was performed and an angular sampling interval of 7.5 degrees was imposed. An offset angling of 5 pixels and offset search step of 1 pixel was used, with no angular searches performed.

To correct for drift and beam-induced movement of particles, 2 rounds of Bayesian polishing and CTF refinement were carried out. The resulting post-processed model was put through a final refine and polishing job, in which C3 symmetry was imposed. UCSF Chimera was used for map visualisation and generation of figures.

2.11.9 Image processing of A31-HA/HK68 homotrimer complex

Single particle processing was performed in RELION version 3.1 (267). Micrograph defocus and astigmatism was determined using Gctf (268). Approximately 3,978 micrographs were collected from a 72 hr collection (with 24 hr 30 ° tilt collection), in which 359,609 particles were selected by crYOLO (269) and classified using two rounds of reference free 2D classification performed to provide 100 classes for 25 iterations with a regularised parameter T value of 2 and mask diameter of 190 Å. 138,831 particles from desirable classes were selected and extracted.

3D classification was performed over 100 iterations with a regularised parameter T value of 4. Classification was performed into 5 classes, with C1 and C3 symmetry imposed. An initial model of David Klebl's HA structure low pass filtered was used. CTF correction was performed and an angular sampling interval of 7.5 degrees was imposed. An offset angling of 5 pixels and offset search step of 1 pixel was used, with no angular searches performed. Of the 3 classes, one class was selected from the C3 imposed symmetry job, containing 72,767 particles.

3D refine was carried out on the selected class imposing C1 and C3 symmetry and an initial low-pass filter of 15 Å. CTF correction was performed and an angular sampling interval of 7.5 degrees was imposed. An offset angling of 5 pixels and offset search step of 1 pixel was used, with no angular searches performed.

To correct for drift and beam-induced movement of particles, 3 rounds of Bayesian polishing and CTF refinement were carried out. The resulting post-processed model was put through a final refine and polishing job, in which C3 symmetry was imposed. UCSF Chimera was used for map visualisation and generation of figures.

2.12 K⁺ channel and its influence on IAV infection

2.12.1 Plaque reduction assay

MDCK cells were seeded at 4×10^5 cells per well in a 12-well tissue culture before being incubated with either TEA or Qd in a concentration dependant manner, or with infection media (control) for 45 mins before adding pre-determined 50 PFU of IAV (Aichi/1968/H3N2) diluted in infection media and incubating for a further 1 hr at 37 °C. The drug concentration was maintained throughout and an Avicel overlay was added following incubation before cells left to incubate for 48 hrs at 37 °C. Cells were fixed and stained with crystal violet, and plaques were visually observed.

2.12.2 Pre-Infection K⁺ channel broad spectrum inhibitor treatments

A549 cells were seeded at 2.5×10^5 cells per well in a 12-well tissue culture treated plate 18 hrs prior to assay. On the day of the assay, a range of ion inhibitor drugs (**Table 2.7**) were diluted in infection media to concentrations deemed non-cytotoxic previously (**2.2.5 and 2.2.6**), and were used to pre-treat A549 cells for 45 mins at 37 °C, 5 % CO₂. Cells were then infected with a variety of IAV strains (**2.1.5**) at a MOI of 0.05 and incubated for 18 hrs, with the presence of individual drugs maintained in infection media for the duration. Cells were lysed in RIPA buffer (140 mM NaCl, 25 mM Tris-HCl, 1 mM EDTA, 0.5 mM EGTA, 1 mM PMSF, 1 % Triton X-100, 0.1 % SDS, 0.1 % protease inhibitor cocktail, pH

7.4) for 15 mins on ice and rocker, before the plate was scraped and cell lysates were collected and assessed via WB **(2.5.2)** (270).

2.12.3 Ammonium chloride time course

A549 cells were seeded at 2.5×10^5 cells per well in a 12 well plate for 24 hrs until 80-90% confluent. Cells were then placed on ice for 15 mins and washed twice with ice cold PBS. Cells were infected at a multiplicity of infection (MOI) of 0.05 with ice cold IAV Aichi/68 **(2.1.5)** and virus was left to sync infection for 15 mins. Wells were replaced with infection media or infection media with the addition of ammonium chloride (NH_4Cl , 10 mM) and placed at 37 °C, 5 % CO_2 . Media was removed and replaced with media + NH_4Cl at increasing post-infection time points; 0, 5, 10, 15, 30, 60, 120, 240 mpi; infection was allowed to proceed for 18 hpi at which point cells were lysed with RIPA buffer for 15 mins on ice and rocker, before the plate was scraped and cell lysates were collected and assessed via WB **(2.5.2)** (271).

2.12.4 K⁺ channel broad spectrum inhibitor time course

Broad-spectrum K⁺ channel inhibitor time courses were set up with the same methodology as in 2.11.2. Rather than NH_4Cl , Qd (100 μM) and dalfampridine (1.25 mM) were added at increasing post-infection time points; 0, 5, 10, 15, 30, 60, 120, 240 mpi; infection was allowed to proceed for 18 hpi at which point cells were lysed with RIPA buffer for 15 mins on ice and rocker, before the plate was scraped and cell lysates were collected and assessed via WB **(2.5.2)** (271).

2.12.5 IAV priming with broad spectrum K⁺ channel inhibitor

A549 cells were seeded the day prior to assay at 2.5×10^5 cells per well in growth media in a 12 well plate. On the day of the assay, IAV MOI = 0.05 was primed with Qd (100 μM), quinine (100 μM) or dalfampridine (1.25 mM) diluted in infection media for 1 hr at 37 °C, 5 % CO_2 . Following incubation, growth media was removed from cells, washed once with PBS and 200 μL of drug-primed IAV samples were added to cells during and incubated for 45 mins, before the volume in each well was topped up to 1 mL with drug concentration maintained throughout infection. Following an 18 hr infection, media was eluted, cells were washed once in PBS and 100 μL of RIPA buffer was added for 15 mins on ice and rocker, before the plate was scraped and cell lysates were collected and assessed via WB **(2.5.2)** (271).

2.12.6 Priming buffers

Buffers were prepared containing 20 mM HEPES for pH 7.4, 30 mM MES for pH 5.8. The desired high-salt concentrations were achieved by addition of 140 mM potassium chloride (KCl), with either 5 mM NaCl or 10 mM NaCl added for pH 7.4 + K⁺ or pH 5.8 + K⁺ (respectively). Buffers were heated to 37 °C and fine adjusted to the desired pH using hydrochloric acid HEPES and MES buffers. The pH was assessed after the 2 hr priming to confirm buffer had not drifted beyond pH +/- 0.5 of the initial pH calculation.

2.2.7 IAV priming with pH and K⁺ ions

As in 2.12.5, A549s were seeded the day prior to infection. IAV with a MOI of 0.05 (20 µL) was primed with priming buffers described in 2.12.6 (200 µL) for 2 hrs at 37 °C, 5 % CO₂. Following incubation with priming buffer, IAV was further diluted in 1 mL infection media and immediately added to cells. Infection was allowed to proceed for 18 hrs prior to cell lysis and WB (2.5.2).

2.2.8 IAV priming with broad spectrum K⁺ channel inhibitor and with pH and K⁺ ions

A549 cells were seeded the day prior to assay at 2.5 x10⁵ cells per well in growth media in a 12 well plate. On the day of the assay, IAV MOI = 0.05 was primed with priming buffers pH 5.8 +/- K⁺ for 2 hrs at 37 °C, 5 % CO₂ as in 2.2.7. With 45 mins remaining of priming incubation, growth media was removed from cells, washed once with PBS and 250 µL of Qd (100 µM), quinine (100 µM) or dalfampridine (1.25 mM) were added to cells and incubated for 45 mins at 37 °C, 5 % CO₂. After incubation, primed virus was added to drug-primed cells and allowed to for 18 hrs, following infection media was eluted, cells were washed once in PBS and 100 µL of RIPA buffer was added for 15 mins on ice and rocker, before the plate was scraped and cell lysates were collected and assessed via WB (2.5.2).

2.12.9 Cryo-electron tomography collection

Cryo-electron tomography (cryo-ET) tilt series data were collected for pH 7.4 and pH 5.8 +/- K⁺ primed IAV lacey carbon grids. The FEI Titan Krios II was utilised with the help of the Astbury Biostructure Laboratory staff to set up automated data collection using Tomography 4 software (FEI). A pixel size of 2.72 Å was used, with an electron dose of 0.501 e⁻/image, at 53,000 x magnification, a defocus of -1 µm and using a Volta phase plate to improve signal-noise. Microscope alignments were kindly performed by Dr Emma Hesketh. Desirable lacey hole positions were selected manually and then Tomography 4 was utilised to perform the autofocus and data collection. Grid angles from -60 to +60

°, at 2 ° increments were carried out across all data sets, with approximately ~20 single axis tilt series collected per condition over a total of 4 days.

2.12.10 Reconstructing 3D tomograms

Following data collections, the tilt series were imported into IMOD software for processing by batch tomogram reconstruction. Pre-processing was carried out initially to remove any outlying pixels and/or artefacts which would hinder reconstruction. An initial alignment was carried out between each 2D projection in a series, gold fiducial particles were used to fine align the tilt series, with some manually selected to create a model to assess particle movement between tilts. Batch tomography enables the user to tomograms to be reconstructed in a high-throughput manner. The gold particle alignment was used by IMOD to reconstruct tilt series into 3D volumes (268). Following reconstruction, a binning factor of 2 was applied to reduce data storage, creating a final pixel size of 5.44 Å .

Image J (FIJI) was used to create images which were Gaussian blur 3D filtered and contrast increased for improved visualisation of virions.

2.13 Data presentation and analysis

2.13.1 Data presentation and analysis

All data analysis was carried out using Microsoft Excel and Graphpad Prism 9.0 (unless otherwise stated).

Chapter 3
Isolation and production of IAV HA-specific Affimer
molecules

3.1 Chapter introduction

Seasonal influenza is predominantly caused by two circulating subtypes of IAV (H1N1 and H3N2), which annually result in 290,000-650,000 mortalities and a much greater magnitude of severe illnesses (3-5 million). This puts a huge strain on health services and has a negative impact on the global economy (272). IAV has a large animal reservoir and mankind's continual encroachment onto wild habitats, alongside intense animal farming, is increasing our proximity to these reservoirs. This close contact raises the chance for strains to cross species barriers into humans and potentially cause pandemic outbreaks. There has been 4 IAV pandemics to date since the 20th century, which have resulted in severe levels of respiratory disease. It is widely accepted that the threat of a pandemic strain emerging is inevitable, with surveillance of avian strains H7N9 and H5N1 causing particular concern (273). Several epidemics in the last decade have been caused by these strains, and a sustained infection in the human population would be possible through just a few amino acid substitutions in the viral proteins, making a pandemic event likely (273).

Pandemic variants have the capacity to have detrimental effects globally, as seen recently with the SARS-CoV-2 outbreak, which at the point of writing (September 2021), stands at ~3.5 million deaths and devastating global economic impacts (274,275). The only therapeutic treatment approved by the FDA is remdesivir (a repurposed broad-spectrum antiviral originally developed to treat Hepatitis C virus), which was licensed on the 22nd of October 2020, almost a year after the pandemic began (276). Worse yet, ~50 antivirals and ~60 novel antibody therapies are still undergoing clinical trials almost a year and a half after the pandemic began (as of July 2021) (277). This highlights the need for new methods to produce therapeutics following such a major outbreak.

Of all the potential IAV antigens to target, possibly one of the most attractive is HA. HA is the most abundant transmembrane protein on influenza viral particles. Each IAV virion is decorated with around 500 HA spike proteins (278). This spike protein is crucial to the virus replication cycle and facilitates multiple life cycle events. It is involved in: 1) cellular receptor binding; 2) fusion of host and viral membranes releasing viral RNPs; and 3) egress of newly formed virions. Due to its wide range of functions, this multifaceted protein has multiple epitopes that can be targeted to inhibit its function. Neutralising monoclonal antibodies are currently the forefront to therapeutic treatments (279), though antibody production can be a complex procedure, as witnessed with the SARS-CoV-2 outbreak, resulting in substantial mortality, morbidity and economic loss in anticipation of their rollout.

Though HA is an excellent target for therapeutic intervention due to its multi-functionality, it is also a difficult antigen to target. Glycosylation near antigenic sites, disrupts binding and limits accessibility for neutralising antibodies (280). IAV has an extremely high mutation rate due to lack of proof-reading by the viral polymerase, causing high error rates (in the order of 10^{-4}) (281). HA is particularly susceptible to mutations as it has evolved to compensate for fitness costs. It is the primary target of the immune system, and as a result, is subjected to evolutionary pressure with 3-4 amino acid substitutions per year, many of which contribute to rapid antigenic drift that deems annual vaccine and antibody efforts redundant (**Figure 3.1 and 3.2**) (282,283). Beyond its canonical role in obstructing Ab binding, recent work demonstrates through the use of the primerID method for error-correcting virus population sequencing, that glycosylation can actually aid in compensating fitness costs imposed due to escape substitutions elsewhere on HA. This glycosylation increases the viability and subsequent emergence of Ab-potential escape variants (284).

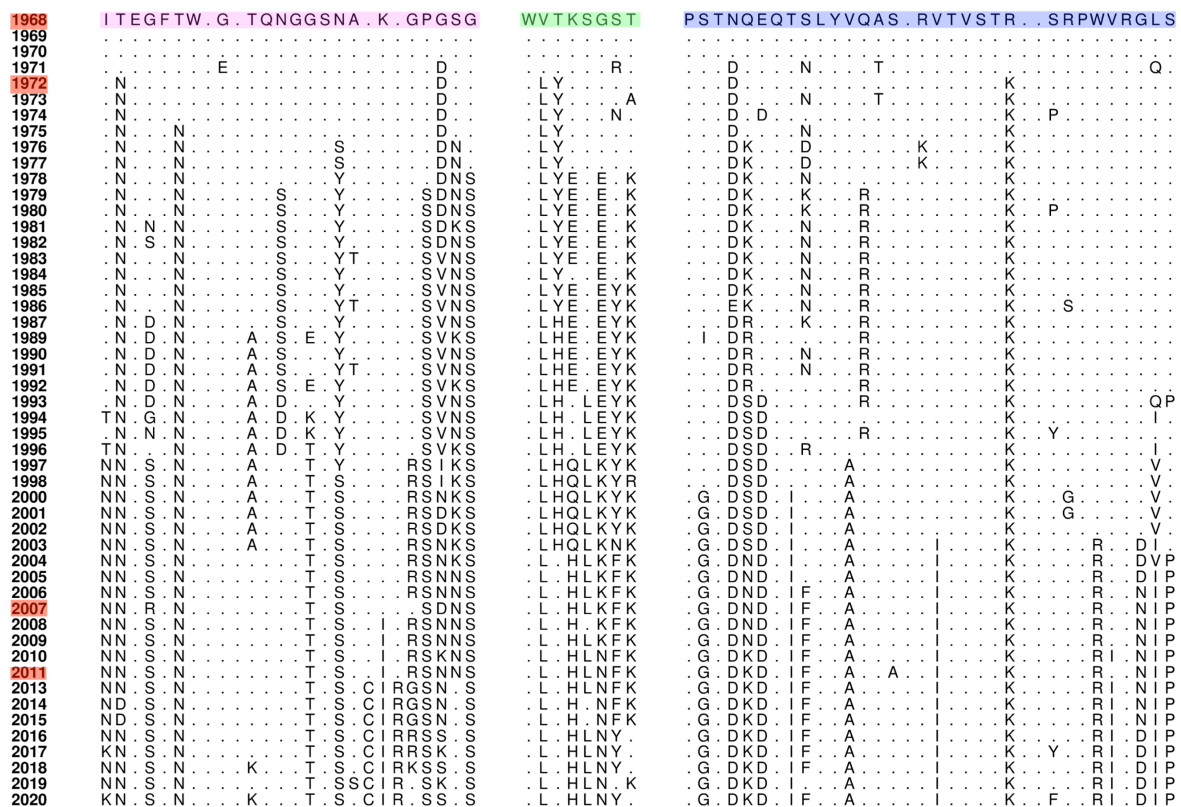


Figure 3.1: Alignment of antigenic sites of IAV (H3N2) surrounding the RBS by year

Known antigenic sites (AS) ((285–289)) are shown for AS-A coloured in pink, AS-B coloured in green and AS-D coloured in violet. Consensus AS residues that map to these sites are shown for the years

1968-2020. Years highlighted in red show viral strains used throughout this project. Alignments were made using Clustal Omega and Aline.

Year	PN	TFN	SHRGKS	R	K	D	KL TN	DEQQSLYSNG	KD	AT				
1933														
1934		NTT	A		E	G	K	KD	NI	Q	E	R		N
1968	K	NIT	A		E	G	SK	ED	KT		RKE	RG		N
1970		ETN	PYA	AN			SK	TD			QA	RG		
1971		ETN	PYA	AN			SK	TD			QA	RG		
1973		ETT	PYA	A			SK	TD			QA	RG		
1974		ETN	PYA	AN			SK	TD			QA	RG		
1975		ETN	PYA	TN			SK	TD			QA	RG		
1976		ETN	PYA	AN			SK	TD			QA	RG		
1977	K	NVT	K		E	G	SK	ED	KT	I	RKEE	RG		N
1978	K	NVT	K		E	G	SK	ED	KT	I	RKEE	RG		N
1979	K	NVT	K		E	G	SK	ED	KT	I	RKEE	RR		NN
1980	K	NVT	K		E	G	SK	EN	KT	I	RKEE	RR		NN
1981	K	NVT	K	C			SK	ED	KT	I	RKEE	RR		NN
1982	K	SVT	K		E	G	SK	ED	KT	I	RKEE	RR		NN
1984		NVT	K		E	G	SK	ED	KT	I	RKEE	RG		NN
1985	E	NVT	K		E	G	SK	ED	KT	I	RKEE	RR		NN
1986		VVT	K	R			SK	GD	RAI		HTEE	RR		NN
1987		VVT	K	R			SK	GD	RAI		HTEE	RR	X	NN
1988		VVT	N				SK	GD	RAI		HTEE	RR		NN
1989		VVT	N	R			SK	GD	RAI		HTEE	RR	G	NN
1990		VVT	N				SK	GN	RAI		HTEE	RR		NN
1991		VVT	N				SK	GD	RAI		HTEE	RR	G	NN
1992		VVT	N				SK	GD	RAI		HTEE	RR		NN
1994		VVT	N				SK	GD	RAI		HTEE	RR		NN
1995		VVT	N		K		SK	GD	RAI		HTEE	RR		NN
1996		VVT	N				SK	GD	RAI		HTEE	RR		NN
1997		VVT	N				SK	GD	RAI		HTEE	RR		NN
1999		VVT	N			G	SK	GD	RA		HTEE	RR		NN
2000		VVT	N			G	SM	GN	RA		HTEE	RR		NN
2001		VVT	N	N	K		SK	GD	RAI		HKEE	RR		NN
2002		VVT	N			G	SK	GD	RA		HTEE	RR		NN
2003		VVT	N			G	SK	GN	RA		HTEE	RR		NN
2004		VVT	N			G	SK	GV	RA		HTEE	RR		NN
2005		VVT	N	E		G	SK	GN	KA		HTEE	RR		NN
2006		VVT	N			G	SK	GD	RA		HTEE	RR		NN
2007		VVT	N	E	K		SK	GD	MT		HKEE	RR		NN
2008		VVT	N	E	K	G	SK	GD	MT		HKEE	RR		NS
2009		DS	P	A	AK		SK	AD			QA	RR		
2010		DS	P	A	AK		SK	AD			QA	RR		
2011		DS	P	A	AK		SK	AD			QA	RR		
2012		DS	P	A	AK		SK	AD			QA	RR		
2013		DT	P	A	TN		SK	AD			QA	RR		
2014		DS	P	A	AK		SK	AD			QA	RR		
2015		DS	P	A	AK		SK	AD			QA	RR		
2016		DS	P	A	AK		SK	AD			QA	RR		
2017		DS	P	A	AK		SK	AD			QA	RR		
2018		DS	P	A	AK		SK	AD			QA	RR		
2019		DS	P	A	AK		SK	AD			QA	RR		
2020		DS	P	A	AR		SK	AD			QA	RR		

Figure 3.2: Alignment of antigenic sites of A/(H1N1) virus RBS by year

AS ((285–289)) are shown for AS-Sa and AS-Sb coloured in green equating to AS-B of H3 RBS AS, and Ca2 coloured in violet, equating to that of the H3 AS-D. RBS AS consensus residues that map to these sites are shown for the years 1968-2020. Dots represent conserved residues, whilst gaps between residues represent gaps in sequence number between AS regions. Years highlighted in red show viral strains used throughout this project. Alignments were made using Clustal Omega and Aline.

Affimer molecules have been isolated with specific binding to a large and diverse collection of protein targets (>300). Though, until recently, there has been very little focus on applying them to viral

antigens. Work carried out on viral antigens has demonstrated Affimer molecules are very much a viable option in a diagnostic or therapeutic capacity (232,239).

Therefore, the aim was to investigate Affimer molecules potential as therapeutics for IAV infection. Affimer molecules are small in size (~13 kDa, ~2 nm), potentially allowing for new, previously undefined pockets to be mapped on HA. To generate therapeutic Affimer molecules, a pure *in vitro* approach (phage display (290)) which only requires the target protein, in this case the HA spike protein, was carried out. This approach means Affimer molecules can be isolated and produced independently of patient samples and the availability of neutralising antibodies from those patients. Thus, therapeutics can be isolated more rapidly in response to initial surveillance of novel IAV strains whilst being ethically mass-expressed in bacteria and purified comparatively cheaper, as opposed to the production of therapeutic antibodies via animals. Furthermore, bacterial expression and the thermal stability of Affimer molecules offer the prospect of a reduced cold chain for distribution around the globe, enabling a global effort to control these outbreaks. This chapter presents the isolation, expression and initial assessment of HA-specific Affimer molecules.

3.2 Isolation of cross-reactive Affimer molecules

To determine whether Affimer molecules could be isolated that were able to bind to a 'universal' pocket of influenza virus HA, a phage display screen was carried out using 3 biotinylated monomeric H3 (H3 Aichi/1968, H3 Fijian/2002 and H3 California/2004, Sinobiological) (screen carried out by Dr. Christian Teide). The pipeline of Affimer screening and isolation was altered from typical protocols carried out by the BSTG (University of Leeds), in order to increase populations of clones with cross-reactive properties (**Figure 3.3**).

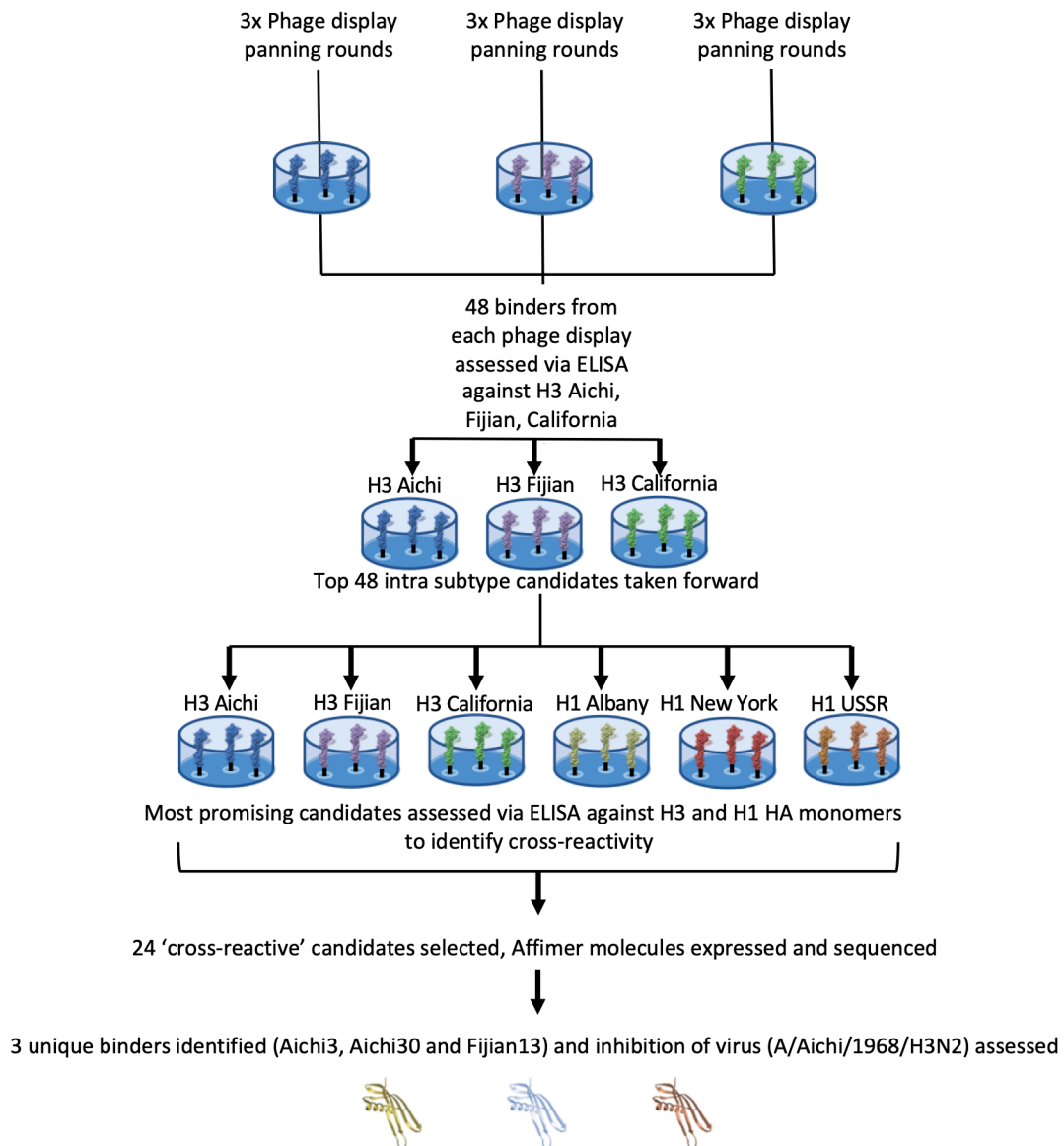


Figure 3.3: Pipeline carried out to isolate broadly binding Affimer molecules against a variety of different HA proteins (H3/1968 Aichi, H3/2002 Fijian, H3/2004 California)

Three panning rounds for each protein: H3/1968 Aichi, H3/2002 Fijian, H3/2004 California were carried out and 48 colonies selected from each screen. A phage ELISA was carried out to assess binding of candidates against each of the H3 proteins. The top 48 candidates, determined by binding profile for all 3 proteins were then carried forward and binding was assessed against the H3 proteins and a further 3 HA proteins of subtype H1 (New York/1918, Albany/1951, USSR/1977). 24 of the best cross-reactive binders of all 6 proteins were then sequenced, revealing 3 unique binders: Aichi 3, Aichi 30 and Fijian 13.

For each of these proteins, three panning rounds were carried out independently. Following the panning rounds, 48 randomly selected colonies were picked from each screen and a phage ELISA was

carried out to assess the binding of Affimer displaying phage to each of the biotinylated H3 targets independently. Absorbance readings were recorded at 620 nm on a MultiSkán Ascent plate reader (Figure 3.4).

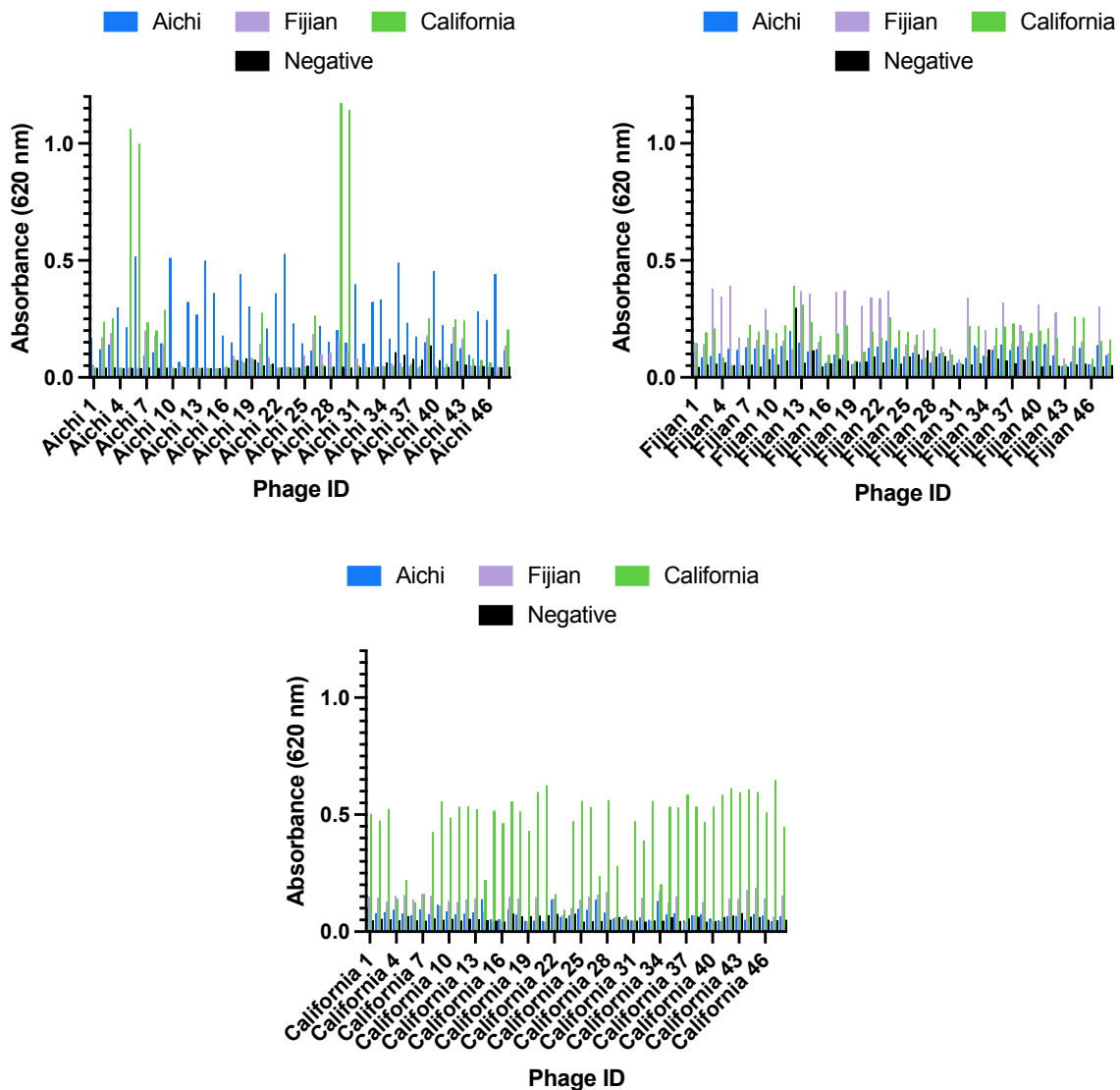


Figure 3.4: Phage ELISA results for Affimer molecules selected against individual H3 proteins H3/1968 Aichi, H3/2002 Fijian, H3/2004 California)

48 colonies randomly selected from each phage display screen were tested in a phage ELISA. Each colony represents one Affimer and was tested for binding against each HA protein (H3/1968 Aichi, H3/2002 Fijian, H3/2004 California) or an empty control well (negative control). Phage binding was detected with an anti-Fd bacteriophage-HRP antibody and quantified by the addition of TMB, measuring absorbance at 620nm for each well.

Following phage ELISA assessment affirming specific binding of Affimer presenting phage to each of the H3 monomers, phage clones were selected based on the overall binding profiles for each H3 target protein. Rather than solely focusing on binders with the highest absorbance at 620 nm. Unexpectedly, some clones from the Aichi panning rounds displayed a greater absorbance for California than for Aichi (Aichi 5, 6, 29 and 30, **Figure 3.4b**). Whilst, clones originating from the Fijian panning rounds appeared to exhibit a higher preference for 'universal' binding profiles for each of the H3 proteins in comparison to those reared from Aichi and California. Overall, the absorbance readings for these clones were very weak (<0.5). This resulted in the selection of 12 clones from Aichi, 20 clones from the Fijian and 16 from California.

The 48 clones that showed most promise as 'universal' binding candidates were taken forward and a further phage ELISA was carried out. This time, successful candidates were assessed for binding profiles against the 3 previously probed H3 proteins, alongside binding exhibited against 3 H1 HA proteins (Albany/1951, New York/1918 and USSR/1977). An empty well negative control was also, tested. Absorbance readings were recorded at 620 nm on a MultiSkan Ascent plate reader (**Figure 3.5**).

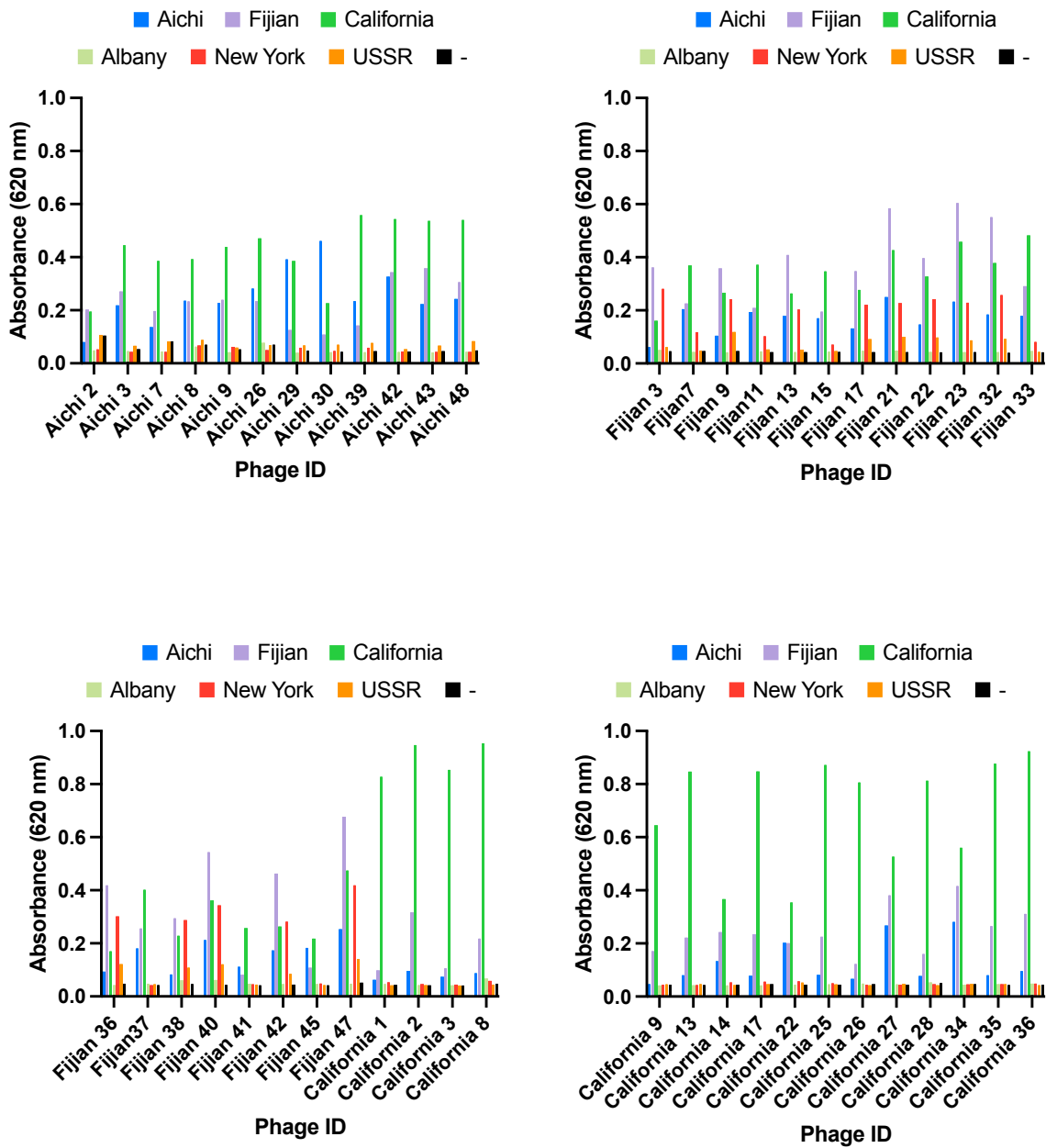


Figure 3.5: Phage ELISA to assess intra-HA subtype (H3/1968 Aichi, H3/2002 Fiji, H3/2004 California) and inter-HA subtype (Albany/1951, New York/1918 and USSR/1977) binding of Affimer molecules

Following the initial 3 rounds of phage display and phage ELISAs against H3 Aichi, H3 Fiji and H3 California, the most promising candidates were tested for binding against a larger panel of HA proteins: Aichi, Fiji, California (H3) and Albany, New York, USSR (H1), alongside an empty control well. Phage binding was detected with anti-Fd bacteriophage-HRP antibody and visualised on addition of TMB. Absorbance at 620nm was measured for each well.

Subsequently, the candidates with the best binding profiles overall for all 6 proteins were selected. Binding profiles for many clones appeared to be synonymous with one another, therefore 24 candidates were selected, based on unique phage-ELISA results. However, sequencing followed by alignment of the sequences revealed that many of the candidates were repeats, with only 3 unique nucleotide sequences of the Affimer candidates present amongst the clones (**Figure 3.6**).

3.3 Expression and purification of Affimer molecules

The three unique Affimer sequences were then sub-cloned from the phagemid vector into a pDhis plasmid for production and purification to allow further characterisation. Protein expression was carried out in *E. coli* induced with IPTG and Affimer expression at 230 rpm for ~66 hrs before harvesting cells (see **2.9.1**). Bacterial cell lysates were solubilised by heating at 50 °C to denature non-specific proteins prior to purification via Magnetic Ni²⁺ beads. An SDS PAGE gel stained with InstantBlue® confirmed the presence of the purified Affimers at ~13 kDa (**Figure 3.6**).

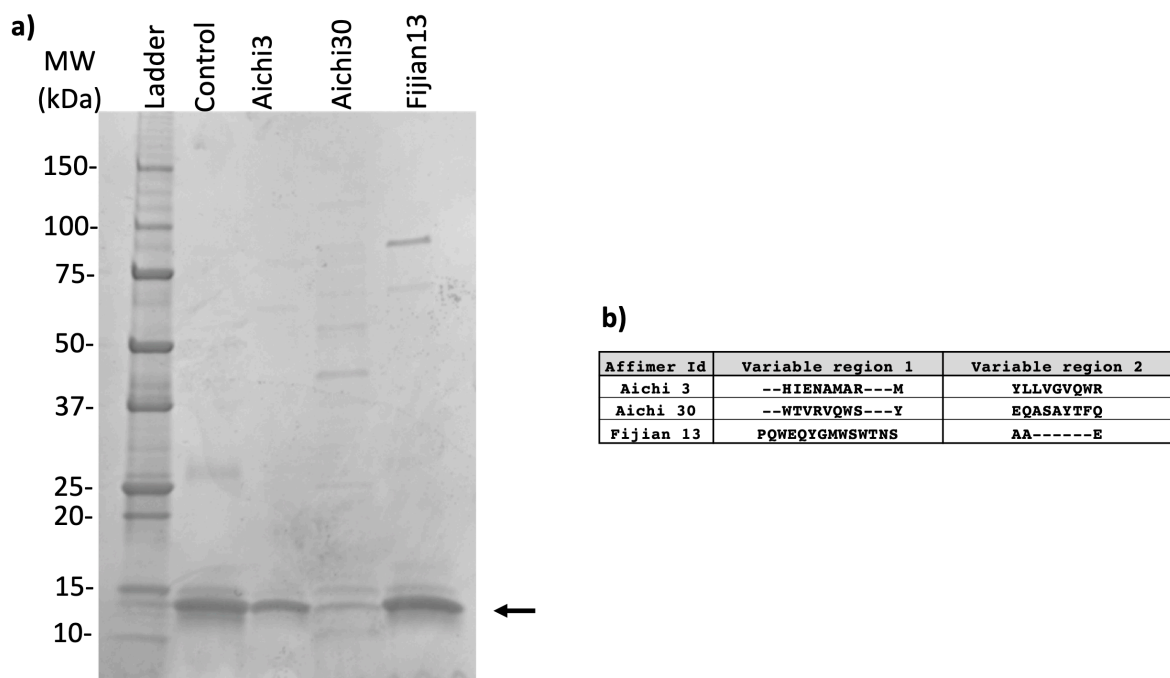


Figure 3.6: Consensus residues of isolated Affimer molecules and purification

a) Purification of Jm83-expressed Affimer molecules. Affimer molecules were purified from bacterial lysate via Ni²⁺ ion affinity. Proteins were analysed by SDS-PAGE and InstantBlue® staining

to confirm purity. The Affimers were visualised at ~13 kDa as indicated by an arrow. Affimer purification is relatively clean, though Aichi30 shows low expression of Affimer and many faint bands caused by contaminants. Fujian 13 also shows an additional band at 100 kDa, though it was deemed 'clean' enough for initial assessment. **b)** Consensus amino acid sequence alignment of variable regions 1 and 2 from the 3 unique binders obtained from phage display library screening. The multiple sequence alignment was generated using Clustal omega

Immediately after purification, the 3 Affimer candidates were dialysed into 1 x PBS + 10 % glycerol and stored at -80 °C.

3.4 Broad spectrum Affimer molecules show no inhibition *in vitro*

In order to effectively carry out cellular assays to characterise Affimer molecules, Aichi 3, Aichi 30 and Fujian 13 were assessed for cytotoxic effects on MDCK cells via an ATPlite cell viability assay., which utilises luminescence to quantify the concentration of ATP in cells, a decrease in ATP compared to control suggests cytotoxic effect on the cells. 100 µg/mL of each Affimer was added to the cells for 72 hrs, alongside a non-specific Affimer control (K3) and negative control. (Figure 3.7). Affimer molecules were found to be non-cytotoxic at 100 µg/mL (7.41 mM) for 72 hrs.

To determine whether the isolated Affimer molecules were capable of neutralising IAV, A high concentration of the Affimer molecules (50 µg/mL or 3.7mM) were incubated with IAV using A/Aichi/1968 (H3N2) MOI 0.001 for 1 hr prior to infection of cells. Upon infection, virus was incubated for 72 hrs, alongside an IAV control, Affimer control (K3) and uninfected mock. Post-infection supernatants were serial diluted from 10^{-2} to 10^{-5} and a plaque assay was performed on MDCK cells to determine the titre of each sample. Following three repeats, titres were quantified and it was found that none of the Affimer molecules isolated were able to neutralise the IAV strain Aichi/68.

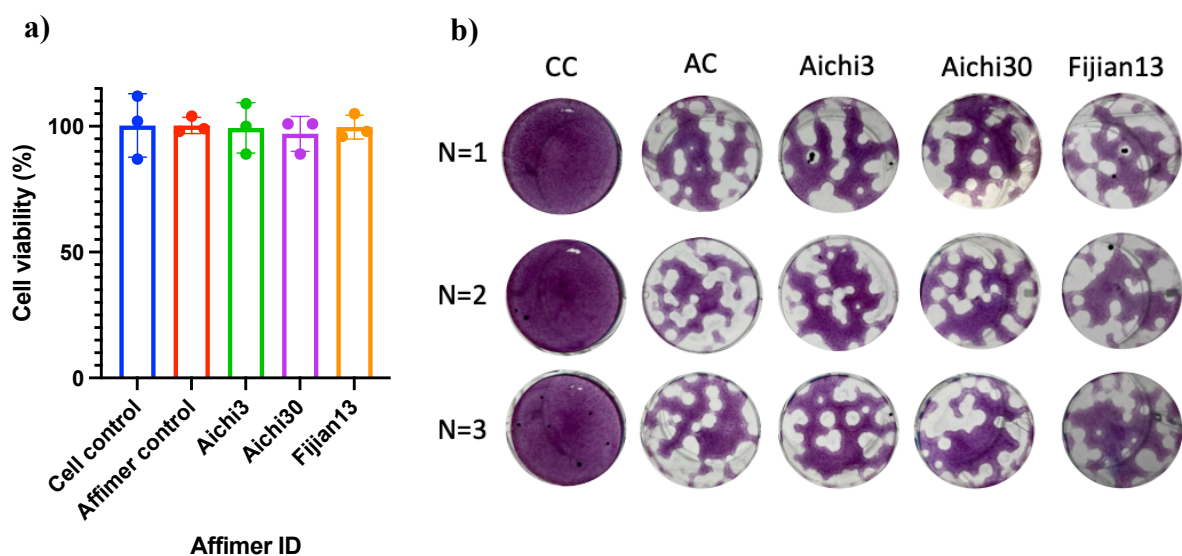


Figure 3.7: Broad-spectrum Affimer cytotoxicity and inhibition properties against A/Aichi/1968 (H3N2)

a) ATPLite cell viability assay of Affimer molecules Aichi 3, Aichi 30 and Fijian 13, non-specific Affimer control and cell only control. 100 $\mu\text{g}/\text{mL}$ of Affimer was incubated with MDCK cells for 72 hrs prior to completion of ATPLite™ Perkin Elmer 1 step protocol. Cells were found to be $\sim 100\%$ viable for all conditions, mean with standard deviation displayed ($n=3$) **b)** Plaque assay to determine inhibition of A/Aichi/1968 (H3N2) IAV. 50 $\mu\text{g}/\text{mL}$ of Affimer reagent or non-specific Affimer control were incubated with IAV for 1 hr prior to infection of MDCK cells for 72 hrs. Cell lysates were then serially diluted and MDCK cells infected for 1 hr with diluents, IAV control or uninfected (mock). Virus was removed and infected cells were incubated for 72 hrs with Avicel/MEM overlay. Cells were fixed with 4 % PFA and stained with crystal violet. Plaques were counted and virus titre determined as $\sim 1 \times 10^6$ PFU/mL ($n=3$).

3.5 Isolation of Aichi-specific Affimer molecules

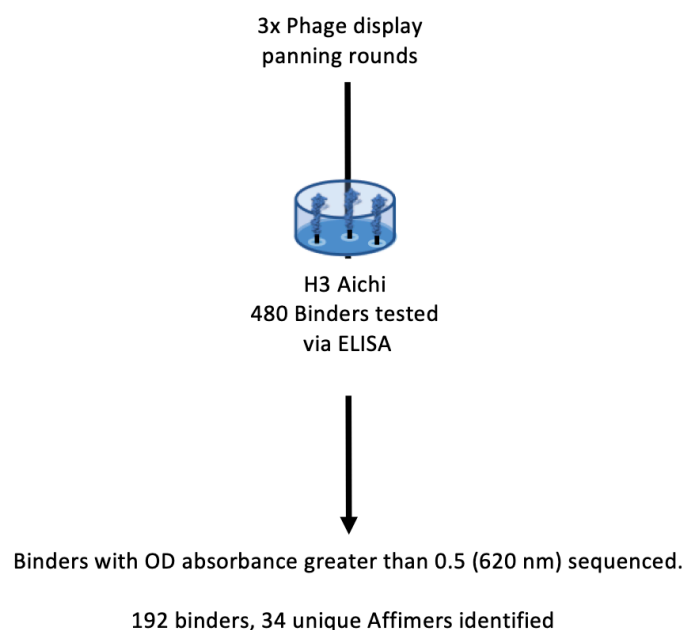


Figure 3.8: Pipeline carried out to isolate Affimer molecules against A/Aichi/1968 (H3N2) HA

3 panning rounds were carried out using biotinylated H3/1968 Aichi. 480 colonies were randomly selected from the phage display screen. A phage ELISA was carried out to assess binding of candidates against the target protein and the best 192 binders were selected (≥ 0.5 absorbance at 620 nm) and sequenced. 34 unique sequences were found.

In order to attempt to isolate a larger pool of the total potential binders from the phage library, a larger more direct approach was carried out to isolate Aichi HA-specific Affimer molecules. This was with the hope to identify a greater diversity of epitopes on the surface of HA, in order to increase the probability of mapping key pockets crucial to IAV infection function, or to identify conserved pockets between HA subtypes that have potential for diagnostic purposes. Therefore, a phage display screen was carried out using only H3 Aichi/68 HA monomer. Following 3 rounds of panning, 480 colonies were randomly selected from test plates and a phage ELISAs were carried out to assess binding to the biotinylated target (H3/1968 Aichi) (**Figure 3.9**).

Figure 3.9a shows the entire population of 480 clones measured for binding against target, with the negative empty well control subtracted. Of the 480 colonies, 192 binders had an absorbance at 620 nm of 0.5 or greater (red line), which were selected and sequenced. Alignments of the consensus

sequences revealed that 34 unique sequences were present amongst the clones (**Figure 3.10a**), the profile for these unique Affimer molecules phage ELISA results are displayed (**Figure 3.9b**). A comparatively much larger panel than the previous attempt.

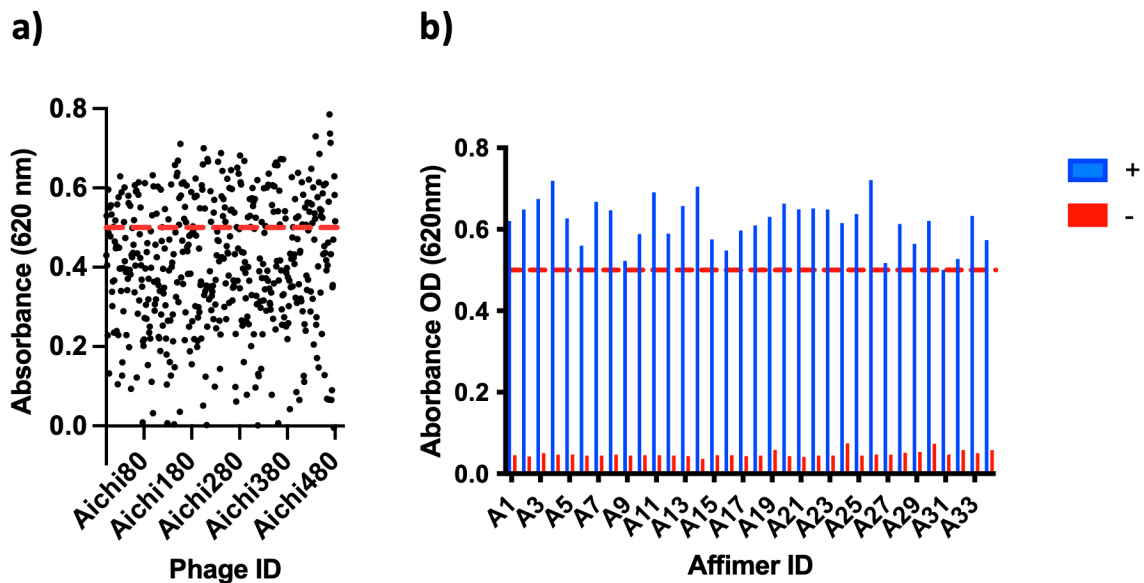


Figure 3.9: Phage ELISA to assess binding of Affimer candidates to H3/Aichi/68

a) All 480 clones which were randomly selected and assessed for binding against biotinylated H3 Aichi Negative empty well control absorbance values have been deducted from each of the respective clone absorbance values. The red dotted line highlights the cut-off point for selection (≥ 0.5 absorbance at 620 nm), an arbitrary value to allow the reduction of candidates to a manageable number. **b)** Phage ELISA results for the unique 34 Affimer molecules and negative control results after 10 mins of incubation with TMB substrate.

a)

Affimer ID	Variable region 1	Variable region 2
A1	HYW---AYSTD	TRQNQFEFM
A2	HSEA---STLDF	FLDSVFGDH
A3	HAFP--ITYGV	EHIGRYSYQ
A4	QHDF-VDYW--Y	AYMPQPHQL
A5	RTIA---QFYME	EYWELEASF
A6	GDP-----DS	ELDIAYHNN
A7	VTGH---VLYEY	AA-----E
A8	QQDF-VDYW--H	AYMPQPHQL
A9	LAGH---TAYEY	AA-----E
A10	HIMD---QNFYM	NYYARSEQM
A11	SMQI---WDWVD	MQINPQPFV
A12	WFWD---VDFQD	NATNNMYHI
A13	HEIN---AMARM	YLLVGQWR
A14	YLAT---DYLYG	SQIHRHHVF
A15	DWWG---KKFSR	TYYGIGEQA
A16	SHRT---WRWSY	WLDKDFEHQ
A17	EMVY---MYTFE	DIMRPEEEA
A18	IYNQ---KVKDF	VMSLFDADV
A19	WIWD--VDFQD	NATNNMYHI
A20	FDHS---WHMDF	WLDLMWEKE
A21	PFGH---TEYEW	AA-----E
A22	SWMK---DTWFK	TQKIRFAYQ
A23	RTMW---QEHYE	TKYDIHNFM
A24	HYYT---RISRY	EKIGKNSIM
A25	PVVV---YWGDH	AA-----E
A26	LFGH---VYYEH	AA-----E
A27	FVSNA---QNYH	VWINQVGAI
A28	SRYL---AEWLH	EFNRLNVFQ
A29	VTISEAHPWI-D	AA-----E
A30	VFKM---RYYAE	MRHNKFEHI
A31	FNY---DQWQDY	FVDSAFETE
A32	RQHA---WWRKI	GQKPRNRGV
A33	QFPW---WDWQR	VQAGTHYYQ
A34	YIVD---SPLVQ	QYFLEQTAL

b)

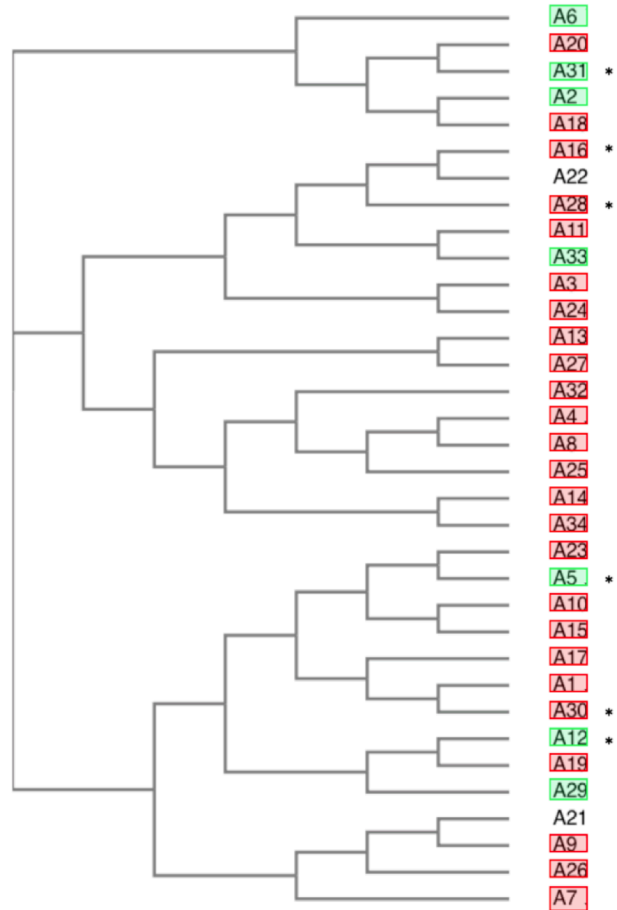


Figure 3.10: Consensus residues of isolated Affimer molecules and phylogenetic tree of sequence similarity between unique Affimer molecules

a) Consensus alignment of the amino acid sequence of variable regions 1 and 2 from the 34 unique binders obtained from phage display library screening. The multiple sequence alignment was generated using Clustal omega. b) Phylogenetic tree showing sequence similarities between the unique binders. Inhibitory Affimer molecules are highlighted in green, whilst non-inhibitory Affimer molecules are highlighted in red, Affimer molecules that were not expressed are not highlighted. An asterisk is next to Affimer molecules which were selected for further characterisation. Phylogenetic tree made using Clustal Omega.

3.6 Expression and purification of HA-specific Affimer molecules

The 34 unique Affimer sequences were then sub-cloned from the phagemid vector into a pDhis plasmid for production and purification as described in section 3.3. An SDS PAGE gel stained with InstantBlue® confirmed the presence of the purified Affimers at ~13 kDa (**Figure 3.11**). Affimer 21 did not show a band suggesting it did not express.

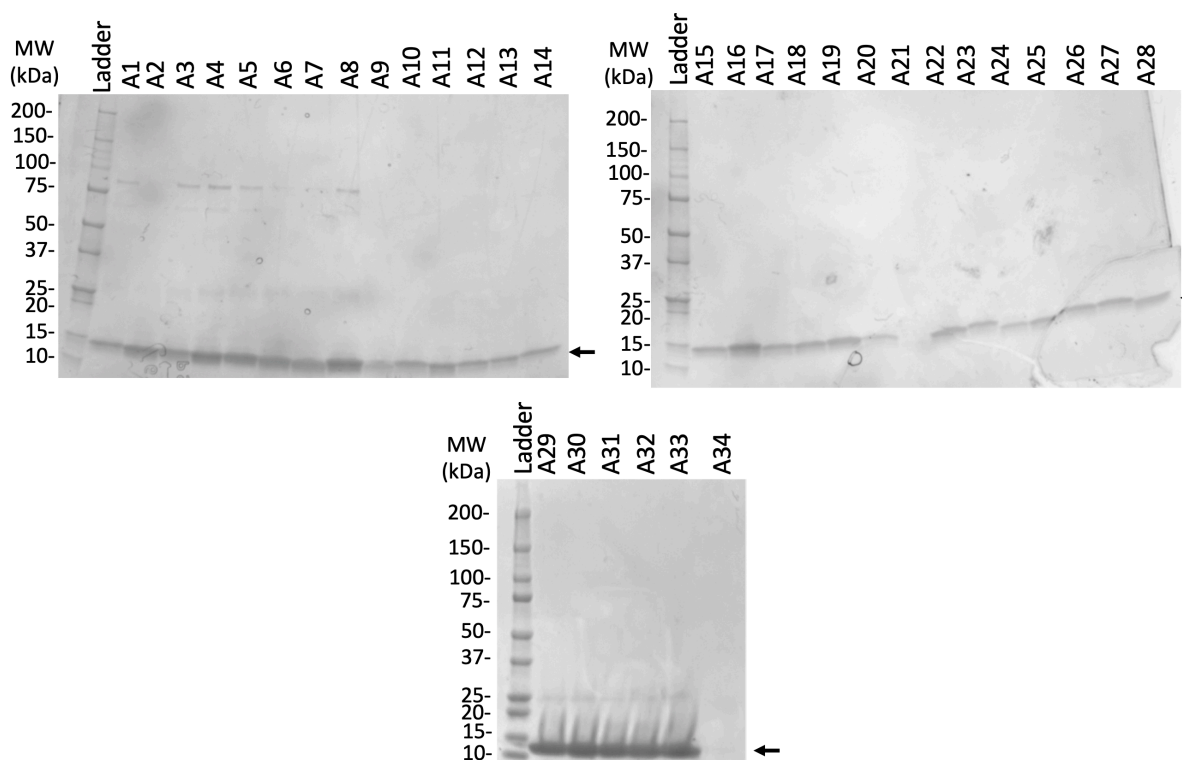


Figure 3.11: Expression and purification of pDhis -Affimer Vectors in Jm83 cells

Affimer molecules were transformed and expressed in Jm83 cells and purified from bacterial lysate via NI magnetic beads using a Kingfisher. Proteins were analysed by SDS-PAGE and InstantBlue® staining to confirm purity. The Affimers visualised at ~13 kDa as indicated by an arrow.

3.7 Initial assessment of Affimer molecules *in vitro*

The 34 Affimer molecules were first added to MDCK cells at a concentration of 100 µg/mL alongside a non-specific Affimer control (K3) and negative control for 72 hrs before carrying out an ATPlite cell viability assay (**Figure 3.12a**). All Affimer molecules were found to be non-cytotoxic for MDCK cells at 100 µg/mL for 72 hrs. The mean viability of cells was >95 % (n=3).

To determine whether the isolated Affimer molecules were capable of neutralising IAV and to enable high-throughput results for a large sample set, a microneutralisation assay was carried out (**Figure 3.12b**). The viral strain (A/Aichi/1968 (H3N2)) was used to assess Affimer neutralisation, Affimer molecules were isolated from the recombinantly expressed HA of this strain. Affimer molecules (50 $\mu\text{g}/\text{mL}$) were incubated with IAV using 100 x TCID_{50} for 1 hr prior to infection for 72 hrs of MDCK cells, alongside an IAV control, Affimer control (K3 50 $\mu\text{g}/\text{mL}$) and uninfected mock. Post-infection, cells were fixed with 4 % PFA and stained with crystal violet. Evidence of inhibition was observed visually by the presence or lack of cell monolayer. Upon observation it was clear that A2, A5, A6, A12, A29, A31 and A33 inhibited IAV infection at a concentration of 50 $\mu\text{g}/\text{mL}$.

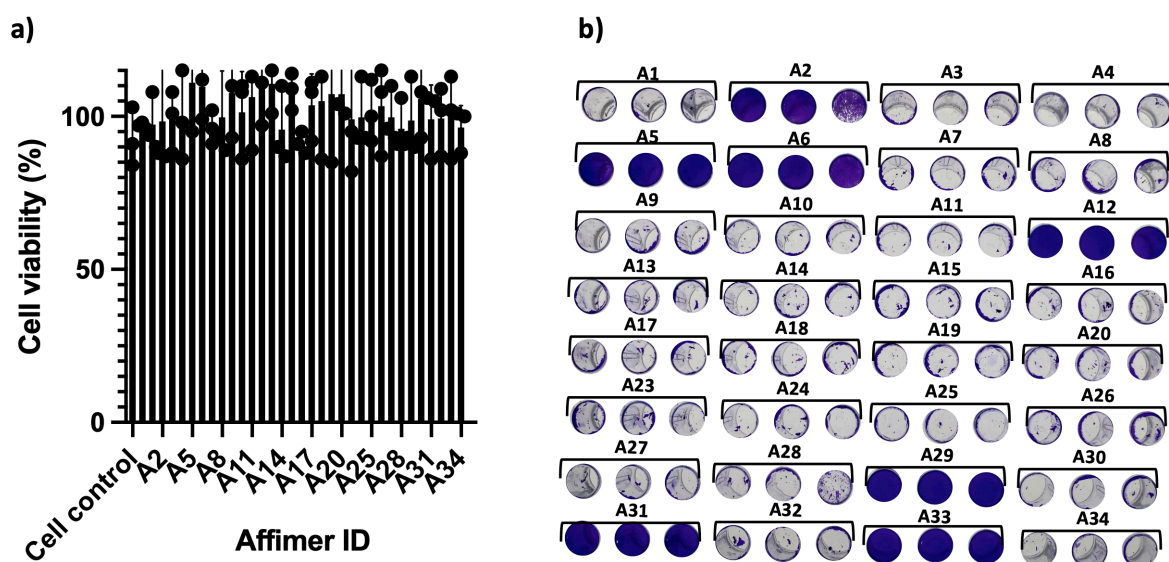


Figure 3.12: Affimer cytotoxicity and microneutralisation assay against A/Aichi/1968(H3N2)

a) ATPLite cell viability assay of 33 of the 34 isolated Affimer molecules, non-specific Affimer control and cell only control. 100 $\mu\text{g}/\text{mL}$ of Affimer was incubated with MDCK cells for 72 hrs prior to completion of ATPLite™ Perkin Elmer 1 step protocol. Cells were found to be >95 % viable for all conditions, mean with standard deviations shown (n=3) **b)** A high-throughput microneutralisation assay was carried out to determine inhibition of A/Aichi/1968 (H3N2) IAV. 50 $\mu\text{g}/\text{mL}$ of Affimer reagent or non-specific Affimer control were incubated with IAV (100 x TCID_{50}) for 1 hr prior to infection of MDCK cells for 72 hrs. Cells were fixed with 4 % PFA and stained with crystal violet. Inhibition was assessed by observing the presence or absence of a stained cell monolayer (n=3).

3.8 Selection of Affimer molecules to be further characterised

A smaller subset of HA-specific Affimer molecules was chosen in order to further characterise them as potential therapeutic (inhibitory) or diagnostic tools (non-inhibitory). Affimer molecules were selected based on whether they were inhibitory or non-inhibitory when incubated with IAV at the specified concentration (3 inhibitors and 3 non-inhibitors were selected) (**Figure 3.12b**), and based on sequence variety using a phylogenetic tree of Affimer protein sequences (**Figure 3.10b**). The premise here being that a diverse range of Affimers would target different HA-epitopes. These HA-specific Affimer molecules (A5, A12, A31, Inhibitors; and A16, A28 and A30, Non-inhibitors) were then sub-cloned into a pET-11a vector for downstream labelling and further characterisation.

3.9 Expression and purification of HA-specific Affimers with free cysteine

Rosetta 2 (DE3) *E. coli* cells were transformed with pET-11a vectors which contained the 6 selected Affimer open reading frames (ORFs), the translatable regions which were subcloned with free cysteine for downstream labelling to enable the addition of biotin or fluorescent labelling for further characterisation. Protein expression was induced with IPTG and Affimer expression carried out at 230 rpm for ~66 hrs before harvesting cells as previously described. Bacterial cell lysates were solubilised by heating at 50 °C to denature non-specific proteins prior to purification via a kingfisher utilising Magnetic Ni²⁺ beads. An SDS PAGE gel stained with InstantBlue® confirmed the presence of the purified Affimers at ~13 kDa (**Figure 3.13**). Of note, all elutions exhibit additional bands, though less prominent, which could be either contaminants or Affimer multimers.

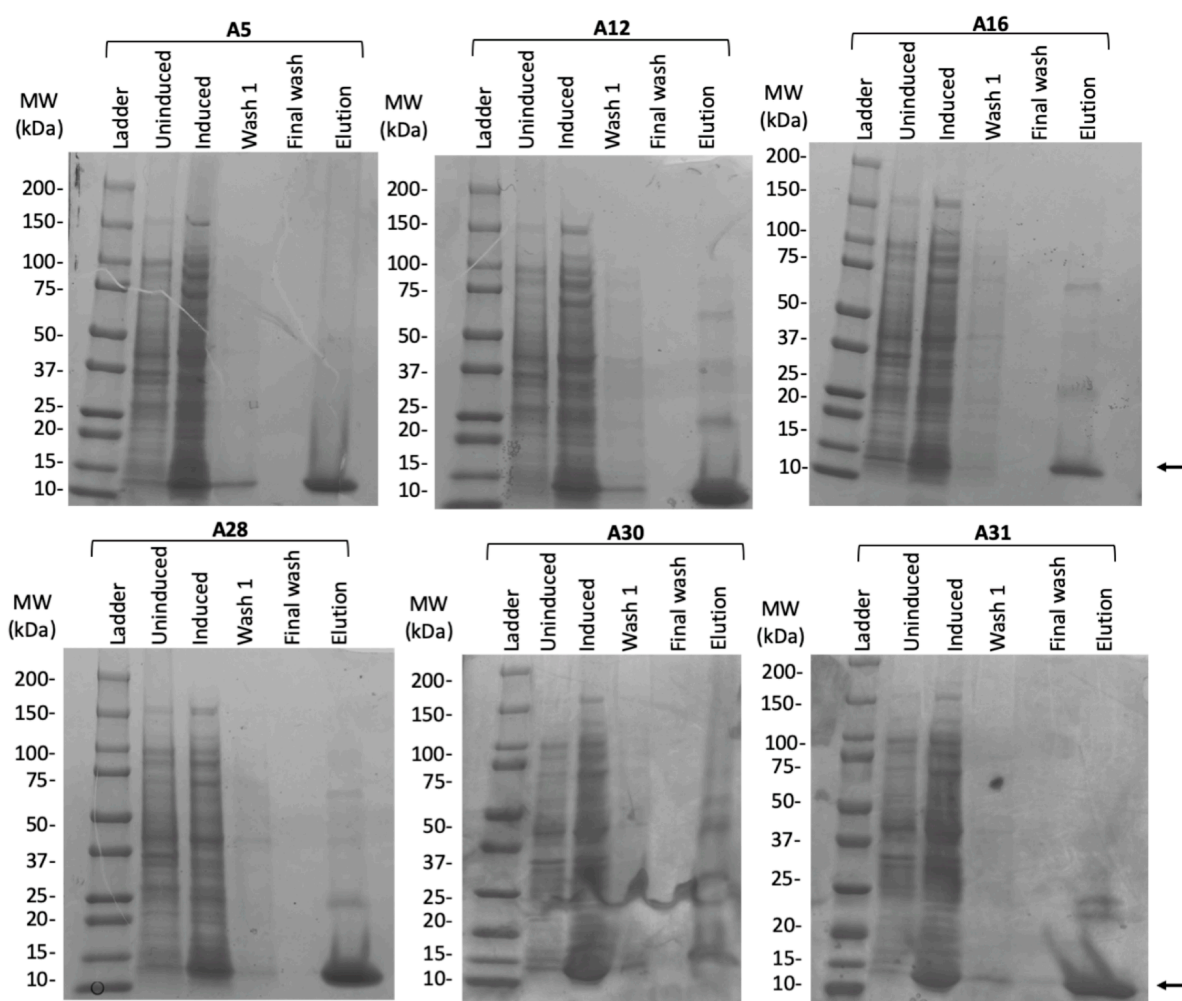


Figure 3.13: Expression and purification of pET-11a-Affimer Vectors in DE3 cells

Affimer molecules were transformed and expressed in DE3 cells and purified from bacterial lysate via Ni^{2+} magnetic beads. Proteins were analysed by SDS-PAGE and InstantBlue[®] staining to confirm purity. The Affimers visualised at ~13 kDa as indicated by an arrow. Sample from the eluted well show a high degree of purity when compared to the uninduced and induced samples. However, some protein contaminants can be seen in all samples, with the exceptions of A5.

3.10 Biotinylation of HA-specific Affimer molecules

Immediately following purification, free cysteine-Affimer molecules were biotinylated to reduce the possibility of disulphide bonds forming between thiol groups of free cysteine residues. Affimer molecules were added to TCEP disulphide reducing gel, in order to ensure reduction of the sulfhydryl groups of the cysteine residues. Covalently linked biotin-maleimide was then used to link biotin to the free C-terminal cysteine residue.

To confirm successful linkage of the biotin-maleimide to Affimer, an ELISA-like assay was carried out. Maxisorb plates were incubated overnight at 4 °C with a range of freshly biotinylated Affimer concentrations (1 μ L, 0.1 μ L, 0.01 μ L and 0.001 μ L), alongside a non-biotinylated Affimer as a negative control. Following incubation, streptavidin-conjugated to HRP was added to each well for 1 hr before the addition of TMB substrate. All biotinylated Affimer molecules presented a concentration-dependant increase in absorbance at 620 nm upon reading the colourmetric change of TMB, thus, confirming the presence of a biotin moiety. No visible colourmetric changes or readable absorbance at 620 nm was observed in the non-biotinylated sample wells, as expected (**Figure 3.14**).

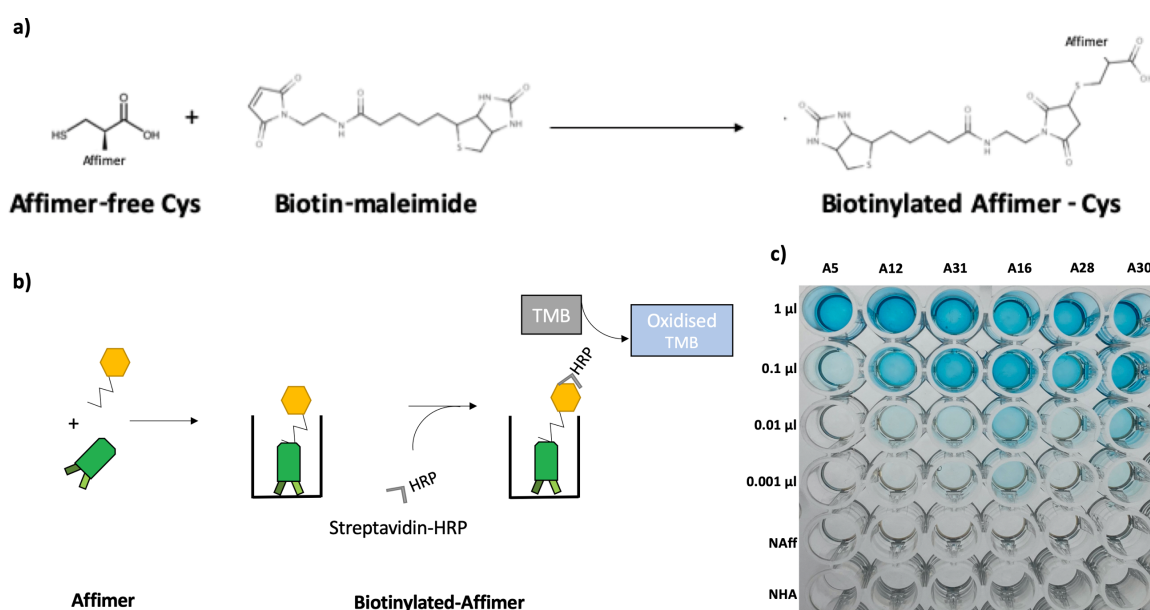


Figure 3.14: Biotinylation of Affimer molecules

a) Schematic representation of the biotinylation of Affimer molecules via the free cysteine residue at the C-terminus of the Affimer scaffold. **b)** Schematic representation of the ELISA-like assay to confirm biotinylation of Affimer molecules using streptavidin conjugated HRP and TMB substrate. **c)** Biotin ELISA of Affimer molecules. Biotinylated target was added to an independent well at varying dilutions (1 μ L, 0.1 μ L, 0.01 μ L and 0.001 μ L) alongside a No-Affimer control and non-biotinylated target control and incubated at 4 °C overnight. High-sensitivity streptavidin conjugated horse radish peroxidase (HRP) was used to detect biotin and biotinylation confirmed by addition of TMB substrate.

Alongside the ELISA-like conformational biotinylation assay, mass of Affimer molecules pre and post biotinylation was determined using LC-MS, carried out by the FBS Mass Spectrometry facility (**Figure 3.15**). 5 μ M of both biotin linked and non-linked Affimer were exposed to LC-MS degrading and analysed for mass measurements. All biotinylated Affimer molecules exhibited a 451 Da mass shift when compared to the mass of non-linked Affimer, further confirming the presence of the maleimide-biotin linker.

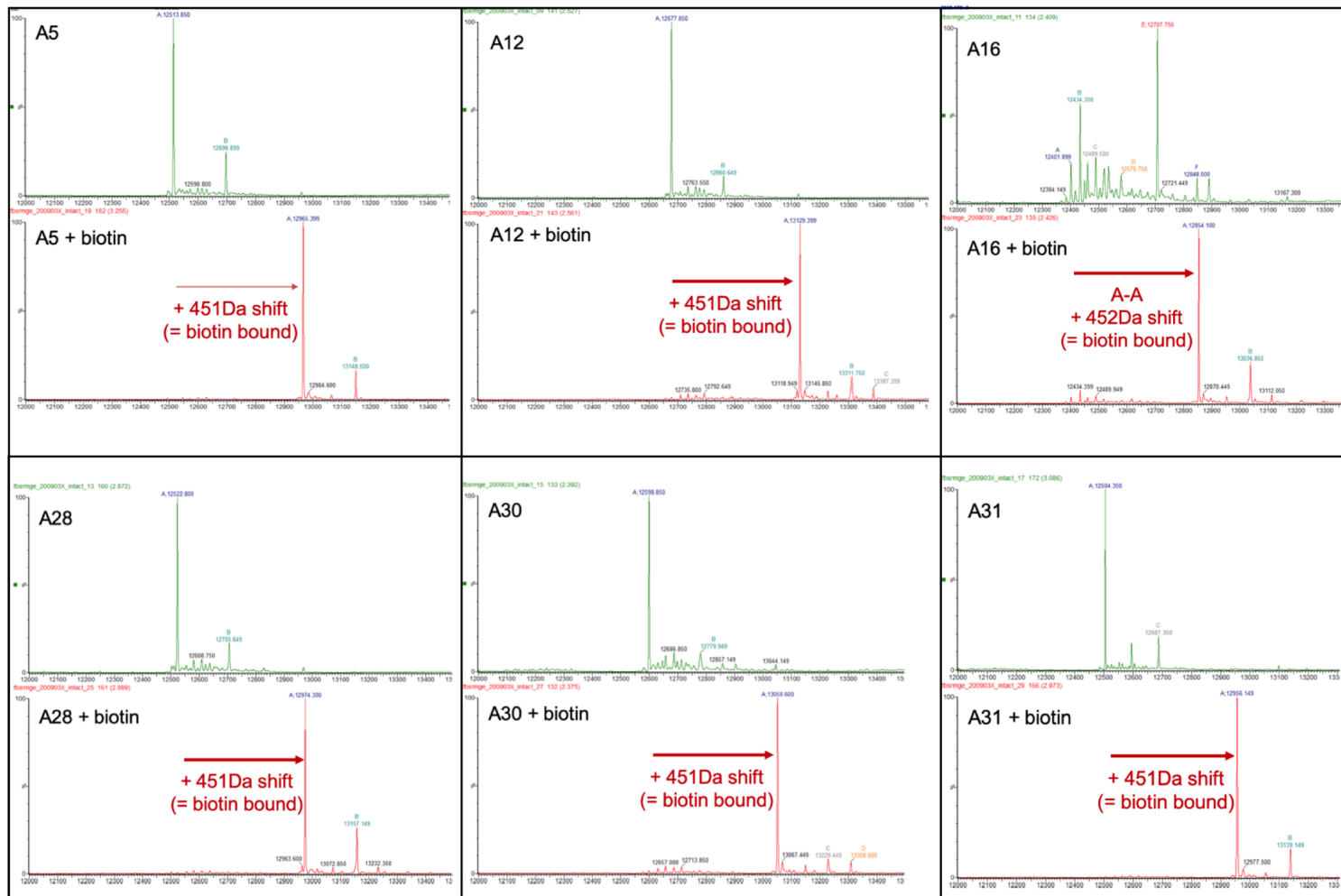


Figure 3.15: LC-MS confirmation of biotinylation

Each Affimer molecules mass was analysed by LC-MS by the FBS Mass Spectrometry facility with and without biotinylation to confirm a successful shift in mass (451 kDa) attributed to a unit of biotin.

3.11 Alexa Fluor-488 labelling of Affimer molecules

Immediately following purification, selected Affimer molecules with a free cysteine were Alexa Fluor-488 linked to reduce the possibility of disulphide bonds forming between thiol groups of free cysteine residues. Affimer molecules were added to TCEP disulphide reducing gel, in order to ensure reduction of the sulfhydryl groups of the cysteine residue. Covalently linked Alexa Fluor-488-maleimide was then used to link Alexa Fluor-488 to the free C-terminal cysteine residue.

To confirm successful linkage of the Alexa-Fluor-488-maleimide to Affimer, an SDS-PAGE gel was run in the dark to prevent fluorescent leakage, and the Affimer linked with Alexa Fluor-488 and a non-linked Affimer control were also run. The gel was read using a G:BOX, exciting the Alexa-Fluor-488 at a wavelength of 488 nm (**Figure 3.16**).

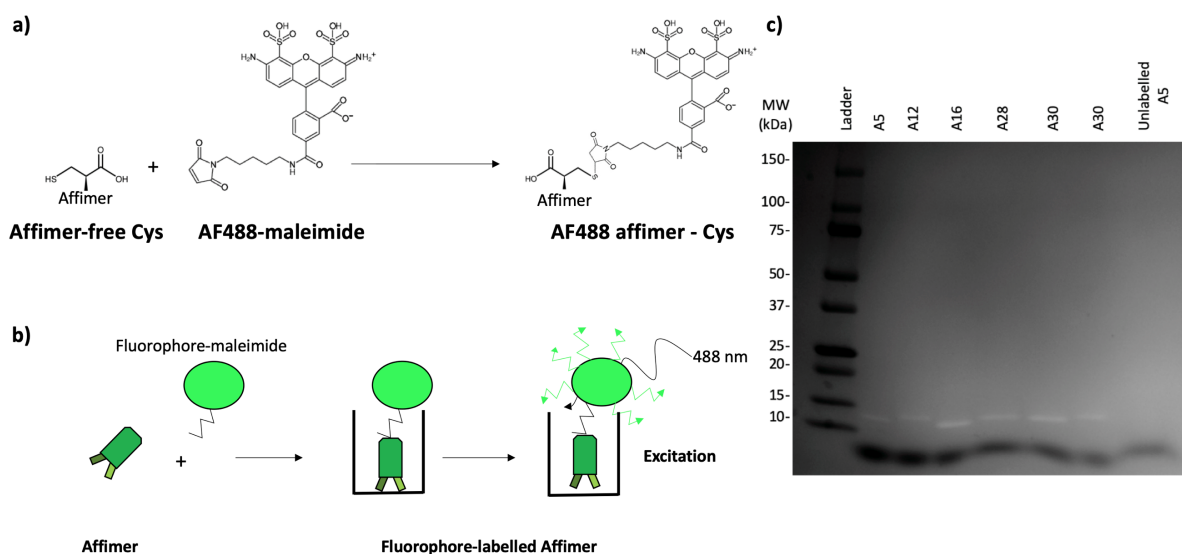


Figure 3.16: Alexa Fluor-488 linking of Affimer molecules

a) Schematic representation of the linking of Affimer molecules via the free cysteine residue at the C-terminus of the Affimer scaffold with Alexa Fluor-488-maleimide. **b)** Schematic representation of the addition of Alexa Fluor-488 to Affimer and excitation of Alexa Fluor-488 with the correct wavelength. **c)** Confirmation of Alexa Fluor linkage. An SDS-PAGE gel was run containing linked targets and a non-Alexa Fluor linked Affimer negative control. SDS-PAGE gel was exposed to a

wavelength 488 nm in a G: BOX. Affimer bands found ~13 kDa are highlighted with an arrow at the correct position.

3.12 Discussion

IAV continues to be a burden to global health, with the risk of a pandemic outbreak likely. Current treatments, such as mAbs, require clinical samples and animals for mass-production, making the production of viable therapeutics slow, expensive and ethically questionable. The aim of chapter 3 was to isolate, express and produce Affimer molecules with specificity to the monomeric form of HA. Two approaches were carried out for this purpose: Isolation of Affimer molecules against a range of monomeric HA proteins, with the aim of isolating broadly neutralising Affimer molecules; and isolation of Affimer molecules against a single monomeric HA protein, with the aim of isolating high potency anti-HA Affimer molecules. Affimer molecules have shown previous success against viral targets and may offer an alternative to IAV therapeutics such as mAbs, whilst removing many of the disadvantages.

The first approach for this chapter aimed to identify conserved epitopes across HA proteins within the H3 subtype and between subtypes of differing groups (H1), with the hope to find a 'universal' neutralising Affimer. Phage display panning was carried out on 3 independent H3 proteins. The Affimers with the best absorbance profiles across each H3 protein were selected to be reassessed against the same H3 proteins, alongside 3 additional H1 monomers. It was found that amongst the 24 selected Affimers based on the best absorbance profiles, only 3 unique sequences were isolated, Aichi 3, Aichi 30 and Fijian 13. Interestingly the cross-reactive phage selected from the California H3 panning round had the same sequence as Aichi 30, suggesting Aichi 30 could have had affinity for both California and Aichi HAs. Overall the absorbance readings were found to be relatively weak, perhaps showing a compromise between 'universal' binding and affinity. The 3 corresponding Affimer molecules were then expressed and purified. An SDS-PAGE gel revealed the high purity of Affimer proteins from elution fractions presenting a band of ~13 kDa, as expected for Affimer- 8xHis products, though Affimer 30 was expressed less effectively. The 3 Affimer molecules were then assessed for neutralisation of IAV (A/Aichi/68 H3N2) at a MOI of 0.001. It was found that none of the three isolated were capable of neutralising IAV at 50 µg/mL. Perhaps emphasising the loss of potency due to a compromise for universal binding. Or, more simply, universal epitopes are located away from sites which would hinder IAV infection.

One reason in which broad spectrum inhibitors may not have been isolated against IAV could be due to the use of a monomeric form of HA for the phage display. This means regions of the protein which would not typically be exposed to immune system in the trimer, and therefore highly conserved due to no immunogenic pressures, were available for binding the Affimer molecules in phage display but not in the infectious virions (**Figure 3.17**). Further to this, it is well known that the phage display system is not fully utilised as there are theoretically 1.3×10^{10} possible unique Affimer molecules available and typically only 48 representative colonies are picked for phage ELISA analysis (237). Selection of colonies containing individual phagemids relies on manual picking as phage ELISA protocols are laborious and time consuming, leaving a limited pool of potential binders to be selected and assessed. Ultimately, it may also be true that a truly 'universal' inhibitory epitope just is not available. Though there are broad spectrum antibodies available, these are not truly universal as virions within a subtype are able to escape protection, along with different subtypes within the group and outside the group being inaccessible to these antibodies (291,292). This is based on the fact that although amino acid sequences of HA proteins within a subtype have homology of more than 90%, homology is drastically lower amongst subtypes within a group (60-74 %) and even less similarity is found between subtypes across groups (40-44 %) (58). Therefore, perhaps the pursuit of individual or multiple conserved epitopes that offer complete coverage of a specific subtype would be a better rationale.

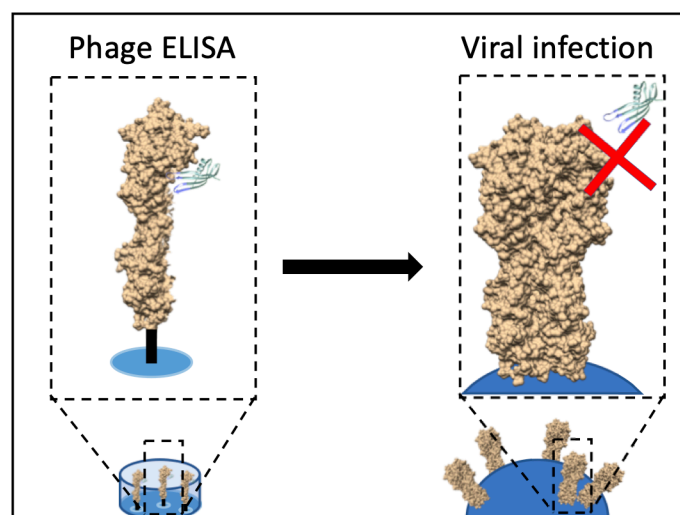


Figure 3.17: Schematic showing the difference in phage display selection and assessment when compared to neutralising IAV

As the attempt to isolate broad-spectrum Affimer molecules that inhibit IAV infection was unsuccessful, an alternative approach was carried out. In this second approach, one HA monomer (H3 Aichi/68), was utilised to isolate specific Affimer molecules. This time, a much larger selection of 480 phage containing colonies from the phage display panning rounds were assessed via phage ELISA, with the hope that a larger selection process would yield more unique epitope binders allowing for later subtype binding characterisation. This approach showed binders with much higher absorbance values for HA and only those with an absorbance above 0.5 (at 620 nm) were selected to be sequenced. 34 unique sequences were identified from the 192 sent for sequencing, showing a dramatic increase in unique binders compared to the previous screen.

Initial expression and purification were carried out in pDhis plasmids to preliminarily characterise the 34 Affimers. Following SDS-PAGE and staining of the elution samples, it was found that expression of 33 Affimer molecules was successful showing a distant band at ~13 kDa (all except A21). When assessing each unique Affimer for its ability to neutralise whole virus, it was found that 7 Affimers (A2, A5, A6, A12, A29, A31 and A33) had the capacity to inhibit IAV infection at a concentration of 50 µg/mL, when assessed alongside a non-specific Affimer and relevant controls. As further characterisation of potential therapeutic and diagnostic isolates was the main aim of this project, it was decided that a smaller subset of Affimer molecules would be assessed at this time, and 3 inhibitors and 3 non-inhibitors were selected (A5, A12 and A31, and A16, A28 and A30, respectively). These particular candidates were selected based on microneutralisation results and on the basis of variable region diversity (through phylogenetic tree classification), with the rationale that the most diverse panel of variable regions would provide candidates binding to a range of different pockets of HA.

For further downstream characterisation, the 6 candidates were subcloned and expressed into pET11a-cys plasmids and purified as before in order to allow biotinylation and fluorophore labelling. Expression and purification was evaluated by SDS-PAGE and InstantBlue® staining and elution fractions presented a predominant band of ~13 kDa, as expected. In some cases, a second band of ~25 kDa or even larger bands were also observed, suggesting the presence of Affimer molecules in their multimeric form in the elution sample, potentially formed by disulphide bonds on the C-terminal cysteines, despite the use of reduction agents in SDS-PAGE analyses, a feature witnessed for other Affimer molecules (293). This multimerisation could be avoided by the immediate expression, purification and linkage of maleimide (biotin/fluorophore) to the free cysteine.

In summary, the results shown here are in line with the first project aim (see **1.8**) demonstrating phage display using only HA monomers is suitable for the isolation of HA-specific Affimer molecules. Affimer molecules which are both inhibitory and non-inhibitory against A/Aichi/1968/H3N2 have been successfully expressed and purified for further characterisation, which will be addressed in the following chapter (**Chapter 4**), where the interaction between Affimer-HA reagents and HA/IAV will be further characterised.

Chapter 4
**HA-Specific Affimer molecules can trap intermediate
conformations of HA**

4.1 Chapter introduction

Our understanding of HA has advanced vastly since the first structural information for IAV neutralising Abs arose in 1995 (294). HA-specific mAbs which directly neutralise influenza virus can target different regions of HA, attributable to HA having multiple functions during the virus life cycle. mAbs can directly neutralise by blocking entry, fusion, egress, viral budding or proteolytic cleavage. Therefore, the mode of viral neutralisation depends on the interaction site and footprint of the antibody on trimeric HA (**Figure 4.1**). Viral entry is blocked by mAbs which target the head domain, through the direct targeting of the receptor binding site on HA or indirectly, through steric hindrance of the Fc (185,295). mAbs targeting the stem of HA interfere with the structural rearrangement of HA as it undergoes fusogenic conditions upon low pH (169,296), or impede HA0 cleavage by extracellular proteases, locking HA in its prefusion conformation (217,297). Both anti-head and anti-stem mAbs can prevent the release of budding virions by binding to HA on the infected cell surface (298,299). Neutralising antibodies typically show moderate to high affinity to HA ($K_d \leq 5$ nM-500 nM) and potent neutralisation ($TCID_{50} < 0.05$ $\mu\text{g}/\text{mL}$ - 0.5 $\mu\text{g}/\text{mL}$), whilst some show the capacity to neutralise a broad range of subtypes, making them the most promising IAV treatment after vaccination schemes.

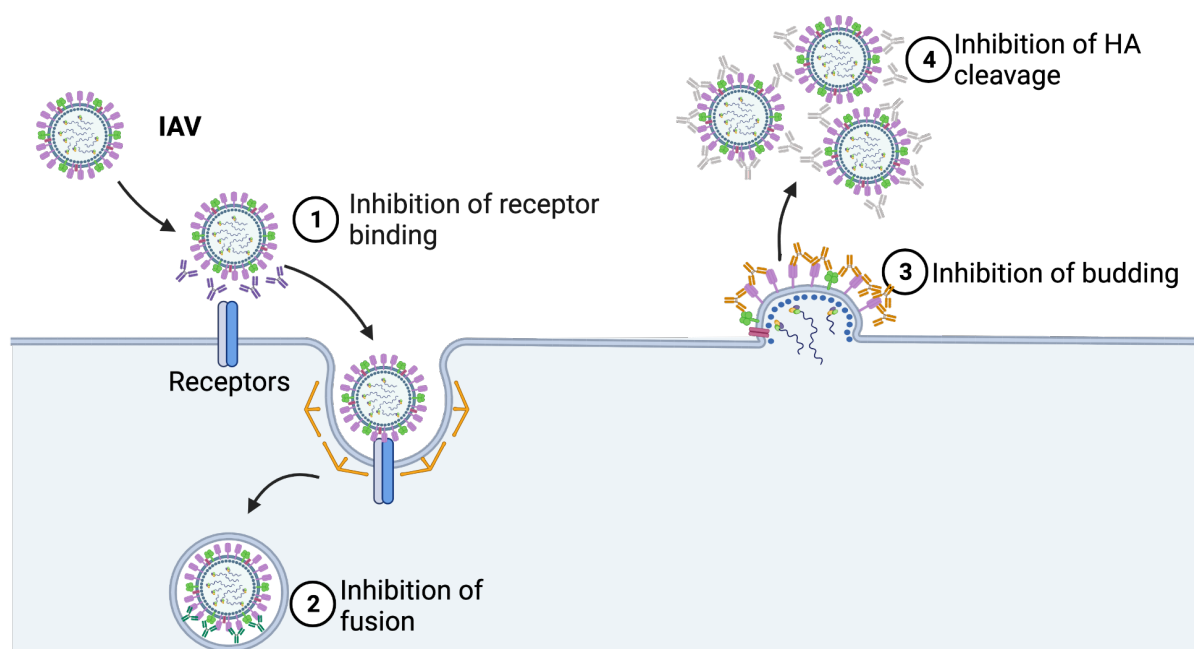


Figure 4.1: Schematic illustrating mechanisms of inhibition monoclonal antibodies undertake when targeting HA

a) Head domain binding antibodies can block cell receptor binding and entry by directly or indirectly blocking the interactions between the RBS and sialic acid. **b)** Stem domain binding antibodies can

inhibit the conformational changes that HA undergoes during membrane fusion, by locking the structure in a prefusogenic conformation. **c)** Both head and stem binding antibodies can prevent newly formed virions from budding away from the cellular membrane. **d)** Stem binding antibodies can inhibit HA0 cleavage by binding around the proteolytic cleavage site located at the stem.
Created with BioRender.com

4.1.1 Head domain binding antibodies

It is well established that the globular head domain of HA is the most immunodominant region of the protein. The analysis of the first HA structure and laboratory escape mutants revealed the major antigenic sites of the head domain well before the structures of the HA-mAb complexes were described (64,142). Five major antigenic sites (ASA-ASE) in the H3 HA were identified in rapid succession throughout the early 1980's through mutagenesis studies (142,286), whilst the corresponding antigenic sites (S_a , S_b , Ca_1 , Ca_2 , C_b) of H1 globular head were identified around the same time (60,61). These antigenic sites are located in and around the RBS. Subsequently, it has been found that antigenic drift in seasonal flu is driven mostly by mutations in these regions (60,61), and that these mutations affect the binding of neutralising antibodies.

A limiting factor for mAbs effectiveness is that they are large, the RBS is approximately 800 \AA^2 (300), whilst most mAb footprints range between $1,200\text{--}1,500 \text{ \AA}^2$ (294). This large footprint is a limiting factor to the vast majority of these mAbs, as access to small conserved pockets is near impossible. Whilst mAbs may sterically block access to the RBS, these interactions with the surrounding antigenic sites leave mAbs vulnerable to loss of affinity through mutations at the antigenic sites. Mutations acquired through antigenic drift can therefore quickly make mAbs redundant against seasonal strains (170). The first structure of an antibody-HA complex was a head domain RBS targeting complex (HC19 (294)). Alongside direct RBS interactions, HC19 interacts with the proximal regions to the RBS, ultimately leading to many escape mutants being identified. It was believed that universal neutralising mAbs could not be achieved due to these rapidly changing antigenic sites, nonetheless, broadly inhibiting mAbs targeting a range of isolates within the same subtype of IAV have been described (295,301). Further still, rare antibodies have been identified that precisely target the sialic acid binding pocket (C05 and F045-092 (168,302)), they exhibit neutralisation across multiple group 1 and 2 strains,

though not all strains are covered, and only a small window of isolates within each subtype are neutralised.

4.1.2 Stalk domain binding antibodies

Compared to the globular head domain in HA1, the stem domain HA2 is much more conserved. It was initially believed that neutralising antibodies targeting the stem domain were not possible, particularly when considering the inaccessibility of these conserved pockets (680 Å²). Through sequence analysis and neutralisation assays, the first stem domain targeting mAb C179 was identified in 1993, in mice (63). Through similar methods first human-derived stem binding mAbs were not isolated until nearly 2 decades later (296,303). Since then, many neutralising mAbs have been structurally characterised. Though stem domain targeting mAbs are less common than their head binding counterparts, they often exhibit a higher breadth and range of IAV subtype and strain neutralisation, due to conserved features in the stem. Group 1 (H1, H2, H5, H6, H8, H9, H11, H12, H13, H16) intersubtypic mAbs are relatively abundant, as there are conserved residues in the hydrophobic pocket (Trp-21) and helix A regions (167,169). Group 2 (H3, H4, H7, H10, H14, H15) heterosubtypic mAbs are less frequently documented (167), which is likely due to a conserved N38-bound glycan found in many group 2 HA proteins, this glycan can sterically hinder mAbs ability to interact with the conserved epitopes. Though the stem domain is much more restricted in its ability to undergo mutation, escape mutants have been isolated against anti-stem mAbs (62,63). Group 1 and 2 universal mAbs, though extremely rare, have been documented. One common feature is that these mAbs appear to adopt different binding conformations, which likely allows them to navigate conserved glycans and to overcome the amino acid diversity, (186,304).

In addition to direct neutralisation, mAbs are capable of stimulating cellular responses through Fc–Fc receptor interactions. Antibody-dependent cell-mediated cytotoxicity (ADCC), is stimulated by mAbs and is essential for optimal protection *in vivo* (305). ADCC is a mechanism in which immune cells are recruited to lyse infected cells. mAbs bound to antigens displayed on infected cell membranes, induce this recruitment (305). Recently it has been found through ADCC assays utilising natural killer cells, that stalk binding mAbs are crucial for this mechanism, whilst it has been found that non-neutralising mAbs are poor inducers of ADCC, and head binding mAbs may even show negative effects on ADCC recruitment (305).

4.1.3 Design and discovery of novel anti-HA drugs

The approved anti-influenza drugs are those which inhibit NA (peramivir, laninamivir, zanamivir and oseltamivir), viral nuclease inhibitor (Baloxavir) and those that act as M2 ion channel blockers (amantadine and rimantadine) (306–308). The adamantines have now been largely rendered outdated due to the viral antigenic drift, creating resistance. For example, 95 % of all current circulating viruses show greatly decreased inhibition, due to a mutation found at S31N (307,309). Considering the rapid viral evolution of influenza and its variability, new antiviral drugs are required, particularly those targeting HA, in order to offer multi-targeted treatment. Though challenging, there are plausible targets for small molecules. The RBS pocket of HA is relatively conserved, whilst molecules with the capacity to block fusion of HA with endosomes, targeting the small conserved pockets at the stem are also possible.

There has been much promise for the delivery of such drugs. Aribidol has been shown to inhibit both group 1 and 2 HA proteins through binding of the hydrophobic pocket in the stem (310). Peptides such as PEP87 have also been found to bind the HA trimer, preventing HA-mediated entry (311). There has been rapid advance in the last decade, in drug and antibody discovery utilising techniques such as deep sequencing and hydrogen-deuterium exchange mass spectrometry to map epitopes decorating HA (312,313). More recent breakthroughs in the drug discovery process have exploited the structural details of broadly neutralising mAbs such as bnAb CR6261 and FI6v3 (186,314); for this, the complementary-determining regions (CDR)-interacting loops were utilised to structurally direct the compound selection process, allowing the selection of small proteins or molecules with much more favourable properties as pharmaceuticals than antibodies.

In this chapter, the isolated Affimer molecules described in chapter 3 are further characterised as therapeutic alternatives targeting the HA protein of IAV, showing that the affinity and potency of these small molecules are comparable to neutralising mAbs. Neutralisation, hemagglutination, ELISA, fusion, and egress assays were used to determine that the Affimers bind to the head domain and that they inhibit sialic acid binding, which has been further validated through structural characterisation by cryo-EM. Furthermore, the variable loop regions of these Affimer molecules have been used to carry out informed compound selection, allowing for identification of small molecules with the potential to be further developed into anti-influenza drugs.

4.2 Affimer molecules show high affinity interactions to HA

As described in chapter 3, 6 Affimers were selected for further characterisation. These included 3 inhibitory and 3 non-inhibitory Affimers against the Aichi H3N2 strain. In order to test the binding kinetics and affinity of the selected Affimer molecules, SPR was employed. Flow cells of a streptavidin sensor chip were either coated with biotinylated Affimer or left as an empty flow cell to act as a negative control. Sensor chips were then exposed to a 1 in 2 dilution series of HA (3.125nM-800 nM). The HA sensograms showed strong binding of inhibitory Affimers A5 and A31 to HA, but surprisingly no binding was observed for the other Affimer-HA interactions that were tested (**Figure 4.2**), suggesting that the affinity for these Affimer molecules were below this range. As monomeric HA was utilised, the HA sensograms were fitted to a Langmuir model, a 1:1 binding interaction model (315). The most accurate fitting corresponded to 200 nM dilution of HA, providing analysis with the lowest of Chi^2 values obtained relative to the response units of the sensogram, giving Chi^2 values of 0.284 for A5 and of 0.203 for A31. The fitted curve for both A5 and A31 showed each Affimer exhibited a low mean K_D in the low nanomolar range (2.80 nM for A5 and 5.94 nM for A31, standard deviations of 1.14 and 3.27, respectively), demonstrating a high affinity interaction to the spike protein of IAV. Both A5 and A31 displayed a relatively slow association rate of ($K_{on} = 1.15 \times 10^5 \text{ M}^{-1} \text{ s}^{-1}$ for A5 and $K_{on} = 2.15 \times 10^4 \text{ M}^{-1} \text{ s}^{-1}$ for A31) and a very slow rate of dissociation ($K_{off} = 1.72 \times 10^{-4} \text{ s}^{-1}$ for A5 and $K_{off} = 1.92 \times 10^{-4} \text{ s}^{-1}$ for A31).

To further confirm interactions between Affimer A5 and A31 with HA, an ELISA was carried out using immobilised HA in Nunc MaxiSorp™ plate. Each well was incubated with a 1 in 3 dilution series of biotinylated A5, A31, K3 (non-specific control) or buffer control. Affimer concentration ranges of 7.41 μM -125.5 pM were employed. Following incubation, high sensitivity HRP-conjugated streptavidin was added before being visualised with the addition of TMB and measurement of absorbance at 620 nm. Both A5 and A31 showed high affinity binding to HA, with mean IC_{50} values of 1.032 nM for A5 and 1.101 nM for A31, within the same magnitude as the values of the SPR data, whilst K3 showed no response (**Figure 4.3**).

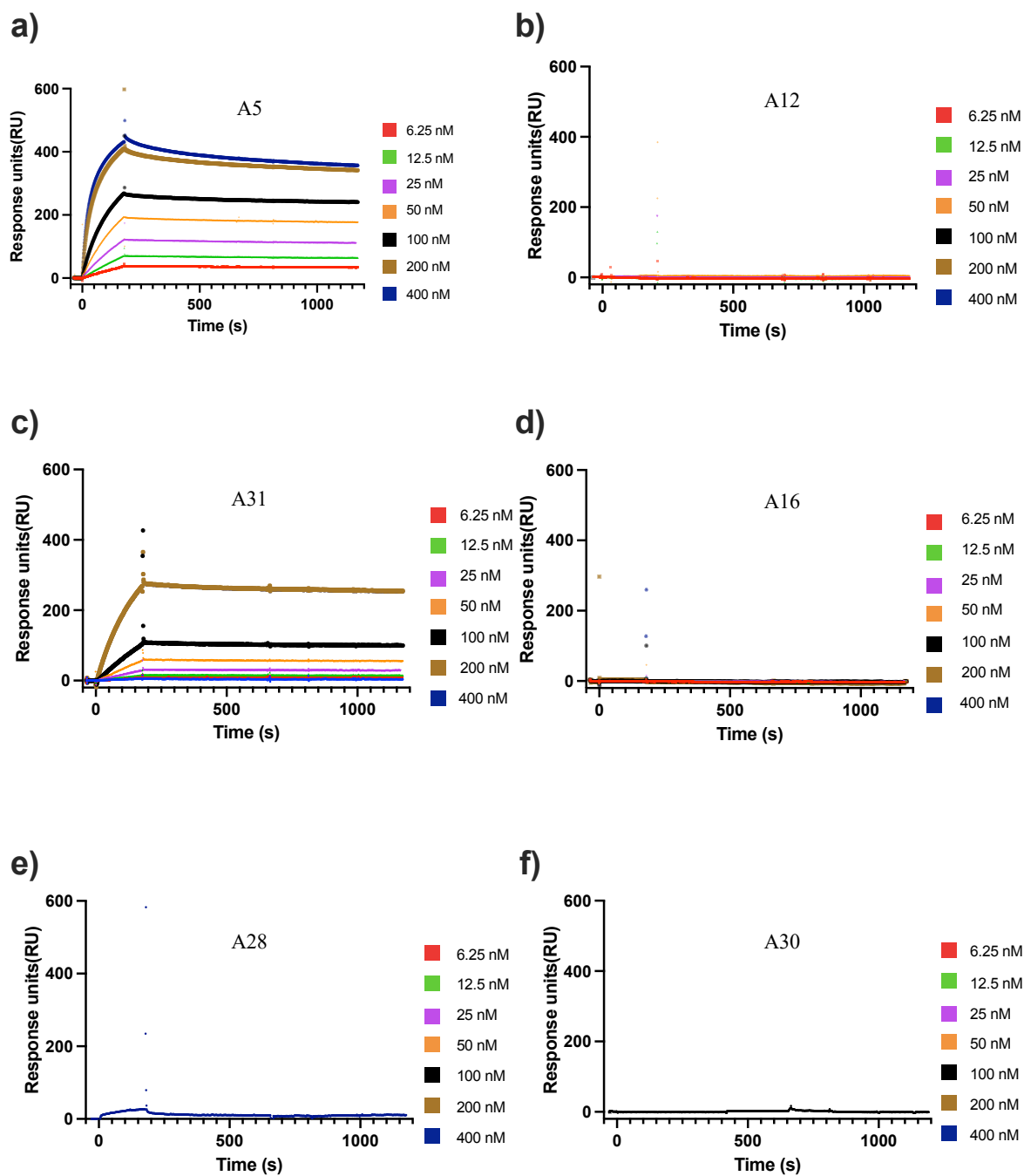


Figure 4.2: SPR analysis of binding kinetics between Affimer molecules and HA

A5, A12, A31, A16, A28, A30 (a, b, c, d, e, f respectively) representative SPR sensograms corresponding to 1 in 2 dilutions of injected HA monomer (A/Aichi/H3) over Affimer coated sensor chips. **a)** A5 exhibited a K_{on} rate = $1.15 \times 10^5 \text{ M}^{-1} \text{ s}^{-1}$ and a K_{off} rate = $1.72 \times 10^{-4} \text{ s}^{-1}$ giving a K_D of 1.5 nM. **c)** A31 exhibited a K_{on} rate = $1.72 \times 10^{-4} \text{ s}^{-1}$ and a K_{off} rate = $1.92 \times 10^{-4} \text{ s}^{-1}$ giving a K_D of 8.94 nM. All other Affimer molecules did not give readable K_D values at concentrations of HA used.

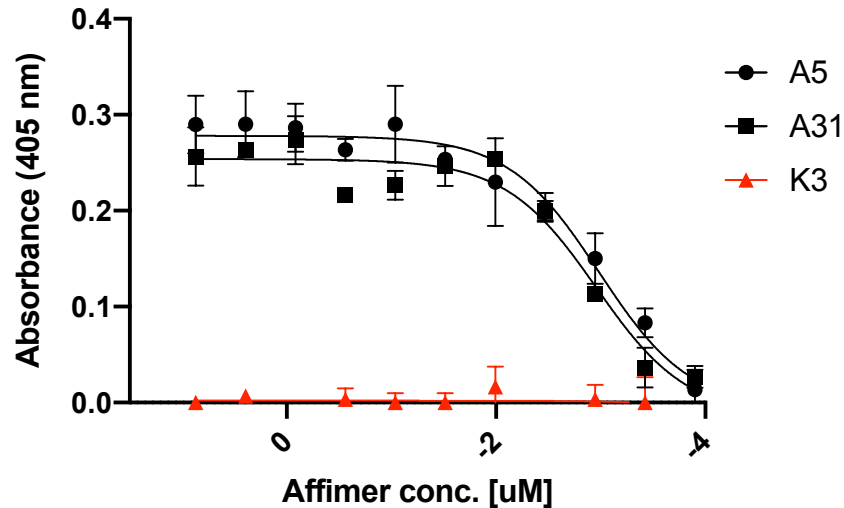


Figure 4.3: A5 and A31 show high affinity to HA via ELISA

ELISA assay to assess Affimer affinity to (A/Aichi/68/H3N2). HA monomers coating wells of a Nunc MaxiSorp™ plate were exposed to a 1 in 3 concentration range of A5, A31 and non-specific K3 (125.5 pM- 7.41 μ M), before adding high sensitivity HRP-conjugated streptavidin and visualising with the addition of TMB and measurement of absorbance at (620 nm), mean with standard deviation displayed. A5 exhibited an IC_{50} value of 1.032 nM and A31 exhibited an IC_{50} value 1.101 nM.

4.3 Affimer molecules show potent inhibition against target strain

To further characterise the selected Affimer molecules capacity to neutralise IAV, a microneutralisation assay was carried out. Affimer molecules, including non-specific K3, diluted in a 1 in 3 dilution series (7.41 μ M-125.5 pM) were first incubated for 1 hr with 100 x $TCID_{50}$ of H3N2 (A/Aichi/2/1968), the strain used to isolate the Affimer molecules. Following incubation, the Affimer-IAV solution was added to MDCK cells and incubated for 72 hrs before fixing and staining with crystal violet. Monolayers were visually inspected for any sign of viral lysis to determine $TCID_{50}$ values. All inhibitory Affimer molecules showed some neutralisation of IAV, whilst the non-inhibitory Affimer molecules exhibited no inhibition, with the exception of A28 at the highest concentration (7.41 μ M). A5 and A31 were shown to be potent inhibitors, with $TCID_{50}$ values of 1.96 nM and 0.44 nM respectively (**Figure 4.4a**), corresponding with the binding interaction results.

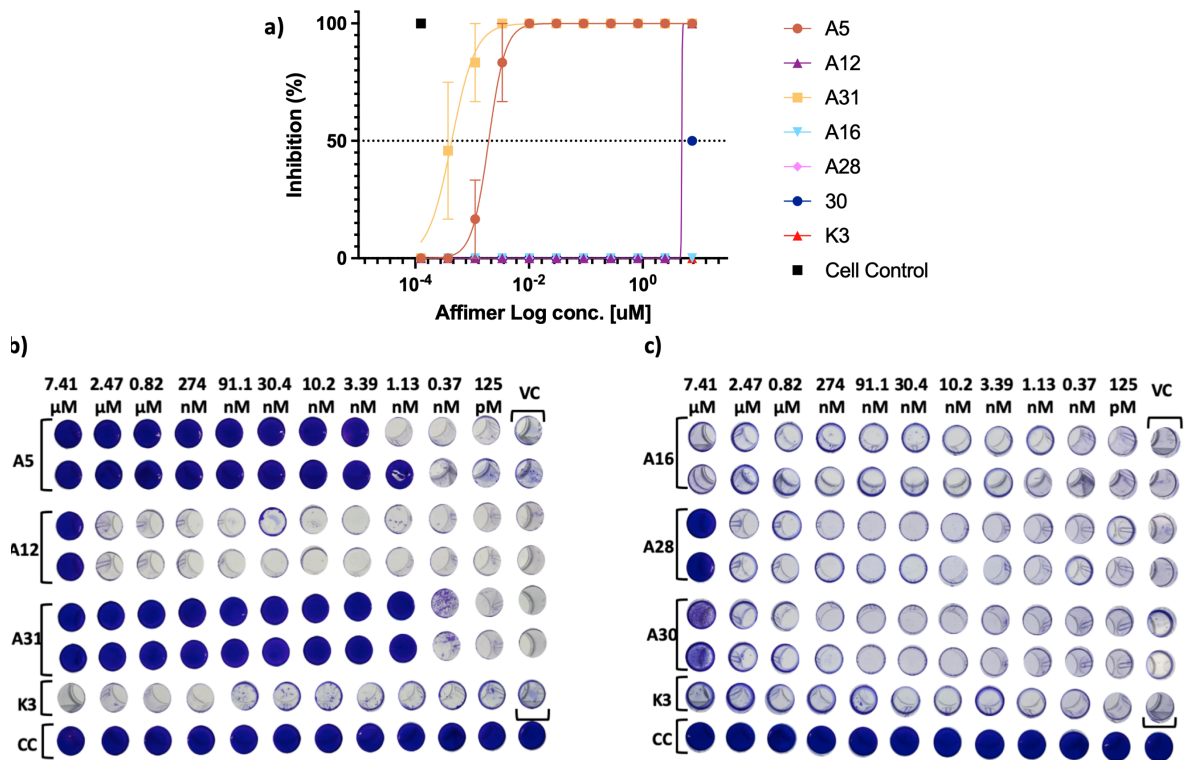


Figure 4.4: Microneutralisation of Affimer isolated IAV

Affimer molecules were added in a 1 in 3 concentration range (125.5 pM-7.41 µM) to IAV A/Aichi/68 before adding to monolayers of MDCK cells. Neutralisation of IAV was observed visually by crystal violet staining of intact monolayers. n=3. **a)** Graph generated in Graphpad Prism to illustrate the neutralisation profiles of each Affimer. Mean and standard deviation calculated and displayed **b)** Representative 'Inhibitory' Affimer molecules stained monolayers. **c)** Representative 'Non-Inhibitory' Affimer molecules stained monolayers.

4.4 Affimer molecules show potency against other H3N2 subtypes

Following the neutralisation assay of H3N2 (A/Aichi/2/1968), a range of H3N2 strains were tested to see whether the Affimer molecules exhibited broad inhibition potency. The H3N2 strains A/Udorn/307/1972, A/Brisbane/10/2007 and A/Victoria/361/2011 were used. Viruses were incubated at 100 x TCID₅₀ with each Affimer. K3 (non-specific Affimer control), a virus only control and a mock infection control were implemented. A 1 in 2 Affimer dilution series was used in order to better capture the effective concentration range of inhibition (7.24 nM-7.41 µM). Affimers and controls were incubated for 1 hr with IAV before being added to MDCK cells and incubated for 72 hrs before fixing

and staining with crystal violet. Monolayers were visually inspected for any sign of viral lysis to determine TCID₅₀ values.

A31 showed good potency against H3N2 (A/Udorn/307/1972), with TCID₅₀ value of 18.22 nM (**Figure 4.5a**), suggesting the epitope targeted by A31 is relatively conserved between this strain and H3N2 Aichi. A5 however, shows decreased inhibition compared to H3N2 Aichi, with a TCID₅₀ value of 3.00 μM, showing a dramatic difference in neutralisation capabilities. Both A12 and A28 show a slight increase in potency (3.51 and 3.61 μM respectively) when compared to H3N2 Aichi TCID₅₀ values (both 4.87 μM). Furthermore, both A16 and A30 exhibit some inhibition against H3N2 Udorn, increasing inhibition when compared to H3N2 Aichi, though still very weak neutralisation capabilities (**Figure 4.4a**).

When assessed for inhibition against more modern H3N2 strains - A/Brisbane/10/2007 and A/Victoria/361/2011, all Affimer molecules demonstrated poor potency, with A16 showing no neutralisation. All Affimer molecules have a TCID₅₀ value of 7.23 μM or greater against both strains, showing only partial inhibition at the very highest concentration of the dilution series. An exception to this is A5, which though shows poor potency, displays slightly better inhibition of 4.83 μM and 3.73 μM (H3N2 (A/Brisbane/10/2007) and H3N2 (A/Victoria/361/2011) respectively). A28 also showed slightly improved inhibition against A/Victoria/361/2011 (TCID₅₀ of 4.27 μM) (**Figure 4.5c**).

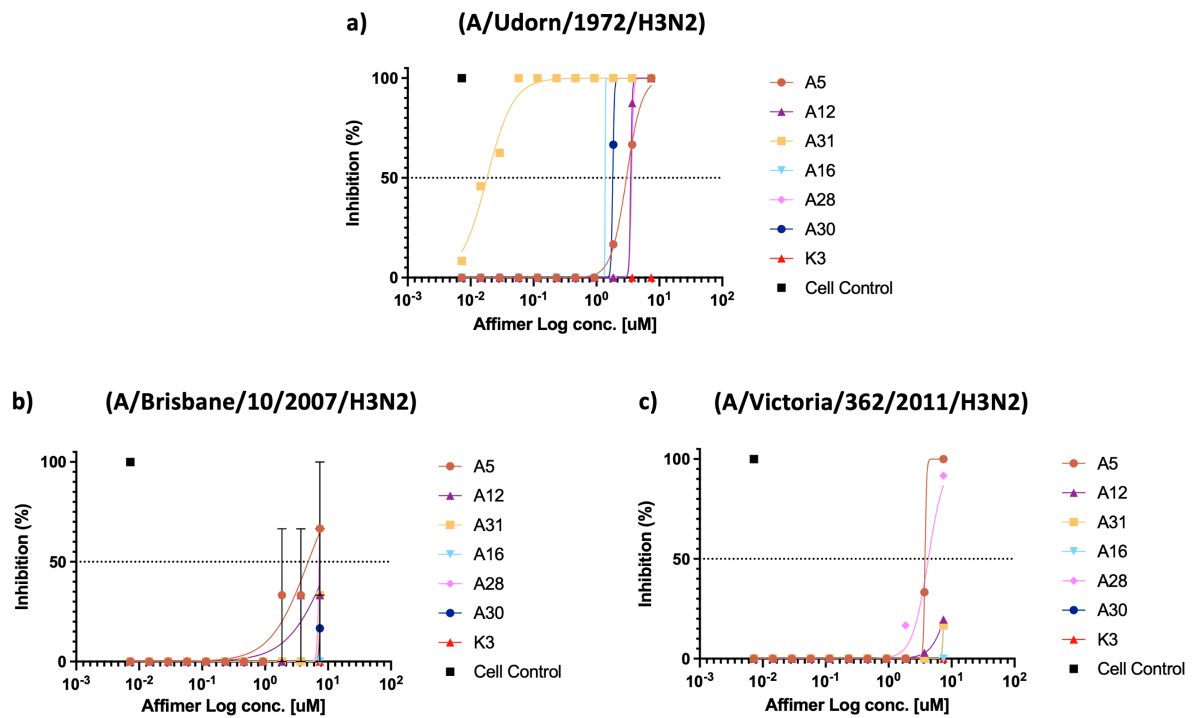


Figure 4.5: Microneutralisation of a range of H3N2 viruses

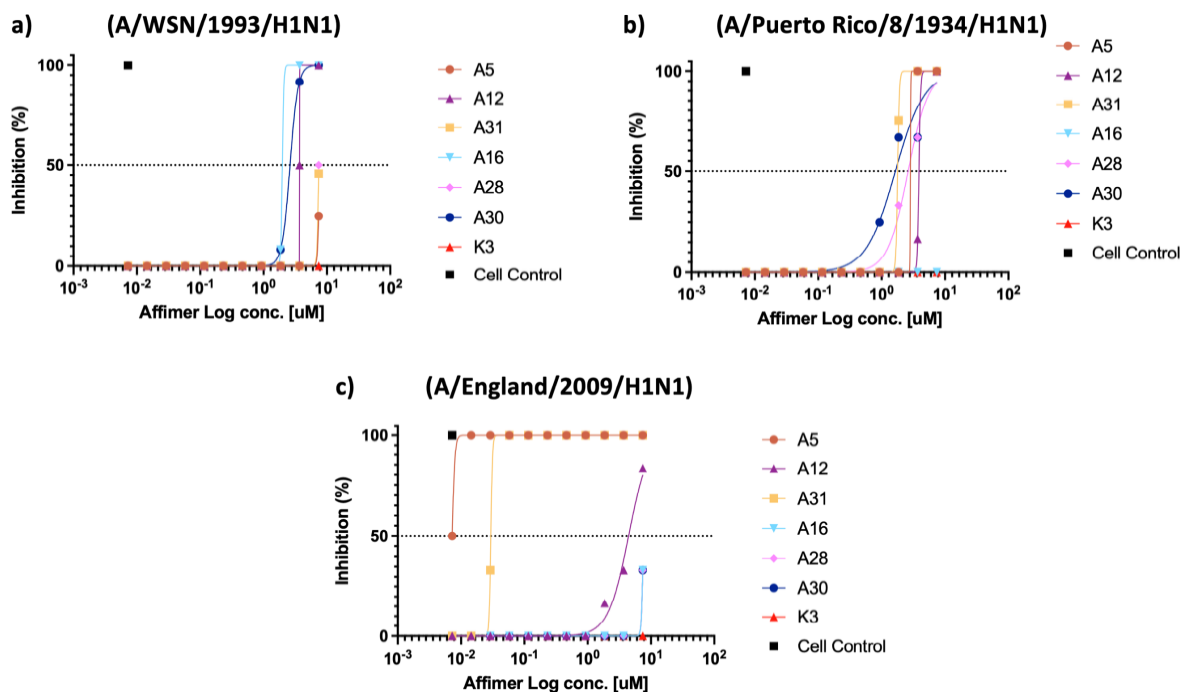
Affimer molecules were added in a 1 in 3 concentration range (125.5 pM-7.41 μ M) to IAV A/Aichi/68 before adding to monolayers of MDCK cells. Neutralisation of IAV was observed visually by crystal violet staining of intact monolayers, mean and standard deviation calculated and displayed. n=3. **a)** A/Udorn/72/H3N2 neutralisation profile **b)** A/Brisbane/10/2007/H3N2 neutralisation profile **c)** A/Victoria/361/2011/H3N2 neutralisation profile. All graphs made in Graphpad Prism.

4.4 Affimer molecules show potency to pandemic H1N1

As the current circulatory strains are H3N2 and H1N1, the selected Affimer molecules against a range of H1N1 strains. The H1N1 strains A/WSN/1933, A/Puerto Rico/8/1934 and A/England/195/09 were used, again incubating 100 x TCID₅₀ of each strain against selected Affimers, K3 (non-specific Affimer control), a virus only control and mock infection control. A 1 in 2 Affimer dilution series was used in order to capture the effective concentration range of inhibition (7.41 μ M-7.24 nM). Affimers or controls were incubated for 1 hr with IAV before being added to MDCK cells and incubated for 72 hrs before fixing and staining with crystal violet. Monolayers were visually inspected for any sign of viral lysis to determine TCID₅₀ values (**Figure 4.6**).

Though they display poor potency, Affimers A5, A12, A31 and A30 showed inhibition against both strains H1N1/WSN and H1N1/Puerto Rico. Both A5 and A31 showed inhibition against H1N1/WSN and H1N1/Puerto Rico with TCID₅₀ values for A5: 7.67 μM and 2.85 μM respectively, and A31: 7.45 μM and 1.79 μM respectively. Perhaps mutations in the AS due to antigenic drift have increased Affimer loop contact with HA, enabling a higher epitopal affinity and ultimately potency (**Figure 4.6b+c**). Though A16 does not appear to inhibit H1N1/Puerto Rico, it shows the most potency when assessed against H1N1/WSN (TCID₅₀ = 1.98 μM) (**Figure 4.6a**).

What is most unexpected is the neutralisation profiles of the ‘inhibitory’ Affimer molecules A5, A12 and A31 against H1N1/Pdm09 strain. A5 showed the greatest potency of the three inhibitors (TCID₅₀ = 7.20 nM), a similar potency to that against H3N2/Aichi, and further still, greater than against all other H3N2 strains tested. A31 also shows good potency against H1N1/pdm09 (TCID₅₀ = 29.56 nM), comparable to its potency against H3N2/Udorn (18.22 nM). The neutralisation profile of A5 and A31 against H3N2 strains and against H1N1/Pdm09 suggests that H1N1/Pdm09 has mutated towards a similar epitope to those of H3N2/Aichi/Udorn, allowing for increased potency by these Affimer molecules. Though A12 shows poor potency in comparison to A5 and A31, its TCID₅₀ (4.43 μM) is comparable to those of H3N2/Aichi/Udorn. Finally, all ‘non-inhibitory’ Affimer molecules tested showed poor potency with each of the respective TCID₅₀ values equalling 7.58 μM (**Figure 4.6a**).



4.5 Affimer molecules block sialic acid binding

IAV achieves infection through successful delivery of its genome into the host cytoplasm. HA-mediated host cell receptor binding, entry and membrane fusion are critical mechanisms which must be carried out in order for this to happen. These mechanisms are also targeted by neutralising antibodies (**Figure 4.1**), and given the similarities between Affimers and antibodies, it was hypothesised that the inhibition mode of Affimers could correspond to blocking one of these mechanisms. To test this, ELISA, hemagglutination, fusion and egress assays were used (**Figure 4.9**).

Initially, the dominant mode of inhibition carried out by antibodies reared against IAV HA was assessed. The HA head domain is the main target of neutralising antibodies perhaps because of the breadth of epitopes available (316). Using a classical IAV hemagglutination assay (**Figure 4.8a**), various concentrations of Affimer (100, 20 and 2 $\mu\text{g}/\text{mL}$ or 7.41, 1.48 and 0.148 μM) were first incubated with 4 HA units of IAV (H3N2/Aichi), before the addition of 1 % human RBC. Inhibition of cell receptor binding is seen when RBC form a spot at the bottom of the well upon incubation for 30-60 mins. When exposed to 100, 20 and 2 $\mu\text{g}/\text{mL}$, both A5 and A31 showed complete hemagglutination. Both A12 and A16 showed hemagglutination at 100 and 20 $\mu\text{g}/\text{mL}$ respectively, and A28 and A30 showed slight hemagglutination only at the highest concentration. These results suggest that all Affimer molecules bind at or close to the RBS (highlighted in orange, **Figure 4.8a**) affecting the ability of IAV to recognise and bind to host cell sialic acid.

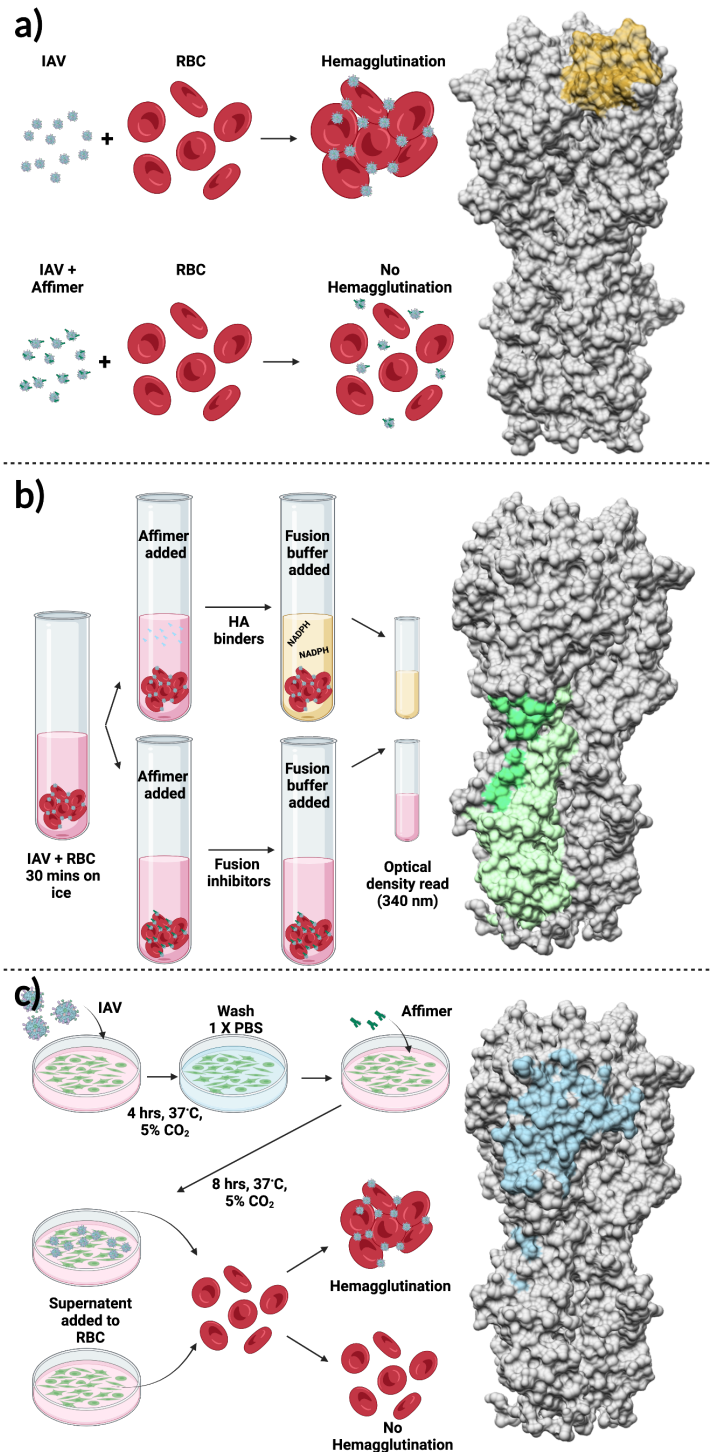


Figure 4.8: Unravelling HA mechanism of action and region of function

a) Schematic to show the results outcomes of a hemagglutination assay. Right, antibody regions for cell receptor binding inhibition are highlighted on a HA trimer. **B)** Schematic of the protocol and outcome of results for the fusion inhibition assay. Right, antibody regions for fusion inhibition are highlighted in green on a HA trimer. **C)** Schematic showing the protocol and outcome of results for egress assay. Right, antibody regions for egress inhibition highlighted in blue on a HA trimer. Created with BioRender.com

In order to confirm initial findings, A5 and A31 were further examined and characterised by performing an ELISA similar to the ELISA carried out in section 4.3, though in this instance, only HA1/head domain of H3N2/Aichi was immobilised in the wells of a Nunc MaxiSorp™ plate. Biotinylated A5 and A31 were incubated in a 1 in 3 dilution series (7.41 μ M-125.5 pM) alongside K3 (non-specific control) or buffer control. Following incubation, high sensitivity HRP-conjugated streptavidin was added before being visualised with the addition of TMB and measurement of absorbance at 620 nm. It was found that both A5 and A31 showed low nM binding to the head domain of HA, with mean IC₅₀ values of 0.928 nM and 2.45 nM respectively for A5 and A31 (**Figure 4.9d**, n=3), exhibiting comparable IC₅₀ values to those of full-length HA and suggesting that binding of these Affimer molecules is strictly to the head domain of HA.

Subsequently, these findings were further validated by assessing other mechanisms of inhibition. Antibody binding to the HA2 domain or stalk domain of HA in key epitopes prevents the conformational changes HA undergoes upon a low pH cue as it passes through the endocytic pathway. To assess this possible interaction between Affimers and HA, an *in vitro* assay was adapted (298), in which RBC cells were incubated on ice with IAV to synchronise binding. Control or Affimer molecules were then added (100 μ g/mL or 7.41 μ M) before exposing the virus to a fusion buffer (pH 5.0) for 30 mins, which results in RBC lysis. Upon cell lysis NADPH is released and can be quantified by absorbance at 340 nm (**Figure 4.9b**). Following absorbance readings and subtraction of mock infection absorbance values, it was found that fusion was complete and no significant difference was found between virus control, non-specific Affimer control (K3) and all specific Affimer molecules (**Figure 4.9b**, n=3). These results suggests that these Affimer molecules do not target fusion inhibiting epitopes on the HA stalk.

Finally, Affimer molecules were evaluated in order to see if they effected IAV egress (**Figure 4.9c**). IAV at a MOI of 5 was used to infect MDCK cells. Following 4 hrs of incubation with the virus, cells were washed and 100 μ g/mL (7.41 μ M) of Affimer, or control (K3) were added. At 8 hpi, supernatants were harvested and viral titre was assessed through a hemagglutination assay (**Figure 4.9a**). It was found that there is no significant difference in hemagglutination units between virus control, non-specific Affimer control (K3) and all specific Affimer molecules (**Figure 4.9c**, n=3). This result suggests that the Affimer molecules do not inhibit viral egress. Taken all these results together, Affimer molecules inhibit through blocking of the RBS, either directly or indirectly.

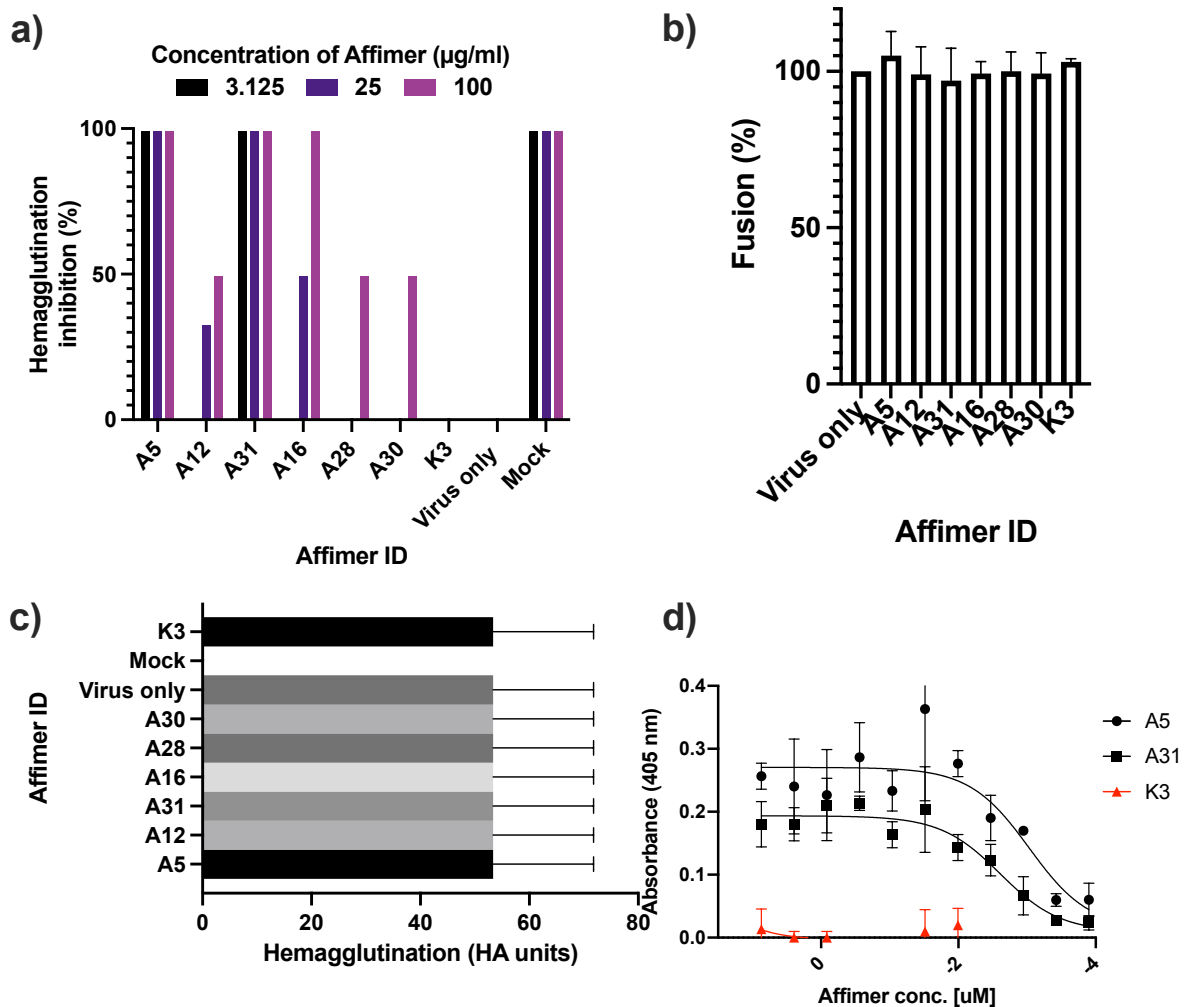


Figure 4.9: Affimer molecules mechanism of action

a) Hemagglutination assay to assess Affimer molecules ability to inhibit receptor binding. Reagents or controls were incubated with 4 HAU units of A/Aichi/68 before the addition of 1 % human RBCs at: 7.41 μ M, 1,48 μ M or 148 nM concentrations n=3. **B)** Fusion assay. Affimer molecules or controls were added to whole virus before being added to 1 % human RBC and adding a low pH buffer to initiate fusion. Inhibition of fusion would result in a reduced NADPH detection. Mock infection control was n=3. **C)** To assess egress, MDCK cells were infected with whole virus, with Affimer or Affimer controls added at 4 hpi. Cell lysates were harvested at 8 hpi and assessed by hemagglutination n=3. **D)** ELISA assay to show Affimer specificity to A/Aichi/68 HA1. 96 well maxisorb plates were coated with HA1 before being exposed to a concentration range of A5, A31 and K3 Affimer molecules. The mean with error bars displaying standard deviation was calculated in all instances. n=3.

4.6 Cryo-electron microscopy confirms A31 binds to HA globular head

4.6.1 Cryo-grid preparation

To further validate the biochemical data, which suggests that A5 and A31 inhibit through binding/obstruction of the RBS of HA, structural information of HA-Affimer complexes was pursued using cryo-EM. HA construct, Trimeric disulphide-stabilized HA HK/68, was utilised throughout (kindly provided by Professor Ian Wilson, The Scripps Research Institute) (317). Due to the biochemical properties of HA, which is notorious for preferred orientation (**Figure 4.10a**) (318–320), grid preparation optimisation was required. Rapid application and vitrification (<500 ms) of sample has been shown to increase side views from 4% of the total population to 19% (320), alternatively, the addition of the detergent N-octyl glucoside to sample buffer at 0.1 % w/v has been shown to increase side views of HA (321).

After testing the addition of detergent and rapid vitrification, the latter resulted in a better distribution of HA molecules (**Figure 4.10**). Therefore, rapid vitrification using a sprayer was employed for all HA cryo-grid preparation (with the help of David Klebl) (266). Quantifoil 300 mesh Cu R1.2/1.3 grids were glow discharged using a Cressington 208 Carbon coater for 99 seconds at 15 mA and 0.1 mbar. The sample was then sprayed onto the grid and rapidly vitrified. The time-delay between spraying and vitrification was calculated to be 12 ms (266). To prepare the HA-Affimer complexes, HA was diluted to a final concentration of 2.9 mg/mL in 1 x TBS buffer, and Affimer reagent was added at a 1.5-fold molar excess to ensure complex formation. On preparation of HA, HA-A5 or HA-A31, it was clear that Affimer complexes had a notable effect on HA and its distribution on grids through visualisation of micrographs. Sprayed and vitrified uncomplexed HA was well distributed across the grids, with clear signs of side views (**Figure 4.10b+c**). The HA-A5 complex (**Figure 4.10d**), showed clustering/aggregation on grids, perhaps showing additional ways in which A5 inhibits IAV, by causing clustering of virions via the HA, preventing entry. This may be highlighted previously, in which possible multimeric forms of A5 can be seen in its purification (dimeric ~30kDa, multimeric ~75 kDa, **Figure 3.11**) HA-A31 showed little to no clustering (**Figure 4.10e+f**), and complexes were reasonably well distributed on the grids. HA-A5 was not taken forward for data collection due to clustering resulting in one orientation of HA, however both HA alone (data collection and processing carried out by David Klebl) and HA-A31 grids were.

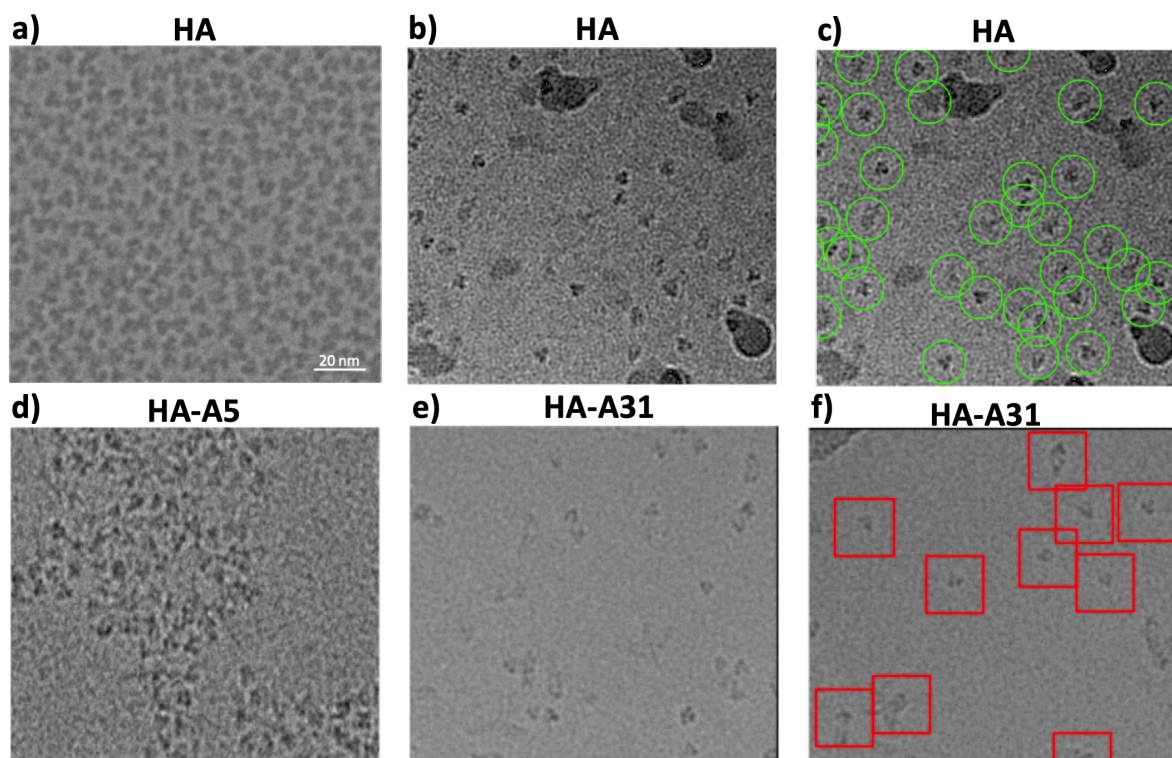


Figure 4.10: Micrographs of HA and HA in complex with Affimers A5 or A31

a) Raw micrograph of HA, displaying preferred orientation **b)** Raw micrograph of HA under rapid vitrification conditions to reduce preferred orientation **c)** crYOLO automated particle picking selection threshold visualised in relion and utilised for downstream processing of HA **d)** Raw micrograph of HA-A5 complex **e)** Raw micrograph of HA-A31 complex under rapid vitrification conditions to reduce preferred orientation **f)** crYOLO automated particle picking selection threshold utilised for downstream processing of HA-A31.

4.6.2 Data collection and image processing

HA and HA-A31 collections were carried out using a FEI Titan Krios equipped with a Falcon 2 direct electron detector at a pixel size of 1.14 Å/pix and a total dose of $\sim 64 \text{ e}^-/\text{Å}^2$ over a 9 second exposure with 40 frames in each micrograph movie. The collection was carried out for a total of 72 hrs, with 12 hrs of this at a 30 ° tilt, to increase the number of oblique and/or side views. Micrographs were collected utilising the FEI EPU automated data collection software. Whole frame motion drift and CTF correction (to align defocus parameters) were carried out using MOTIONCORR and Gctf within the Relion software package, respectively (322). Micrographs had a defocus range of -0.75 to -2.75 μM .

A total of 359,605 particles were extracted from micrographs using crYOLO automated picking. For this a suitable threshold was applied to micrographs in order to collect the maximum number of particles without introducing 'noise' to the dataset (**Figure 4.10f**). The particles were subjected to 2 rounds of reference-free 2D class averaging into 100 classes over 25 iterations, using a box size of 252 pixels and a mask diameter of 190 Å. This allowed removal of any 'noise' or poor-quality particles.

Of the 359,605 particles extracted, 138,831 particles that contributed to 2D classes that clearly resembled HA were taken forward (**Figure 4.11**). The discarded particles resembled the edge of carbon, contamination, or particles in too close a proximity to one another. Side views are clearly visible within the 2D classes, with what appeared to be extra density at the head domain, suggesting HA-A31 complexes were present amongst the particle population. The selected particles were then carried forward for 3D structure determination.

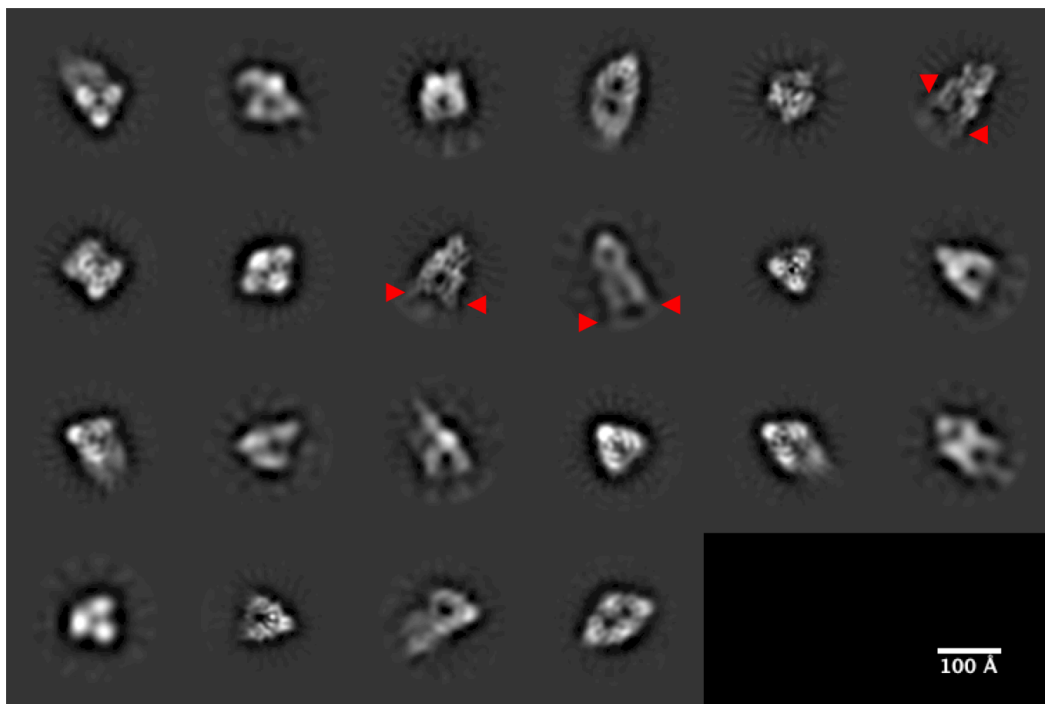


Figure 4.11: 2D classes selected for downstream processing

Resulting 2D classes from 2 rounds of 2D classification, showing a range of orientations. Scale bar, 100 Å. Additional density observed is highlighted by red arrowheads.

3D classification was performed over 100 iterations. Due to HA being homotrimeric, C3 symmetry was imposed in order to extract the most structural information possible. 3D classification without imposed symmetry was also performed, as a control. A reference model was used – the low-pass filtered (50 Å) initial model of HA (generated by David Klebl). 3D reconstructions were classified into 5 classes, in both C3 or no imposed symmetry datasets, to identify heterogeneity in the datasets (e.g. fully or partially occupied HA with A31, or unbound HA particles). C3 imposed symmetry showed slightly more structural detail when compared to non-symmetry imposed C1 reconstructions of HA-A31; as the overall structures appeared comparable it was assumed no bias had been introduced and the C3 symmetry-imposed model was carried forward (**Figure 4.12**). However, C1 symmetry was imposed independently at each step of further processing to ensure no symmetry-related bias. Of the 5 C3 classes, 2 of them resembled HA with extra density at the head domain of the structure, the class with the most structural information was selected and this particle stack of 87,634 particles was used for high-resolution 3D refinement.

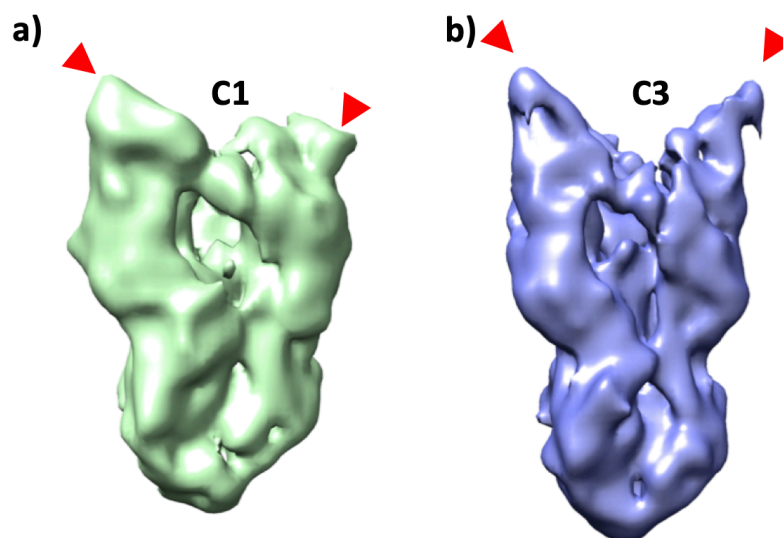


Figure 4.12: 3D classes showing extra density in both C1 and C3 imposed symmetry

a) Best representative 3D class of the HA-A31 complex, with C1 imposed symmetry. **b)** Best representative 3D class of the HA-A31 complex, with C3 imposed symmetry. Extra density can be observed at the head domain of both C1 and C3 imposed symmetry classes (highlighted by red arrowheads). The class with C3 imposed symmetry exhibited greater structural information and was therefore carried further for more downstream processing.

For high resolution 3D structure refinement, the low-pass filtered initial model from David Klebl was utilised as a starting model. Using the auto-refine function, with C3 symmetry imposed, refinement converged after 16 iterations. The resolution of the unsharpened and unmasked map was estimated at 7.4 Å. These particles were subjected to 3 rounds of Bayesian polishing and CTF refinement, to account for effects of beam induced movement during exposure and utilising an estimated B-factor to carry out weighted averaging of particles in aligned movie frames to reduce weighting of radiation-induced damage; and to carry out a CTF estimation per particle. The final 3D map was then sharpened and masked to make high-resolution features more distinguishable. This yielded a final map of 4.8 Å resolution, at a 0.143 cut-off (gold standard (323)) (**Figure 4.13**).

In the final reconstruction, secondary structural information is clearly defined in the main body, with the characteristic alpha helices of HA2 visible. The density for the Affimer molecules is less well defined, likely due to: low particle numbers, the Affimer being flexible and/or not all Affimer-binding sites being occupied in all particles. Though the resolution is not high enough to conclusively define HA-A31 to atomic resolution, including the precise interactions between Affimer variable loops and the HA head domain, it is clear that Affimer density is present at the head domain, confirming the biochemical findings of A31-RBS interactions (**Figure 4.13a**).

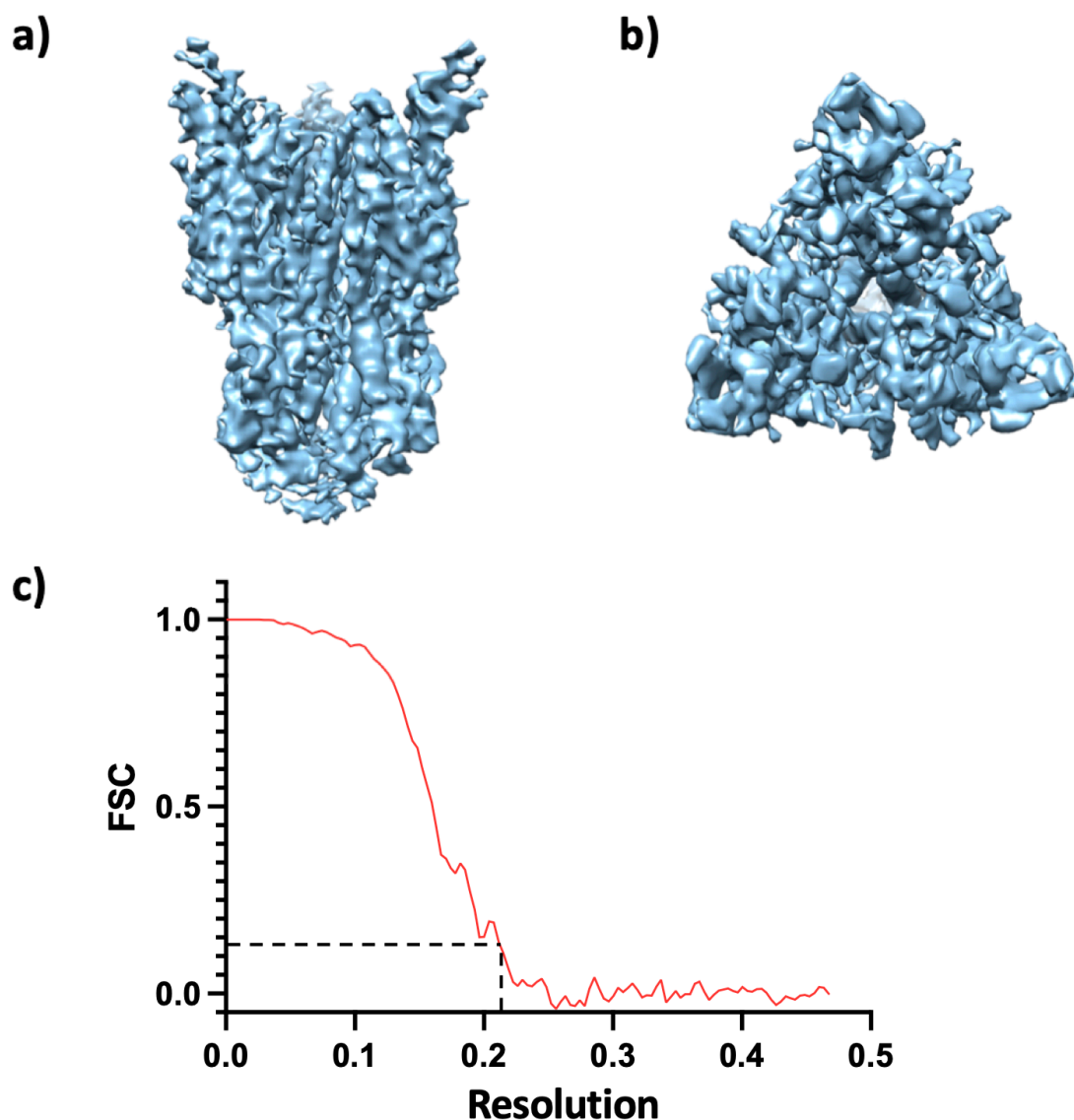


Figure 4.13: Final reconstruction of HA-A31 at 4.8 Å resolution

Lateral a) and top b) views of HA-A31 complex at 4.8 Å resolution. c) Gold-standard Fourier Shell Correlation (FSC) curve (cut-off of 0.143).

4.6.3 Flexible fitting of crystal structure

When fitting an HA atomic model into the HA-A31 average, it was instantly noticeable that the HA spike appeared to be truncated at the stalk domain, with a dilated head domain when compared to the native HA (using the HA HK/68 atomic model, PDB: 4ZCJ (317)). Unexpectedly this HA-A31 complex resembled an intermediate structure (termed 'Dilated conformation 2' PDB: 6Y5J; (321)) (**Figure 4.14**).

To better understand the structure of the HA-A31 complex, and the potential structural reorganisation A31 induces. First, the HA-A31 map complex was assessed for 'best average map value' utilising the fit-in-map functions in Chimera. It was found that dilated form 2 HA gave the best score: 0.012 (**Figure 4.14d**), and so, the HA-A31 complex was flexibly fitted to the dilated conformation 2 structure of HA, created using the ChimeraX plugin Isolde, based on both of these structures.

To produce the most accurate model, the crystal structure of HK/68 (PDB: 4ZCJ) was first flexibly fitted to resemble the dilated form 2 HA structure (PDB:6Y5J), before flexibly fitting it to the HA-A31 density map. Finally a resolved Affimer crystal structure (Adhiron92, PDB:4N6T (237)) was fitted into the extra density which could not be accounted for by the HA. While the exact HA amino acids the Affimer interacts with cannot be determined due to the resolution of the Affimer density, this model confirms that the Affimer variable loops are in close proximity to the HA RBS.

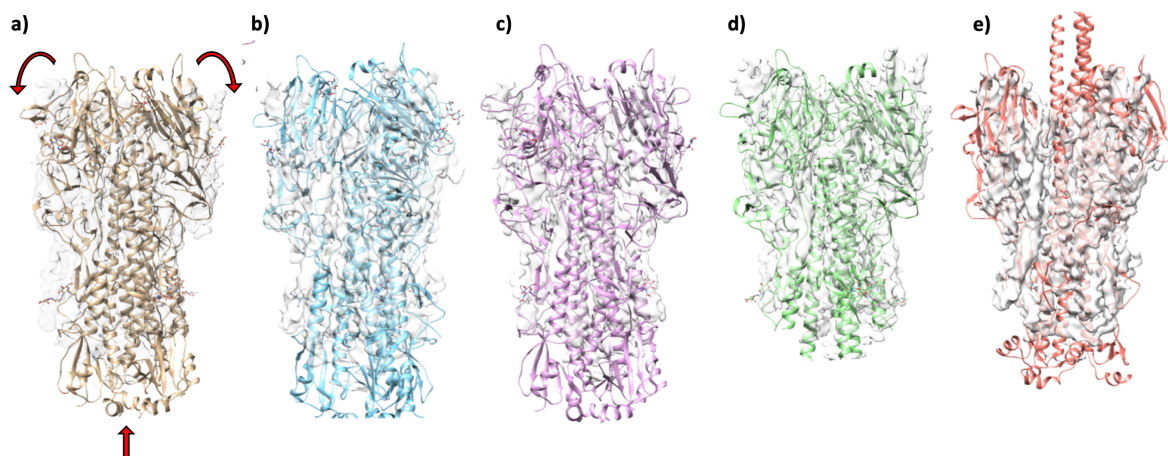


Figure 4.14: Fit comparison of the HA-A31 map to the structural conformations of HA

a) Pre-fusion pH 8 HA (PDB: 6Y5G (144)), fit with HA-A31 map. Fit-in-map scoring gave an average map value = 0.01065 for 12036 atoms, 9374 outside contour. Red arrows highlight the structural transitions of HA as it undergoes fusion. **b)** Pre-fusion pH5 HA (PDB: 6Y5H (144)), fit with HA-A31 map. Fit-in-map scoring gave an average map value = 0.01077 for 11994 atoms, 9324 outside contour. **c)** Dilated form 1 HA (PDB: 6Y5I (144)), fit with HA-A31 map. Fit-in-map scoring gave an average map value = 0.01046 for 11928 atoms, 9396 outside contour. **d)** Dilated form 2 HA (PDB:6Y5J (144)), fit with HA-A31 map. Fit-in-map scoring gave an average map value = 0.01205 for 9609 atoms, 7174 outside contour. **e)** Full extended HA2 (PDB: 6Y5K (144)), fit with HA-A31 map.

Fit-in-map scoring gave an average map value = 0.009271 for 10614 atoms, 8783 outside contour. The HA-A31 complex map is shown in all figures as grey transparent, in order to visualise fit, better.

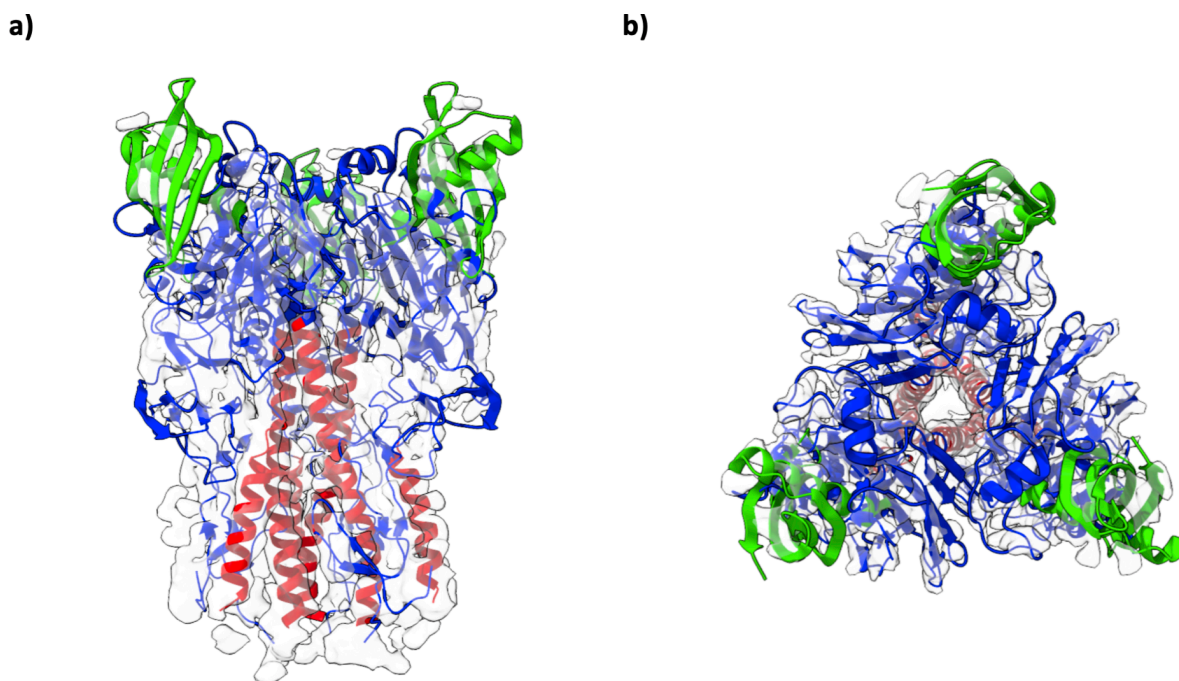


Figure 4.15: HA-A31 reconstruction with flexibly fitted HA model

HA-A31 complex map (transparent grey) was flexibly fitted using ChimeraX plugin Isolde to fit dilated conformation 2 HA (PDB: 6Y5J (144)) (HA1 blue, HA2 red) into 4.815 Å resolution reconstruction. Adhiron92 (PDB: 4N6T) has been loosely docked into extra density (green), to show possible binding.

4.7 Affimer variable loops can be used to identify novel anti-IAV small molecules

4.7.1 Variable loop compound selection

Small molecules are good therapeutic candidates, as evidenced by the fact that 90 % of all FDA approved pharmaceuticals are small molecules (222). Due to Affimers' specificity and high throughput screening they are good templates for rational drug design, thus we wanted to assess whether Affimer variable loops could be used to identify novel small molecules as a potential anti-influenza

therapeutic. In order to do this without structural detail, a homology model of Affimer A5 was created for compound screening as A5 potency and loop structure gave most promise. The model was created using SWISS-MODEL (324) by uploading the protein sequence of A5 and selecting a structure with the highest sequence identity to act as the scaffold backbone (a Bcl-2 specific Affimer with 90.91 % sequence identity, PDB: 6HJL (325)). All Affimer loop mimic compound selections were carried out by Alex Flynn. The two loops of the Affimer molecule were isolated using Pymol, and used as query molecules in the shape comparison software ROCS (OpenEye). The Affimer loops of A5 were then screened against the full library of eMolecules (1.2 million compounds), which had been prepared with 10 maximum potential structural confirmations using Omega (OpenEye). The top 1,000 hits from ROCs were then screened using EON (OpenEye), which compares the electrostatic properties of the ROC hits against each of the individual Affimer loops. Following comparison, the top 150 compounds were visually inspected by Alex Flynn using VIDA (OpenEye), looking for similarities in side chain and structure of hits and Affimer loops, and selecting compounds with maximal coverage of Affimer loops. Following compound screening, 8 of the 15 compounds were selected based on availability (**Table 4.1**). These 8 compounds were then initially assessed in cellular assays for the highest tolerable *in vitro* concentration and ability to neutralise IAV (H3N2 A/Aichi/1968).

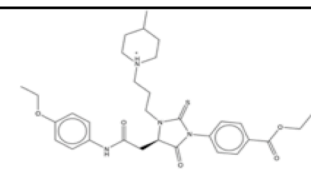
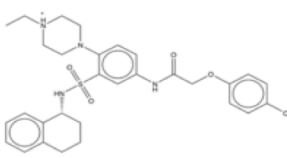
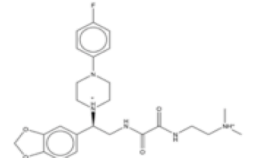
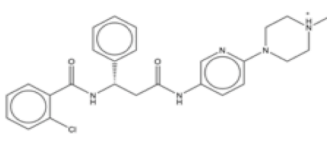
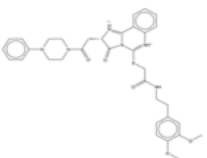
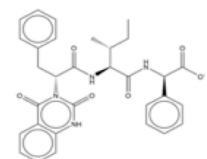
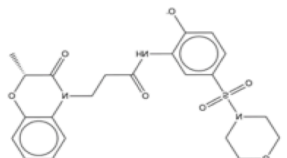
Compound ID	eMolecule ID	Skeletal representation
OA1	24349224	
OA2	25554783	
OA3	5574762	
OA4	11996489	
OA5	24365658	
OA7	26433038	
OA8	11832541	

Table 4.1: Table showing compounds selected using variable loop regions of A5

Table showing compounds with similar structural properties to the loop regions of A5. All chemical schematics were generated in ChemDraw.

4.7.2 Initial characterisation shows promise for therapeutic variable loop mimic compounds

In order to identify tolerable doses in cell culture, the 8 selected compounds were assessed for cytotoxic effects on MDCK cells via an ATPlite cell viability assay to identify the maximum viable compound concentration. A 1 in 2 dilution range was used (24.4 nM-1 mM) and added to cells for 72

hrs, alongside a negative cell only control. The ATPLite cell viability assay was carried out according to ATPLite™ Perkin Elmer 1 step protocol with minor modifications (see methods; (260)). All A5 loop compounds were found to be tolerable (>95 % cell viability in MDCK cells) between low and moderate μM concentrations, with the exception of OA6, which resulted in a cell viability of <95% even at the lowest compound concentration (**Figure 4.16**). All compounds were carried forward, with the exception of OA6 to assess whether they were capable of neutralising IAV (H3N2 A/Aichi/1968), the strain against which Affimer molecules were raised.

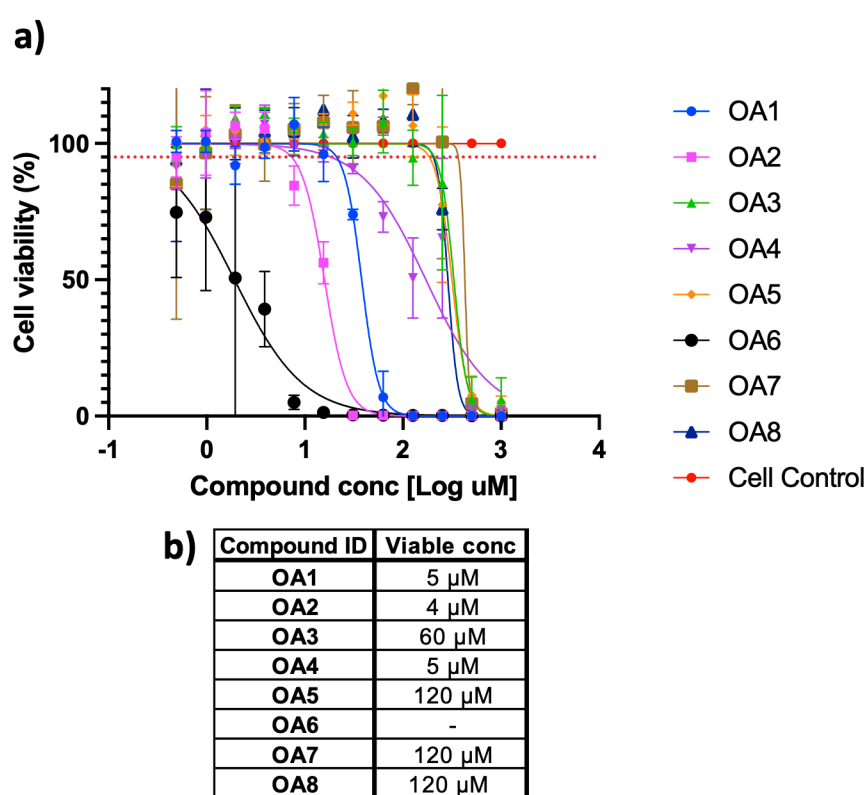


Figure 4.16: Affimer-mimic compound Cytotoxicity

a) ATPLite cell viability assay of Affimer loop compounds. A 1 in 2 dilution series of each compound was incubated with MDCK cells for 72 hrs prior to completion of ATPLite™ Perkin Elmer 1 step protocol with minor modifications (260). Viable concentration was determined by the highest concentration which resulted in >95 % cell viability mean with standard deviation calculated and displayed $n=3$. **b)** Summary table of viable concentrations for each Affimer loop compound.

To identify whether the A5 loop compounds had the capacity to neutralise IAV, a microneutralisation assay was carried out. Affimer A5 loop compounds, were diluted in a 1 in 2 dilution series, starting at the highest tolerable concentration in MDCK cells for each individual compound (**Figure 4.17b**). A positive control was also included (Affimer A5) in a 1 in 3 dilution series (125.5 pM-7.41 μ M), along with virus only and mock infection controls. Compounds or controls were first incubated with 100 x TCID₅₀ of H3N2 (A/Aichi/2/1968) for 1 hr. Following incubation, compounds-IAV solutions were added to MDCK cells and incubated for 72 hrs before fixing and staining with crystal violet. Monolayers were visually inspected for any sign of viral lysis to determine TCID₅₀ values (**Figure 4.17b**). All compounds investigated with the exemption of OA3 showed no neutralisation of IAV. The positive control (A5) showed expected results with a TCID₅₀ value of 1.96 nM. OA3 showed some neutralisation of IAV at its highest 3 concentrations, resulting in a TCID₅₀ value of 11.14 μ M (n=3, **Figure 4.17a and c**). These results suggest Affimer molecules which have known interactions with targets, may be used to isolate small molecules with the potential to be developed into potent therapeutics.

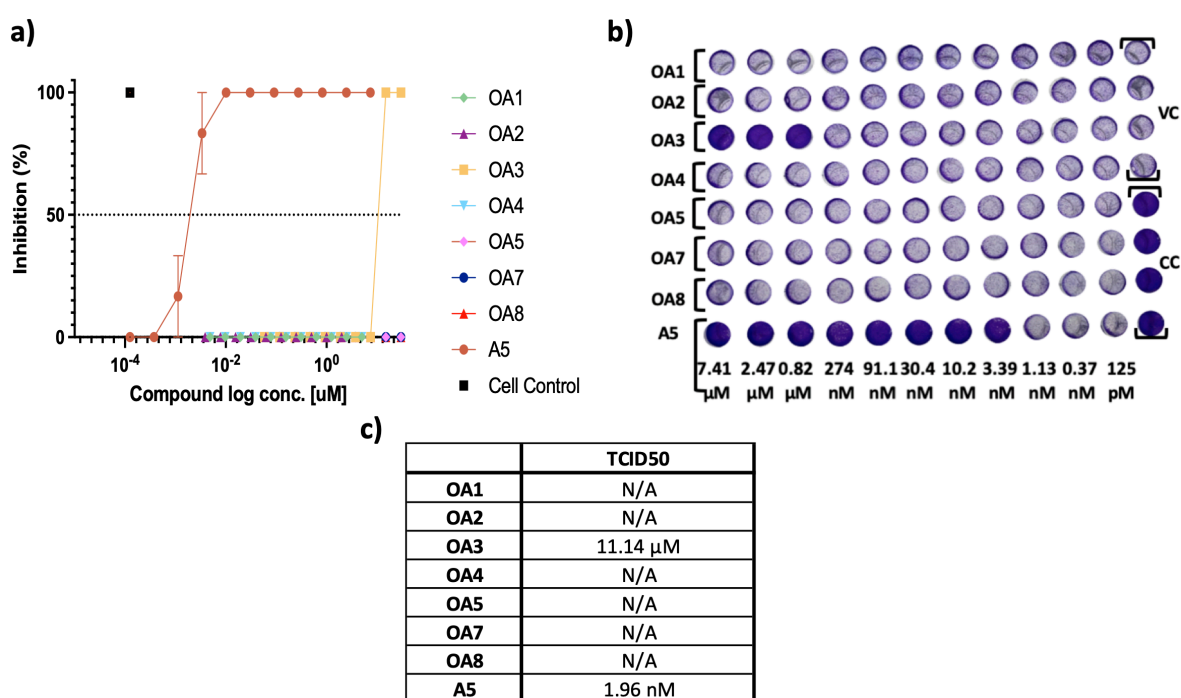


Figure 4.17: Microneutralisation of Affimer loop compounds

a) Results of the IAV microneutralisation of Affimer loop compounds. Affimer loop compounds were added in a 1 in 2 dilution series, beginning at highest viable concentration. A5 positive control was diluted in a 1 in 3 dilution range (7.41 μ M-125.5 pM) before adding to influenza A virus A/Aichi/68 for 1 hr before adding to MDCK cells and incubating for 72 hrs, mean with standard deviations

calculated and displayed. **b)** Inhibition of cytopathic effects of influenza virus was then assessed visually following crystal violet staining. **c)** Final TCID₅₀ values achieved by compounds and positive control

4.8 Discussion

Given the certainty of a future influenza virus pandemic, additional solutions are required to tackle rapidly evolving influenza virus infections, alongside the high-throughput identification, testing and distribution of treatments needed for pandemic variants. Following vaccination strategies, mAb treatment shows high promise, though this comes with drawbacks such as the size limitations, with reduced tissue penetration compared to small molecules and limited access to conserved residues due to large mAb footprints. Alongside production issues, requiring clinical samples which is time consuming, the need for animal use and expense of overall production and distribution (220). A number of small antibody-like molecules have been developed, to complement and overcome shortfalls antibodies encounter (229). For example, Affimer molecules are well characterised for over 300 protein targets, in which low nanomolar affinities have been achieved (237). In this chapter, 6 of the isolated Affimer molecules described in chapter 3 have been characterised. This characterisation involved assessing the affinity between Affimers and HA (H3/Aichi/68), and testing their ability to neutralise a range of IAV strains, using an array of *in vitro*, biochemical biophysical and structural techniques.

Using SPR and ELISA assays, A5 and A31 were shown to similarly exhibit high affinity for HA, demonstrating low nanomolar K_D values (K_D >10 nM), comparable to those of neutralising antibodies. Neutralising antibodies that bind to the HA1 domain typically target the RBS, preventing HA from interacting with SA on host cells (220). Although it is not conclusive that A5 and A31 interact directly with the RBS, the hemagglutination assays show that both Affimer molecules block the interaction between sialic acid and HA, potentially preventing cell receptor binding and entry of IAV. A12 was found to have limited affinity, alongside the non-inhibitory Affimer molecules. Due to the lack of affinity, these Affimer molecules were not further pursued.

Antibodies which recognise sites on both group 1 and group 2 HA subtypes are extremely rare, though examples have been reported, sparking hopes for a 'universal' influenza treatment (326,327). Therefore, the ability of A5 and A31 could neutralise a range of IAV strains. Both Affimers were shown

to potently neutralise both A/Aichi/1968/H3N2 and A/Udorn/307/1972/H3N2 viruses. Furthermore, both showed potency against A/England/195/09/H1N1. Though some broad neutralisation is seen with these Affimer molecules, complete H3N2 or H1N1 subtype coverage was not observed. Specifically, both A5 and A31 showed limited or no inhibition when assessed against modern H3N2 strains (A/Brisbane/10/2007 and A/Victoria/361/2011) and dated H1N1 strains (A/WSN/1933 and A/Puerto Rico/8/1934). This trend is observed in broadly neutralising antibodies, in which the large footprint of the antibody is susceptible to mutations in the antigenic sites surrounding the RBS (**Figure 4.7b,c** (221)), suggesting Affimer variable loops interact with non-conserved residues. Additionally, the number of N-glycosylation sites in H3N2 HA domains has increased in the past years (221), likely further restricting broad inner subtype coverage. Surprisingly, A5 and A31 showed considerable potency against the H1N1 2009 pandemic strain, even though little-no inhibition was seen against more recent circulating H3 strains. Neutralisation across HA groups is extremely rare, though some cases have been illustrated such as C05, which shows H1 and H3 neutralisation, through binding with a single HCDR3 loop, though this mAb does not neutralise extensive inner subtype strains. With this in mind A5 and A31 may interact in a similar manner, binding to residues or unique regions of HA, which are conserved across specific strains such as A/Aichi/1968/H3N2 and A/England/195/09/H1N1 (168).

A better understanding of the interaction of A31 with HA was achieved through the cryo-EM of the HA-A31 complex. Though at the time of writing, the complex was not resolved to a resolution that provides insight as to the precise HA amino acids A31 interacts with, it is clear A31 binds to the head domain of HA, close to the RBS. Most interestingly the globular head domains of HA were locked in a dilated form when in complex with A31 (**Figure 4.13d+ 4.14a**). ‘Breathing’ of the HA trimer has been reported in recent literature (**Figure 4.18**) (144,328). In 2019, four papers were published, identifying a novel epitope at the trimer interface of HA1, which may be hidden within the ‘closed’ state of HA, but accessible upon ‘breathing’ or ‘open’ state of HA (329–332). The dilation of the globular domains of HA enable access of these antibodies to these otherwise sterically blocked epitopes. A further mechanism of action may have been identified using A5, in which HA was shown to aggregate upon addition, potentially causing the aggregation of whole virus (**Figure 4.9b**). Whilst Affimer molecules are supposed to be monomers, multimers have been described. In this case this may be advantageous, as the aggregation may aid to A5 potency. Furthermore, linking antibody mimics is possible (215), linking two different Affimer molecules could increase neutralisation, whilst also reducing escape mutants.

Utilising the variable loop regions of my A5 homology model, Alex Flynn was able to carry out computer-based compound screening for potential anti-influenza drugs. This technique has been increasingly used to identify molecules which mimic the CDR-interacting loops of broadly neutralising antibodies with promising success (186,314). One such approach identified a small binding protein with a cystatin scaffold, the hallmark of Affimer molecules, which bound directly to the RBS, mimicking the activity of broadly neutralising C05 monoclonal antibody (333,334). Of the 1.2 million molecules screened, 8 compounds were selected based on properties of the A5 loops. 1 of these compounds (OA3) showed promise for development of an anti-influenza drug. Whilst the potency of this compound was low in comparison to A5, potency improvement alongside pharmacological requirements can be improved through structural analogues, improving functional groups away from the key scaffold. Highlighting, the potential of Affimer molecules as templates for rational drug design, in this case identifying small anti-influenza molecules.

In summary, Affimer molecules have been shown to have high affinity, along with broad neutralisation against the IAV strain they were raised against, and some neutralisation of other IAV strains. The selected Affimers achieve viral inhibition through blocking of the RBS; specifically, A31 locks HA in a dilated conformation, possibly owing to some of its potency. Though Affimer molecules have not been fully investigated for therapeutic purposes, the small size, high stability, solubility and rapid tissue penetration make them highly attractive candidates (237,335). Further still, the variable loops can be used to intelligently design small molecules which build upon therapeutic requirements for drug delivery.

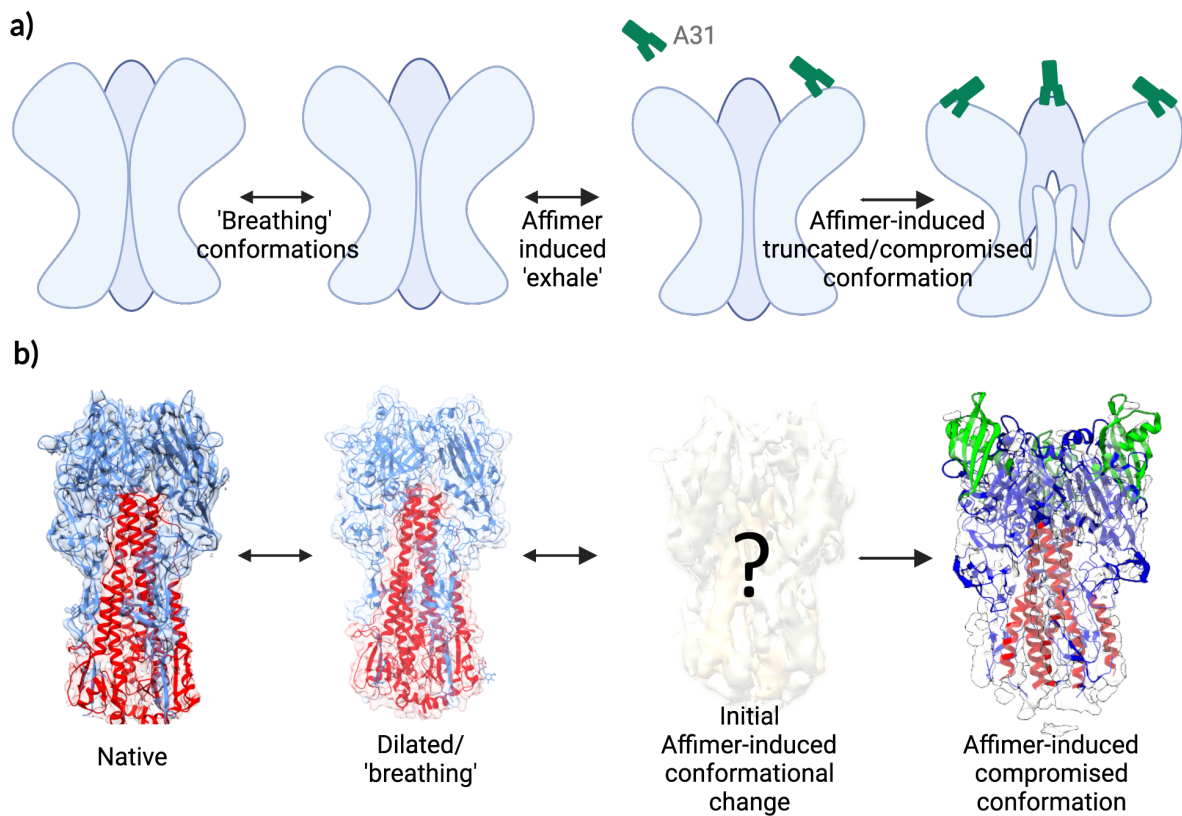


Figure 4.18: Schematic showing the potential mechanism in which A31 alters HA structure

a) Schematic of the interchangeable dilation of HA globular head, upon initial Affimer binding, dilation is exaggerated allowing multiple Affimers to bind the partly concealed epitope, locking HA in a dilated state. **b)** David Klebl's native and dilated HA maps fitted with atomic models (PDB: 6Y5H, 6Y5I) and the HA-A31 complex map fitted with atomic models (PDB:6Y5J and 4N6T). Created with BioRender.com

Chapter 5
Targeting K⁺ ion channels as therapeutic targets for IAV
infections

5.1 Introduction

Most enveloped viruses enter cells via the endocytic pathway (336). This intracellular system is a complex network of membrane compartments that facilitates and regulates the uptake of molecules, whilst also degrading and recycling various cellular cargoes and membrane proteins (145). Following endocytosis (i.e., receptor-mediated endocytosis or micropinocytosis), extracellular cargo is transported to early endosomes, late endosomes, and eventually lysosomes. Within this system, as endosomes mature, a complex transition of pH and ionic molecules is regulated via a series of endosomal ion channels. These endosomal ion channels, amongst the other known ion channels distributed along the plasma membrane of cells and membranes of organelles, play a pivotal role in the regulation of cells. For example, dysfunction of these channels often results in channelopathies which have detrimental consequences for both the cells and the organism (241). As such, ~18 % of all FDA approved small-molecule drugs target ion channels for therapeutic activity, highlighting the importance of regulating ionic composition (337). Influenza viruses, alongside many other viruses, encode viral ion channels coined 'viroporins', which regulate the ionic balance within virions. This highlights the significance of ions not only for cellular homeostasis but also during viral infections (72,338,339). Viruses have successfully been targeted via inhibition of the viroporins; for example, IAV inhibition has been achieved through the inhibition of the M2 viroporin by adamantanes (78,79). This has led to variety of research aiming to unravel the complex regulation of ions in viral infection and the requirement or dependency of these viruses on ion channels expressed by the organisms cells.

IAV infection is well-known to occur through the internalisation of virions via both clathrin-mediated and clathrin independent endocytosis (136,340,341). Virions are transported via the endocytic pathway to LEs (42) where exposure to an acidic environment (<pH 5.5) induces a conformational change in the viral HA. This allows the fusion of endosomal and viral membranes and subsequently the release of the vRNPs into the cytosol of the organisms cell (42). Prior to the HA conformational change, a decrease in the endosomal pH activates the M2 viroporin which facilitates proton (H^+) influx into virions and enables disassembly of the IAV M1 matrix layer (sometimes referred to as the viral core), by relinquishing the association of M1 with vRNPs (42). Blocking this viral channel does not prevent fusion occurring, but the uncoating and release of the vRNPs is halted, as demonstrated by the attenuation of mutants lacking this channel in both tissue culture and animal studies (42,78,79). Although the M2 channel is selective for protons, it has more recently been shown to conduct the cations Na^+ and K^+ into virions, albeit with far less selectivity than for H^+ (in the range of 10^5 - 10^6 fold lower affinity) (342,343). Recent work has utilised priming of IAV virions with mildly acidic conditions +/- Na^+ or +/- K^+ , alongside the facilitation of western blots to probe for the presence of viral proteins

in viral pellets; from these findings, it was predicted that M1 layer uncoating occurs in two steps, facilitated by the M2 viroporin. First, a mildly acidic pH (<6.5) induces a conformational change in the linker sequence of the C-terminal domain of M1, weakening M1 interactions with the vRNPs. A lower pH (< pH 6.0) and the presence of K⁺ ions subsequently induce additional changes in the M1 layer, alongside a further loss of stability in the vRNP bundle. This work suggests that the switch from Na⁺ to K⁺ in maturing endosomes, alongside lowering of the pH, are required to efficiently prime and disassemble viral cores for efficient infection in the organism cell (76).

The complexity of viral infections and the need for ions to successfully carry out these infections is only beginning to be appreciated. Whilst viruses can be targeted directly via their respective viroporins, resistance to these drugs is easily attained (reviewed in (72)). However, the dependency on organism cell ion channels to deliver endolysosomal ions could provide an alternative method of reducing infection and limiting resistance, allowing for a new wave of potential therapeutics to be investigated. Further to the necessity of K⁺ ions in IAV infection, K⁺ channels have been implicated in the entry process of other RNA viruses. K⁺ involvement in viral entry for the bunyaviruses, Bunyamwera virus (BUNV) and HAZV, has been well characterised. Utilising known K⁺ channel inhibitors, it has been shown that blocking the K_{2p} inhibits the early-stages of BUNV lifecycle (344). Subsequently, BUNV virion priming using both acidic pH (6.3) and a high K⁺ ion concentration (mimicking conditions in LEs), alongside work utilising fluorescent microscopy techniques revealed pH and K⁺ are crucial biochemical cues for efficient endosomal escape (271). Work carried out with HAZV similarly revealed a dependency for a high K⁺ concentration during entry. In this instance it was illustrated through cryo-ET that the glycoprotein spikes of HAZV require K⁺ ions to induce a conformational change in these spikes, which enabled interactions with co-purified membranes to occur (345). It is worth noting that bunyaviruses do not encode any known viroporins, so in this case K⁺ must have an effect on the viral glycoproteins, rather than in the interior of the virus. Human immunodeficiency virus (HIV) infection has also been inhibited through blocking organism K⁺ channels with either ifenprodil or the broad spectrum inhibitor TEA (346). This pharmacological study identified distinct K⁺ channels, which when inhibited, reduced HIV infection, these including members of the K_{ir}, G protein coupled (GIRK) and K_{ATP} which play a role in HIV entry. The need for an influx of K⁺ ions into endosomes is not limited to RNA viruses. It was recently shown that K⁺ and Ca²⁺ channels are required during Merkel cell polyomavirus (MCPyV, the causative agent of Merkel cell carcinoma) infection, by again utilising ion channel modulators, which targeted either K⁺ or Ca²⁺ channels, ultimately disrupting the regulation of these ions within endosomes (347). The specific role of K⁺ channels in MCPyV entry

into cells was also determined using the inhibitor dalfampridine, which targets K_v through high-throughput fluorescence-based detection assays .

Current treatments approved for IAV infection are directly targeting. As previously discussed, these direct-acting therapeutics quickly lose potency due to viral mutations. An indirect method of reducing IAV infection through host cell modulation is a highly attractive alternative which could be used in combination with other treatments. Indeed, ion channel inhibitors which are already FDA approved have been re-purposed and shown to significantly reduce virus infection. The plethora of evidence demonstrating the importance of host cell ion channels in viral entry, particularly K^+ channels for the viruses BUNV, HAZV, HIV and MCPyV, emphasises this shared host cell factor can be manipulated to inhibit viral infections. Furthermore, work carried out by Stauffer *et al.*, highlights the mechanical importance of K^+ ions in disassembly of the M1 layer for efficient uncoating and the release of vRNPs into the cytosol (76). Although a direct link was not made to endosomal K^+ channels, it is likely that inhibiting host cell K^+ channels pharmacologically would prevent IAV endosomal escape, similar to that observed for BUNV (271). It was therefore decided to pursue the use of K^+ channel inhibitors as potential therapeutics against IAV. This chapter illustrates work carried out repurposing approved ion channel modulators to reduce infection by a range of IAV strains. Alongside this, cryo-ET has been employed to visualise structural changes that occur to primed viruses, in the hopes to fill the gap between biochemical and structural significance of pH and K^+ and their role in efficient IAV infection.

5.2 Initial probing with K^+ channel inhibitors confirms K^+ plays a significant role in IAV infection

Previous work carried out at the University of Leeds utilised broad spectrum K^+ channel inhibitors including TEA and Qd against -ssRNA viruses (BUNV and HAZV), resulting in the reduction of infection (271,345). To initially assess K^+ channels as potential therapeutic targets for IAV, the effect TEA and Qd had on infection was investigated through a plaque reduction assay. MDCK cells (used for high viral titre production properties) were first incubated with pharmacologically relevant concentrations of either TEA (5-20 mM) or Qd (25-100 μ M), or with infection media (control), for 45 mins (348,349). 50 PFU of IAV (Aichi/1968/H3N2) was then diluted in infection media and added to cells for a further 1 hr. Each drug concentration was maintained throughout infection and an Avicel overlay was added following incubation before cells were left to incubate for 48 hrs. Cells were fixed and stained with crystal violet, and plaque formation was visually assessed (**Figure 5.1b**).

Following visual inspection of plaques (n=3), it was clear that TEA had no effect on IAV viral infection, even at the highest concentration (20 mM); this was further confirmed by quantifying plaques (**Figures 5.1a and b**). Qd however, showed inhibition of IAV in a concentration-dependant manner. Inhibition of IAV can be observed at both 50 μ M and 100 μ M with both concentrations reducing plaque numbers to an average number of 38 and 22 plaques respectively and P values of 0.006 and < 0.001 respectively (**Figure 5.1a**). Furthermore, the size of most plaques at 100 μ M are noticeably smaller, suggesting attenuated infection when Qd is present.

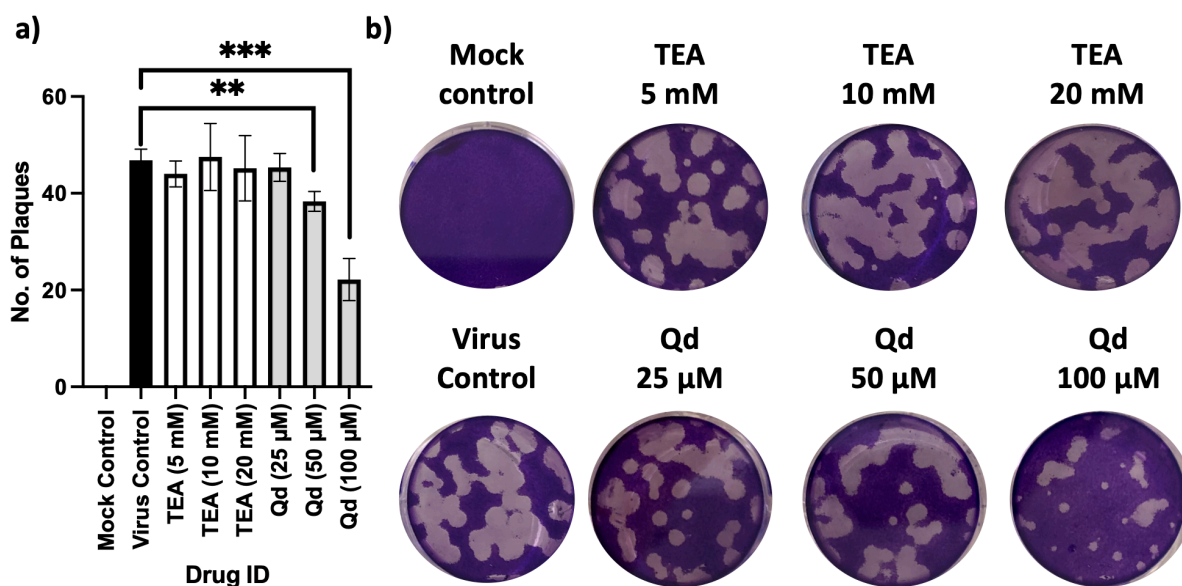


Figure 5.1: Initial assessment shows quinidine inhibits IAV plaque formation

MDCK cells were pre-treated with a concentration range of either TEA or Qd prior to infection with 50 PFU of IAV (Aichi/1968/H3N2) diluted in infection media. Avicel overlay was then added and cells left to incubate, before cells were fixed and stained, and plaques were visually observed. **a)** Graph quantifying the number of visible plaques from n=3 experiments. Bars indicate standard deviation and p values determined via one-way ANOVA against virus control (** P<0.05, *** P<0.005). **b)** Representative images of plaque assay for each condition described.

5.3 Selection of channel modulators based on previously published RNAi knockout studies

Following the initial work carried out with TEA and Qd against IAV, the role of K⁺ channels and the potential for targeting these channels for therapeutics was further explored. A MetaOMICS paper, combining 8 independent RNA interference studies, and characterising the effect of these on IAV infection was published by Tripathi *et al.*, (350), and used here to identify additional K⁺ channels potentially required for IAV replication (350). Utilising this data, these channels were then taken forward to investigate potential therapeutics already available that could be more potent than Qd. The number of standard deviations from the mean (Z_RSA score) from these studies, is used to indicate the impact of the knocked down proteins on IAV infection, the more negative the score the greater the role the protein has. First, the webservice 'DrugBank' (351), was used to identify any channel proteins that Qd targets and the most negative Z_RSA score of these channels was used as a baseline for further therapeutic identification (-0.824)(**Table 5.1a**). All K⁺ channel proteins previously identified with a Z_RSA score of -0.824 or lower were then collated and DrugBank was again utilised to identify any currently available therapeutics which target these proteins (**Table 5.1b**).

The potassium channel K_{2p}6.1, was the highest Z_RSA scoring gene (-0.824) that was targeted by Qd. Qd is a broad-spectrum K⁺ channel inhibitor with activity against a number of channels, including: KCNK7 a two-pore potassium channel (Z_RSA score: -1.202), KCNH2 a voltage-gated channel (Z_RSA score: -1.375) and the two-pore potassium channel KCNK17 (Z_RSA score: -1.781). Therefore, the potency of Qd against IAV (and other viruses) may be due to targeting one of these specific proteins or the combination of multiple channel proteins. The voltage-gated K⁺ channel K_v4.3 exhibited the most negative Z_RSA score (-2.457), suggesting this channel has the most impact on IAV infection amongst all K⁺ channels.

Utilising this data, dalfampridine, ibutilide, miconazole and Qd were identified as FDA-approved and available drugs which targeted many of the channels which featured in the collated table (**Table 5.1b**). Further drugs (quinine, TEA, amiloride, barium chloride (BaCl₂), maurotoxin, KCl) were selected based on the drug target (K channel protein). The resulting selected drug panel displays a good coverage of a range of different K⁺ ion channels (**Figure 5.2a**), providing insight into the role of these channels in endocytosis and how this influences IAV infection.

a)

Gene no.	Gene	Protein encoded	Z_RSA
89822	KCNK17	(K2p17.1) potassium channel, subfamily K, member 17	-1.781
3746	KCNH2	(Kv11.1) potassium voltage-gated channel, subfamily H (eag-related), member 2	-1.375
3767	KCTD7	potassium channel tetramerization domain containing 7	-1.292
65987	KCNK6	(K2p6.1) potassium channel, subfamily K, member 6	-0.824

b)

Gene no	Gene	Protein encoded	Z_RSA	Protein targetting drugs
3752	KCND3	(Kv4.3) Voltage-gated channel, Shal-related subfamily, member 3	-2.457	Dalfampridine , Nifedipine, Vernakalant, Disopyramide
3764	KCNJ8	(Kir6.1) Inwardly-rectifying channel, subfamily J, member 8	-2.332	Levosimendan, Thiomyal, Phenformin, Glisoxepide, Gliquidone
56888	KCMF1	Channel modulatory factor 1	-1.902	
130535	KCTD18	Channel tetramerization domain containing 18	-1.788	
89822	KCNK17	(K2P17.1) Channel, subfamily K, member 17	-1.781	Quinidine, Dalfampridine, Ibutilide
3746	KCNC1	(KV3.1, KV4, NGK2, EPM7) voltage-gated channel, SR subfamily, member 1	-1.604	Dalfampridine
3767	KCNJ11	(Kir6.2) Inwardly-rectifying channel, subfamily J, member 11	-1.539	Ibutilide , Glimepiride, Verapamil, Thiomyal, Isavuconazole
65987	KCTD14	Channel tetramerization domain containing 14	-1.536	
3757	KCNH2	(Kv11.1) Voltage-gated channel, subfamily H (eag-related), member 2	-1.375	Quinidine, Dalfampridine, Ibutilide
3787	KCNS1	Voltage-gated channel, delayed-rectifier, subfamily S, member 1	-1.365	Dalfampridine
3781	KCN22	KCa2.2) Intermediate conductance Ca ²⁺ -activated channel, subfamily N, member	-1.333	Miconazole
27094	KCNMB3	Large conductance calcium-activated channel, subfamily M beta member 3	-1.322	Miconazole, Trimebutine, Procaine
283219	KCTD21	Channel tetramerization domain containing 21	-1.299	
154881	KCTD7	Channel tetramerization domain containing 7	-1.292	
10089	KCNK7	(K2P7.1) Channel, subfamily K, member 7	-1.202	Quinidine, Ibutilide
3760	KCNJ3	(Kir3.1) Inwardly-rectifying channel, subfamily J, member 3	-1.193	
3761	KCNJ4	(Kir2.3) Inwardly-rectifying channel, subfamily J, member 4	-1.095	Carvedilol
54207	KCNK10	(K2P10.1) Channel, subfamily K, member 10	-1.077	
50801	KCNK4	(K2p4.1, TRAAK, TRAAK1) Channel, subfamily K, member 4	-1.068	
3773	KCNJ16	(Kir5.1) Inwardly-rectifying channel, subfamily J, member 16	-1.053	
3742	KCNA6	(Kv1.6) Voltage-gated channel, shaker-related subfamily, member 6	-1.039	Dalfampridine
3758	KCNJ1	(Kir1.1) Inwardly-rectifying channel, subfamily J, member 1	-1.019	Glimepiride, Acetohexamide, Tolbutamide, Glycodiazine
51133	KCTD3	Channel tetramerization domain containing 3	-0.896	
83892	KCTD10	Channel tetramerization domain containing 10	-0.883	
57528	KCTD16	Channel tetramerization domain containing 16	-0.878	
9424	KCNK6	(K2P6.1) Channel, subfamily K, member 6	-0.824	Quinidine, Ibutilide

Table 5.1: Top K⁺ channels implicated in IAV infection, along with known ion channel modulators

Z_RSA score from the meta-OMICs study is used to indicate the impact of the knocked down proteins on IAV infection, the more negative the score the greater the role the protein has (350). **a)** K channel proteins from of IAV infection which Qd targets. The least impactful Qd targetting K channel in IAV infection (K2P6.1, Z_RSA score 0.824), was used as a baseline for selection of other broad spectrum K channel modulators. **b)** Therapeutic ion channel modulators which target respective K channels, were acquired using DrugBank (351). Bold=Protein name or selected drugs. Red=lowest scoring Qd targetting channel protein.

5.4 K⁺ channel modulators reduce IAV (H3N2 A/Aichi/1968) infectivity in A549 cells

To assess the drug panels capacity to inhibit infection, cytotoxicity assays were carried out to identify the highest viable concentration of each drug. A549 cells were treated with serial dilutions of each drug, alongside a no-drug negative control, for 72 hrs and then ATPlite cell viability assays were performed (260). All drugs were found to be tolerable (>95 % cell viability in A549 cells) between low μM and low mM concentrations (**Figure 5.2b and c**), therefore all drugs were carried forward to assess the inhibitory effects on IAV (H3N2 A/Aichi/1968) infection.

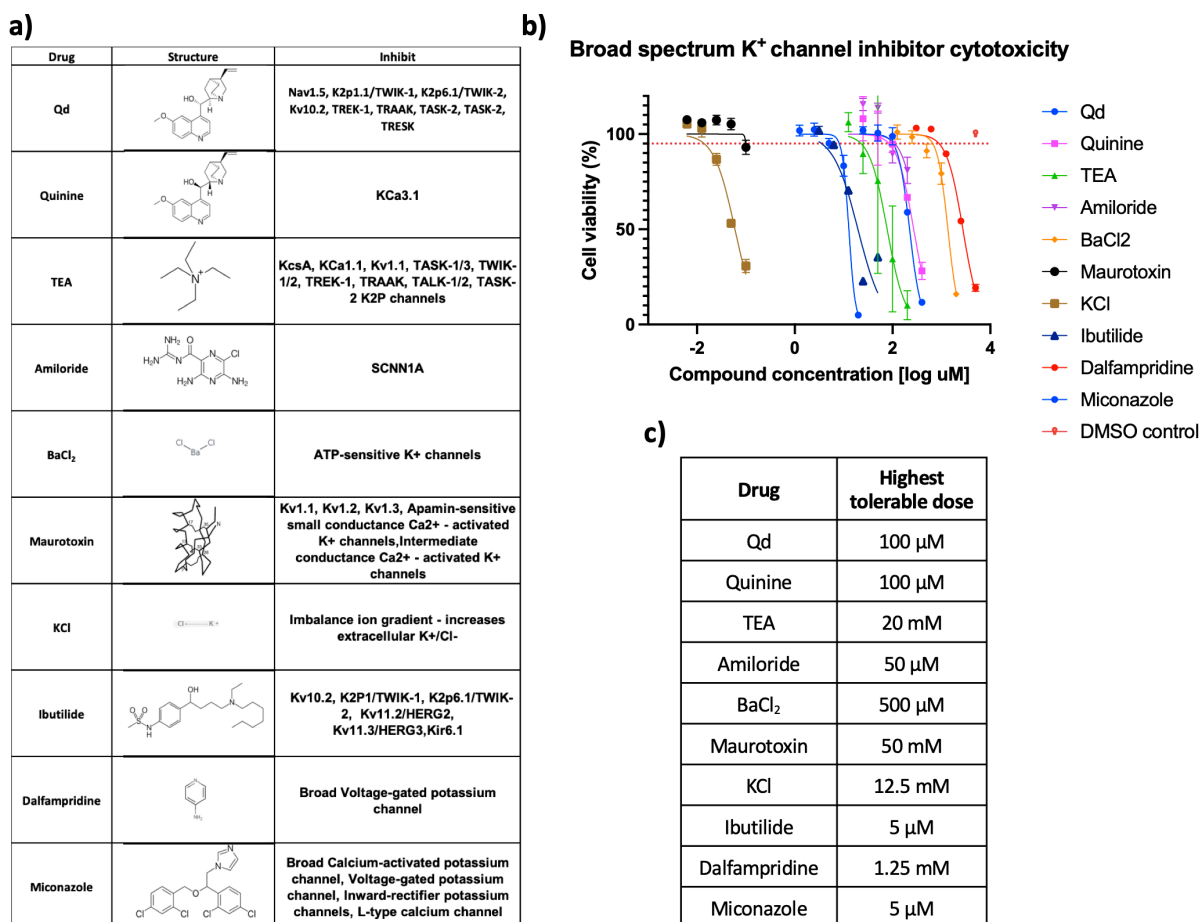


Figure 5.2: A panel of K⁺ channel inhibitors can be utilised in A549s at non-cytotoxic doses

a) Table showing selected channel modulator, structure, along with some of the known K channels inhibited (351). **b)** ATPlite cell viability assay (260). A 1 in 2 dilution range for each drug was carried out alongside a negative control (n=3). Red dotted line indicates the cut-off for acceptable drug concentrations for further work, error bars show standard deviation of repeats. **c)** Table summarising the maximum acceptable concentration of each channel modulator (cell viability of > 95 %), as determined in **b**.

In order to evaluate the ability of K⁺ channel modulators to inhibit IAV infection, the model viral strain X-31 (A/Aichi/1968/H3N2) was initially used. Inhibitors were diluted to the highest non-cytotoxic concentration (**Figure 5.2c**), and assessed for IAV infection inhibition in A549 cells. Drugs or infection media (virus only or mock control) were first incubated with A549 cells for 45 mins to pre-load the cells with drug. Following incubation, IAV was added at a MOI of 0.05 to cells and incubated for 18 hrs

before lysing cells. The effects on IAV infection were then assessed by western blot of cell lysates against IAV-NP (**Figure 5.3a and b**). IAV-NP band intensity was quantified by densitometry, normalised to the GAPDH loading control and then to the virus only control (**Figure 5.3c**).

Following three biological repeats, all K⁺ channel modulators exhibited a reduction in IAV-NP expression, with the exception of quinine and amiloride. Drugs which elicited a statistically significant reduction of IAV-NP expression were Qd, KCl, ibutilide, dalfampridine and miconazole, which resulted in ~63 %, ~65 %, ~64 %, ~28 % and ~44 % IAV-NP expression, respectively, when compared to the virus-only control. Qd showed a reduction in infection similar to that seen in MDCK cells, with IAV-NP expression averaging ~67 % of the virus only control. Overall, the use of K⁺ channel inhibitors appeared to be viable for the reduction of IAV (A/Aichi/1968/H3N2), confirming previous findings of K⁺ influence on IAV infection (42).

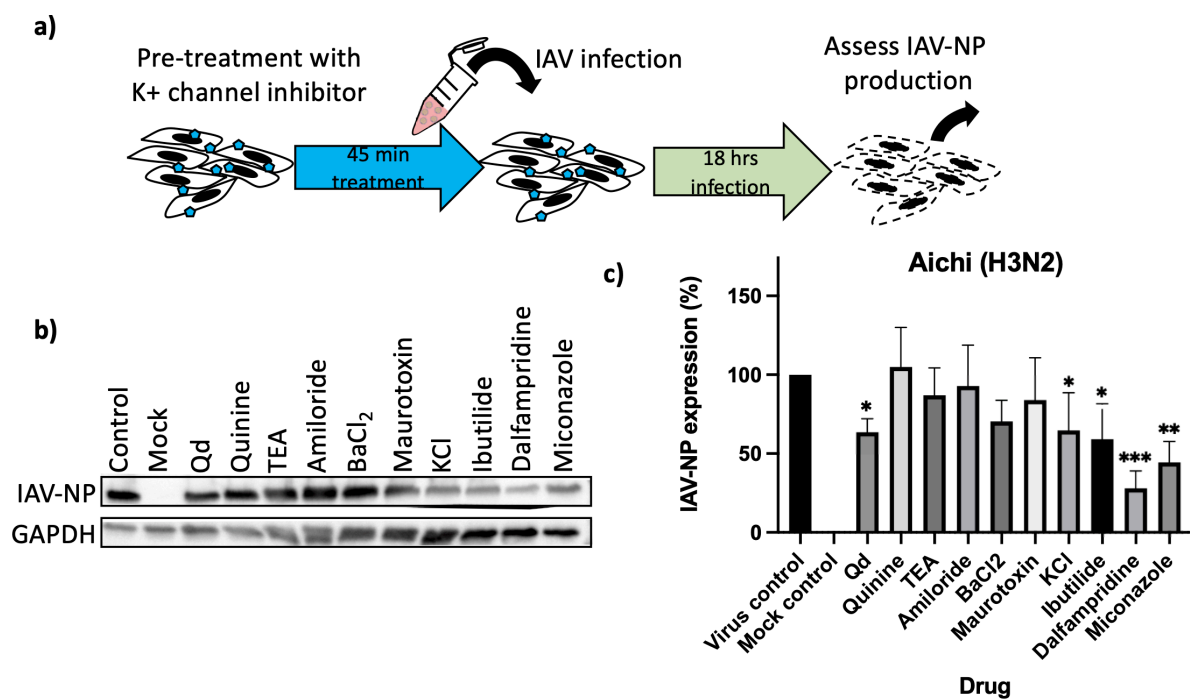


Figure 5.3: K⁺ channel modulators inhibit IAV (A/Aichi/1968/H3N2) infection when challenged in A549 cells

a) Schematic showing experimental procedure. A549 cells were preincubated (45 min) with drugs, or infection media (virus control or mock control). Following incubation, IAV was added at a MOI of 0.05 to cells in the presence of the drugs, and incubated before cells were lysed. **b)** Cell lysates were probed for IAV-NP and GAPDH by western blot (n=3). **c)** Densitometry was utilized to quantify

inhibition, first by normalising with the loading control (GAPDH), before mean infection percentage was normalised to the virus control. Bars indicate standard deviation and p values determined via one-way ANOVA against virus control (* P <0.033, ** P <0.0022, *** P <0.001).

5.5 K⁺ channel modulators inhibit infection of multiple IAV strains in A549 cells

Following the success of the broad-spectrum K⁺ channel inhibitors against IAV (A/Aichi/1968/H3N2), the scope of these inhibitors was assessed against a range of H1N1 and H3N2 strains (A/WSN/1933/H1N1, A/Udorn/307/1972/H3N2, and A/Victoria/361/2011/H3N2). Universal activity would suggest the necessity for K⁺ is an evolutionary requirement and would overcome issues with directly acting treatments which often lack cross subtype effectivity. A549 cells were pre-treated with K⁺ inhibitors, and following this infected with different IAV strains as described above, and infection inhibition was analysed by western blot against NP (**Figure 5.4**).

Further confirmation of the effectiveness of K⁺ channel pre-treatment of A549 cells with either Qd and dalfampridine is shown in these results, with A/WSN/1933/H1N1 exhibiting significant reduction in IAV-NP expression of ~39 % and ~28 %, respectively. Quinine also showed significant reduction of WSN infection with an IAV-NP expression of ~61% (n=3) (**Figure 5.4a & b**). A/Udorn/307/1972/H3N2 displayed a significant reduction in IAV-NP expression for Qd, BaCl₂, dalfampridine and miconazole, with reductions of: ~50 %, ~58 %, 34 % and ~53 % respectively (n=3) (**Figure 5.4c & d**). A/Victoria/361/2011/H3N2 showed an extensive reduction in IAV-NP expression for many of the modulators tested (Qd, quinine, amiloride, BaCl₂, dalfampridine and miconazole) (n=1) (**Figure 5.4e & f**). Perhaps surprisingly, ibutilide appears to have limited reduction in infection, when compared to Qd, though they target many similar channel proteins, showing reduction in IAV-NP in only A/Aichi/1968/H3N2 and A/WSN/1933/H1N1 59.1 % and 75.5 % respectively. Interestingly, miconazole shows no inhibition but a slight increase in IAV-NP expression in A/WSN/1933/H1N1 (108 %), whilst pre-treatment in cells infected with H3N2 strains (A/Aichi/1968, A/Udorn/307/1972 and A/Victoria/361/2011) shows a large reduction in IAV-NP (44.3 %, 53.2 % and 10.85 % respectively); perhaps suggesting H1N1 strains require different K channels at various stages of its infectious cycle, lacking channels which are targeted by miconazole. Overall, both quinidine and dalfampridine show great promise, exhibiting comparable reductions in infection when assessed against all strains.

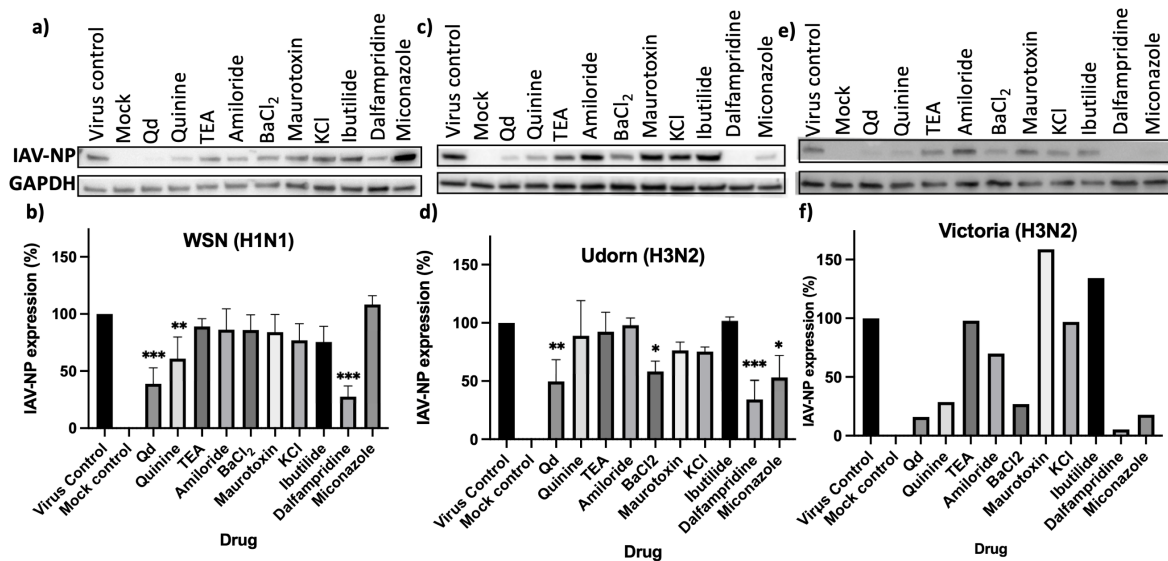


Figure 5.4: K⁺ channel modulators reduce infection across multiple IAV strains

Cells were pre-treated with drugs and infected with virus as described in Figure 5.5a. Infection was assessed by western blot, showing the effects of K⁺ channel drugs on IAV-NP expression after infection by A/WSN/1933/H1N1, A/Udorn/307/1972/H3N2 or A/Victoria/361/2011/H3N2. **a-b)** Western blot analysis of A/WSN/1933/H1N1 and graph showing mean reduction of infection when compared to virus control (n=3). **c-d)** Western blot analysis of A/Udorn/307/1972/H3N2 and graph showing mean reduction of infection when compared to virus control (n=3). **e-f)** Western blot analysis of A/Victoria/361/2011/H3N2 and graph showing mean reduction of infection when compared to virus control (n=1). As in Figure 5.4, densitometry was utilised to determine band intensity. Bars indicate standard deviation and p values determined via one-way ANOVA against virus control (* P < 0.033, ** P < 0.0022, *** P < 0.001).

5.6 Treatment of A549 cells with dalfampridine affects IAV entry via the endocytic pathway

In order to better understand the mechanism in which K⁺ channels play a role in IAV infection and to confirm its influence on early infection, a time course utilising the best K⁺ channel inhibitor, dalfampridine, was carried out. Cells were infected at a MOI of 0.05 with ice-cold IAV (A/Aichi/1968/H3N2) at 4 °C to synchronise entry and infection. Virus inoculum was replaced with infection media, then the drugs NH₄Cl (10 mM) or Dalfampridine (1.25 mM) were added at increasing post-infection time points, ranging from 0 to 240 mpi. All conditions were then lysed with RIPA buffer at 18 hpi and cell lysates were assessed via western blot for IAV-NP expression (**Figure 5.5a and b**).

Densitometry analysis was carried out and IAV-NP bands were normalised against GAPDH as previously (**Figure 5.5c and d**).

Consistent with the literature NH_4Cl , a lysomotropic agent known to neutralise the pH of intracellular endo-lysosomes, completely inhibits IAV infection when present at early timepoints post-infection (352). Inhibition begins to reduce at 60 mpi, with a complete loss of inhibition by 120 mpi. Following endocytosis, HA fusion of viral and cellular membranes is known to occur after ~ 1 hour (352,353), this is concurrent with data where the neutralisation of endo-lysosomal pH using NH_4Cl is less effective at inhibiting IAV entry >60 mpi (352). Further to this, dalfampridine shows a similar profile, in which IAV-NP expression is reduced substantially until 60 mpi, after which point (120 and 240 mpi) K^+ channel inhibition using dalfampridine is increasingly less effective at inhibiting IAV and is completely lost by 240 mpi. This matching timeframe suggests that the inhibition of K^+ channels influences IAV infection during endocytic trafficking.

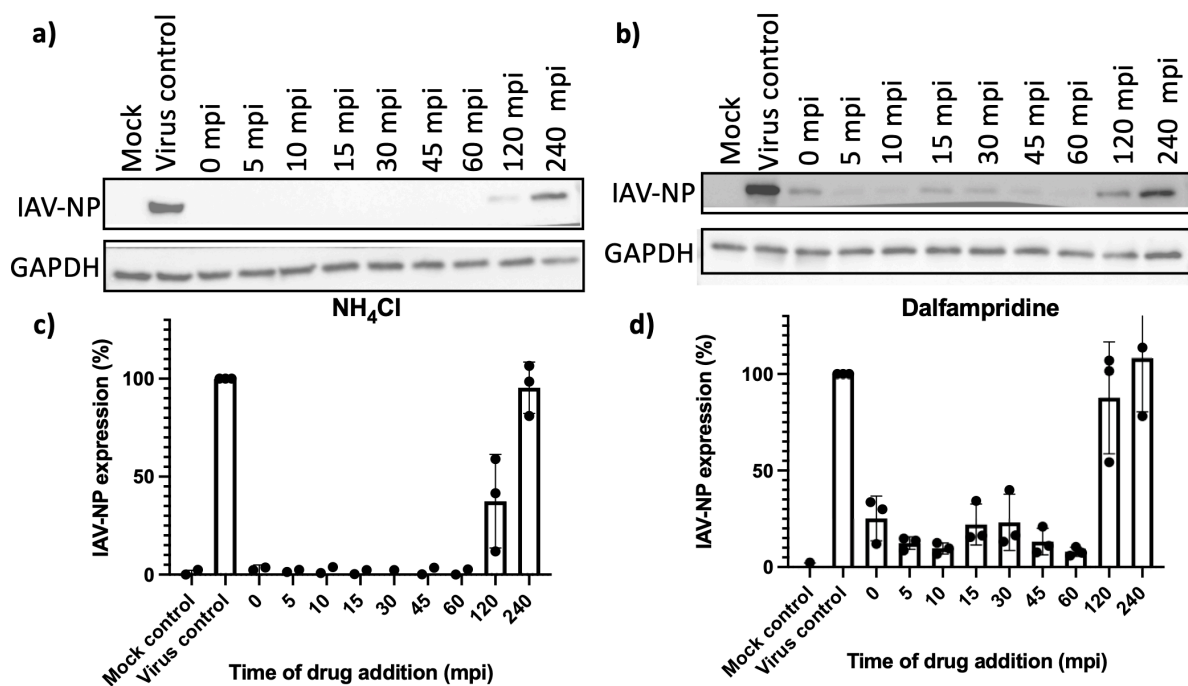


Figure 5.5: Time of addition assay to define the mode of IAV inhibition by dalfampridine

A549 cells were infected with ice cold IAV (A/Aichi/1968/H3N2), allowed to sync before treating with either NH_4Cl or dalfampridine at various timepoints. As in Figure 5.+5., infection was assessed by western blot. **a-b)** Representative western blot of NH_4Cl treated cells and graph. **c-d)** Representative western blot of dalfampridine treated A549 cells. synchronise on A549s. Wells were

replaced with infection media or infection media with the addition of NH_4Cl (10 mM) or dalfampridine (1.25 mM) and incubated. Media was then replaced by either NH_4Cl or Dalfampridine at increasing post-infection time points; 0, 5, 10, 15, 30, 60, 120, 240 mpi; with the infection left to proceed for 18 hpi at which point cells were lysed with RIPA buffer and cell lysates were collected and assessed via WB for IAV-NP expression (n=3). **c-d)** Average infection percentage when compared to virus-only control, utilising densitometry values for the above. As in Figure 5.4 + 5., densitometry was utilised to determine band intensity. Bars indicate standard deviation. As in Figure 5.4, densitometry was utilised to determine band intensity. Bars indicate standard deviation and p values determined via one-way ANOVA against virus control (* P <0.033, ** P <0.0022, *** P <0.001).

5.7 Priming of IAV virions confirms K^+ plays a role in early stages of infection

It is largely accepted that at pH 5.8 or lower, interactions between the vRNPs and the M1 layer are compromised and the interaction between M1-M1 is likely to be weakened (82,354). More recently, it has been suggested that following entry into late endocytic compartments, the increase in K^+ concentration primes the virion via its M2 viroporin and further affects interactions between vRNPs and M1 (76,355). In this instance, work was carried out to confirm that priming of IAV with K^+ has an effect on infection. Priming was carried out using a high concentration of K^+ (KCl, 140 mM), with the aim to replicate the high K^+ environment of the late endosomes, enabling virions to undergo chemical or structural changes induced by this ion, and possibly circumventing inhibition by K^+ channel inhibitors. IAV was primed for 2 hrs in a buffer of pH 5.8 +/- high $[K^+]$; supplemented using 140 mM KCl. 45 mins prior to the end of priming, A549 cells were pre-treated with either quinine, Qd, dalfampridine or infection media (virus control). Following priming, buffers were diluted out and cells were infected with primed IAV or mock control (infection media only). The infection was then left to proceed for 18 hpi at which point cells were lysed with RIPA buffer and cell lysates were collected and assessed via western blot for IAV-NP expression (**Figure 5.6**) (n=1).

The viral control showed a ~2-fold increase when primed with both pH 5.8 and high K^+ as opposed to pH 5.8 priming alone, confirming previously findings that suggest K^+ has a role during IAV entry (76). In this case, K^+ priming appears to enhance infection by ~1.5 – 3 fold that of priming with pH 5.8 alone (76). The expression of IAV-NP when cells were pre-treated with channel inhibitors and infected with pH 5.8 primed virus was consistent with previous results using non-primed virus (**Figure 5.3**), in which quinine shows no inhibition, and Qd and dalfampridine both show significant reduction in IAV-NP expression. This reduction is slightly reduced here (**Figure 5.6c**), which may be due to the effect of priming with mildly acidic pH 5.8, enhancing infection through the priming of the HA spikes. When cells are pre-treated and virus is primed with both pH and K^+ , all samples show enhanced expression of IAV-NP, and K^+ channel inhibitors are no longer effective at inhibiting IAV entry. These findings suggest that priming with both pH and K^+ enhances infection when compared to pH priming alone. Further still, priming with K^+ can enable IAV to bypass inhibition by the ion channel blockers, further validating the importance of K^+ in IAV entry, likely through the enhanced M1 disassembly/disorganisation induced by an increase in H^+ and K^+ .

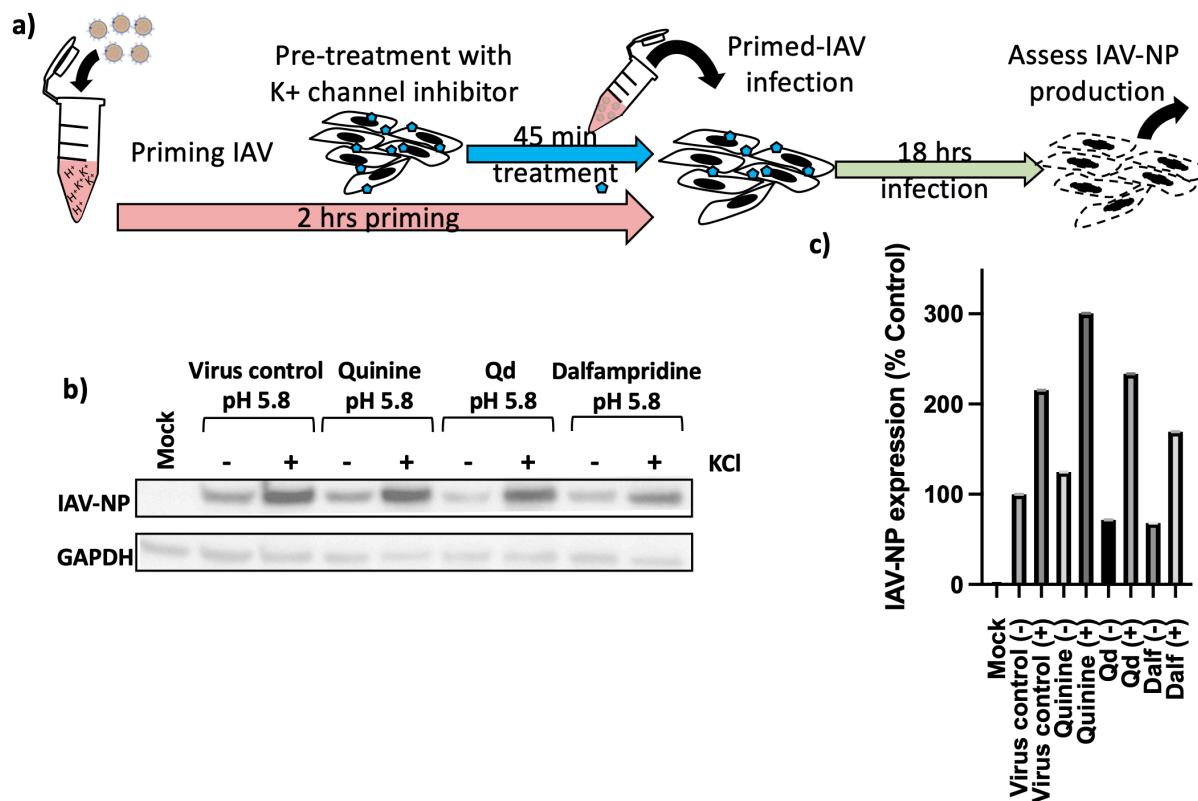


Figure 5.6: Priming IAV virions reduces ion channel modulator inhibition

a) Schematic showing experimental procedure. IAV (A/Aichi/1968/H3N2) was primed for 2 hrs in a buffer of pH 5.8 +/- K⁺ (140 mM KCl). 45 mins prior to the end of priming, A549 cells were pre-treated with either quinine, Qd, dalfampridine or infection media. Priming buffers were then diluted out and cells infected by relevant conditions. As before, cell lysates were assessed by western blot (n=1). **b)** Western blot of primed samples. **c)** Infection percentage when compared to virus-only control, utilising densitometry to determine band intensity.

A possibility for the action of K⁺ channel inhibitors on IAV infection, may be that they act directly on influenza virions. The IAV viroporin M2, conducts ions into virions to enable the destabilisation of the M1 layer and vRNPs, and drugs such as amantadine have been shown to prevent the core uncoating through blocking of the M2 channel (356). In order to confirm ion channel inhibitors were acting on the cells as opposed to virions, IAV was directly treated with quinine Qd, dalfampridine or infection media for 2 hrs. Following priming, drugs were diluted out (as in previous experiments) and A549s were infected with drug-treated IAV, virus only or a mock control (infection media only). The infection left to proceed for 18 hpi. Upon completion, lysates were assessed as previously described (**Figure 5.7a and b**). Densitometry analysis was carried out and IAV-NP band intensity was normalised against

the corresponding GAPDH before being analysed as a percentage of the virus only control (**Figure 5.7c**).

Following analysis of IAV-NP bands ($n=3$), it was found that when the selected K^+ channel inhibitors were added directly to IAV, there was no inhibition of infection. This therefore suggests that the inhibitory effects of K^+ channel modulators observed previously (**Figure 5.3**) were likely due to their effects on cellular K^+ channels not on the virions themselves.

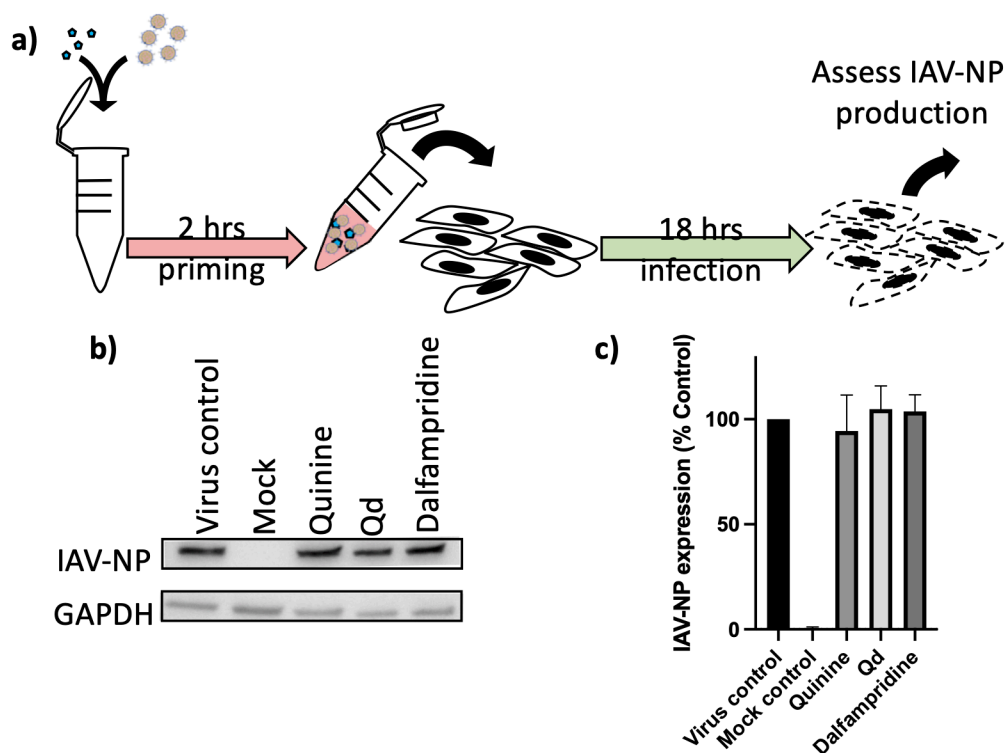


Figure 5.7: Effect of IAV priming with ion channel modulators

a) Schematic showing experimental procedure. IAV (A/Aichi/1968/H3N2) was treated with Qd, quinine, dalfampridine or infection media before cells were infected with drug-treated IAV, virus only or a mock control (infection media only). Following infection, lysates were assessed by western blot as in Figure 5.4 **b)** Western blot probing against IAV-NP and GAPDH. **c)** Densitometry of IAV-NP normalised to GAPDH and normalised to virus-only control as previous ($n=3$). Bars indicate standard deviation and p values determined via one-way ANOVA against virus control (* $P < 0.033$, ** $P < 0.0022$, *** $P < 0.001$).

In order to better understand the importance of K^+ ions and the effect it induces on IAV infection through viral morphological changes, structural work was carried out.

5.8 Priming of influenza virions with K^+ enhances the uncoating of the M1 layer

Previously it has been found that priming with a mildly acidic pH of 5.8 and KCl at a high concentration (140 mM) can cause the dissociation of the viral core more efficiently as opposed to priming with pH 5.8 alone, suggesting K^+ ions have an influence on viral core uncoating (76). Stauffer et al., used an *in vitro* uncoating assay to assess the effect of this priming on M1 and NP content. It was found M1 and NP were dissociated by 40 % and 75 %, respectively (at pH 5.8 + 135 mM KCl), in comparison to 15 % and 20 % respectively (pH 5.8 alone), (76). Here, in order to assess these morphological changes visually, virions were primed with pH 7.4 and pH 5.8, in the presence or absence of 140 mM K^+ (KCl) for 1 hr at 37 °C. In this instance the A/Aichi/1968/H3N2 strain was imaged by cryo-electron tomography. In order to determine priming was successful, a sample of each condition was taken, priming buffers were diluted out and A549s were infected with the different primed virions or a mock control (infection media only). The infection was then left to proceed for 18 hpi, after which cells were lysed and assessed by western blot for IAV-NP expression (**Figure 5.8a**) (n=1). Densitometry analysis was carried out and IAV-NP bands were normalised against GAPDH before being analysed as a percentage of the virus only control (**Figure 5.8b**). Though western blot bands show less apparent differences, the densitometry analysis of the bands revealed priming at a mildly acidic pH of 5.8 showed infection was enhanced by 1.2-fold over priming virions at a neutral pH of 7.4 (**Figure 5.8 a and b**). Whilst priming with mildly acidic pH and in combination with K^+ showed a 1.3-fold increase when compared to the neutral pH 7.4 primed virions. Interestingly when neutral pH 7.4 virions were primed with K^+ , an increase in infection was also observed. These observations remained similar to previously findings (76), though, the magnitude in which priming increased infection was less exaggerated in this case.

Before cryo-grids were made, colloidal gold fiducials were added to each of the undiluted-primed samples (resulting in a 1:1:1 dilution, IAV: buffer: gold (μ l)) and samples were applied to lacey carbon grids before being plunge-frozen in liquid ethane. A data collection series for each of the conditions was collected: pH 7.4, pH 7.4 + K^+ , pH 5.8, pH 5.8 + K^+ . The central slices of tomograms revealed pleomorphic virions, with the majority of the population observed as spherical virions of diameter 80-120 nm, alongside some filamentous virions, consistent with previous findings (357). Upon visual comparison of the different priming conditions, it was apparent that each condition exhibited slightly

different morphologies (**Figure 5.8 d-f**). Most notably, the clustering of virions was extremely prominent in mildly acidic pH 5.8, which was not observed at neutral pH. This is commonly observed when IAV virions are subjected to acidic conditions, in which HA is activated inducing interactions with neighbouring membranes (in this case, other virions) (358). Alongside this clustering, disorganised glycoproteins could be observed on some virions which had been primed with a low pH (pH 5.8) (358). When observing virions which possessed an M1 layer, virions which were primed in the absence of K^+ (both at pH 7.4 or at pH 5.8), showed a greater proportion of M1 layer-containing virions, with ~66 % of the population containing M1 layers. Interestingly, when both datasets which had been primed with K^+ were analysed for M1 layer occupancy, it was found that the percentage of virions with an M1 layer had reduced to ~46 % of the population. These findings are consistent with previous biochemical work, which found priming with K^+ at mildly acidic pH, reduced M1 protein content in pelleted virions, alongside some reduction when priming at neutral pH(76), supporting the role of K^+ ions in the disassembly of the M1 layer, even in the absence of a lowering pH cue.

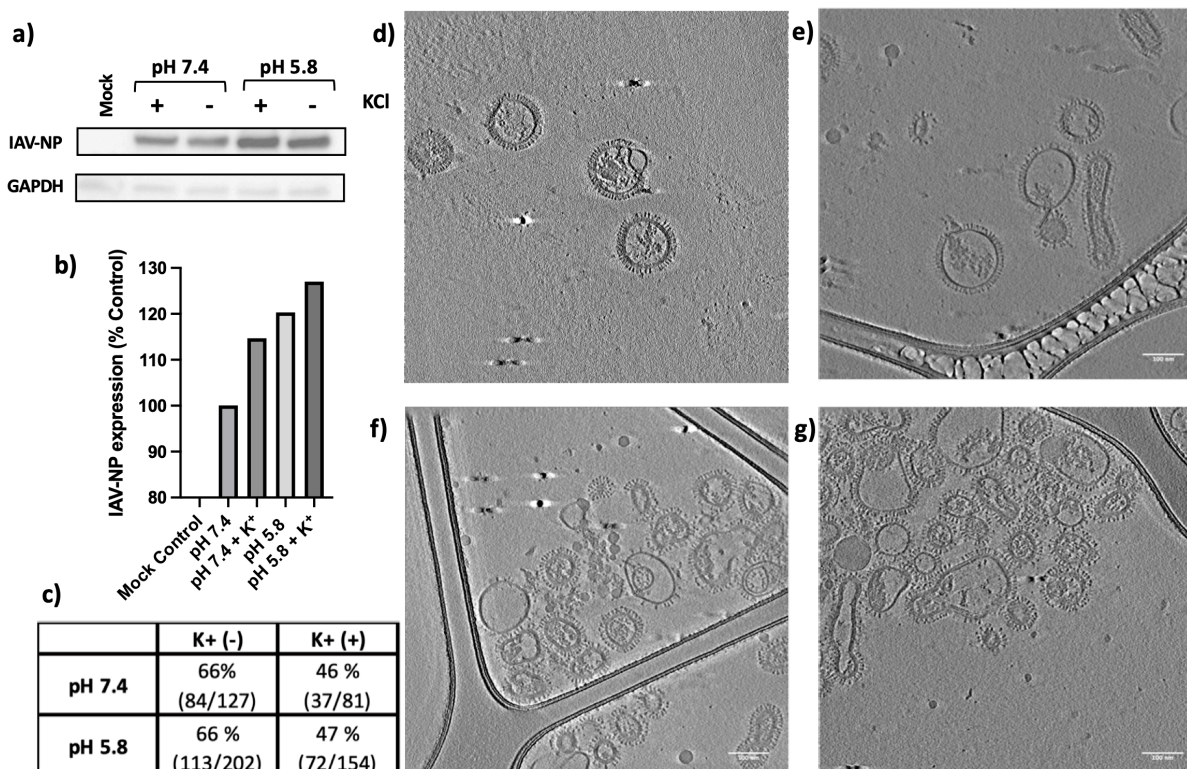


Figure 5.8: The morphological effect of priming IAV virions with mildly acidic pH and/or K^+

IAV virions were primed at pH 7.4 or pH 5.8 \pm K^+ (140 mM KCl) for 1 hr. **a)** Successful priming was determined for a sample of each condition used for cryo-ET by western blotting against IAV-NP and

GAPDH (n=1). **b)** Average infection percentage normalised to neutral pH without priming (pH 7.4 (-)) utilising densitometry values. **c)** Table to show % of virions observed with an M1 layer **d-f)** Samples were loaded onto cryo-EM grids and plunge-frozen. Tomographic tilt series (cryo-ET) were collected for each condition from -60 ° to +60 ° and computationally reconstructed into 3D volumes. **d** = pH 7.4, **e** = pH7.4 + K⁺, **f** = pH 5.8, **g** = pH 5.8 + K⁺. Central slices of a tomogram from each priming data set is shown. Scale bars = 100 nm.

X-31 (A/Aichi/1968/H3N2) virions at neutral pH have been assigned to five morphologically distinct classes previously, in which virions were defined by morphology of the virion, presence/absence of the M1 layer and also the arrangement of RNPs (40). When observing the wildtype virus at neutral pH 7.4, virions could be broken down into further sub-populations (**Figure 5.9**). In this sample set, virions could be classified according to the presence or absence of an M1 layer. These two groupings could then be further distinguished by the presence or absence of RNP bundles packaged inside. ~61 % of the dataset consisted of virions which had a resolved M1 layer. This percentage could be further broken down into a sub-set of ~59 % of the population containing vRNPs alongside an M1 layer, and ~2 % of the dataset were found to be virions which lacked vRNPs but had a M1 layer. Whilst the virions lacking an M1 layer, which constituted ~34 % of the total population, could be divided into ~30 % with vRNPs and ~4 % lacking vRNPs.

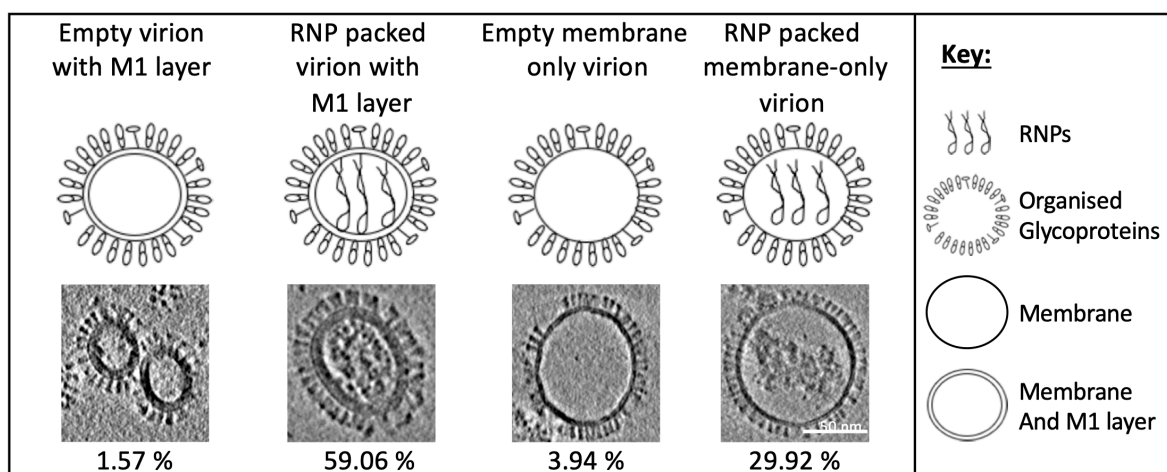


Figure 5.9: Infection population consists of a range of morphologically distinct virions

Morphologically distinct virions identified in the neutral pH 7.4 cryo-ET dataset (as in **Figure 5.8 d**). The percentage of each type of virion of the total population is listed below a central slice of an example virion along with a schematic of each. Scale bar = 50 nm.

5.9 Structural information provides visual insight into virion entry and fusion mechanisms

IAV virions have previously been found to present gaps in the matrix layer, which have been termed as 'molecular fontanels' (40). The molecular fontanels have been conjectured to be the focal point in which virions bud from host cells, and these gaps have been hypothesised to aid in the mechanism of fusion, which requires the membrane/matrix layer to have a level of pliability (40). Here, these molecular fontanels or partial M1 layers can be observed in all priming conditions, though clear differences in the partial M1 layers, both in abundance and appearance can be observed between the different priming conditions (**Figure 5.10**). Of the observed M1 layers in the neutral dataset (pH 7.4), 9 of 69 virions with an M1 layer observed exhibited a partial M1 layer (~13 %) (**Figure 5.10a & b**). Similarly, the observation by Harris *et al.*, showed gaps ranged in size. The most consistent distance of these gaps was ~25 nm, but they extended to ~80 nm in some instances (40). In the K⁺-primed neutral dataset (pH 7.4 + K⁺) the number of partial M1 layers increased, with 17 of 36 virions with an M1 layer observed displaying gaps, making up ~47 % of the population of virions with an M1 layer. The size of the gaps in these M1 layers seemed consistent with virions primed at pH 7.4 alone, though the quantity of gaps per virion appeared to increase when primed with K⁺. 22 of 98 (22%) virions primed with a mildly acidic pH (pH 5.8) containing M1 had partial M1 layers. Once again, the majority of the gaps in the M1 layer were around ~25 nm but could also extended up to ~85 nm. Finally, the virions primed with mildly acidic pH and K⁺ (pH 5.8 + K⁺) showed the largest proportion of M1 layer containing virions with partial membranes, 25 of 46 virions showed gaps (~54%). These gaps appeared to be slightly larger on average at around ~35 nm, with many of these virions displaying multiple gaps and more frequent extended gaps. Of note, some virions from samples primed with K⁺ (both pH 7.4 + K⁺ and pH 5.8 + K⁺) (n=1), appeared to have inconsistent/disorganised M1 layers typically with elongated gaps or multiple gaps in the M1 layer. This might point towards the mechanism of M1 disassembly. The percentages observed here of extended and disorganised M1 layers may be lower than the true percentage, as disorganised vRNPs could be easily misinterpreted as sections of the M1 layer (to avoid overinterpreting the results, partial M1 layers were only counted if the M1 layer was clearly resolved).

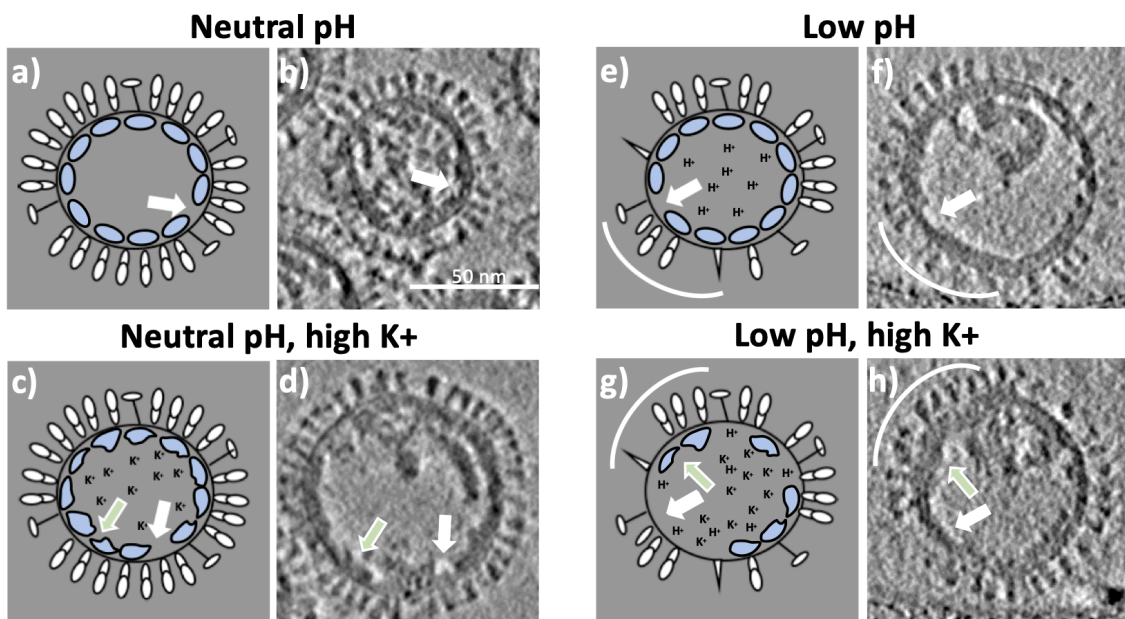


Figure 5.10: Morphological differences seen under different priming conditions

a, b) Schematic representation and example central slice of a virion primed at a neutral pH. **c, d)** As in a-b of a virion primed at a neutral pH + K^+ . **e, f)** As in a-b of a virion primed at a mildly acidic pH. **g, h)** As in a-b of a virion primed at a mildly acidic pH + K^+ . White arrows highlight 'molecular fontanels'. Green arrows highlight disorganised M1. White curved line highlights partially disorganised glycoproteins. Scale bar = 50 nm.

The glycoproteins in neutral pH primed virions appear to be organised and continuous, whilst those primed at mildly acidic pH 5.8 show instances of disorganised glycoproteins (**Figure 5.12d + i**). These disorganised glycoproteins were present in all virions with multiple gaps in the M1 layer and those with disorganised vRNPs.

Findings in the literature suggest a drop in pH initially weakens the interaction between M1 layer and the vRNPs (76). A conformational change in a linker sequence and the C-terminal domain of M1 (which binds interacts with the vRNPs), after exposure to a pH below 6.5 is hypothesised to cause this, followed by a further drop in pH to $<pH 6.0$ and an influx of K^+ ions, which causes further destabilisation of the M1 layer and the loss of stability of the vRNP bundles (76). Data presented here seems to visually agree with findings regarding the M1 layer and vRNP bundle and the dynamic changes which occur upon the lowering of pH and increase in K^+ ions. Virions at a neutral pH, both with and without K^+ priming (**Figure 5.11a, b, c, d, e, f**) exhibit regular vRNP bundles in all virions. Whilst virions at a mildly acidic pH, whether primed with or without K^+ ions, seem to show denser

vRNPs which localise to the inner layer of the virion, suggesting they are destabilised (**Figure 5.11g, h, i, j, k, l**). This appears to agree with Stauffer *et al.*, the vRNPs interaction with the M1 layer is disassembled upon pH values lower than 6.0, causing the RNP bundle to aggregate at the edge of the internal M1 layer/membrane (76). This aggregation can be observed in all virions which contain a vRNP bundle. Of note, the density of these bundles does not appear to be as large as previous cryo-ET work carried out at pH 4.9 (no K⁺ priming was used) (359), perhaps suggesting further aggregation/destabilisation of the bundle occurs at a pH lower than 5.8. Perhaps, though the M1 layer can become destabilised by K⁺ ions, even at a neutral pH, complete destabilisation of the vRNPs requires a pH close to that in which fusion events occur.

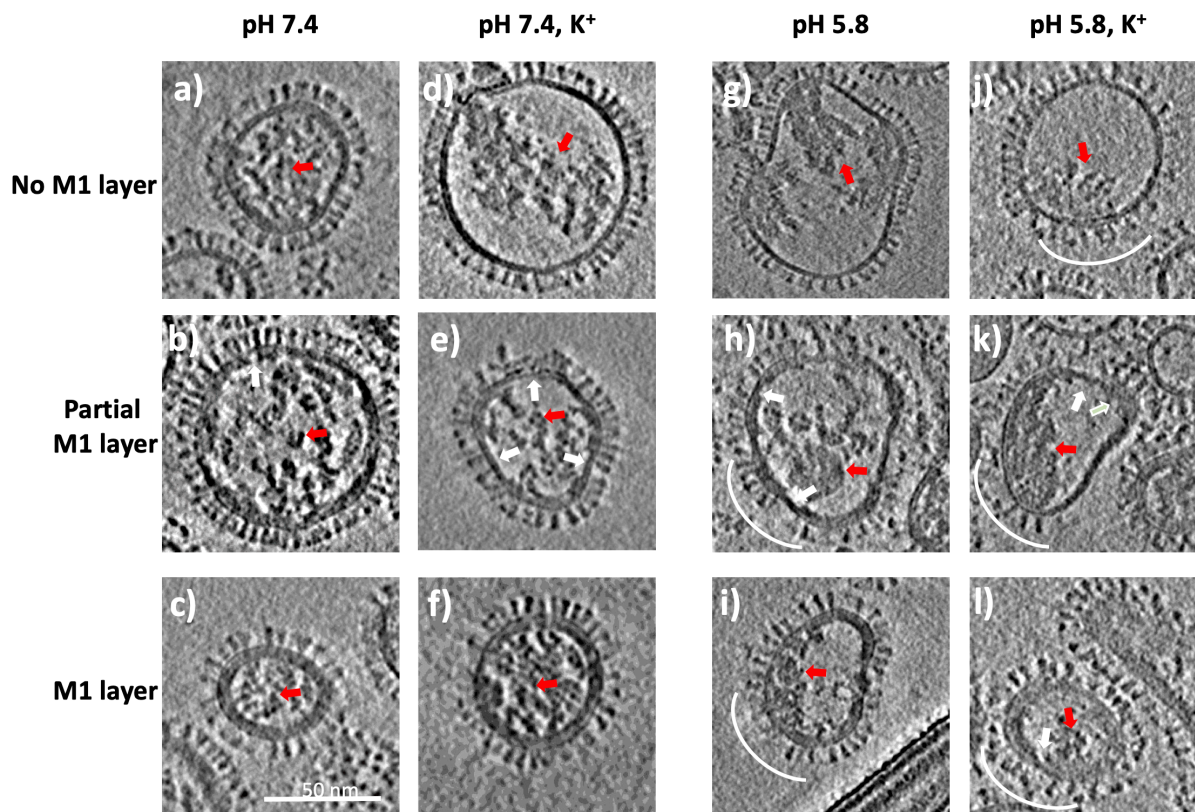


Figure 5.11: Morphological differences seen in the vRNP bundle under different priming conditions

Central sections of influenza virions under different priming conditions. **a-c**, pH 7.4; **d-f**, pH 7.4 with 140 mM K⁺; **g-i**, pH 5.8; **j-l**, pH 5.8 with 140 mM K⁺. **a, d, g, j**) Virions lacking an M1 layer. **b, e, h, k**) Virions under different priming conditions showing ‘molecular fontanelles’. **c, f, i, l**) Virions under different priming conditions showing visible M1 layers. Red arrows highlight vRNP bundles. White

arrows show 'molecular fontanel's'. White curved lines highlight disorganised glycoproteins. Scale bar =50nm.

5.10 Discussion

The evidence that ionic balance plays an important role in virus infection has recently been characterised for many viruses, highlighting cellular ion channels as new targets for viral therapeutic intervention (reviewed in (146)). It has also been determined biochemically that IAV core uncoating requires both a low pH and K^+ priming to efficiently disassemble the M1 layer and release the vRNP bundle during fusion (146). In this chapter the potential for repurposing already clinically-approved K^+ ion channel modulators to reduce IAV infection efficiency was assessed, and cryo-ET was employed to better understand structurally the functional significance of IAV K^+ priming.

Initial work carried out with K^+ channel modulators TEA and Qd showed significant inhibition of IAV in a dose dependant manner when used to pre-treat cells prior to infection, suggesting host cell K^+ regulation plays a crucial role during the IAV life cycle. To better understand the relationship between IAV and host K^+ channels, a meta-OMICs study collating channels identified in multiple RNA interference studies was utilised to select a larger panel of ion channel modulators (350). Channel modulators were selected which targeted multiple channels with a Z_RSA score equal to or more negative than those targeted by Qd (the channel with the lowest Z_RSA score was $K_{2p6.1}$, with a Z_RSA of -0.824). These findings unveiled that K^+ channels play an important role in IAV infection, across all subtypes tested here (**Table 5.2**), with significant reduction in infection caused by dalfampridine, showing infection was decreased to <35 % of the virus-only control in all strains. Dalfampridine is a broad-spectrum inhibitor of voltage-gated K^+ channels (360), including the top scoring channel ($K_v4.3$ with a Z_RSA score of: -2.457; **Table 5.1b**). Qd also shows consistent reduction in infection to <67 % in all strains tested. Qd is a broad inhibitor of a range of channels, and notably also targets two of the K_v channels targeted by dalfampridine. Interestingly, Miconazole showed good potency against all H3N2 strains, though it appeared to have no effect on H1N1 infection. Miconazole non-specifically inhibits a range of potassium channels, including: K_{Ca} , K_v and K_{ir} , perhaps highlighting H1N1 enters via an alternative endocytic route to H3N2, taking advantage of the K^+ influx facilitated by different channels, though further work is required in order to determine which part of IAV lifecycle miconazole effects. Maurotoxin selectively inhibits $K_v1.2$ but also blocks $K_v1.1$ and $K_v1.3$ (361). Maurotoxin did not inhibit IAV, suggesting these K_v channels are not involved in the regulation of K^+ during IAV infection. All strains assessed in this work appear to be significantly affected by K_v channel blockage, this is

confirmed by RNAi studies (Meta-OMICs), suggesting the requirement for K⁺ is widely conserved across all IAV strains, likely largely facilitated by these K_v channels across endosomal membranes. Though more subtypes would need to be assessed, in order to confirm whether this inhibition is universal. Host cell K⁺ channels as a therapeutic for IAV is a promising alternative to directly acting treatments as this potentially enables universal IAV treatment and could also act as an effective combined therapy, reducing further mutations.

Drug	Channel targets	Inhibitory?			
		Aichi	WSN	Udorn	Victoria *
Quinine	Kv1.3, KCa3.1	NS	++	NS	Yes
Qd	Kv11.1, K2P6.1, K2P7.1, K2P17.1,	+	+++	++	Yes
TEA	TASK-1/3, TWIK-1/2, TREK-1, TRAAK, TALK-1/2, TASK-2, K2P	NS	NS	NS	No
Amiloride	ATP sensitive K ⁺ channel inhibitor	NS	NS	NS	Yes
BaCl ₂	Kir inhibitor	NS	NS	+	Yes
Maurotoxin	Kv1.1, Kv1.2, Kv1.3, SKCa	NS	NS	NS	No
KCl	Disruption of K ⁺ gradient	+	NS	NS	No
Ibutilide	Kv11.1, Kir6.2, K2P6.1, K2P7.1	+	NS	NS	No
Dalfampridine	Kv1.6, Kv3.1, Kv4, Kv4.3, Kv9.1, Kv11.1, K2P17.1, NGK2, EPM7	+++	+++	+++	Yes
Miconazole	KCa2.2, BK(Ca)	++	NS	+	Yes

Table 5.2: Summary of drugs used and inhibition of IAV

A summary table to show drugs used, channels they target and inhibition of strains used in this study. (NS P>0.033, + P <0.033, ++ P <0.0022, +++ P <0.001). Victoria* strain was only assessed for n=1.

The inhibition of the host cell K_v channels by dalfampridine was shown to prevent IAV in the early stages of its life cycle (as the drug lost its effectiveness when added >1-2 hrs post infection), suggesting K⁺ has an effect on the IAV early life cycle as it passages through the endocytic pathway. These findings are consistent with the timeline of IAV entry (internalised within 1-2 hrs), and the increase in K⁺ content in maturing endosomes (352,353,355,362). Priming with a mildly acidic pH alone reduced Qd and dalfampridine inhibition slightly, though viral infection was still reduced (**Figure 5.6 b+c**). This desensitisation was perhaps due to the activation of HA with a mild pH, allowing for more efficient fusion (363). Priming with both mild pH and high K⁺ showed not only inhibition circumvention from ion modulators, but a 2-fold increase of IAV infection (**Figure 5.8b**). This further exemplifies the role of K⁺ and agrees with previous findings, in which a 2-fold increase in infection was seen when priming with both K⁺ and pH compared to priming with pH alone (76). This reaffirms the necessity for a high K⁺ concentration as well as a low pH to cue IAV for uncoating events, as infection is reduced through host K⁺ channel blockade.

The influence of K^+ ions on IAV infection has previously been proposed to aid in the dissociation of the M1 layer, allowing for efficient uncoating of the viral core and the release of the vRNPs (76). Work presented here shows K^+ clearly plays a crucial role in IAV infection, likely enhancing the successful escape of virions from the endocytic pathway. This may be explained in part by the morphology of virions during infection. The samples imaged here by cryo-ET displayed a range of morphologically distinct IAV virions, in which virions with and without an M1 layer can be observed, as has been previously identified (40,359). However, it is worth noting that in this case, virions without an M1 layer appear to be in greater abundance than previously observed (~33 % as opposed to ~6 % and ~5 %) (40,359), this difference may in part be explained due to the purification methods of whole virus utilised in this study, compared to previous observations (364). As it is thought K^+ plays a role in the disassembly of the M1 layer, virions lacking an M1 layer might be capable of delivering the vRNPs to the cytosol in the absence of a high K^+ concentration (**Figure 5.12**). Work carried out here in which virions were primed with a buffer either at neutral pH or at pH 5.8 and in the presence or absence of K^+ (+/- K^+) show clear differences in populations with or without an M1 layer. Virions primed at either neutral pH or with a mildly acidic pH (pH 5.8) showed consistent proportions of virions with an M1 layer (~66 % of population). Whilst virions primed with K^+ ions, both at neutral pH and at a mildly acidic pH, showed a significant reduction in the proportion of M1 layer virions (~46 % of population), agreeing with previously reported biochemical findings (76). Previously, molecular fontanelles or partial M1 layers have been described at neutral pH (40), and are observed here in all datasets. These partial M1 layers (which make up part of the M1 layer proportions observed here) are present in all instances, though clear differences can be observed. The number of partial M1 layers observed increased 2-fold with pH 5.8 priming alone, 4-fold with K^+ priming alone and 5-fold with pH 5.8 + K^+ priming. Of note a lower pH appeared to increase the number of these M1 layer gaps, whilst also increasing the distances between the M1 layer sections, and K^+ priming appeared to cause the M1 layer to become disorganised (**Figure 5.11**). With this in consideration, the data presented here would suggest that the disassembly of the M1 layer is a 2-part process: mildly acidic pH seems to extend pre-existing molecular fontanelles, whilst the influx of K^+ ions appears to further disrupt the M1-M1 interactions. These observations structurally confirm the biochemical interpretations of the roles of pH and K^+ in M1 disassembly (76).

It has been hypothesised that the increase in K^+ plays a role in the disorganisation of the vRNP bundle (76). Here, vRNPs can be seen to be organised at neutral pH (independently of K^+ priming), showing regular vRNPs located in the centre of virions. At a pH of pH 5.8 virions are observed with disorganised

vRNPs (again, independently of K^+ priming); these vRNPs appear to aggregate, forming a large density within virions that relocates to the one side of the virion, in close contact with the envelope/M1-layer. An acidic pH alone appears to be sufficient here as the cue required for vRNP disruption. This is further affirmed through previous cryo-ET work, in which Fontana *et al.*, observed large density representing the disorganised and aggregated vRNPs when virions were primed without K^+ at pH 4.9 (359). The vRNP density appeared much stronger, perhaps suggesting further disorganisation occurs upon a lower pH cue than carried out here (<pH 5.8).

Taking into account the results presented here, an updated mechanism for infection during the early stages in IAV is suggested (**Figure 5.13**). A mixed population of virions enters the host cell via clathrin-mediated endocytosis or via clathrin-independent endocytosis and are shuttled via the endocytic pathway (136). Within the early endosomes (pH 7.5 to 6.0), a HA-dependent molecular change occurs (365). As the endosomes begin to acidify (<pH 6.5), the influx of protons via M2 causes internal acidification, in which M1 molecular fontanelles to be extended, due to weakening the interactions between M1-M1 interactions and the C-terminus of the M1 layer and vRNP bundles (366,367). This weakening causes the vRNPs to become disorganised and aggregate inside the virions. At a mildly acidic pH (~pH 5.8) within late endosomes, IAV glycoproteins begin to adopt intermediate fusion conformations (321). Additionally, at this stage IAV is exposed to a 10-fold increase in K^+ ions within the endosome (355), which results in K^+ internalisation via M2, and aids the further weakening of M1-M1 interactions leading to a disorganised M1 layer. At this stage molecular fontanelles created by the lower pH, are extended further by the H^+ and K^+ ion concentration, causing complete M1 layer disassembly. Though H^+ alone appears to be sufficient to allow infection, K^+ seems to improve the % of virions which escape late endosomes, enhancing the successful release of vRNPs. As fusion conditions are met (~pH 5.0), further disorganisation in the glycoproteins can be observed due to fusogenic conformational changes. The vRNPs/M1 layer can be visibly seen to form more dense aggregates, suggesting a final stage in disorganisation, facilitated by the concentration of internal H^+ and K^+ ions (359). Fusion then occurs rapidly, allowing for efficient release of the now disorganised vRNPs. The population of virions lacking an M1 layer undergo similar vRNP aggregation and disorganisation, though the efficient release of these is not dependant on the disassembly of an M1 layer and so, not hindered by the presence or absence of K^+ in the endosomes.

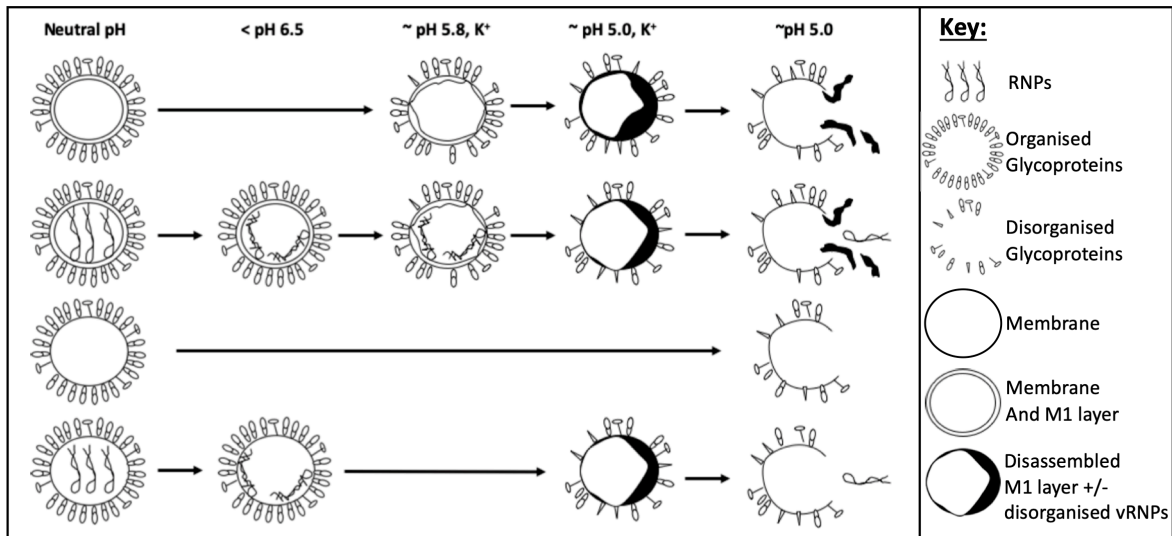


Figure 5.12: Schematic of the mechanism of IAV entry

Each of the four virion morphologies are depicted in the first ‘neutral pH’ column. Each row shows the morphological changes which occur due to biological cues as the virions pass through the endocytic pathway. It is likely K⁺ does not enhance infection by virions lacking an M1 layer.

As a result of this mechanism, those virions lacking an M1 layer, though a very small percentage of the viral population (<33%) are shuttled through the endocytic pathway without the requirement of an increased K⁺ concentration within the endosomal lumen. When challenged with ion channel modulators, the inhibition of this influx of K⁺ prevents efficient release of the majority of infecting virions with an M1 layer (>66%), reducing the number of successfully delivered disorganised vRNPs into the cytosol (**Figure 5.13d**).

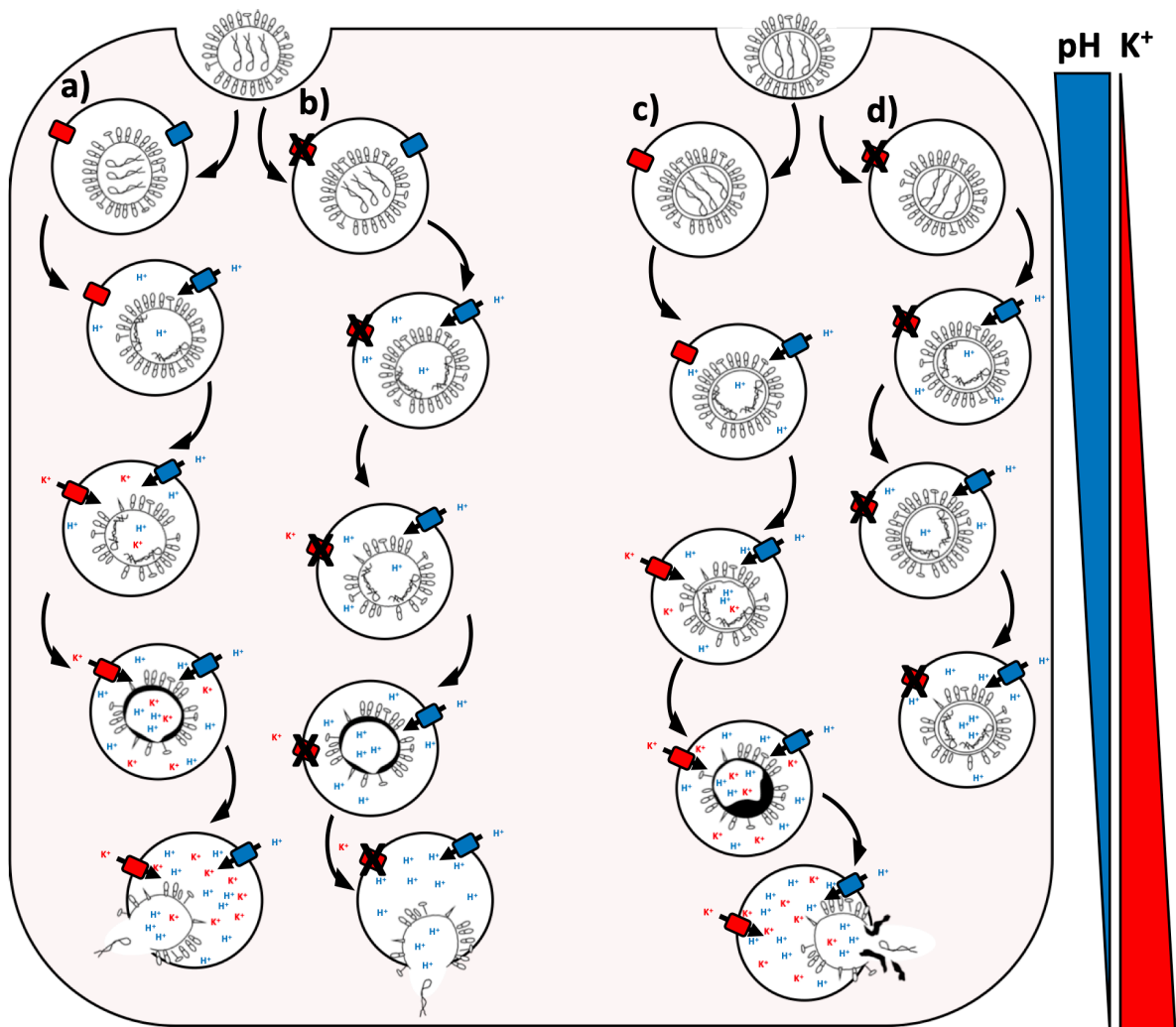


Figure 5.13: Schematic of the early stages of IAV infection, illustrating the hypothesised mechanism of inhibition when ion channel modulators are used

a) Entry of virions lacking an M1 layer. **b)** Entry of virions lacking an M1 layer when cells have been treated with dalfampridine. **c)** Entry of virions with an M1 layer. **d)** Entry of virions with an M1 layer when cells have been treated with dalfampridine. The ionic threshold is high for complete M1 disassembly, therefore only a small population of these virions may escape. Red rectangles = K⁺ channels, Blue rectangles = H⁺ proton pumps. Concentration gradients of both H⁺ and K⁺ ions are indicated to the right.

It is becoming clear that viral infections require specific ionic conditions in order to effectively infect host cells, with the requirement or manipulation of host ion channels playing an important role (146). K⁺ channels have previously been highlighted to play an important role in IAV infection (350,368), whilst biochemical assays have shown the importance of K⁺ in M1 disassembly (76). Here, it has been

confirmed visually through cryo-electron tomography, that K^+ plays a significant role in the disorganisation and disassembly of the M1 layer, bridging the gap between structural and biochemical evidence and confirming the link between K^+ channels role in IAV infection and K^+ ions role in virion M1 disruption. Repurposing K^+ ion channel modulators has revealed that K_v channels play a crucial role during early IAV infection in A549 cells, with dalfampridine showing particular promise as a potent therapeutic. Dalfampridine has also shown similar success in reducing infection of other viruses, notably the recent pandemic SARS-CoV-2 virus, in which CRISPR was used to identify $K_v1.6$ as a key channel required in SARS-CoV-2 infection. MCPyV has been found to depend on a K^+ ion influx via K_v channels, and consequently inhibited by dalfampridine (347,369). Providing further validation for the repurposing of these ion channel modulators as treatments for viral infection. Particularly as IAV is listed as one of the WHO's greatest threats to human health, due to its high mutation rate, and the potential for new strains to cause pandemics (4).

Chapter 6

Concluding remarks

The main aim of this project was to explore alternative methods of treating IAV infection. Specifically, with the objective to provide a rapid response to outbreaks, including pandemic variants of IAV, and to explore alternative treatments which may reduce the ability for IAV to develop drug resistance. The three objectives, previously described in section 1.8, established to address this criteria, have been fulfilled during this project and are briefly discussed below.

Objective 1: Isolation, expression and production of monomeric HA-specific Affimer molecules.

HA is the most abundant protein on the surface of IAV (57). Its role in entry, by facilitating host-cell receptor recognition, internalisation and fusion of viral and cellular membranes, and its role in egress, cleaving sialic acid to allow virus release, makes HA an ideal target for therapeutics and diagnostics (57). Affimer molecules are synthetic antibody-mimics, which can be screened using an extensive phage display library, allowing rapid selection of highly specific binders (290). This method is further advantageous, as only the intended target, or subsection of the target is required (in this instance monomeric HA), potentially alleviating the demand and delay required for clinical isolates.

Two methods of isolating Affimer molecules were employed. The first, isolation against a range of monomeric HA proteins, with the aim of isolating broadly neutralising Affimer molecules; and second, isolation of Affimer molecules against a single monomeric HA protein, with the aim of isolating high potency anti-HA Affimer molecules. In both instances, Affimer molecules were isolated by the BSTG (University of Leeds) and initially validated. Three Affimer molecules were successfully isolated with broad strain binding capabilities; however, these failed to inhibit Aichi/68 (H3N2), one of the strains used to isolate the molecules and thus a universal inhibitor was not produced via this method. Thirty-four Affimer molecules were isolated and validated aiming to be specific to HA/Aichi/68 (H3N2). Following initial validation, in which viral inhibition was assessed using a high concentration of Affimer. Six of these molecules were selected for further characterisation (Objective 2) as potential diagnostic and therapeutic molecules, three exhibiting inhibition of IAV (therapeutics) and three non-inhibiting (diagnostic potential).

Objective 2: Characterisation and validation of HA-specific Affimer molecules using a range of virology, biophysical and biochemical techniques.

The six selected Affimers were characterised using a range of biochemical and biophysical techniques. The affinity and kinetics were assessed through IC50 ELISA and SPR. Binding between monomeric HA

(Aichi/68 (H3N2) the strain used to isolate Affimer molecules) and two of the six Affimer molecules (A5 and A31) showed high affinity, with slow on/slow off kinetic rates. High affinity to the intended target guarantees tight binding and a high specificity, whilst a slow off rate ensures persistent obstruction of function.

Neutralisation assays were carried out to define the potency of the selected Affimer molecules. Two Affimers, A5 and A31, showed high potency neutralisation, comparable to those seen in neutralising mAbs, against the strain which Affimer molecules were isolated (Aichi). Furthermore, both molecules showed high potency against an HA from the same subtype, Udorn/72 (H3N2) HA, showing scope for inhibiting circulatory strains for a minimum of four years, resisting antigenic drift which often renders many treatments rapidly obsolete. Though potency appeared to be in large specific to H3N2 strains closely related to the target strain, potency against the 2009 pandemic strain (H1N1) was observed. These results require further investigation to deliver in depth understanding of the precise mechanism by which this is possible. Though, it is clear it is possible to isolate Affimer molecules which deliver high potency and specificity to the intended target, achieving the intended objective. To enhance strain coverage, to achieve a universal inhibitor, more sophisticated methods could be utilised. The phage display system is not fully utilised as there are theoretically 1.3×10^{10} possible unique Affimer molecules available of which, few are chosen for phage ELISA analysis (237). Isolating Affimer molecules in a high-throughput system would ensure a greater coverage of potential binders/inhibitors. Alternative methods, such as using chimeric HA proteins for panning have been described and could be implemented here (187). In this methodology, the stalk domain remains constant through panning rounds, whilst the head domain is changed, enhancing the isolation of stalk-binding proteins (187).

In order to identify the mode in which infection is inhibited, a range of assays were carried out. The classical hemagglutination assay revealed both A5 and A31 prevented hemagglutination, suggesting that these Affimer molecules bind close or at the sialic acid pocket found on the head domain of HA. This was further confirmed by ELISA using the immobilised head domain of HA, in which both Affimer molecules showed similar potency profiles as those found in full length monomeric HA, affirming inhibition is likely related to head binding (entry and/or egress inhibition). Furthermore, fusion and egress assays showed that Affimer molecules do not inhibit these processes.

Cryo-EM data of the complex formed between A31 and HA showed an extra density, consistent with that of an Affimer molecule, bound to the head domain of each of the HA monomers, validating biochemical findings with structural information. Interestingly, when bound in a complex, HA appears shortened, with the head domains dilated when compared to native HA. In fact, this conformation is similar to an intermediate fusion state previously described (ref). Recent literature has identified

neutralising mAbs induce similarly dilated and shortened conformations in HA, suggesting A31 too binds at the interface of HA monomers within the trimer, locking it in a dilated state whilst obstructing the sialic acid pocket (329–332).

Currently, few treatments are readily available for circulating IAV, in large due to the continual mutations each protein undergoes. Therefore, there is an urgent need for novel therapeutics against IAV, particularly ones which can be produced rapidly and relatively cheaply. Due to the small size of Affimer molecules, their rapid tissue penetration, high stability and solubility make them attractive candidates as therapeutic molecules (237,335). Additionally, bacterial expression of Affimer molecules permits cheap and rapid production almost anywhere in the world. All of which are beneficial to keep-pace with ever evolving circulatory strains and provide the potential to deliver a therapeutic immediately after a pandemic strain arises. Here, work has been carried out to optimise the isolation, purification and characterisation of Affimer molecules against HA. These optimised methods could be taken through to a high throughput setting, in which characterised Affimer could be produced within a few months.

Objective 3: Screening and characterisation of a panel of broad-inhibiting K⁺ channel inhibitors as therapeutics of IAV

The third objective of this project was to explore further therapeutic possibilities, in this instance, indirect-acting therapeutics. Ion channel modulators intended for channelopathies are some of the most prevalently FDA-approved drugs (337). Some of these channel modulators have already been repurposed and demonstrated to inhibit infection from a range of viruses, including HAZV, BUNV, and MCPyV (271,344,347). Previous studies showed K⁺ concentration and channels to have an influence on IAV infection, therefore repurposing K⁺ channel modulators as in-direct drugs was explored. With this in mind, work was carried out to explore the possibility of repurposing K⁺ channel modulators as anti-influenza drugs. A selection of drugs were chosen based on channels previously identified to effect IAV infection.

Following treatment of cells with a panel of K⁺ channel modulators identified in large, through meta-OMICs, multiple drugs were found to significantly reduce the infection of multiple strains of IAV (both H3N2 and H1N1). In particular, dalfampridine, a broad voltage gated K⁺ channel modulator, was found to be a potent inhibitor of the strains tested. This agreed with the identification of dalfampridine as an inhibitor of the most impactful K⁺ channels in the Meta-OMIC study (350).

Time of addition assays carried out here suggest that the necessity for K⁺ ions is during the early stages of IAV infection, likely as virions are trafficked into the late endosomal compartments (352,353).

These findings agree with Stauffer *et al.*, who found that K^+ ions play a role in the disassembly of the M1 matrix layer (76). Disassembly of the matrix layer occurs prior to fusion of viral and cellular membranes, allowing the efficient release of vRNPs to the nucleus, escaping lysosomal degradation. Further assays confirmed that Qd and dalfampridine do not act directly on IAV itself (i.e. they do not affect the M2 ion channel), rather the cells in which IAV infects. Priming virions with a low pH and high K^+ concentration reduced the inhibition caused by these channel modulators, likely by bypassing the requirement of a high K^+ environment found in the late endosomes. This suggests channel modulators work by disrupting the environment required by IAV in the late endosomes.

To further understand the role of K^+ ions in IAV infection, structural information was sought after, through the means of cryo-ET. Using this approach visualisation of the resultant low pH and high K^+ phenotype was sought after and became immediately apparent that when virions were primed with a high concentration of K^+ ions (with or without a low pH), the percentage of virions lacking an M1 layer was larger than in the absence of K^+ and also there was a greater number of virions with gaps in the M1 layer, known as 'molecular fontanelles' (40). These results combined with results generated through the use of ion channel modulators, suggest that K^+ plays an important role in improving the efficiency of M1 disassembly. The inhibition of this high K^+ concentration (through channel modulators) significantly impacts infection by IAV, highlighting the importance of K^+ ions in the IAV lifecycle. These results not only build upon the current understanding of K^+ ions in IAV infection and the role of ions in viruses, but provide a potential therapeutic treatment, using drugs that are already approved clinically. As this therapeutic inhibits several strains of IAV, it is likely inhibiting a conserved mechanism, thus, less likely that IAV will be able to evolve to make this treatment redundant. Furthermore, this treatment, alongside a direct-acting treatment would provide a potent combinational therapy.

In conclusion, the work presented in this project represents a step forward on the development of novel treatments for the highly pathogenic IAV, as well as adding to our understanding of this virus' complex interaction with its host cells. The work carried out here has the potential to be translated to other emerging viruses, for which rapid and potent treatment may be required for potential future outbreaks.

Chapter 7

References

1. Pappas G, Kiriaze IJ, Falagas ME. Insights into infectious disease in the era of Hippocrates. *Int J Infect Dis.* 2008;12(4):347–50.
2. Smith W, Andrewes CH, Laidlaw PP. A VIRUS OBTAINED FROM INFLUENZA PATIENTS. *Lancet* . 1933;222(5732):66–8. Available from: <https://www.sciencedirect.com/science/article/pii/S0140673600785412>
3. Shope RE. The incidence of neutralizing antibodies for swine influenza virus in the sera of human beings of different ages. *J Exp Med.* 1936;63(5):669–84.
4. The WHO. Ten threats to global health in 2019 . 2019. Available from: <https://www.who.int/news-room/spotlight/ten-threats-to-global-health-in-2019>
5. Xu X, Lindstrom SE, Shaw MW, Smith CB, Hall HE, Mungall BA, et al. Reassortment and evolution of current human influenza A and B viruses. *Virus Res.* 2004;103(1–2):55–60.
6. Memorandum WHO. A revision of the system of nomenclature for influenza viruses: a WHO memorandum. *Bull World Health Organ.* 1980;58(4):585–91.
7. Xiao Y, Nolting JM, Sheng ZM, Bristol T, Qi L, Bowman AS, et al. Design and validation of a universal influenza virus enrichment probe set and its utility in deep sequence analysis of primary cloacal swab surveillance samples of wild birds. *Virology.* 2018;524(May):182–91.
8. Peasah SK, Azziz-Baumgartner E, Breese J, Meltzer MI, Widdowson M-A. Influenza cost and cost-effectiveness studies globally – A review. *Vaccine* . 2013;31(46):5339–48. Available from: <https://www.sciencedirect.com/science/article/pii/S0264410X13012401>
9. Gasparini R, Amicizia D, Lai PL, Panatto D. Clinical and socioeconomic impact of seasonal and pandemic influenza in adults and the elderly. *Hum Vaccin Immunother* . 2012 Jan 1;8(1):21–8. Available from: <https://doi.org/10.4161/hv.8.1.17622>
10. World Health Organisation. Global Influenza Strategy Summary 2019-2030 Influenza. *Glob Influenza Strateg 2019-2030 Influenza.* 2019;1:1.
11. Alimi Y, Lim WS, Lansbury L, Leonardi-Bee J, Nguyen-Van-Tam JS. Systematic review of respiratory viral pathogens identified in adults with community-acquired pneumonia in Europe. *J Clin Virol* . 2017/08/05. 2017 Oct;95:26–35. Available from: <https://pubmed.ncbi.nlm.nih.gov/28837859>
12. Krammer F, Smith GJD, Fouchier RAM, Peiris M, Kedzierska K, Doherty PC, et al. Influenza. *Nat Rev Dis Prim.* 2018;4(1):1–21.
13. Olsen B, Munster VJ, Wallensten A, Waldenström J, Osterhaus ADME, Fouchier RAM. Global patterns of influenza A virus in wild birds. *Science (80-)*. 2006;312(5772):384–8.
14. Hutchinson EC. Influenza Virus. *Trends Microbiol.* 2018;26(9):809–10.
15. Sauter NK, Bednarski MD, Wurzburg BA, Hanson JE, Whitesides GM, Skehel JJ, et al. Hemagglutinins from two influenza virus variants bind to sialic acid derivatives with millimolar dissociation constants: a 500-MHz proton nuclear magnetic resonance study. *Biochemistry* . 1989 Oct 17;28(21):8388–96. Available from: <https://doi.org/10.1021/bi00447a018>
16. Shinya K, Ebina M, Yamada S, Ono M, Kasai N, Kawaoka Y. Influenza virus receptors in the human airway. *Nature* . 2006;440(7083):435–6. Available from: <https://doi.org/10.1038/440435a>
17. Van Riel D, Munster VJ, De Wit E, Rimmelzwaan GF, Fouchier RAM, Osterhaus ADME, et al. H5N1 virus attachment to lower respiratory tract. *Science (80-)*. 2006;312(5772):399.
18. Ito T, Nelson J, Couceiro SS, Kelm S, Baum LG, Krauss S, et al. Molecular Basis for the Generation in Pigs of Influenza A Viruses with Pandemic Potential. *J Virol.* 1998;72(9):7367–73.
19. Lowen AC, Mubareka S, Steel J, Palese P. Influenza virus transmission is dependent on relative humidity and temperature. *PLoS Pathog.* 2007;3(10):1470–6.
20. Hussain M, Galvin HD, Haw TY, Nutsford AN, Husain M. Drug resistance in influenza a virus: The epidemiology and management. *Infect Drug Resist.* 2017;10:121–34.

21. Drake JW. Rates of spontaneous mutation among RNA viruses. *Proc Natl Acad Sci U S A*. 1993;90(9):4171–5.
22. Hope-Simpson RE, Golubev DB. A new concept of the epidemic process of influenza A virus. *Epidemiol Infect*. 1987;99(1):5–54.
23. Neuzil KM, Hohlbein C, Zhu Y. Illness Among Schoolchildren During Influenza Season: Effect on School Absenteeism, Parental Absenteeism From Work, and Secondary Illness in Families. *Arch Pediatr Adolesc Med* . 2002 Oct 1;156(10):986–91. Available from: <https://doi.org/10.1001/archpedi.156.10.986>
24. Childs R a, Palma AS, Wharton S, Matrosovich T. Europe PMC Funders Group Receptor-binding specificity of pandemic influenza A (H1N1) 2009 virus determined by carbohydrate microarray. *Nat Biotechnol*. 2013;27(9):797–9.
25. Long JS, Mistry B, Haslam SM, Barclay WS. Host and viral determinants of influenza A virus species specificity. *Nat Rev Microbiol* . 2019;17(2):67–81. Available from: <http://dx.doi.org/10.1038/s41579-018-0115-z>
26. Yamashita M, Krystal M, Fitch WM, Palese P. Influenza B virus evolution: Co-circulating lineages and comparison of evolutionary pattern with those of influenza A and C viruses. *Virology*. 1988;163(1):112–22.
27. Rota PA, Wallis TR, Harmon MW, Rota JS, Kendal AP, Nerome K. Cocirculation of two distinct evolutionary lineages of influenza type B virus since 1983. *Virology*. 1990;175(1):59–68.
28. Martini M, Gazzaniga V, Bragazzi NL, Barberis I. The Spanish Influenza Pandemic: A lesson from history 100 years after 1918. *J Prev Med Hyg*. 2019;60(1):E64–7.
29. Saunders-Hastings PR, Krewski D. Reviewing the history of pandemic influenza: Understanding patterns of emergence and transmission. *Pathogens*. 2016;5(4).
30. Olga J. Pandemic Risk. *Financ Dev* . 2014;51(4):16–7. Available from: https://www.worldbank.org/content/dam/Worldbank/document/HDN/Health/WDR14_bp_Pandemic_Risk_Jonas.pdf
31. Lenzen M, Li M, Malik A, Pomponi F, Sun YY, Wiedmann T, et al. Global socio-economic losses and environmental gains from the coronavirus pandemic. *PLoS One*. 2020;15(7 July):1–13.
32. Mittal N, Medhi B. The bird flu: a new emerging pandemic threat and its pharmacological intervention. *Int J Health Sci (Qassim)* . 2007;1(2):277–83. Available from: <http://www.ncbi.nlm.nih.gov/pubmed/21475439>
<http://www.pubmedcentral.nih.gov/articlerender.fcgi?artid=PMC3068632>
33. Claas ECJ, Osterhaus ADME, Van Beek R, De Jong JC, Rimmelzwaan GF, Senne DA, et al. Human influenza A H5N1 virus related to a highly pathogenic avian influenza virus. *Lancet*. 1998;351(9101):472–7.
34. Webby RJ, Yang Z. The changing landscape of A H7N9 influenza virus infections in China. *Lancet Infect Dis* . 2017 Aug;17(8):783—784. Available from: [https://doi.org/10.1016/S1473-3099\(17\)30337-7](https://doi.org/10.1016/S1473-3099(17)30337-7)
35. Zhou J, Wang D, Gao R, Zhao B, Song J, Qi X, et al. Biological features of novel avian influenza A (H7N9) virus. *Nature*. 2013;499(7459):500–3.
36. Poovorawan Y, Pyungporn S, Prachayangprecha S, Makkoch J. Global alert to avian influenza virus infection: From H5N1 to H7N9. *Pathog Glob Health*. 2013;107(5):217–23.
37. Badham MD, Rossman JS. Filamentous Influenza Viruses. *Curr Clin Microbiol Reports* . 2016;3(3):155–61. Available from: <http://dx.doi.org/10.1007/s40588-016-0041-7>
38. Seladi-Schulman J, Steel J, Lowen AC. Spherical Influenza Viruses Have a Fitness Advantage in Embryonated Eggs, while Filament-Producing Strains Are Selected In Vivo . *J Virol*. 2013;87(24):13343–53.
39. Dadonaite B, Vijayakrishnan S, Fodor E, Bhella D, Hutchinson EC. Filamentous influenza viruses. *J Gen Virol*. 2016;97(8):1755–64.
40. Harris A, Cardone G, Winkler DC, Heymann JB, Brecher M, White JM, et al. Influenza virus pleiomorphy characterized by cryoelectron tomography. *Proc Natl Acad Sci U S A*.

- 2006;103(50):19123–7.
41. Gamblin SJ, Skehel JJ. Influenza hemagglutinin and neuraminidase membrane glycoproteins. *J Biol Chem* . 2010;285(37):28403–9. Available from: <http://dx.doi.org/10.1074/jbc.R110.129809>
 42. Sieczkarski SB, Whittaker GR. Differential requirements of Rab5 and Rab7 for endocytosis of influenza and other enveloped viruses. *Traffic*. 2003;4(5):333–43.
 43. Hao W, Wang L, Li S. Roles of the non-structural proteins of influenza A virus. *Pathogens*. 2020;9(10):1–19.
 44. Yamayoshi S, Watanabe M, Goto H, Kawaoka Y. Identification of a Novel Viral Protein Expressed from the PB2 Segment of Influenza A Virus. *J Virol*. 2016;90(1):444–56.
 45. McGeoch D, Fellner P, Newton C. Influenza virus genome consists of eight distinct RNA species. *Proc Natl Acad Sci U S A*. 1976;73(9):3045–9.
 46. Knipe DM, Howley PM, Noda T, Kawaoka Y, Gao P, Halfmann P, et al. References and Notes 1. 2012;338(December):1634–8.
 47. Fodor E, Seong BL, Brownlee GG. Photochemical cross-linking of influenza A polymerase to its virion RNA promoter defines a polymerase binding site at residues 9 to 12 of the promoter. *J Gen Virol*. 1993;74(7):1327–33.
 48. Hsu M, Parvin JD, Gupta S, Krystal M, Palese P. Terminal Panhandle. *Proc Natl Acad Sci U S A* . 1987;84(November):8140–4. Available from: <https://www.pnas.org/content/84/22/8140.long>
 49. Moeller A, Kirchdoerfer RN, Potter CS, Carragher B, Wilson IA. Organization of the influenza virus replication machinery. *Science* (80-). 2012;338(6114):1631–4.
 50. Daniel E Shumer HHS Public Access. *Physiol Behav*. 2017;176(12):139–48.
 51. Dadonaite B, Gilbertson B, Knight ML, Trifkovic S, Rockman S, Laederach A, et al. The structure of the influenza A virus genome. *Nat Microbiol* . 2019;4(11):1781–9. Available from: <http://dx.doi.org/10.1038/s41564-019-0513-7>
 52. Aw JGA, Shen Y, Wilm A, Sun M, Lim XN, Boon KL, et al. In Vivo Mapping of Eukaryotic RNA Interactomes Reveals Principles of Higher-Order Organization and Regulation. *Mol Cell* . 2016;62(4):603–17. Available from: <http://dx.doi.org/10.1016/j.molcel.2016.04.028>
 53. Noda T, Murakami S, Nakatsu S, Imai H, Muramoto Y, Shindo K, et al. Importance of the 1+7 configuration of ribonucleoprotein complexes for influenza A virus genome packaging. *Nat Commun*. 2018;9(1):1–10.
 54. Williams GD, Townsend D, Wylie KM, Kim PJ, Amarasinghe GK, Kutluay SB, et al. Nucleotide resolution mapping of influenza A virus nucleoprotein-RNA interactions reveals RNA features required for replication. *Nat Commun* . 2018;9(1):1–12. Available from: <http://dx.doi.org/10.1038/s41467-018-02886-w>
 55. Liang Y, Hong Y, Parslow TG. cis -Acting Packaging Signals in the Influenza Virus PB1, PB2, and PA Genomic RNA Segments . *J Virol*. 2005;79(16):10348–55.
 56. McCauley JW, Mahy BWJ. Structure and function of the influenza virus genome. *Biochem J*. 1983;211(2):281–94.
 57. Harrison SC. Viral membrane fusion. *Nat Struct Mol Biol*. 2008;15(7):690–8.
 58. Zhang Y, Xu C, Zhang H, Liu GD, Xue C, Cao Y. Targeting Hemagglutinin : Approaches for Broad. *Viruses*. 2019;11:1–24.
 59. Matrosovich M, Tuzikov A, Bovin N, Gambaryan A, Klimov A, Castrucci MR, et al. Early Alterations of the Receptor-Binding Properties of H1, H2, and H3 Avian Influenza Virus Hemagglutinins after Their Introduction into Mammals. *J Virol*. 2000;74(18):8502–12.
 60. Caton AJ, Brownlee GG, Yewdell JW, Gerhard W. The antigenic structure of the influenza virus A/PR/8/34 hemagglutinin (H1 subtype). *Cell* . 1982;31(2, Part 1):417–27. Available from: <https://www.sciencedirect.com/science/article/pii/0092867482901350>
 61. Fitria et al., *J Chem Inf Model*. 2013;53(9):1689–99.
 62. Tharakaraman K, Subramanian V, Cain D, Sasisekharan V, Sasisekharan R. Broadly neutralizing

- influenza hemagglutinin stem-specific antibody CR8020 targets residues that are prone to escape due to host selection pressure. *Cell Host Microbe* . 2014;15(5):644–51. Available from: <http://dx.doi.org/10.1016/j.chom.2014.04.009>
63. Okuno Y, Isegawa Y, Sasao F, Ueda S. A common neutralizing epitope conserved between the hemagglutinins of influenza A virus H1 and H2 strains. *J Virol*. 1993;67(5):2552–8.
 64. Wu NC, Wilson IA. Structural biology of influenza hemagglutinin: An amaranthine adventure. *Viruses*. 2020;12(9):1–18.
 65. Varghese JN, Laver WG, Colman PM. Structure of the influenza virus glycoprotein antigen neuraminidase at 2.9 Å resolution. *Nature*. 1983;303(5912):35–40.
 66. Russell RJ, Haire LF, Stevens DJ, Collins PJ, Lin YP, Blackburn GM, et al. The structure of H5N1 avian influenza neuraminidase suggests new opportunities for drug design. *Nature*. 2006;443(7107):45–9.
 67. Basak S, Tomana M, Compans RW. Sialic acid is incorporated into influenza hemagglutinin glycoproteins in the absence of viral neuraminidase. *Virus Res*. 1985;2(1):61–8.
 68. Palese P, Tobita K, Ueda M, Compans RW. Characterization of temperature sensitive influenza virus mutants defective in neuraminidase. *Virology*. 1974;61(2):397–410.
 69. McAuley JL, Corcilius L, Tan HX, Payne RJ, McGuckin MA, Brown LE. The cell surface mucin MUC1 limits the severity of influenza A virus infection. *Mucosal Immunol* . 2017;10(6):1581–93. Available from: <http://dx.doi.org/10.1038/mi.2017.16>
 70. Amaro RE, Swift R V., Votapka L, Li WW, Walker RC, Bush RM. Mechanism of 150-cavity formation in influenza neuraminidase. *Nat Commun*. 2011;2(1).
 71. Air GM, Webster RG, Lentz MR. Site-Directed Mutation of the Active Site of Influenza Neuraminidase and Implications for the Catalytic Mechanism. *Biochemistry*. 1987;26(17):5351–8.
 72. Nieva JL, Madan V, Carrasco L. Viroporins: Structure and biological functions. *Nat Rev Microbiol*. 2012;10(8):563–74.
 73. Jason R. Schnell and James J. Chou*. Structure and Mechanism of the M2 Proton Channel of Influenza A Viruss. *Nature* . 2008;23(1):1–7. Available from: <https://www.ncbi.nlm.nih.gov/pmc/articles/PMC3624763/pdf/nihms412728.pdf>
 74. Leiding T, Wang J, Martinsson J, DeGrado WF, Årsköld SP. Proton and cation transport activity of the M2 proton channel from influenza A virus. *Proc Natl Acad Sci U S A*. 2010;107(35):15409–14.
 75. Shimbo K, Brassard DL, Lamb RA, Pinto LH. Ion selectivity and activation of the M2 ion channel of influenza virus. *Biophys J*. 1996;70(3):1335–46.
 76. Stauffer S, Feng Y, Nebioglu F, Heilig R, Picotti P, Helenius A. Stepwise Priming by Acidic pH and a High K⁺ Concentration Is Required for Efficient Uncoating of Influenza A Virus Cores after Penetration. *J Virol*. 2014;88(22):13029–46.
 77. Iwatsuki-Horimoto K, Horimoto T, Noda T, Kiso M, Maeda J, Watanabe S, et al. The Cytoplasmic Tail of the Influenza A Virus M2 Protein Plays a Role in Viral Assembly. *J Virol*. 2006;80(11):5233–40.
 78. Schnell JR. NIH Public Access. *Bone* . 2014;23(1):1–7. Available from: <https://www.ncbi.nlm.nih.gov/pmc/articles/PMC3624763/pdf/nihms412728.pdf>
 79. Blair R. HHS Public Access. *Physiol Behav*. 2017;176(3):139–48.
 80. Furuse Y, Suzuki A, Kamigaki T, Oshitani H. Evolution of the M gene of the influenza A virus in different host species: Large-scale sequence analysis. *Viol J*. 2009;6:1–13.
 81. Nayak DP, Hui EKW, Barman S. Assembly and budding of influenza virus. *Virus Res*. 2004;106(2 SPEC.ISS.):147–65.
 82. Harris A, Forouhar F, Qiu S, Sha B, Luo M. The crystal structure of the influenza matrix protein M1 at neutral pH: M1-M1 protein: Interfaces can rotate in the oligomeric structures of M1. *Virology*. 2001;289(1):34–44.
 83. Peukes J, Xiong X, Erendsson S, Qu K, Wan W, Calder LJ, et al. The native structure of the

- assembled matrix protein 1 of influenza A virus. *Nature*. 2020;587(7834):495–8. Available from: <http://dx.doi.org/10.1038/s41586-020-2696-8>
84. Zhang J, Lamb RA. Characterization of the membrane association of the influenza virus matrix protein in living cells. *Virology*. 1996;225(2):255–66.
 85. Bui M, Whittaker G, Helenius A. Effect of M1 protein and low pH on nuclear transport of influenza virus ribonucleoproteins. *J Virol*. 1996;70(12):8391–401.
 86. Noton SL, Medcalf E, Fisher D, Mullin AE, Elton D, Digard P. Identification of the domains of the influenza A virus M1 matrix protein required for NP binding, oligomerization and incorporation into virions. *J Gen Virol*. 2007;88(8):2280–90.
 87. Shimizu T, Takizawa N, Watanabe K, Nagata K, Kobayashi N. Crucial role of the influenza virus NS2 (NEP) C-terminal domain in M1 binding and nuclear export of vRNP. *FEBS Lett* . 2011;585(1):41–6. Available from: <http://dx.doi.org/10.1016/j.febslet.2010.11.017>
 88. Ali A, Avalos RT, Ponimaskin E, Nayak DP. Influenza Virus Assembly: Effect of Influenza Virus Glycoproteins on the Membrane Association of M1 Protein. *J Virol*. 2000;74(18):8709–19.
 89. Mosier PD, Chiang MJ, Lin Z, Gao Y, Althufairi B, Zhou Q, et al. Broad Spectrum Anti-Influenza Agents by Inhibiting Self-Association of Matrix Protein 1. *Sci Rep* . 2016;6(June):1–10. Available from: <http://dx.doi.org/10.1038/srep32340>
 90. Mena I, Jambrina E, Albo C, Perales B, Ortín J, Arrese M, et al. Mutational Analysis of Influenza A Virus Nucleoprotein: Identification of Mutations That Affect RNA Replication. *J Virol*. 1999;73(2):1186–94.
 91. Albo C, Valencia A, Portela A. Identification of an RNA binding region within the N-terminal third of the influenza A virus nucleoprotein. *J Virol*. 1995;69(6):3799–806.
 92. Elton D, Medcalf L, Bishop K, Harrison D, Digard P. Identification of Amino Acid Residues of Influenza Virus Nucleoprotein Essential for RNA Binding. *J Virol*. 1999;73(9):7357–67.
 93. Wang P, Palese P, O’Neill RE. The NPI-1/NPI-3 (karyopherin alpha) binding site on the influenza a virus nucleoprotein NP is a nonconventional nuclear localization signal. *J Virol*. 1997;71(3):1850–6.
 94. Biswas SK, Boutz PL, Nayak DP. Influenza Virus Nucleoprotein Interacts with Influenza Virus Polymerase Proteins. *J Virol*. 1998;72(7):5493–501.
 95. Honda A, Ueda K, Nagata K, Ishihama A. RNA polymerase of influenza virus: Role of NP in RNA chain elongation. *J Biochem*. 1988;104(6):1021–6.
 96. Portela A, Digard P. The influenza virus nucleoprotein: A multifunctional RNA-binding protein pivotal to virus replication. *J Gen Virol*. 2002;83(4):723–34.
 97. Yang F, Pang B, Lai KK, Cheung NN, Dai J, Zhang W, et al. Discovery of a Novel Specific Inhibitor Targeting Influenza A Virus Nucleoprotein with Pleiotropic Inhibitory Effects on Various Steps of the Viral Life Cycle. *J Virol*. 2021;95(9).
 98. Su CY, Cheng TJR, Lin MI, Wang SY, Huang WI, Lin-Chua SY, et al. High-throughput identification of compounds targeting influenza RNA-dependent RNA polymerase activity. *Proc Natl Acad Sci U S A*. 2010;107(45):19151–6.
 99. Chang S, Sun D, Liang H, Wang J, Li J, Guo L, et al. Cryo-EM Structure of Influenza Virus RNA Polymerase Complex at 4.3Å Resolution. *Mol Cell*. 2015;57(5):925–35.
 100. Tomescu AI, Robb NC, Hengrung N, Fodor E, Kapanidis AN. Single-molecule FRET reveals a corkscrew RNA structure for the polymerase-bound influenza virus promoter. *Proc Natl Acad Sci U S A*. 2014;111(32).
 101. Guilligay D, Tarendeau F, Resa-Infante P, Coloma R, Crepin T, Sehr P, et al. The structural basis for cap binding by influenza virus polymerase subunit PB2. *Nat Struct Mol Biol*. 2008;15(5):500–6.
 102. Hara K, Schmidt FI, Crow M, Brownlee GG. Amino Acid Residues in the N-Terminal Region of the PA Subunit of Influenza A Virus RNA Polymerase Play a Critical Role in Protein Stability, Endonuclease Activity, Cap Binding, and Virion RNA Promoter Binding. *J Virol*. 2006;80(16):7789–98.

103. Dias A, Bouvier D, Crépin T, McCarthy AA, Hart DJ, Baudin F, et al. The cap-snatching endonuclease of influenza virus polymerase resides in the PA subunit. *Nature*. 2009;458(7240):914–8.
104. Robertson JS, Schubert M, Lazzarini RA. Polyadenylation sites for influenza virus mRNA. *J Virol*. 1981;38(1):157–63.
105. Pflug A, Guilligay D, Reich S, Cusack S. Structure of influenza A polymerase bound to the viral RNA promoter. *Nature*. 2014;516(7531):355–60.
106. Hengrung N, El Omari K, Serna Martin I, Vreede FT, Cusack S, Rambo RP, et al. Crystal structure of the RNA-dependent RNA polymerase from influenza C virus. *Nature*. 2015;527(7576):114–7.
107. Pagadala NS, Bhat R, Kumar D J, Landi A. Discovery of anti-influenza nucleoside triphosphates targeting the catalytic site of A/PR/8/34/H1N1 polymerase. *Med Chem Res* . 2020;29(8):1463–77. Available from: <http://dx.doi.org/10.1007/s00044-020-02561-0>
108. Fukuyama S, Kawaoka Y. The pathogenesis of influenza virus infections: The contributions of virus and host factors. *Curr Opin Immunol*. 2011;23(4):481–6.
109. Rosário-Ferreira N, Preto AJ, Melo R, Moreira IS, Brito RMM. The central role of non-structural protein 1 (NS1) in influenza biology and infection. *Int J Mol Sci*. 2020;21(4).
110. Jagger BW, Wise HM, Kash JC, Walters KA, Wills NM, Xiao YL, et al. An overlapping protein-coding region in influenza A virus segment 3 modulates the host response. *Science (80-)*. 2012;337(6091):199–204.
111. Ortigoza MB, Dibben O, Maamary J, Martinez-Gil L, Leyva-Grado VH, Abreu P, et al. A novel small molecule inhibitor of influenza A viruses that targets polymerase function and indirectly induces interferon. *PLoS Pathog*. 2012;8(4).
112. Shen Z, Lou K, Wang W. New small-molecule drug design strategies for fighting resistant influenza A. *Acta Pharm Sin B*. 2015;5(5):419–30.
113. Berman HM, Battistuz T, Bhat TN, Bluhm WF, Bourne PE, Burkhardt K, et al. The protein data bank. *Acta Crystallogr Sect D Biol Crystallogr*. 2002;58(6 Pt 1):899–907.
114. Zhao L, Xia H, Huang J, Zheng Y, Liu C, Su J, et al. Features of nuclear export signals of NS2 protein of influenza D virus. *Viruses*. 2020;12(10).
115. Orvell C. *Vi rology*. *Arch Virol*. 1992;279–94.
116. Lommer BS, Luo M. Structural plasticity in influenza virus protein NS2 (NEP). *J Biol Chem*. 2002;277(9):7108–17.
117. O’Neill RE, Talon J, Palese P. The influenza virus NEP (NS2 protein) mediates the nuclear export of viral ribonucleoproteins. *EMBO J*. 1998;17(1):288–96.
118. Huang S, Chen J, Chen Q, Wang H, Yao Y, Chen J, et al. A Second CRM1-Dependent Nuclear Export Signal in the Influenza A Virus NS2 Protein Contributes to the Nuclear Export of Viral Ribonucleoproteins. *J Virol*. 2013;87(2):767–78.
119. Chutiwitoonchai N, Mano T, Kakisaka M, Sato H, Kondoh Y, Osada H, et al. Inhibition of CRM1-mediated nuclear export of influenza A nucleoprotein and nuclear export protein as a novel target for antiviral drug development. *Virology* . 2017;507(March):32–9. Available from: <http://dx.doi.org/10.1016/j.virol.2017.04.001>
120. Gottschalk A. Chemistry of virus receptors. *Viruses*. 1959;3:51–61.
121. Palese P. Orthomyxoviridae: the viruses and their replication. *Fields Virol*. 2007;1647–89.
122. Karakus U, Pohl MO. Breaking the Convention : Sialoglycan Variants , Coreceptors , .
123. Chan CM, Chu H, Zhang AJ, Leung LH, Sze KH, Kao RYT, et al. Hemagglutinin of influenza A virus binds specifically to cell surface nucleolin and plays a role in virus internalization. *Virology* . 2016;494:78–88. Available from: <http://dx.doi.org/10.1016/j.virol.2016.04.008>
124. Ho JW, Hershkovitz O, Peiris M, Zilka A, Bar-Ilan A, Nal B, et al. H5-Type Influenza Virus Hemagglutinin Is Functionally Recognized by the Natural Killer-Activating Receptor NKp44. *J Virol*. 2008;82(4):2028–32.
125. Mandelboim O, Lieberman N, Lev M, Paul L, Arnon TI, Bushkin Y, et al. NKp46_{HA}_Influenza.

- 2001;(Table 1):1055–60.
126. Eierhoff T, Hrincius ER, Rescher U, Ludwig S, Ehrhardt C. The epidermal growth factor receptor (EGFR) promotes uptake of influenza A viruses (IAV) into host cells. *PLoS Pathog.* 2010;6(9).
 127. Fujioka Y, Nishide S, Ose T, Suzuki T, Kato I, Fukuhara H, et al. A Sialylated Voltage-Dependent Ca²⁺ Channel Binds Hemagglutinin and Mediates Influenza A Virus Entry into Mammalian Cells. *Cell Host Microbe* . 2018;23(6):809-818.e5. Available from: <https://doi.org/10.1016/j.chom.2018.04.015>
 128. Byrd-Leotis L, Jia N, Dutta S, Trost JF, Gao C, Cummings SF, et al. Influenza binds phosphorylated glycans from human lung. *Sci Adv.* 2019;5(2):1–10.
 129. Pöhlmann S, Zhang J, Baribaud F, Chen Z, Leslie GJ, Lin G, et al. Hepatitis C Virus Glycoproteins Interact with DC-SIGN and DC-SIGNR. *J Virol.* 2003;77(7):4070–80.
 130. Curtis BM, Scharnowske S, Watson AJ. Sequence and expression of a membrane-associated C-type lectin that exhibits CD4-independent binding of human immunodeficiency virus envelope glycoprotein gp120. *Proc Natl Acad Sci U S A.* 1992;89(17):8356–60.
 131. Lozach PY, Burleigh L, Staropoli I, Navarro-Sanchez E, Harriague J, Virelizier JL, et al. Dendritic cell-specific intercellular adhesion molecule 3-grabbing non-integrin (DC-SIGN)-mediated enhancement of dengue virus infection is independent of DC-SIGN internalization signals. *J Biol Chem.* 2005;280(25):23698–708.
 132. Reading PC, Miller JL, Anders EM. Involvement of the Mannose Receptor in Infection of Macrophages by Influenza Virus. *J Virol.* 2000;74(11):5190–7.
 133. Upham JP, Pickett D, Irimura T, Anders EM, Reading PC. Macrophage Receptors for Influenza A Virus: Role of the Macrophage Galactose-Type Lectin and Mannose Receptor in Viral Entry. *J Virol.* 2010;84(8):3730–7.
 134. Tong S, Zhu X, Li Y, Shi M, Zhang J, Bourgeois M, et al. New World Bats Harbor Diverse Influenza A Viruses. *PLoS Pathog.* 2013;9(10).
 135. Zhu X, Yu W, McBride R, Li Y, Chen LM, Donis RO, et al. Hemagglutinin homologue from H17N10 bat influenza virus exhibits divergent receptor-binding and pH-dependent fusion activities. *Proc Natl Acad Sci U S A.* 2013;110(4):1458–63.
 136. de Vries E, Tscherne DM, Wienholts MJ, Cobos-Jiménez V, Scholte F, García-Sastre A, et al. Dissection of the influenza A virus endocytic routes reveals macropinocytosis as an alternative entry pathway. *PLoS Pathog.* 2011;7(3).
 137. Sieczkarski SB, Whittaker GR. Influenza Virus Can Enter and Infect Cells in the Absence of Clathrin-Mediated Endocytosis. *J Virol.* 2002;76(20):10455–64.
 138. Chen C, Zhuang X. Epsin 1 is a cargo-specific adaptor for the clathrin-mediated endocytosis of the influenza virus. *Proc Natl Acad Sci U S A.* 2008;105(33):11790–5.
 139. Rooks, M.G and Garrett, W.S 2016. HHS Public Access. *Physiol Behav.* 2017;176(3):139–48.
 140. Huotari J, Helenius A. Endosome maturation. *EMBO J.* 2011;30(17):3481–500.
 141. Galloway SE, Reed ML, Russell CJ, Steinhauer DA. Influenza HA Subtypes Demonstrate Divergent Phenotypes for Cleavage Activation and pH of Fusion: Implications for Host Range and Adaptation. *PLoS Pathog.* 2013;9(2).
 142. Wilson IA, Skehel JJ, Wiley DC. Structure of the haemagglutinin membrane glyco^o resolution. *Nature*, protein of influenza virus at 3. a. 1981;289:366–73.
 143. Chen J, Skehel JJ, Wiley DC. N- and C-terminal residues combine in the fusion-pH influenza hemagglutinin HA2 subunit to form an N cap that terminates the triple-stranded coiled coil. *Proc Natl Acad Sci U S A.* 1999;96(16):8967–72.
 144. Benton DJ, Gamblin SJ, Rosenthal PB, Skehel JJ. Structural transitions in influenza haemagglutinin at membrane fusion pH. *Nature.* 2020;583(7814):150–3.
 145. Scott CC, Gruenberg J. Ion flux and the function of endosomes and lysosomes: PH is just the start: The flux of ions across endosomal membranes influences endosome function not only through regulation of the luminal pH. *BioEssays.* 2011;33(2):103–10.

146. Charlton FW, Pearson HM, Hover S, Lippiat JD, Fontana J, Barr JN, et al. Ion Channels as therapeutic targets for viral infections: Further discoveries and future perspectives. *Viruses*. 2020;12(8).
147. Stewart M. Molecular mechanism of the nuclear protein import cycle. *Nat Rev Mol Cell Biol*. 2007;8(3):195–208.
148. Fodor E. The RNA polymerase of influenza A virus: Mechanisms of viral transcription and replication. *Acta Virol*. 2013;57(2):113–22.
149. Jorba N, Coloma R, Ortín J. Genetic trans-complementation establishes a new model for influenza virus RNA transcription and replication. *PLoS Pathog*. 2009;5(5).
150. Paterson D, Fodor E. Emerging Roles for the Influenza A Virus Nuclear Export Protein (NEP). *PLoS Pathog*. 2012;8(12).
151. Mühlbauer D, Dzieciolowski J, Hardt M, Hocke A, Schierhorn KL, Mostafa A, et al. Influenza Virus-Induced Caspase-Dependent Enlargement of Nuclear Pores Promotes Nuclear Export of Viral Ribonucleoprotein Complexes. *J Virol*. 2015;89(11):6009–21.
152. Kawaguchi A, Hirohama M, Harada Y, Osari S, Nagata K. Influenza Virus Induces Cholesterol-Enriched Endocytic Recycling Compartments for Budozone Formation via Cell Cycle-Independent Centrosome Maturation. *PLoS Pathog*. 2015;11(11):1–19.
153. Vale-Costa S, Amorim MJ. Clustering of Rab11 vesicles in influenza A virus infected cells creates hotspots containing the 8 viral ribonucleoproteins. *Small GTPases*. 2017;8(2):71–7.
154. De Castro Martin IF, Fournier G, Sachse M, Pizarro-Cerda J, Risco C, Naffakh N. Influenza virus genome reaches the plasma membrane via a modified endoplasmic reticulum and Rab11-dependent vesicles. *Nat Commun* . 2017;8(1). Available from: <http://dx.doi.org/10.1038/s41467-017-01557-6>
155. Gerl MJ, Sampaio JL, Urban S, Kalvodova L, Verbavatz JM, Binnington B, et al. Quantitative analysis of the lipidomes of the influenza virus envelope and MDCK cell apical membrane. *J Cell Biol*. 2012;196(2):213–21.
156. Barman S, Adhikary L, Chakrabarti AK, Bernas C, Kawaoka Y, Nayak DP. Role of Transmembrane Domain and Cytoplasmic Tail Amino Acid Sequences of Influenza A Virus Neuraminidase in Raft Association and Virus Budding. *J Virol*. 2004;78(10):5258–69.
157. Zurcher T, Luo G, Palese P. Mutations at palmitoylation sites of the influenza virus hemagglutinin affect virus formation. *J Virol*. 1994;68(9):5748–54.
158. Takeda M, Leser GP, Russell CJ, Lamb RA. Influenza virus hemagglutinin concentrates in lipid raft microdomains for efficient viral fusion. *Proc Natl Acad Sci U S A*. 2003;100(25):14610–7.
159. Chen BJ, Leser GP, Morita E, Lamb RA. Influenza Virus Hemagglutinin and Neuraminidase, but Not the Matrix Protein, Are Required for Assembly and Budding of Plasmid-Derived Virus-Like Particles. *J Virol*. 2007;81(13):7111–23.
160. Chlanda P, Schraidt O, Kummer S, Riches J, Oberwinkler H, Prinz S, et al. Structural Analysis of the Roles of Influenza A Virus Membrane-Associated Proteins in Assembly and Morphology. *J Virol*. 2015;89(17):8957–66.
161. Lewnard JA, Cobey S. Immune history and influenza vaccine effectiveness. *Vaccines*. 2018;6(2):1–14.
162. Oxford JS, Schild GC, Potter CW, Jennings R. The specificity of the anti-haemagglutinin antibody response induced in man by inactivated influenza vaccines and by natural infection. *J Hyg (Lond)*. 1979;82(1):51–61.
163. Kilbourne ED. Comparative Efficacy of Neuraminidase-Specific and Conventional Influenza Virus Vaccines in Induction of Antibody to Neuraminidase in Humans. *J Infect Dis* . 1976 Oct 1;134(4):384–94. Available from: <https://doi.org/10.1093/infdis/134.4.384>
164. Hirst BYGK. <Influenza - 1942 - Hirst 49.pdf>. *Jounal Exp Med*. 1941;75(1):49–64.
165. Paules CI, Marston HD, Eisinger RW, Baltimore D, Fauci AS. The Pathway to a Universal Influenza Vaccine. *Immunity* . 2017;47(4):599–603. Available from: <https://doi.org/10.1016/j.immuni.2017.09.007>

166. Paules CI, McDermott AB, Fauci AS. Immunity to Influenza: Catching a Moving Target To Improve Vaccine Design. *J Immunol*. 2019;202(2):327–31.
167. Ekiert DC, Bhabha G, Elsliger M, Friesen RHE, Jongeneelen M, Throsby M, et al. Conserved Influenza Virus Epitope. *Exposure*. 2009;1857(April):246–51.
168. Ekiert DC, Kashyap AK, Steel J, Rubrum A, Bhabha G, Khayat R, et al. Cross-neutralization of influenza A viruses mediated by a single antibody loop. *Nature*. 2012;489(7417):526–32.
169. Sui J, Hwang WC, Perez S, Wei G, Aird D, Chen LM, et al. Structural and functional bases for broad-spectrum neutralization of avian and human influenza A viruses. *Nat Struct Mol Biol*. 2009;16(3):265–73.
170. Zost SJ, Lee J, Gumina ME, Parkhouse K, Henry C, Wu NC, et al. Identification of Antibodies Targeting the H3N2 Hemagglutinin Receptor Binding Site following Vaccination of Humans. *Cell Rep*. 2019;29(13):4460-4470.e8. Available from: <https://doi.org/10.1016/j.celrep.2019.11.084>
171. Soema PC, Kompier R, Amorij JP, Kersten GFA. Current and next generation influenza vaccines: Formulation and production strategies. *Eur J Pharm Biopharm*. 2015;94:251–63. Available from: <http://dx.doi.org/10.1016/j.ejpb.2015.05.023>
172. Soema PC, Kompier R, Amorij JP, Kersten GFA. Current and next generation influenza vaccines: Formulation and production strategies. *Eur J Pharm Biopharm*. 2015;94:251–63.
173. Belongia EA, Skowronski DM, McLean HQ, Chambers C, Sundaram ME, De Serres G. Repeated annual influenza vaccination and vaccine effectiveness: review of evidence. *Expert Rev Vaccines*. 2017 Jul 3;16(7):723–36. Available from: <https://doi.org/10.1080/14760584.2017.1334554>
174. Janelle J, Montroya, Ryan P, Bowlesb, Lori E, Skibbec, Megan M, McClellandd and FJM. HHS Public Access. *Physiol Behav*. 2017;176(1):139–48.
175. Belongia EA, Simpson MD, King JP, Sundaram ME, Kelley NS, Osterholm MT, et al. Variable influenza vaccine effectiveness by subtype: a systematic review and meta-analysis of test-negative design studies. *Lancet Infect Dis*. 2016 Aug 1;16(8):942–51. Available from: [https://doi.org/10.1016/S1473-3099\(16\)00129-8](https://doi.org/10.1016/S1473-3099(16)00129-8)
176. Dunkle LM, Izikson R, Patriarca P, Goldenthal KL, Muse D, Callahan J, et al. Efficacy of Recombinant Influenza Vaccine in Adults 50 Years of Age or Older. *N Engl J Med*. 2017;376(25):2427–36.
177. Lee JKH, Lam GKL, Shin T, Kim J, Krishnan A, Greenberg DP, et al. Efficacy and effectiveness of high-dose versus standard-dose influenza vaccination for older adults: a systematic review and meta-analysis. *Expert Rev Vaccines*. 2018 May 4;17(5):435–43. Available from: <https://doi.org/10.1080/14760584.2018.1471989>
178. Wilkinson K, Wei Y, Szwajcer A, Rabbani R, Zarychanski R, Abou-Setta AM, et al. Efficacy and safety of high-dose influenza vaccine in elderly adults: A systematic review and meta-analysis. *Vaccine*. 2017;35(21):2775–80. Available from: <http://dx.doi.org/10.1016/j.vaccine.2017.03.092>
179. Camilloni B, Basileo M, Di Martino A, Donatelli I, Iorio AM. Antibody responses to intradermal or intramuscular MF59-adjuvanted influenza vaccines as evaluated in elderly institutionalized volunteers during a season of partial mismatching between vaccine and circulating A(H3N2) strains. *Immun Ageing*. 2014;11(1):1–9.
180. Carter DM, Darby CA, Lefoley BC, Crevar CJ, Alefantis T, Oomen R, et al. Design and Characterization of a Computationally Optimized Broadly Reactive Hemagglutinin Vaccine for H1N1 Influenza Viruses. *J Virol*. 2016;90(9):4720–34.
181. Manuscript A. *Mice and Ferrets*. 2012;29(16):3043–54.
182. Elliott STC, Keaton AA, Chu JD, Reed CC, Garman B, Patel A, et al. A Synthetic Micro-Consensus DNA Vaccine Generates Comprehensive Influenza A H3N2 Immunity and Protects Mice Against Lethal Challenge by Multiple H3N2 Viruses. *Hum Gene Ther*. 2018;29(9):1044–55.

183. Crevar CJ, Carter DM, Lee KYJ, Ross TM. Cocktail of H5N1 COBRA HA vaccines elicit protective antibodies against H5N1 viruses from multiple clades. *Hum Vaccines Immunother.* 2015;11(3):572–83.
184. Bridges-Webb C. Research articles. *Aust Fam Physician.* 2009;38(7):473–473.
185. Dreyfus C, Laursen NS, Kwaks T, Zuijdgeest D, Khayat R, Ekiert DC, et al. NIH Public Access. 2013;337(6100):1343–8.
186. Corti D, Agatic G, Bianchi S, Giacchetto-sasselli I, Calder L, Langedijk JPM, et al. A Neutralizing Antibody Selected from. *Science.* 2011;333(August):850–6.
187. Krammer F, Pica N, Hai R, Margine I, Palese P. Chimeric Hemagglutinin Influenza Virus Vaccine Constructs Elicit Broadly Protective Stalk-Specific Antibodies. *J Virol.* 2013;87(12):6542–50.
188. Hai R, Krammer F, Tan GS, Pica N, Eggink D, Maamary J, et al. Influenza Viruses Expressing Chimeric Hemagglutinins: Globular Head and Stalk Domains Derived from Different Subtypes. *J Virol.* 2012;86(10):5774–81.
189. Yassine HM, McTamney PM, Boyington JC, Ruckwardt TJ, Crank MC, Smatti MK, et al. Use of hemagglutinin stem probes demonstrate prevalence of broadly reactive group 1 influenza antibodies in human sera. *Sci Rep .* 2018;8(1):1–11. Available from: <http://dx.doi.org/10.1038/s41598-018-26538-7>
190. Yoshida R, Igarashi M, Ozaki H, Kishida N, Tomabechi D, Kida H, et al. Cross-protective potential of a novel monoclonal antibody directed against antigenic site B of the hemagglutinin of influenza A viruses. *PLoS Pathog.* 2009;5(3).
191. Eichelberger MC, Monto AS. Neuraminidase, the Forgotten Surface Antigen, Emerges as an Influenza Vaccine Target for Broadened Protection. *J Infect Dis.* 2019;219(Suppl 1):S75–80.
192. Stadlbauer D, Zhu X, McMahon M, Turner JS, Teddy J, Schmitz AJ, et al. HHS Public Access. 2020;366(6464):499–504.
193. Job ER, Ysenbaert T, Smet A, Christopoulou I, Strugnell T, Oloo EO, et al. Broadened immunity against influenza by vaccination with computationally designed influenza virus N1 neuraminidase constructs. *npj Vaccines .* 2018;3(1):1–11. Available from: <http://dx.doi.org/10.1038/s41541-018-0093-1>
194. Kolpe A, Schepens B, Fiers W, Saelens X. M2-based influenza vaccines: recent advances and clinical potential. *Expert Rev Vaccines .* 2017 Feb 1;16(2):123–36. Available from: <https://doi.org/10.1080/14760584.2017.1240041>
195. Neiryck S, Deroo T, Saelens X, Vanlandschoot P, Jou WM, Fiers W. A universal influenza A vaccine based on the extracellular domain of the M2 protein. *Nat Med.* 1999;5(10):1157–63.
196. Ramos EL, Mitcham JL, Koller TD, Bonavia A, Usner DW, Balaratnam G, et al. Efficacy and Safety of Treatment With an Anti-M2e Monoclonal Antibody in Experimental Human Influenza. *J Infect Dis .* 2015 Apr 1;211(7):1038–44. Available from: <https://doi.org/10.1093/infdis/jiu539>
197. Turley CB, Rupp RE, Johnson C, Taylor DN, Wolfson J, Tussey L, et al. Safety and immunogenicity of a recombinant M2e–flagellin influenza vaccine (STF2.4xM2e) in healthy adults. *Vaccine .* 2011;29(32):5145–52. Available from: <https://www.sciencedirect.com/science/article/pii/S0264410X11007614>
198. Bernasconi V, Bernocchi B, Ye L, Lê MQ, Omokanye A, Carpentier R, et al. Porous Nanoparticles With Self-Adjuvanting M2e-Fusion Protein and Recombinant Hemagglutinin Provide Strong and Broadly Protective Immunity Against Influenza Virus Infections. *Front Immunol .* 2018 Sep 12;9:2060. Available from: <https://pubmed.ncbi.nlm.nih.gov/30271406>
199. Mullarkey CE, Boyd A, Van Laarhoven A, Lefevre EA, Veronica Carr B, Baratelli M, et al. Improved adjuvanting of seasonal influenza vaccines: Preclinical studies of MVA-NP+M1 coadministration with inactivated influenza vaccine. *Eur J Immunol.* 2013;43(7):1940–52.
200. Antrobus RD, Berthoud TK, Mullarkey CE, Hoschler K, Coughlan L, Zambon M, et al. Coadministration of seasonal influenza vaccine and MVA-NP+M1 simultaneously achieves potent humoral and cell-mediated responses. *Mol Ther .* 2013/07/08. 2014 Jan;22(1):233–8.

- Available from: <https://pubmed.ncbi.nlm.nih.gov/23831594>
201. Dong G, Peng C, Luo J, Wang C, Han L, Wu B, et al. Adamantane-resistant influenza A viruses in the world (1902-2013): Frequency and distribution of M2 gene mutations. *PLoS One*. 2015;10(3):1–20.
 202. Kamali A, Holodniy M. Influenza treatment and prophylaxis with neuraminidase inhibitors: A review. *Infect Drug Resist*. 2013;6:187–98.
 203. Meijer A, Lackenby A, Hungnes O, Lina B, van der Werf S, Schweiger B, et al. Oseltamivir-Resistant Influenza Virus A (H1N1), Europe, 2007–08 Season. *Emerg Infect Dis*. 2009;15(4):552–60.
 204. Hayden FG, Shindo N. Influenza virus polymerase inhibitors in clinical development. *Curr Opin Infect Dis* . 2019;32(2). Available from: https://journals.lww.com/co-infectiousdiseases/Fulltext/2019/04000/Influenza_virus_polymerase_inhibitors_in_clinical.15.aspx
 205. Hirotsu N, Sakaguchi H, Sato C, Ishibashi T, Baba K, Omoto S, et al. Baloxavir marboxil in Japanese pediatric patients with influenza: Safety and clinical and virologic outcomes. *Clin Infect Dis*. 2020;71(4):971–81.
 206. Song MS, Kumar G, Shadrack WR, Zhou W, Jeevan T, Li Z, et al. Identification and characterization of influenza variants resistant to a viral endonuclease inhibitor. *Proc Natl Acad Sci U S A*. 2016;113(13):3669–74.
 207. Clark MP, Ledebor MW, Davies I, Byrn RA, Jones SM, Perola E, et al. Discovery of a Novel, First-in-Class, Orally Bioavailable Azaindole Inhibitor (VX-787) of Influenza PB2. *J Med Chem* . 2014 Aug 14;57(15):6668–78. Available from: <https://doi.org/10.1021/jm5007275>
 208. Vanderlinden E, Vrancken B, Houdt J Van, Rajwanshi VK, Gillemot S, Andrei G, et al. Distinct Effects of T-705 (Favipiravir) and ribavirin on influenza virus replication and Viral RNA Synthesis. *Antimicrob Agents Chemother*. 2016;60(11):6679–91.
 209. Schroeder Jr HW, Cavacini L. Structure and function of immunoglobulins. *J Allergy Clin Immunol* . 2010 Feb;125(2 Suppl 2):S41–52. Available from: <https://pubmed.ncbi.nlm.nih.gov/20176268>
 210. Schroeder Jr HW, Cavacini L. Structure and function of immunoglobulins. *J Allergy Clin Immunol*. 2010 Feb;125(2 Suppl 2):S41–52.
 211. Vidarsson G, Dekkers G, Rispens T. IgG subclasses and allotypes: from structure to effector functions. *Front Immunol* . 2014 Oct 20;5:520. Available from: <https://pubmed.ncbi.nlm.nih.gov/25368619>
 212. Parren PWHL, Lugovskoy AA. Therapeutic antibody engineering. *MAbs*. 2013;5(2):175–7.
 213. Hooks MA, Wade CS, Millikan Jr. WJ. Muromonab CD-3: A Review of Its Pharmacology, Pharmacokinetics, and Clinical Use in Transplantation. *Pharmacother J Hum Pharmacol Drug Ther* . 1991 Jan 2;11(1):26–37. Available from: <https://doi.org/10.1002/j.1875-9114.1991.tb03595.x>
 214. Hooks MA, Wade CS, Millikan Jr. WJ. Muromonab CD-3: A Review of Its Pharmacology, Pharmacokinetics, and Clinical Use in Transplantation. *Pharmacother J Hum Pharmacol Drug Ther*. 1991 Jan;11(1):26–37.
 215. Baum A, Fulton BO, Wloga E, Copin R, Pascal KE, Russo V, et al. Antibody cocktail to SARS-CoV-2 spike protein prevents rapid mutational escape seen with individual antibodies. *Science* (80-). 2020;369(6506):1014–8.
 216. Logan PGB and GD. NIH Public Access. *Bone* . 2014;23(1):1–7. Available from: <https://www.ncbi.nlm.nih.gov/pmc/articles/PMC3624763/pdf/nihms412728.pdf>
 217. Kallewaard NL, Corti D, Collins PJ, Neu U, McAuliffe JM, Benjamin E, et al. Structure and Function Analysis of an Antibody Recognizing All Influenza A Subtypes. *Cell*. 2016 Jul;166(3):596–608.
 218. Downloaded from https://academic.oup.com/ofid/article/4/suppl_1/S587/4296027 by AB Shetty Memorial Institute of Dental Sciences user on 06 April 2021 Poster Abstracts • OFID

- 2017 : 4 (Suppl 1) • S587. 2017;4(Suppl 1):2017.
219. McBride JM, Lim JJ, Burgess T, Deng R, Derby MA, Maia M, et al. crossm and Efficacy of MHAA4549A , a Broadly Model. 2017;61(11):1–12.
 220. Chames P, Van Regenmortel M, Weiss E, Baty D. Therapeutic antibodies: Successes, limitations and hopes for the future. *Br J Pharmacol*. 2009;157(2):220–33.
 221. Zost SJ, Lee J, Gumina ME, Parkhouse K, Henry C, Wu C, et al. Receptor Binding Site following Vaccination of Humans. 2020;29(13):4460–70.
 222. Makurvet FD. Biologics vs. small molecules: Drug costs and patient access. *Med Drug Discov*. 2021;9:100075.
 223. Brinkmann U, Kontermann RE. The making of bispecific antibodies. *MAbs* . 2017;9(2):182–212. Available from: <http://dx.doi.org/10.1080/19420862.2016.1268307>
 224. Gaiotto T, Ramage W, Ball C, Risley P, Carnell GW, Temperton N, et al. Nanobodies mapped to cross-reactive and divergent epitopes on A(H7N9) influenza hemagglutinin using yeast display. *Sci Rep* . 2021;11(1):1–15. Available from: <https://doi.org/10.1038/s41598-021-82356-4>
 225. Hanke L, Knockenhauer KE, Brewer RC, van Diest E, Schmidt FI, Schwartz TU, et al. The antiviral mechanism of an influenza A virus nucleoprotein-specific single-domain antibody fragment. *MBio*. 2016;7(6).
 226. Bates A, Power CA. David vs. Goliath: The Structure, Function, and Clinical Prospects of Antibody Fragments. *Antibodies*. 2019;8(2):28.
 227. Bird RE. Erratum: Single-chain antigen-binding proteins (*Science* (423)). *Science* (80-). 1989;244(4903):409.
 228. Vazquez-Lombardi R, Phan TG, Zimmermann C, Lowe D, Jermutus L, Christ D. Challenges and opportunities for non-antibody scaffold drugs. *Drug Discov Today* . 2015;20(10):1271–83. Available from: <http://dx.doi.org/10.1016/j.drudis.2015.09.004>
 229. Vazquez-Lombardi R, Phan TG, Zimmermann C, Lowe D, Jermutus L, Christ D. Challenges and opportunities for non-antibody scaffold drugs. *Drug Discov Today*. 2015;20(10):1271–83.
 230. Simeon R, Chen Z. In vitro-engineered non-antibody protein therapeutics. *Protein Cell*. 2018;9(1):3–14.
 231. Skerra A. Alternative non-antibody scaffolds for molecular recognition. *Curr Opin Biotechnol* . 2007;18(4):295–304. Available from: <https://www.sciencedirect.com/science/article/pii/S0958166907000808>
 232. Álvarez-Rodríguez B, Tiede C, Hoste ACR, Surtees RA, Trinh CH, Slack GS, et al. Characterization and applications of a Crimean-Congo hemorrhagic fever virus nucleoprotein-specific affimer: Inhibitory effects in viral replication and development of colorimetric diagnostic tests. *PLoS Negl Trop Dis*. 2020;14(6):1–20.
 233. Sars-cov- A. Liverpool Covid-SMART Pilot. *Sage*. 2020;72(December).
 234. Walser M, Rothenberger S, Hurdiss DL, Schlegel A, Calabro V, Fontaine S, et al. Highly potent anti-SARS-CoV-2 multi-DARPin therapeutic candidates. *bioRxiv*. 2020;1–39.
 235. Stadler LKJ, Hoffmann T, Tomlinson DC, Song Q, Lee T, Busby M, et al. Structure-function studies of an engineered scaffold protein derived from Stefin A. II: Development and applications of the SQT variant. *Protein Eng Des Sel*. 2011;24(9):751–63.
 236. Hoffmann T, Stadler LKJ, Busby M, Song Q, Buxton AT, Wagner SD, et al. Structure-function studies of an engineered scaffold protein derived from Stefin A. I: Development of the SQM variant. *Protein Eng Des Sel*. 2010;23(5):403–13.
 237. Tiede C, Tang AAS, Deacon SE, Mandal U, Nettleship JE, Owen RL, et al. Adhiron: A stable and versatile peptide display scaffold for molecular recognition applications. *Protein Eng Des Sel*. 2014;27(5):145–55.
 238. Tiede C, Bedford R, Heseltine SJ, Smith G, Wijetunga I, Ross R, et al. Affimer proteins are versatile and renewable affinity reagents. *Elife*. 2017;6(c):1–35.
 239. Hesketh EL, Tiede C, Adamson H, Adams TL, Byrne MJ, Meshcheriakova Y, et al. Affimer

- reagents as tools in diagnosing plant virus diseases. *Sci Rep*. 2019;9(1):1–9.
240. O’Connell AD, Morton MJ, Hunter M. Two-pore domain K⁺ channels - Molecular sensors. *Biochim Biophys Acta - Biomembr*. 2002;1566(1–2):152–61.
 241. Jarzembowski JA. Channelopathies. *Pathobiol Hum Dis A Dyn Encycl Dis Mech*. 2014;57(1):194–194.
 242. Müller M, Slivinski N, Todd EJAA, Khalid H, Li R, Karwatka M, et al. Chikungunya virus requires cellular chloride channels for efficient genome replication. *PLoS Negl Trop Dis*. 2019;13(9):1–19.
 243. Costa V V., Del Sarto JL, Rocha RF, Silva FR, Doria JG, Olmo IG, et al. N-Methyl-D-Aspartate (NMDA) receptor blockade prevents neuronal death induced by Zika virus infection. *MBio*. 2017;8(2):1–16.
 244. Capera J, Serrano-Novillo C, Navarro-Pérez M, Cassinelli S, Felipe A. The potassium channel odyssey: Mechanisms of traffic and membrane arrangement. *Int J Mol Sci*. 2019;20(3).
 245. MacKinnon R. Potassium channels. *FEBS Lett*. 2003;555(1):62–5.
 246. Gutman GA, Chandy KG, Adelman JP, Aiyar J, Bayliss DA, Clapham DE, et al. International Union of Pharmacology. XLI. Compendium of Voltage-Gated Ion Channels: Potassium Channels. *Pharmacol Rev*. 2003;55(4):583–6.
 247. Hibino H, Inanobe A, Furutani K, Murakami S, Findlay I, Kurachi Y. Inwardly rectifying potassium channels: Their structure, function, and physiological roles. *Physiol Rev*. 2010;90(1):291–366.
 248. J. *Physiol*. (1952). *Current*. 1951;424–48.
 249. Li N, Wu JX, Ding D, Cheng J, Gao N, Chen L. Structure of a Pancreatic ATP-Sensitive Potassium Channel. *Cell*. 2017;168(1–2):101–110.e10. Available from: <http://dx.doi.org/10.1016/j.cell.2016.12.028>
 250. Miller C. An overview of the potassium channel family. *Genome Biol*. 2000;1(4):1–5.
 251. Gierten J, Ficker E, Bloehs R, Schlömer K, Kathöfer S, Scholz E, et al. Regulation of two-pore-domain (K^{2P}) potassium leak channels by the tyrosine kinase inhibitor genistein. *Br J Pharmacol*. 2008;154(8):1680–90.
 252. Levitz J, Royal P, Comoglio Y, Wdziekonski B, Schaub S, Clemens DM, et al. Heterodimerization within the TREK channel subfamily produces a diverse family of highly regulated potassium channels. *Proc Natl Acad Sci*. 2016 Apr 12;113(15):4194 LP – 4199. Available from: <http://www.pnas.org/content/113/15/4194.abstract>
 253. et al. 2013 Sheean. NIH Public Access. *Bone*. 2008;23(1):1–7.
 254. Mi Hwang E, Kim E, Yarishkin O, Ho Woo D, Han K-S, Park N, et al. A disulphide-linked heterodimer of TWIK-1 and TREK-1 mediates passive conductance in astrocytes. *Nat Commun*. 2014;5(1):3227. Available from: <https://doi.org/10.1038/ncomms4227>
 255. Enyedi P, Czirják G. Molecular background of leak K⁺ currents: Two-pore domain potassium channels. *Physiol Rev*. 2010;90(2):559–605.
 256. Jentsch TJ, Hübner CA, Fuhrmann JC. Ion channels: Function unravelled by dysfunction. *Nat Cell Biol*. 2004;6(11):1039–47.
 257. Jensen BS, Ødum N, Jørgensen NK, Christophersen P, Olesen SP. Inhibition of T cell proliferation by selective block of Ca²⁺-activated K⁺ channels. *Proc Natl Acad Sci U S A*. 1999;96(19):10917–21.
 258. Thompson-Vest N, Shimizu Y, Hunne B, Furness JB. The distribution of intermediate-conductance, calcium-activated, potassium (IK) channels in epithelial cells. *J Anat*. 2006;208(2):219–29.
 259. Zhong YS, Wang J, Liu WM, Zhu YH. Potassium ion channels in retinal ganglion cells (Review). *Mol Med Rep*. 2013;8(2):311–9.
 260. Riss TL, Moravec RA, Niles AL, Duellman S, Benink HA, Worzella TJ, et al. Cell Viability Assays. *Assay Guid Man*. 2004;(Md):1–25. Available from: <http://www.ncbi.nlm.nih.gov/pubmed/23805433>

261. Wang TT, Tan GS, Hai R, Pica N, Petersen E, Moran TM, et al. Broadly protective monoclonal antibodies against H3 influenza viruses following sequential immunization with different hemagglutinins. *PLoS Pathog.* 2010;6(2).
262. Desta IT, Porter KA, Xia B, Kozakov D, Vajda S. Performance and Its Limits in Rigid Body Protein-Protein Docking. *Structure* . 2020;28(9):1071-1081.e3. Available from: <https://doi.org/10.1016/j.str.2020.06.006>
263. Sollott MAASCMJ and; SJ. HHS Public Access. *Physiol Behav.* 2017;176(3):139–48.
264. Rose Khavari Nicholas Dias YP. HHS Public Access. *Physiol Behav.* 2017;176(3):139–48.
265. Liggett. NIH Public Access. *Bone.* 2014;23(1):1–7.
266. Kontziampasis D, Klebl DP, Iadanza MG, Scarff CA, Kopf F, Sobott F, et al. A cryo-EM grid preparation device for time-resolved structural studies. *IUCrJ.* 2019;6:1024–31.
267. Scheres SHW. RELION-3.1-tutorial. *Manuals.* 2013;1–21.
268. Cope J, Heumann J, Hoenger A. Cryo-electron tomography for structural characterization of macromolecular complexes. Vol. 1, *Current Protocols in Protein Science.* 2011. 735–770 p.
269. Wagner T, Merino F, Stabrin M, Moriya T, Antoni C, Apelbaum A, et al. SPHIRE-crYOLO is a fast and accurate fully automated particle picker for cryo-EM. *Commun Biol* . 2019;2(1):1–13. Available from: <http://dx.doi.org/10.1038/s42003-019-0437-z>
270. Markosyan RM, Kielian M, Cohen FS. Fusion Induced by a Class II Viral Fusion Protein, Semliki Forest Virus E1, Is Dependent on the Voltage of the Target Cell. *J Virol.* 2007;81(20):11218–25.
271. Hover S, Foster B, Fontana J, Kohl A, Goldstein SAN, Barr JN, et al. Bunyavirus requirement for endosomal K⁺ reveals new roles of cellular ion channels during infection. *PLoS Pathog.* 2018;14(1):1–21.
272. World Health Organization. *Influenza (Seasonal).* 2018.
273. Pu Z, Xiang D, Li X, Luo T, Shen X, Murphy RW, et al. Potential Pandemic of H7N9 Avian Influenza A Virus in Human. *Front Cell Infect Microbiol.* 2018;8(November):1–7.
274. Hu B, Guo H, Zhou P, Shi ZL. Characteristics of SARS-CoV-2 and COVID-19. *Nat Rev Microbiol* . 2020;(December). Available from: <http://dx.doi.org/10.1038/s41579-020-00459-7>
275. WHO. Covid-19 mortality. 2021.
276. FDA. Remdesivir approved Covid-19. 2020;
277. Administration UF and D. Coronavirus Treatment Acceleration Program (CTAP). FDA website. 2020;1–7.
278. Mancini N, Solforosi L, Clementi N, De Marco D, Clementi M, Burioni R. A potential role for monoclonal antibodies in prophylactic and therapeutic treatment of influenza. *Antiviral Res* . 2011;92(1):15–26. Available from: <http://dx.doi.org/10.1016/j.antiviral.2011.07.013>
279. Vigil A, Frias-Staheli N, Carabeo T, Wittekind M. Airway Delivery of Anti-influenza Monoclonal Antibodies Results in Enhanced Antiviral Activities and Enables Broad-Coverage Combination Therapies. *J Virol.* 2020;94(22):1–20.
280. Wang CC, Chen JR, Tseng YC, Hsu CH, Hung YF, Chen SW, et al. Glycans on influenza hemagglutinin affect receptor binding and immune response. *Proc Natl Acad Sci U S A.* 2009;106(43):18327–32.
281. Ahlquist P. RNA-dependent RNA polymerases, viruses, and RNA silencing. *Science (80-)*. 2002;296(5571):1270–3.
282. Bhatt S, Holmes EC, Pybus OG. The genomic rate of molecular adaptation of the human influenza A virus. *Mol Biol Evol.* 2011;28(9):2443–51.
283. Smith DJ. Mapping the Antigenic and Genetic. *Science (80-)*. 2004;305(July):371–6.
284. Kosik I, Ince WL, Gentles LE, Oler AJ, Kosikova M, Angel M, et al. Influenza A virus hemagglutinin glycosylation compensates for antibody escape fitness costs. *PLoS Pathog.* 2018;14(1).
285. Yang H, Carney PJ, Chang JC, Guo Z, Villanueva JM, Stevens J. Structure and receptor binding preferences of recombinant human A(H3N2) virus hemagglutinins. *Virology* . 2015;477:18–

31. Available from: <http://dx.doi.org/10.1016/j.virol.2014.12.024>
286. Wiley DC, Wilson IA, Skehel JJ. Structural identification of the antibody-binding sites of Hong Kong influenza haemagglutinin and their involvement in antigenic variation. *Nature*. 1981;289(5796):373–8.
287. Stray SJ, Pittman LB. Subtype- and antigenic site-specific differences in biophysical influences on evolution of influenza virus hemagglutinin. *Virology*. 2012;9:1–16.
288. Popova L, Smith K, West AH, Wilson PC, James JA, Thompson LF, et al. Immunodominance of antigenic site B over site a of hemagglutinin of recent H3N2 influenza viruses. *PLoS One*. 2012;7(7).
289. Daniels RS, Douglas AR, Skehel JJ, Wiley DC. Analyses of the antigenicity of influenza haemagglutinin at the pH optimum for virus-mediated membrane fusion. *J Gen Virol*. 1983;64(8):1657–62.
290. Takakusagi Y, Takakusagi K, Sugawara F, Sakaguchi K. Use of phage display technology for the determination of the targets for small-molecule therapeutics. *Expert Opin Drug Discov*. 2010;5(4):361–89.
291. Qiu Y, Stegalkina S, Zhang J, Boudanova E, Park A, Zhou Y, et al. Mapping of a Novel H3-Specific Broadly Neutralizing Monoclonal Antibody Targeting the Hemagglutinin Globular Head Isolated from an Elite Influenza Virus-Immunized Donor Exhibiting Serological Breadth. *J Virol*. 2019;94(6):1–17.
292. Wang Y, Hu D, Wu Y, Ying T. Recent advances in “universal” influenza virus antibodies: the rise of a hidden trimeric interface in hemagglutinin globular head. *Front Med*. 2020;14(2):149–59.
293. Michel MA, Swatek KN, Hospenthal MK, Komander D. Ubiquitin Linkage-Specific Affimers Reveal Insights into K6-Linked Ubiquitin Signaling. *Mol Cell*. 2017 Oct 5;68(1):233-246.e5. Available from: <http://www.ncbi.nlm.nih.gov/pubmed/28943312>
294. Bizebard T, Gigant B, Rigolet P, Rasmussen B, Diat O, Bösecke P, et al. Structure of influenza virus haemagglutinin complexed with a neutralizing antibody. *Nature*. 1995;376(6535):92–4.
295. Xiong X, Corti D, Liu J, Pinna D, Foglierini M, Calder LJ, et al. Structures of complexes formed by H5 influenza hemagglutinin with a potent broadly neutralizing human monoclonal antibody. *Proc Natl Acad Sci U S A*. 2015;112(30):9430–5.
296. Throsby M, van den Brink E, Jongeneelen M, Poon LLM, Alard P, Cornelissen L, et al. Heterosubtypic neutralizing monoclonal antibodies cross-protective against H5N1 and H1N1 recovered from human IgM+ memory B cells. *PLoS One*. 2008;3(12).
297. Ekiert DC, Friesen RHE, Bhabha G, Kwaks T, Yu W, Ophorst C, et al. *Viruses*. 2012;333(6044):843–50.
298. Tan GS, Lee PS, Hoffman RMB, Mazel-Sanchez B, Krammer F, Leon PE, et al. Characterization of a Broadly Neutralizing Monoclonal Antibody That Targets the Fusion Domain of Group 2 Influenza A Virus Hemagglutinin. *J Virol*. 2014;88(23):13580–92.
299. Brandenburg B, Koudstaal W, Goudsmit J, Klaren V, Tang C, Bujny M V., et al. Mechanisms of hemagglutinin targeted influenza virus neutralization. *PLoS One*. 2013;8(12).
300. Weis W, Brown JH, Cusack S, Paulson JC, Skehel JJ, Wiley DC. Structure of the influenza virus haemagglutinin complexed with its receptor, sialic acid. *Nature*. 1988 Jun;333(6172):426–31.
301. Benjamin E, Wang W, McAuliffe JM, Palmer-Hill FJ, Kallewaard NL, Chen Z, et al. A Broadly Neutralizing Human Monoclonal Antibody Directed against a Novel Conserved Epitope on the Influenza Virus H3 Hemagglutinin Globular Head. *J Virol*. 2014;88(12):6743–50.
302. Lee PS, Ohshima N, Stanfield RL, Yu W, Iba Y, Okuno Y, et al. Receptor mimicry by antibody F045-092 facilitates universal binding to the H3 subtype of influenza virus. *Nat Commun*. 2014;5.
303. Kashyap AK, Steel J, Oner AF, Dillon MA, Swale RE, Wall KM, et al. Combinatorial antibody libraries from survivors of the Turkish H5N1 avian influenza outbreak reveal virus neutralization strategies. *Proc Natl Acad Sci U S A*. 2008;105(16):5986–91.

304. Wu Y, Cho MS, Shore D, Song M, Choi JA, Jiang T, et al. A potent broad-spectrum protective human monoclonal antibody crosslinking two haemagglutinin monomers of influenza A virus. *Nat Commun.* 2015;6(China CDC).
305. He W, Tan GS, Mullarkey CE, Lee AJ, Lam MMW, Krammer F, et al. Epitope specificity plays a critical role in regulating antibody-dependent cell-mediated cytotoxicity against influenza A virus. *Proc Natl Acad Sci U S A.* 2016;113(42):11931–6.
306. Rubenstein R. Lines of defence. *Total Telecom.* 2008;(OCT.):32–3.
307. Wang J, Wu Y, Ma C, Fiorin G, Wang J, Pinto LH, et al. Structure and inhibition of the drug-resistant S31N mutant of the M2 ion channel of influenza A virus. *Proc Natl Acad Sci U S A.* 2013;110(4):1315–20.
308. Jones JC, Pascua PNQ, Fabrizio TP, Marathe BM, Seiler P, Barman S, et al. Influenza A and B viruses with reduced baloxavir susceptibility display attenuated in vitro fitness but retain ferret transmissibility. *Proc Natl Acad Sci.* 2020;117(15):8593–601.
309. Spanakis N, Pitiriga V, Gennimata V, Tsakris A. A review of neuraminidase inhibitor susceptibility in influenza strains. *Expert Rev Anti Infect Ther.* 2014;12(11):1325–36. Available from: <https://doi.org/10.1586/14787210.2014.966083>
310. Kadam RU, Wilson IA. Structural basis of influenza virus fusion inhibition by the antiviral drug Arbidol. *Proc Natl Acad Sci U S A.* 2017;114(2):206–14.
311. Kingsley CN, Antanasijevic A, Palka-Hamblin H, Durst M, Ramirez B, Lavie A, et al. Probing the metastable state of influenza hemagglutinin. *J Biol Chem.* 2017;292(52):21590–7.
312. Masson GR, Jenkins ML, Burke JE. An overview of hydrogen deuterium exchange mass spectrometry (HDX-MS) in drug discovery. *Expert Opin Drug Discov.* 2017;12(10):981–94. Available from: <https://doi.org/10.1080/17460441.2017.1363734>
313. Wu NC, Young AP, Al-Mawsawi LQ, Olson CA, Feng J, Qi H, et al. High-throughput profiling of influenza A virus hemagglutinin gene at single-nucleotide resolution. *Sci Rep.* 2014;4:1–8.
314. Dongen MJP Van, Kadam RU, Juraszek J, Lawson E, Brandenburg B, Schmitz F, et al. *virus.* 2019;363(6431):1–28.
315. Masson L, Mazza A, De Crescenzo G. Determination of Affinity and Kinetic Rate Constants Using Surface Plasmon Resonance. In: Holst O, editor. *Bacterial Toxins: Methods and Protocols.* Totowa, NJ: Humana Press; 2000. p. 189–201. Available from: <https://doi.org/10.1385/1-59259-052-7:189>
316. Mathew NR, Angeletti D. Recombinant Influenza Vaccines: Saviors to Overcome Immunodominance. *Front Immunol.* 2020;10(January):1–10.
317. Lee PS, Zhu X, Yu W, Wilson IA. Design and Structure of an Engineered Disulfide-Stabilized Influenza Virus Hemagglutinin Trimer. *J Virol.* 2015;89(14):7417–20.
318. Zi Tan Y, Baldwin PR, Davis JH, Williamson JR, Potter CS, Carragher B, et al. Addressing preferred specimen orientation in single-particle cryo-EM through tilting. *Nat Methods.* 2017;14(8):793–6.
319. Tan YZ, Rubinstein JL. Through-grid wicking enables high-speed cryoEM specimen preparation. *Acta Crystallogr Sect D Struct Biol.* 2020;76:1092–103.
320. Noble AJ, Wei H, Dandey VP, Zhang Z, Tan YZ, Potter CS, et al. Reducing effects of particle adsorption to the air–water interface in cryo-EM. *Nat Methods.* 2018;15(10):793–5. Available from: <http://dx.doi.org/10.1038/s41592-018-0139-3>
321. Benton DJ, Gamblin SJ, Rosenthal PB, Skehel JJ. Structural transitions in influenza haemagglutinin at membrane fusion pH. *Nature.* 2020;583(7814):150–3. Available from: <http://dx.doi.org/10.1038/s41586-020-2333-6>
322. Scheres SHW. RELION: implementation of a Bayesian approach to cryo-EM structure determination. *J Struct Biol.* 2012 Dec;180(3):519–30.
323. Marzano L, Keith H, Rivlin A, Smith EN, Fazel S. Europe PMC Funders Group Prevention of Suicidal Behavior in Prisons : 2016;37(5):323–34.
324. Waterhouse A, Bertoni M, Bienert S, Studer G, Tauriello G, Gumienny R, et al. SWISS-MODEL:

- homology modelling of protein structures and complexes. *Nucleic Acids Res.* 2018 Jul;46(W1):W296–303.
325. Miles JA, Hobor F, Trinh CH, Taylor J, Tiede C, Rowell PR, et al. Selective Affimers Recognise the BCL-2 Family Proteins BCL-xL and MCL-1 through Noncanonical Structural Motifs**. *ChemBioChem.* 2021;22(1):232–40.
 326. Kanekiyo M, Joyce MG, Gillespie RA, Gallagher JR, Creanga A, Leung K, et al. HHS Public Access. 2019;20(3):362–72.
 327. Krause JC, Tsibane T, Tumphey TM, Huffman CJ, Basler CF, Crowe JE. A Broadly Neutralizing Human Monoclonal Antibody That Recognizes a Conserved, Novel Epitope on the Globular Head of the Influenza H1N1 Virus Hemagglutinin. *J Virol.* 2011;85(20):10905–8.
 328. Benhaim M, Lee KK. Single-Molecule Analysis of a Viral Fusion Protein Illuminates a Fusion-Active Intermediate State. *Cell.* 2018;174(4):775–7. Available from: <https://doi.org/10.1016/j.cell.2018.07.026>
 329. Bajic G, Maron MJ, Adachi Y, Onodera T, McCarthy KR, McGee CE, et al. Influenza Antigen Engineering Focuses Immune Responses to a Subdominant but Broadly Protective Viral Epitope. *Cell Host Microbe.* 2019;25(6):827-835.e6. Available from: <https://doi.org/10.1016/j.chom.2019.04.003>
 330. Bangaru S, Lang S, Schotsaert M, Vandervlen HA, Zhu X, Kose N, et al. A Site of Vulnerability on the Influenza Virus Hemagglutinin Head Domain Trimer Interface. *Cell.* 2019;177(5):1136-1152.e18.
 331. Watanabe A, McCarthy KR, Kuraoka M, Schmidt AG, Onodera T, Tonouchi K, et al. HHS Public Access. 2020;177(5):1124–35.
 332. Turner H, Pallesen J, Lang S, Bangaru S, Urata S, Li S, et al. Potent anti-influenza H7 human monoclonal antibody induces separation of hemagglutinin receptor binding head domains. *bioRxiv.* 2018;436642.
 333. Strauch EM, Bernard SM, La D, Bohn AJ, Lee PS, Anderson CE, et al. Computational design of trimeric influenza-neutralizing proteins targeting the hemagglutinin receptor binding site. *Nat Biotechnol.* 2017;35(7):667–71.
 334. Wu NC, Wilson IA. anti-influenza therapies. 2018;25(February).
 335. Carter PJ. Introduction to current and future protein therapeutics: A protein engineering perspective. *Exp Cell Res.* 2011;317(9):1261–9. Available from: <http://dx.doi.org/10.1016/j.yexcr.2011.02.013>
 336. Marsh M. The entry of enveloped viruses into cells by endocytosis. *Biochem J.* 1984;218(1):1–10.
 337. Farre C, Fertig N. New strategies in ion channel screening for drug discovery: Are there ways to improve its productivity? *Expert Opin Drug Discov.* 2014;9(10):1103–7.
 338. Royle J, Dobson SJ, Müller M, Macdonald A. Emerging roles of viroporins encoded by DNA viruses: Novel targets for antivirals? *Viruses.* 2015;7(10):5375–87.
 339. To J, Torres J. Viroporins in the Influenza Virus. *Cells.* 2019;8(7):654.
 340. Yoshimura A, Ohnishi S. Uncoating of influenza virus in endosomes. *J Virol.* 1984;51(2):497–504.
 341. Rust MJ, Lakadamyali M, Zhang F, Zhuang X. Assembly of endocytic machinery around individual influenza viruses during viral entry. *Nat Struct Mol Biol.* 2004;11(6):567–73.
 342. Mould JA, Li HC, Dudlak CS, Lear JD, Pekosz A, Lamb RA, et al. Mechanism for proton conduction of the M2 ion channel of influenza A virus. *J Biol Chem.* 2000;275(12):8592–9. Available from: <http://dx.doi.org/10.1074/jbc.275.12.8592>
 343. Mustafa M, Henderson DJ, Busath DD. Free-energy profiles for ions in the influenza M 2-TMD channel. *Proteins Struct Funct Bioinforma.* 2009;76(4):794–807.
 344. Hover S, King B, Hall B, Loundras EA, Taqi H, Daly J, et al. Modulation of potassium channels inhibits bunyavirus infection. *J Biol Chem.* 2016;291(7):3411–22. Available from: <http://dx.doi.org/10.1074/jbc.M115.692673>

345. Punch EK, Hover S, Blest HTW, Fuller J, Hewson R, Fontana J, et al. Potassium is a trigger for conformational change in the fusion spike of an enveloped RNA virus. *J Biol Chem*. 2018;293(26):9937–44.
346. Dubey RC, Mishra N, Gaur R. G protein-coupled and ATP-sensitive inwardly rectifying potassium ion channels are essential for HIV entry. *Sci Rep* . 2019;9(1):1–9. Available from: <http://dx.doi.org/10.1038/s41598-019-40968-x>
347. Dobson SJ, Mankouri J, Whitehouse A. Identification of potassium and calcium channel inhibitors as modulators of polyomavirus endosomal trafficking. *Antiviral Res*. 2020;179(April).
348. Sanchez DY, Blatz AL. Block of neuronal fast chloride channels by internal tetraethylammonium ions. *J Gen Physiol*. 1994;104(1):173–90.
349. Peluffo RD, Hara Y, Berlin JR. Quaternary Organic Amines Inhibit Na,K Pump Current in a Voltage-dependent Manner: Direct Evidence of an Extracellular Access Channel in the Na,K-ATPase. *J Gen Physiol*. 2004;123(3):249–63.
350. Tripathi S, Pohl MO, Zhou Y, Rodriguez-frandsen A, Wang G, Stein DA, et al. HHS Public Access. 2016;18(6):723–35.
351. Wishart DS, Knox C, Guo AC, Cheng D, Shrivastava S, Tzur D, et al. DrugBank: A knowledgebase for drugs, drug actions and drug targets. *Nucleic Acids Res*. 2008;36(SUPPL. 1):901–6.
352. Di Trani L, Savarino A, Campitelli L, Norelli S, Puzelli S, D’Ostilio D, et al. Different pH requirements are associated with divergent inhibitory effects of chloroquine on human and avian influenza A viruses. *Virology*. 2007;4:1–8.
353. Banerjee I, Yamauchi Y, Helenius A, Horvath P. High-Content Analysis of Sequential Events during the Early Phase of Influenza A Virus Infection. *PLoS One*. 2013;8(7):1–9.
354. Zhirnov OP. Solubilization of matrix protein M1/M from virions occurs at different pH for orthomyxo- and paramyxoviruses. *Virology*. 1990;176(1):274–9.
355. Steinberg BE, Touret N, Vargas-Caballero M, Grinstein S. In situ measurement of the electrical potential across the phagosomal membrane using FRET and its contribution to the proton-motive force. *Proc Natl Acad Sci U S A*. 2007;104(22):9523–8.
356. Martin K, Helenius A. Nuclear transport of influenza virus ribonucleoproteins: The viral matrix protein (M1) promotes export and inhibits import. *Cell*. 1991;67(1):117–30.
357. Choppin PW. Multiplication of two kinds of influenza A2 virus particles in monkey kidney cells. *Virology* . 1963;21(3):342–52. Available from: <https://www.sciencedirect.com/science/article/pii/0042682263901958>
358. Fontana J, Steven AC. from electron microscopy. 2016;86–97.
359. Fontana J, Cardone G, Heymann JB, Winkler DC, Steven AC. Structural Changes in Influenza Virus at Low pH Characterized by Cryo-Electron Tomography. *J Virol*. 2012;86(6):2919–29.
360. Caggiano A, Blight A, Parry TJ. Effects of dalfampridine and its metabolites on cloned human potassium channels K v 1.1, K v 1.2, and K v 1.4 expressed in human embryonic kidney cells . *J Drug Assess*. 2013;2(1):58–66.
361. Chen R, Chung SH. Structural Basis of the Selective Block of Kv1.2 by Maurotoxin from Computer Simulations. *PLoS One*. 2012;7(10):1–8.
362. Huotari J, Helenius A. Endosome maturation. *EMBO J* . 2011;30(17):3481–500. Available from: <http://dx.doi.org/10.1038/emboj.2011.286>
363. Russell CJ. Hemagglutinin stability and its impact on influenza a virus infectivity, pathogenicity, and transmissibility in avians, mice, swine, seals, ferrets, and humans. *Viruses*. 2021;13(5).
364. Sugita Y, Noda T, Sagara H, Kawaoka Y. Ultracentrifugation deforms unfixed influenza A virions. *J Gen Virol*. 2011;92(11):2485–93.
365. Steven M. Singer#, Marc Y. Fink VVA. HHS Public Access. *Physiol Behav*. 2019;176(3):139–48.
366. Ye Z, Liu T, Offringa DP, McInnis J, Levandowski RA. Association of Influenza Virus Matrix

- Protein with Ribonucleoproteins. *J Virol.* 1999;73(9):7467–73.
367. Baudin F, Petit I, Weissenhorn W, Ruigrok RWH. In vitro dissection of the membrane and RNP binding activities of influenza virus M1 protein. *Virology.* 2001;281(1):102–8.
368. Karlas A, Machuy N, Shin Y, Pleissner KP, Artarini A, Heuer D, et al. Genome-wide RNAi screen identifies human host factors crucial for influenza virus replication. *Nature.* 2010;463(7282):818–22.
369. Wang AC, Dinesh RK, Qu Y, Rustagi A, Erdemic ET, Tanudtanud K, et al. 1,2,3,† . 2021;1–25.